UNIVERSITAT DE BARCELONA

Computational methods applied to chemical engineering

Ruben Cabello Gallego

UNIVERSITAT DE BARCELONA

Programa de doctorat d'Enginyeria i Ciències aplicades

Computational methods applied to chemical engineering

Ruben Cabello Gallego

Directors
Dra. Alexandra Plesu Popescu i Dr. David Curcó Cantarell
Tutor
Dr. Joan Llorens Llacuna
Departament d'Enginyeria Química i Química Analítica
Universitat de Barcelona

UNIVERSITAT DE BARCELONA

Programa de doctorat d'Enginyeria i Ciències aplicades

Mètodes computacionals aplicats a l'Enginyeria Química

Ruben Cabello Gallego

Directors
Dra. Alexandra Plesu Popescu i Dr. David Curcó Cantarell
Tutor
Dr. Joan Llorens Llacuna
Departament d'Enginyeria Química i Química Analítica
Universitat de Barcelona

Publications derived from this thesis

Heat transfer in pipes with twisted tapes: CFD simulations and validation

Cabello, R., Plesu Popescu, A.E., Bonet-Ruiz, J., Curcó Cantarell, D., Llorens, J.

Computers and Chemical Engineering, 2022, 166, 107971

Validation of CFD Models for Double-Pipe Heat Exchangers with Empirical Correlations

Cabello, R., Popescu, A.E.P., Bonet-Ruiz, J., Cantarell, D.C., Llorens, J.

Chemical Engineering Transactions, 2021, 88, pp. 1243–1248

Discrete Element Method Optimization Simulation of Planetary Ball Mills Operating Conditions

Cabello, R., Han, J., Plesu Popescu, A.E., Barreneche, C., Dosta, S.

Chemical Engineering Transactions, 2024, 114, pp. 571–576

Performance Evaluation of CFD and Gaussian Plume Models: Application in the Prairie Grass Project

Ruben Cabello, Carles Troyano Ferré, Alexandra Elena Plesu Popescu, Jordi Bonet, Joan Llorens, and Raúl Arasa Agudo

Submitted to Sustainability Journal, under review.

Funding

The author of this thesis, his directors and tutor would like to thank the financial support of the Fundació Privada Mir Puig who provided the opportunity to complete this research.

Part of the research of thesis has been done in the scope of the Thermodust project, which provided financial support for its realization.

Acknowledgments

After so many years of dedication, there are moments when the journey can feel burdensome.

This section is dedicated to all those who have selflessly contributed to the progress of this thesis.

My sincerest gratitude goes to Dr. Joan Llorens, the architect of this project and a pioneer of the ideas reflected in it. He gave me the opportunity to embark on this adventure and secured resources from the Mir Puig Private Foundation to help bring it to fruition.

To my office colleagues, Dr. Alexandra Plesu and Dr. Jordi Bonet. To her, for always looking out for me, encouraging me, and always having a word of support or a thoughtful reflection when I was feeling down. To him, for deeply engaging with my thesis despite not being my supervisor or tutor, always offering good advice and maintaining a cheerful and constructive attitude. Both of them have been like my "academic parents." I couldn’t have had better mentors on this path I have chosen.

To Dr. Sergi Dosta and Dr. Camila Barreneche, for welcoming me into the Thermodust project and providing me with knowledge and resources that allowed me to work in the field of Materials Engineering, a discipline outside my expertise.

To Dr. David Curcó, for his attention to detail and precision in correcting the bold claims that I, somewhat recklessly and without much rigor, made throughout my thesis.

To the future Dr. Carles Troyano, fellow PhD candidate and adventure companion, with whom I have endured the struggle of trying to meet a reviewer's demands or navigating the endless university bureaucracy.

To Genís Clavé, who made the meetings and presentations of the Thermodust project more enjoyable and, most importantly, shorter.

To Keong, Lorena, Carlos, Mar, and Xavi, all future doctors, who helped make the long hours at the faculty more bearable.

To my parents and my sister, who, always concerned about me, somehow managed to ask the most piercing question one can ask a PhD student: "When are you finishing your thesis?" I know very well that they have endured my disorder, distraction, and stress throughout this time. Despite this, they have always been by my side, offering me unconditional support.

To my partner, Maria, the person who has spent the most hours enduring me turning my back on her while staring at this Word document or some article on fluid dynamics. Without her empathy, love, and motivation, these years would have been much harder. For the immense amount of emotional support she has given me, she deserves at least an honorary doctorate in psychology.

To all the people and animals who have accompanied me throughout these years, thank you very much.

Agraïments

Després de tants anys de dedicació, hi ha moments en els quals el camí es pot fer feixuc. Aquesta secció és per a tots aquells que, de manera desinteressada, han contribuït al progrés d'aquesta tesi.

Els meus més sincers agraïments al Dr. Joan Llorens, arquitecte d'aquest projecte i pioner en les idees que en ell es reflecteixen, qui em va donar l'oportunitat d'embarcar-me en aquesta aventura i va aconseguir recursos de la mà de la Fundació Privada Mir Puig per a tirar-ho endavant.

Als meus companys de despatx, la Dra. Alexandra Plesu i el Dr. Jordi Bonet. A ella, per estar sempre pendent de mi donant-me empenta, sempre tenint una paraula d'ànim o una reflexió encertada quan tinc una davallada. A ell, per implicar-se profundament en la meva tesi tot i no ser un director ni tutor i tenir sempre un bon consell i una actitud alegre i constructiva. Tots dos han estat com els meus "pares acadèmics". No podria haver tingut millors referents en aquest camí que he escollit.

Al Dr. Sergi Dosta i a la Dra. Camila Barreneche, per acollir-me al projecte Thermodust i proporcionar-me coneixements i recursos que m'han permès treballar en l'àmbit de l'Enginyeria de Materials, una disciplina que no és la meva especialitat.

Al Dr. David Curcó, per la seva atenció al detall i precisió a l'hora de corregir les agosarades afirmacions que, alegrement i sense gaire rigor, anava deixant per la tesi.

Al futur Dr. Carles Troyano, company de doctorat i d'aventures, amb qui tantes penes he passat per intentar complir els desitjos d'un reviewer o completant la interminable burocràcia associada a la universitat. Al Genís Clavé, amb qui les reunions i exposicions del projecte Thermodust se'm feien més amenes i, sobretot, curtes. Al Keong, la Lorena, el Carlos, la Mar i el Xavi, tots futurs doctors, que han ajudat a amenitzar les hores que hem passat a la Facultat.

Als meus pares i a la meva germana, els quals, sempre preocupats per mi, trobaven el millor moment per fer la pregunta més afilada que es pot fer a un doctorand: "Quan acabes la tesi?". Jo sé de bona tinta que ells han patit el meu desordre, distracció i estrès durant aquest temps. Tot i així, sempre han estat al meu costat i m'han donat incondicional suport.

A la meva parella Maria, la persona que durant més hores ha suportat que li donés l'esquena tot mirant aquest full de Word o algun article de dinàmica de fluids. Sense la seva empatia, amor i motivació se m'haguessin fet molt més feixucs tots aquests anys. Per la immensa quantitat de suport emocional que m'ha donat, ella es mereix com a mínim un doctorat honorífic en psicologia.

A totes aquelles persones i animals que m'han acompanyat al llarg d'aquests anys, moltes gràcies.

Acronyms list

Acronym	Definition
AEGL	Acute Exposure Guideline Levels
ALOHA	Areal Locations of Hazardous Atmospheres
BLEVE	Boiling Liquid Expanding Vapor Explosions
BSL	Baseline k-ω turbulent model
CAMEO	Computer-Aided Management of Emergency Operations
CFD	Computational Fluid Dynamics
CRL	Cell Refine Level
DEM	Discrete Element Method
DFT	Density Functional Theory
EWT	Enhanced Wall Treatment
GPM	Gaussian Plume Model
HDNNP	High-Dimensional Neural Network Potential
INSST	Instituto Nacional de Seguridad e Salud en el Trabajo
LES	Large Eddy Simualtion
Low-Re	Low Reynolds correction for the k-ω turbulent model
MAE	Mean Absolute Error
MAPE	Mean Absolute Percentage Error
MD	Molecular Dynamics
ML	Menther-Lechner
N1	Geometrical parameter related to the width of the corrugated tube
N2	Geometrical parameter related to the pitch of the twisted tape (also defined as TR)
N3	Geometrical parameter related to the height of the corrugated tube
NEWF	Non-equilibrium wall functions
NIST	National Institute of Standards and Technology
NOAA	National Oceanic and Atmospheric Administration
NP	Power Number
NS	Navier Stokes

NVT	Ensemble in MD with constant particle number N, constant volume V and a temperature fluctuating around an equilibrium value.
PBM	Population Balance Model
PSD	Particle Size Distribution
RANS	Reynolds Averaged Navier Stokes
RSM	Reynolds Stress Models
SST	Shear Stress Transport k-ω turbulent model
SWF	Scalable Wall Functions
TPF	Thermal Performance Factor
TR	Twist Ratio of a twisted tape insert
TT	Twisted Tape
URF	Under-relaxation factor
VCE	Vapour cloud explosions
VOF	Volume of Fluid

Figure list

8. Flow in partially full pipes' results

9. Results of simulations in Materials Engineering

Thesis contents

Summary

Computational tools, and more specifically Computational Fluid Dynamics (CFD) have seen a rapid development and increase in use in recent years thanks to the exponential growth that computing power experiences every few years. These techniques have been historically implemented by physicists and aerospace engineers to unravel the complex turbulence phenomena and aid in the design of new aircrafts or fast land vehicles. Nowadays, these tools are starting to see use in all kinds of engineering environments, including chemical engineering. This thesis is based on the evaluation of the usefulness and accuracy of various methods of computer simulation applied to chemical and materials engineering units. The thesis is divided into various Chapters, each studying different units chosen for having a characteristic phenomenon occurring on them. In Chapters 5-10 CFD is used in different scenarios that are fundamental of chemical engineering. Chapter 11 is based on aiding in the development of new nanomaterials by using various computational tools and techniques, that range from the atomic scale to a full unit.

Chapter 5 is dedicated to heat transfer. In this Chapter different configurations of heat exchangers are studied via CFD with increasing geometrical complexity. First, a simple double pipe heat exchanger is simulated, and the results of various turbulent modelling techniques are compared against semiempirical correlations used historically by chemical engineers. Next, a similar study is conducted for tubes with a passive heat transfer enhancement insert: the twisted tape. These inserts induce turbulence by creating a swirling motion inside the tube. For these units there are still some correlations and experimental data to compare them against. Finally, a new type of heat exchanger is created combining various passive heat transfer enhancement techniques: the twisted tape and an extended corrugated surface. The geometry of this new unit is optimized based on the geometrical parameters of the system and the efficiency of the heat exchanger is maximized.

In Chapter 6, other important transport phenomenon is studied: mass transfer. For such task an atmospheric gas release is studied with CFD. Numerous experimental points of gas dispersion on plain terrain are reproduced with CFD and other classical modelling tools like Gaussian plume model (GPM) or the software ALOHA (Areal Locations of Hazardous Atmospheres) developed by the National Oceanic and Atmospheric Administration (NOAA). All these tools are compared against each other and the experimental points to assess their accuracy in this scenario. Additionally, Aloha and CFD tools are compared in a case with obstacles, where the differences between the two may be more extreme than when studying simple terrain.

Chapter 7 revolves around momentum transfer, which is especially important in agitation of highly viscous fluids like the ones found in polymerization reactors. Here, a batch agitated reactor is studied with different fluid viscosities and the relationship between the agitation Reynolds number (dependant on the viscosity) and the power required to agitate is found. Moreover, different agitator blade angles are tested to discern which one better

suits the specific operational requirements (more power efficiency, enhanced heat transfer or faster product mixing among others).

A study of multiphase flow is conducted in Chapter 8, where partially filled pipes or canals are studied with CFD. This type of flows have been historically modelled with the Manning equation, which relates slope angle, fluid flow, depth and velocity. With CFD an analysis of the Manning coefficients has been performed for simple half-filled pipes. The flow stabilization is analysed at different entrance conditions at the inlet of the pipe. Additionally, an elbow geometry is studied and its effect on the flow structures that are created as the fluid passes through it.

Lastly, Chapter 9 is a compilation of different studies performed in the scope of the European project "Thermodust", which aims at creating new dust nanomaterials with various thermal properties. For this part, various types of simulations are performed, as the process of producing these nanomaterials must be understood from an industrial perspective but also taking into account the interatomic interactions of the powder. For studying the production process, performed in a planetary mill, this unit is studied by Discrete Element Method (DEM) different conditions found in experimental. Feedback with experimental procedures is provided both ways: simulations used experimental feedback to validate and create the particle comminution modelling and experimental then uses simulation feedback to scale and improve the process efficiency and powder quality. To study the collision between particles inside the mill, Finite Element Analysis is conducted with the software LS-DYNA from Ansys. Finally, to better understand the materials interactions, different Molecular Dynamics simulations (MD) are performed. These simulations are realized accurately thanks to the use of a neural network that was trained using Density Functional Theory (DFT). The simulations performed with DFT for the training of the neural network is an *ab initio* technique that estimates different atomic interactions present on the system with quantum mechanics.

This thesis looks over a vast variety of themes in chemical engineering and analyses them via simulation tools like CFD. The studied cases are closely examined thanks to these microscopical simulation methods, and they are optimized and improved when possible. The sum of the techniques detailed in this thesis and many more, constitutes a clear advancement in engineering design and analysis that will keep growing in importance and use especially for chemical and materials engineering, where empirical correlations that are decades old are still the preferred design choice.

Keywords

CFD, DEM, simulation, modeling, heat transfer, gas dispersion, rheology, DFT, FEA.

Resum

Les eines computacionals estan transformant la investigació en diversos camps, inclosa l'Enginyeria Química. Aquesta tesi explora l'aplicació de mètodes computacionals avançats en processos i operacions unitàries d'aquesta disciplina, centrant-se en la Dinàmica de Fluids Computacional (CFD). A través de CFD, s'analitzen interaccions de fluids a petita escala en problemes fonamentals de l'Enginyeria Química com intercanviadors de calor, sistemes de dispersió de gasos, reactors de tanc agitat i fluxos a canal obert, aportant nous coneixements sobre fenòmens de transport i optimització de sistemes.

Un dels focus principals és l'estudi d'intercanviadors de calor, essencials en la transferència d'energia. S'analitzen diverses configuracions amb CFD, des d'un intercanviador de doble tub fins a dissenys innovadors amb cintes trenades i superfícies corrugades, optimitzant l'eficiència tèrmica. També s'investiga la dispersió de gasos mitjançant CFD, comparant els resultats amb models tradicionals com el Model de Ploma Gaussiana i el programari ALOHA de la NOAA, destacant la capacitat del CFD per millorar la predicció en escenaris reals.

L'estudi de la transferència de moment es focalitza en reactors de polimerització amb fluids altament viscosos. S'analitza com la viscositat influeix en el nombre de Reynolds i el consum energètic, provant diferents angles de pales per optimitzar la mescla industrial. Per aquest tema també es simulen fluxos multifàsics en canonades parcialment plenes i canals oberts, comparant els resultats amb l'equació de Manning per validar els models hidràulics clàssics envers el CFD.

Finalment, la tesi contribueix al projecte europeu *Thermodust*, que investiga nanomaterials amb propietats tèrmiques avançades. Es fan servir tècniques com la Dinàmica Molecular (MD) i el Mètode d'Elements Discrets (DEM) per estudiar la síntesi i interaccions a escala atòmica, validant resultats experimentals i millorant processos. L'ús d'una xarxa neuronal basada en la Teoria del Funcional de la Densitat (DFT) permet modelar amb precisió aquestes interaccions, connectant la química computacional amb aplicacions industrials.

Aquesta tesi demostra com eines computacionals avançades, com CFD, DEM i MD, milloren la comprensió i optimització de sistemes complexos en Enginyeria Química i de Materials, impulsant el disseny basat en dades i l'eficiència industrial.

Paraules clau

CFD, DEM, simulació, modelització, transferència de calor, dispersió de gasos, reologia, DFT, FEA.

1. Introduction

This section aims to provide the theoretical background to follow the reasoning and contents covered by this thesis. The topics addressed in this research include various transport phenomena themes: momentum, heat and species transfer, applied to various chemical engineering unit operations. First, the historical journey of Computational fluid Dynamics and related tools is followed alongside its relationship with the chemical engineering advancements. Then, the reader is provided with a theorical review on transport phenomena alongside its transition to computational methods for solving its equations. Finally, the different chemical engineering topics simulated with these computational tools are inspected in a detailed manner, covering all the studied cases.

Computational fluid dynamics is a tool that started developing in the 1930s. The need for solving the equations of motion of fluids was firstly of interest of physicists, mathematicians and aerospace engineers that had special interest for different reasons: mathematicians cared about the complexity of resolution of the Navier-Stokes equations, physicists cared mostly about weather prediction and aerospace engineers wanted to study the vortices induced by their aircrafts to predict drag and lift. The combined research of these experts pushed CFD research and has allowed for the creation of more efficient and reliable codes and models. Despite this fact CFD has always been conditioned by the computational power available at the time. CFD started with modest calculations performed about 2D fluid flow cases. Nowadays, the development of faster, more efficient, and more compact computational hardware allows for calculations that the pioneers of CFD could only dream of. The 2D simplifications are no longer necessary, allowing to study full scale flows with even more reliability.

When fluid resolution became a computationally inexpensive task, researchers started to add more transport phenomena equations into the mix: Fourier's heat equation and Fick's equations of species diffusion. The implementation of coupled fluid flow and heat and mass transfer opened a wide range of possible applications allowing for calculations of heat exchange, pollutant dispersion, and many more. Computational fluid dynamics tool then became a useful tool for a variety of disciplines, including chemical engineering.

The design of chemical processes was historically based on empirical correlations and heuristics. When a new process or unit was to be implemented, researchers had to perform optimization with experimental apparatus in pilot plants. The optimal values found in smaller pilot plants were then scaled up to the process, often needing a few in-between steps of scaling to obtain the desired results. When trying to optimize a process or unit, the number of experiments required scales exponentially with the number of parameters considered (2k for factorial designs). This means that for the number of parameters involved even in the simplest chemical reactor researchers had to either dismiss some parameters as non-relevant or perform hundreds or even thousands of experiments, with the associated costs that they require. CFD codes have offered chemical engineering designers a tool to reduce the cost of experimentation considerably. Current CFD codes allow researchers to reproduce the exact conditions they have on their process but

virtually in a machine. Once a virtual model is set up and validated with experimental results, the optimization process can be performed virtually and with the full range of parameters present in the process. The optimal points are then tested experimentally to verify the results and a narrow and guided experimental optimization can be performed if necessary.Fluid dynamics applied to chemical engineering is a tool that started developing in the middle of the XX century, being one of its main milestones the publication of the textbook of Bird et al (1960). Initially, chemical engineering was descriptive of processes, studying each process independently. Later, in the first half of the 20th century, the concept of unit operations was developed which meant that despite there being thousands of processes, they can be achieved by combining a few unit operations that share the same mathematical model, regardless of the process in which they are used. All unit operations are governed by the same principles of conservation of balances at a microscopic level. When deeper knowledge was required in understanding of such unit operations, chemical engineers had to study them with transport phenomena. According to Meyer et al. (2022) the mathematical description of transport phenomena is the second chemical engineering paradigm and ensured the development of quantitative models based on transport phenomena. Since then, computational tools based on transport phenomena developed rapidly and its use exploded in the early 2000s (with Bird's 2001 second edition) alongside the computational power increase described by Moore's Law (Figure1). Since then, researchers have delved deeper into the used of CFD for a diverse range of subjects, increasing the number of publications in which it is involved exponentially, as can be seen in Figure 2.

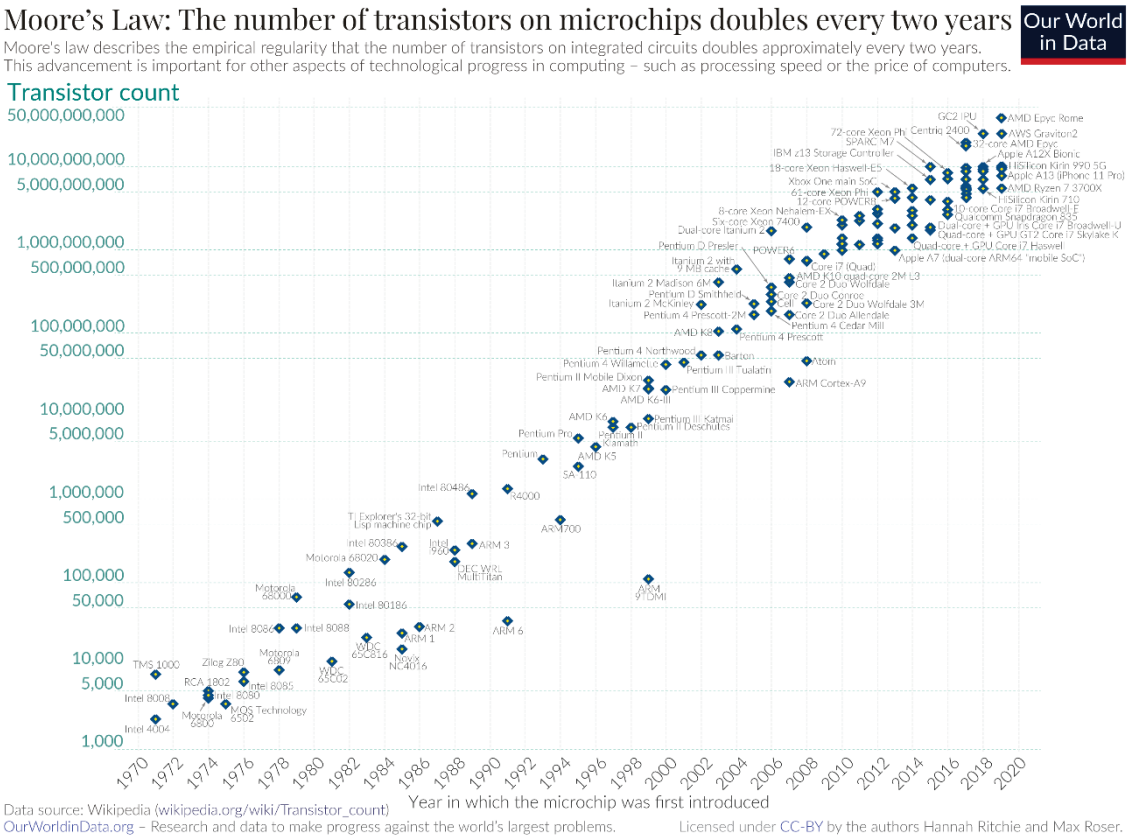

Figure 1: *Moore's law visualization describing the time evolution of the number of transistors in a circuit. (Our World in Data, 2020)*

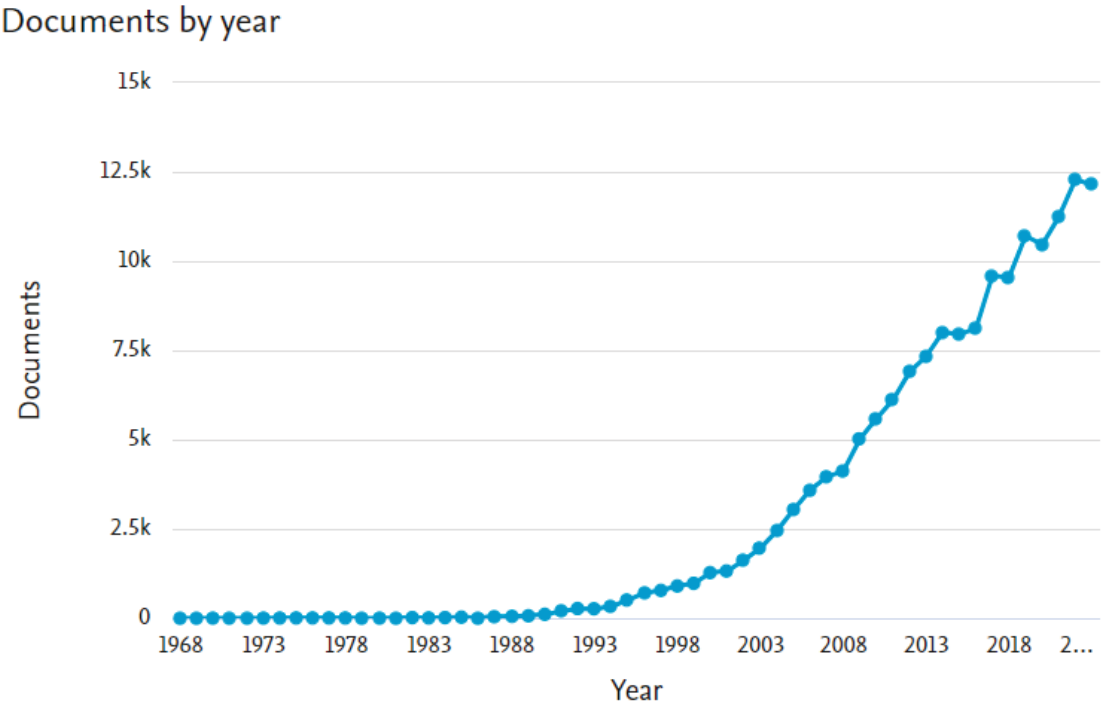

Figure 2: **Documents published by year with search keyword "CFD" on Scopus.**

In the next subsections, the mathematical model that governs any unitary operation will be examined from a transport phenomena perspective. Given that an analytical solution is only feasible for highly simplified cases, section 1.2.1 presents the discretization process required for numerical resolution and justifies the choice of the Finite Volume Method (FVM). Subsequently, section 1.2.2 addresses turbulence modelling, outlining the criteria for selecting an appropriate turbulence model to ensure accurate, consistent, and robust simulations while maintaining reasonable computational costs.

Following this, various case studies will be presented, comparing CFD simulation results with experimental data or established macroscopic models, and optimizing units via simulation when possible once the models are validated.

The first case study, discussed in sections 1.3, 4.1 and 5 evaluates the influence of turbulence model selection on CFD simulation results in the context of a heat exchanger. An optimization is later performed for a distinct heat exchanger geometry.

The second case study, presented in sections 1.4, 4.2 and 6 examines gas dispersion in chimneys, with a focus on turbulence modeling for large-scale systems.

The subsequent case study, in sections 1.5, 4.3 and 7 will examine hydrodynamics inside a reactor, illustrating the capabilities of CFD compared to macroscopic models, which are limited to perfect mixing or plug flow approximations.

Then, in sections 1.6, 4.4 and 8 the case of partially filled pipelines will be presented to demonstrate the simulation of multiphase systems.

Finally, the last case study will focus on milling, showcasing the potential of simulation in unitary operations involving solids, which are difficult to model with macroscopic approaches. In this last case, the Discrete Element Method (DEM), Finite Element Analysis and Density Functional Theory (DFT) simulations are used instead of CFD. This study can be found in sections 1.7, 4.5 and 9.

1.1. Transport phenomena

This section aims at covering the most relevant equations and concepts of transport phenomena, providing enough information to be able to follow this thesis and without an overwhelmingly detailed mathematical formulation.

Transport phenomena are all irreversible processes on the statistical behaviour of molecules incurring the Brownian motion of molecules, that is why it is often called Thermodynamics of Irreversible Processes. The properties of the systems studied in this manner exhibit an average trend which is described by using conservation laws (which describe how a magnitude is conserved with time) and constitutive equations (which describe the relationship between different magnitudes, e.g. how the heat flux responds to a temperature gradient). In short, transport phenomena studies the fundamental mechanisms governing the transfer of momentum, mass and energy. These magnitudes are especially useful for the representation of fluids and the equations that emerge from transport phenomena are the basis for CFD models.

1.1.1. Governing equations

The equations of transport involving momentum, mass and energy all exhibit the same pattern: The flux of said magnitude is proportional to a gradient. This is the basis for the three basic laws of transport phenomena.

In fluid dynamics, transport phenomena analyse the behaviour of fluids (liquids and gases) in motion, encompassing phenomena like laminar and turbulent flow, boundary layer dynamics, and turbulence modelling. This understanding is crucial in optimizing the performance of various engineering systems, from aircraft design to chemical reactors. Molecular momentum transfer is described by Newton's law, Eq. 1:

$$\bar{\bar{\tau}} = -\mu \cdot \nabla \vec{v} \tag{1}$$

Here, $\bar{\bar{\tau}}$ is the shear stress tensor, μ is the viscosity of the fluid and $\nabla \vec{v}$ is the spatial gradient of the velocity vector [Pa].

Mass transfer examines the movement of chemical species within a medium, encompassing diffusion, advection, and chemical reactions. It is vital in processes such as separation technologies (e.g., distillation, chromatography), drug delivery systems, and environmental remediation. Molecular mass transfer is described by Fick's law (Eq. 2):

$$J_k = -D_k \cdot \nabla \omega_k \tag{2}$$

Where J_k is the diffusion flux, which is the amount of substance k that will flow through a unit area during a unit time [kg/ (s m^2)], D_k [m^2/s] is the diffusivity of the substance k through its medium and $\nabla \omega_k$ is the spatial gradient of the concentration ω_k [kg/m^3].

Heat transfer within transport phenomena investigates the mechanisms by which thermal energy is transferred between objects or regions due to temperature gradients. This includes conduction, convection, and radiation, which are fundamental to the design of heat exchangers, refrigeration systems, and thermal management solutions in electronics. Molecular heat transfer is described by Fourier's law (Eq. 3):

$$q = -k \cdot \nabla T \tag{3}$$

Similarly to the other two equations, q is the heat flux [J/(s m^2)], k is the conductivity of the material or fluid and ∇T is the spatial gradient of temperature.

The proportional terms in such equations are called transport coefficients and can be rearranged with other quantities in other to obtain the same diffusivity units (Eqs. 4-6):

$$\nu = \frac{\mu}{\rho}\left[\frac{m^2}{s}\right](momentum\ diffusivity) \tag{4}$$

$$D\left[\frac{m^2}{s}\right](mass\ diffusivity) \tag{5}$$

$$\alpha = \frac{k}{C_p\,\rho}\left[\frac{m^2}{s}\right](heat\ diffusivity) \tag{6}$$

From the relationship between such quantities forms dimensionless parameters that describe the differential behaviour of fluids when multiple phenomena are involved. These are the Prandtl, the Schmidt and the Lewis numbers, which describe the relationship between momentum and energy, momentum and mass and mass and energy respectively (Eqs. 7-9):

$$Pr = \frac{\nu}{\alpha} = \frac{c_p\,\mu}{\rho} \tag{7}$$

$$Sc = \frac{\nu}{D} = \frac{\mu}{\rho\,D} \tag{8}$$

$$Le = \frac{\alpha}{D} = \frac{k}{\rho\,D\,c_p} \tag{9}$$

The physical interpretation of these numbers relates to which phenomena develop faster and describes the size relationship between the boundary layers that develop in a system. A clear example is for the Prandtl number, where for a Pr=1 (like in most gases), the thickness of the thermal boundary layer and the momentum boundary layer will be similar. This in turn means that both boundary layers will develop at similar rates.

The generalized equation of transport is conceived by performing the balance of a magnitude in an infinitesimal volume. Here, not only molecular transport is accounted, it is considered for a fluid in motion, which also experiences convection. The terms ordered are (Eq. 10):

Accumulation + In/Out by convection = In/Out by molecular transport + Generation/Destruction

$$\frac{\mathrm{d}\rho\varphi}{\mathrm{dt}} + \nabla\cdot[\rho\cdot\varphi\cdot\vec{v}\,] = \nabla\cdot\Gamma\,\nabla\varphi + S_{\varphi} \tag{10}$$

Where φ is a variable related to mass, energy, or momenta. Γ is the molecular transport coefficient multiplying the quantity gradient, as seen in equations 1-3. S_{φ} is the generation/destruction of such variable. Table 1 describes the different values that the variables in equation 10 can take.

Table 1: *Schematic of the different equations resulting from equation 10*

	φ	Γ	S_{φ}
Mass	1	0	0
Momentum	$\vec{v}$	μ	$-\nabla P + \rho\vec{g}$ *
K species	Y_k	$\rho\, D$	R_k
Temperature	T	K/C_p	Q'''/C_p

***** Not accounting for electric, magnetic, or self-gravitational forces.

As seen in Table 1, the first equation accounts for the conservation of mass, therefore mass is neither diffused nor produced or destructed in the system, which corresponds to equation 11. Second equation stands for momentum, the source of which is generally pressure gradients ($\nabla P\ [\frac{Pa}{m}]$) or gravity ($\vec{g}\ [\frac{m}{s^2}]$) but can be other forces such centrifugal or electromagnetic. Third is the diffusion of specie k (with mass fraction $Y_k\ [-]$) in the fluid and the source term usually relates to the reaction between chemical species $R_k\ [\frac{kg}{s\,m^3}]$. Finally, the energy equation is here displayed in terms of temperature, although it is also often seen in terms of enthalpy per unit mass (h $[m^2/s^2]$). The source term is then the heat produced of absorbed $\frac{Q'''}{C_p}\,[\frac{kg\,K}{s\,m^3}]$.

If only the first two rows of Table 1 are used, then this system becomes the equations of continuity and Navier-Stokes (NS), that describe the motion of a fluid (Eqs. 11-12):

$$\frac{\mathrm{d}\rho}{\mathrm{dt}} + \nabla\cdot[\rho\cdot\vec{v}\,] = 0 \tag{11}$$

$$\frac{\mathrm{d}\rho\vec{v}}{\mathrm{dt}} + \nabla\cdot[\rho\cdot\vec{v}\,\vec{v}^{T}\,] = \nabla\cdot\mu\,\nabla\vec{v} - \nabla P + \rho\vec{g} \tag{12}$$

By utilizing dimensional analysis with the Buckingham Pi Theorem (Buckingham, 1914) the dimensionless Reynolds number for a cylinder whose geometry becomes defined by the diameter (D) is derived (Eq. 13):

$$\mathrm{Re} = \frac{\rho \, v \, D}{\mu} \tag{13}$$

The Reynolds number is then the ratio between inertial and viscous forces and it is used to predict the state of a particular flowing fluid. The vortex structures change shape and size with changing Reynolds numbers. Laminar flow occurs at low Reynolds numbers and has absence of such vortex structures. For the case of flow inside a tube, when Re < 2300 it is considered laminar flow. This type of flow is characterized for being steady thus independent of time. At 2300 < Re < 2900 the flow is in the transition zone between turbulent and laminar. In this region the turbulent structures oscillate periodically. At Re > 2900 the flow regime becomes turbulent, and the turbulence becomes chaotic and aperiodic. Figure 3 represents the laminar and turbulent flow regimes for a pipe.

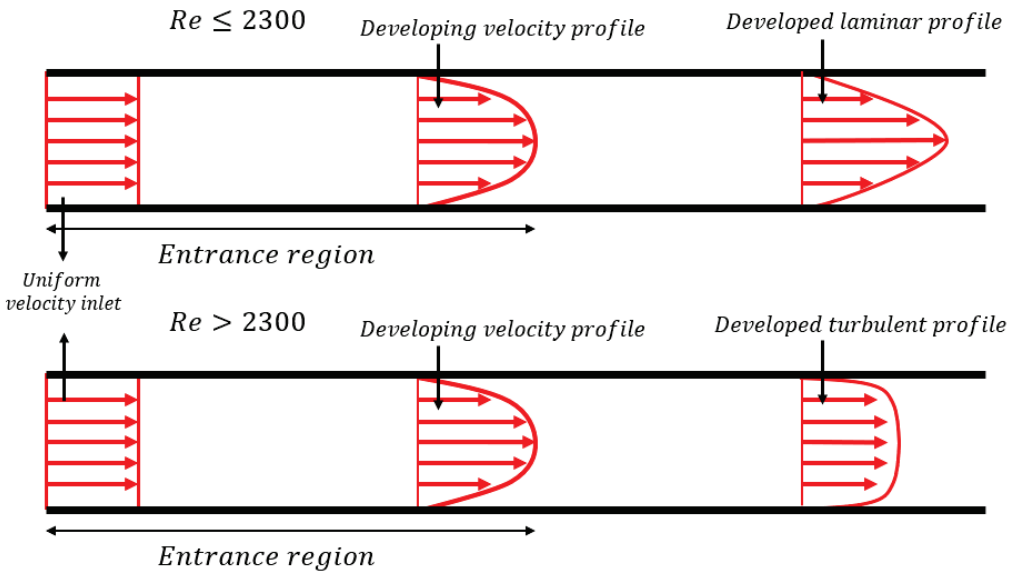

Figure 3: *Velocity profiles of turbulent and laminar flow regimes. The fluid enters the domain with a uniform profile that is shaped depending on the flow regime.*

The Reynolds number depends on the characteristic length, which is different for each studied system. For instance, when studying the appearance of turbulence in a flow past a cylindrical obstacle, the characteristic length is the cylinder diameter. This fact means that turbulence may appear at different Reynolds numbers depending on the system and the characteristic length chosen.

Figure 4 represents the Reynolds effect for a flow across a cylindrical shaped obstacle. The Reynolds number calculated with respect to the cylinder diameter varies from 5 to 10000 and different turbulent structures arise. At Reynolds 5 the flow sticks to the cylindrical walls. With Reynolds 40 symmetrical vortices are created behind the cylinder. At a Reynolds number of 150 periodic behaviour typical of transitional flow can be observed. This early transition is a widely studied subject and has been observed by other authors like (Mittal & Raghuvanshi, 2001). With increasing Reynolds these turbulences become stronger and more chaotic, as seen in the 500 and 10000 Reynolds cases (notice

how the velocities associated with turbulence are in a stronger colour contrast with the mean flow velocity). In the Re=10000 case turbulence can be seen to become chaotic at the end of the domain, losing the periodic behaviour characteristic of transitional flow.

a) Re=5

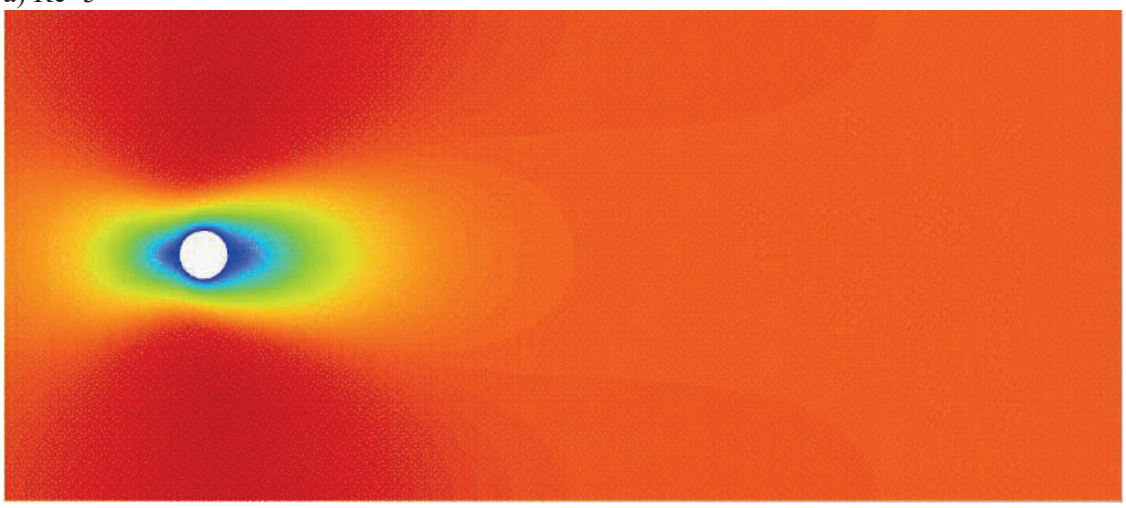

b) Re=40

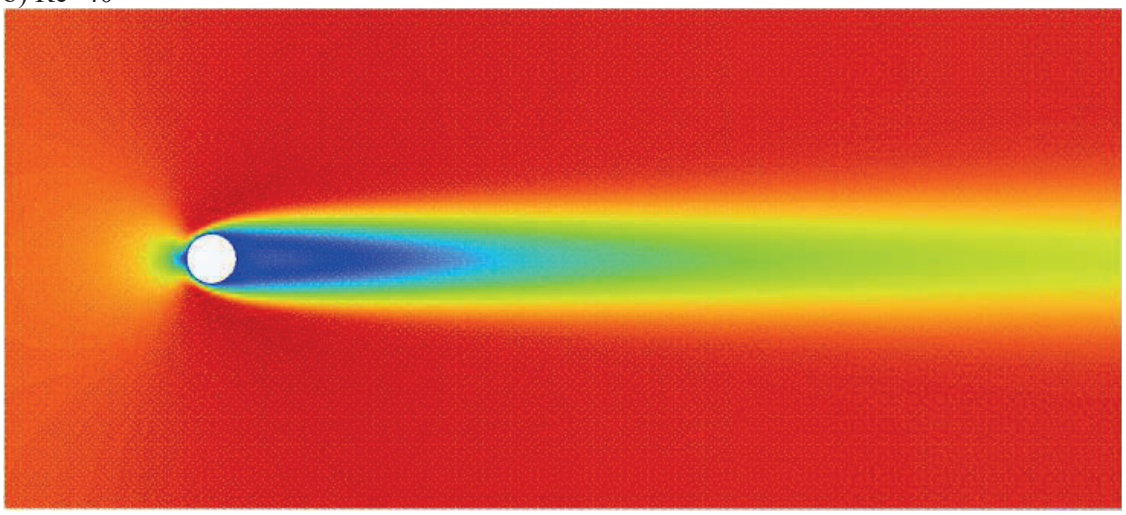

c) Re=150

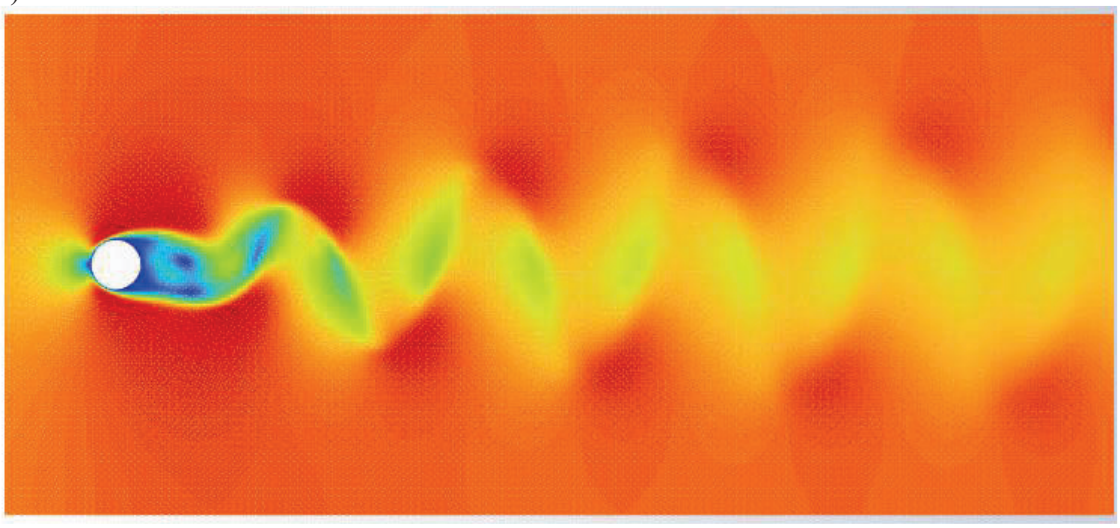

d) Re=500

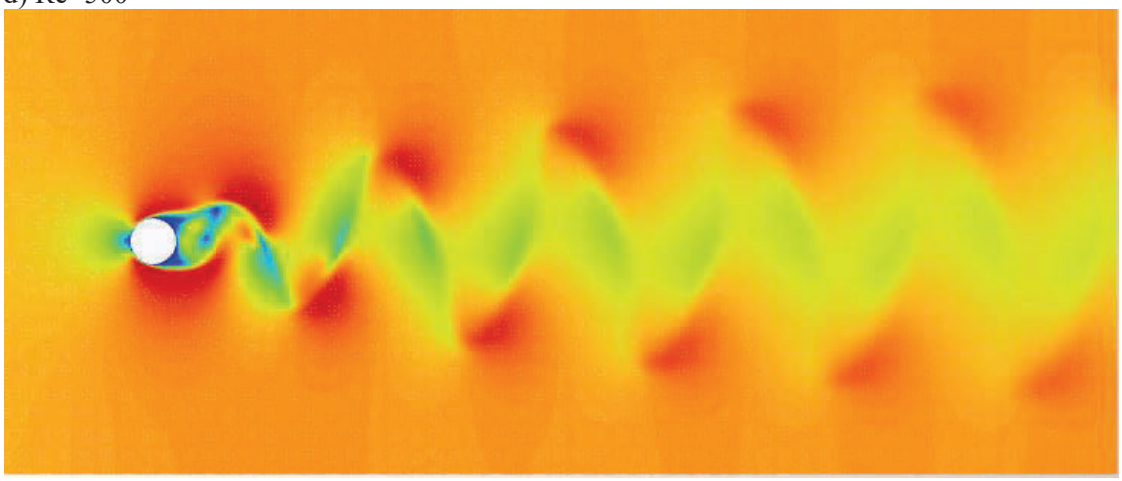

e) Re=10000

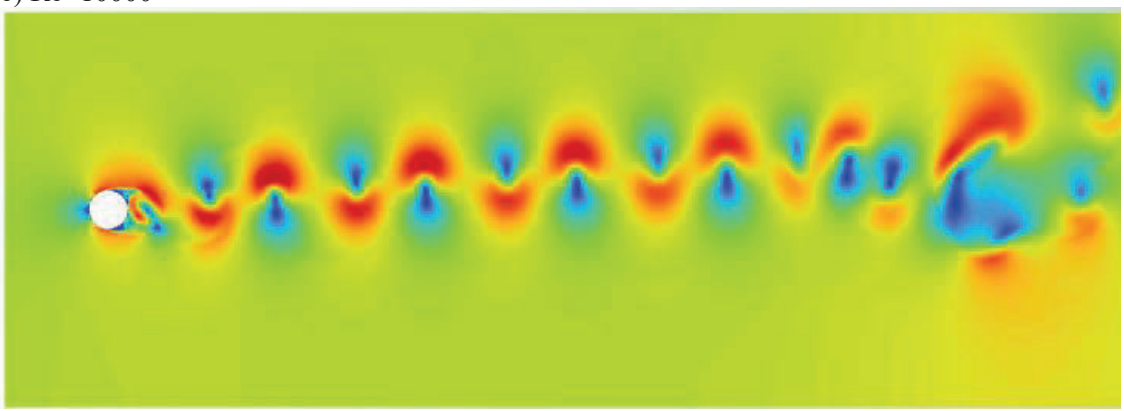

Figure 4: *Velocity contour plot of flow past a cylindrical object at different Reynolds. Snapshots of temporally periodic solutions. Velocities range linearly from 0 with color blue to the highest velocity in red. a) Re = 5 b) Re=40 c) Re=150 d) Re=500 e) Re=10000. Source: own elaboration with Ansys Fluent®.*

As illustrated previously in Figure 4, depending on the geometry and the Reynolds number, the flow patterns that arise are very different, thus turbulence requires careful consideration of these facts. Exact analytical solutions of these equations are rare, only occurring in simple laminar conditions such as laminar flow over an infinite plate. For the rest of cases, numerical methods are required to obtain solutions to these problems.

1.2. Turbulence and CFD Codes

The reality of transfer phenomena is not so straightforward as one may deduce by looking at the generalized equation of transport (Eq. 10). If not performed carefully, numerical methods can fail when applied to these equations, especially when the momentum equation is involved (Eq. 12) due to the presence of turbulence at high Reynolds numbers. The equations, depending on the Reynolds number will produce different shapes and

scales of turbulent swirls called eddies. Energy is transferred between the different eddy scales: whirling rotating motions produces friction with smaller eddies transferring energy from one to the other in what is called energy cascade. Typically, the energy injected on the system produces the largest eddies and these in turn transfer this energy to smaller ones until the size of the eddy is small enough to dissipate its energy into heat. This is called the dissipative scale or Kolmogorov scale (Kolmogorov, 1962). Energy can also be transferred backwards in an inverse energy cascade. The energy transfer occurs mostly on the inertial range where $E(l) \propto l^{-5/3}$, Figure 5. Here l is the wavenumber of the eddy [m^{-1}] also defined as the $\frac{2\pi}{r}$ (with r being eddy size [m]) and *E(l)* is energy spectrum. The turbulent kinetic energy (k [J/kg]) of eddies with a size ranging from l_1 to l_2 is defined as $k = \int_{l_1}^{l_2} E(l)\, dl$. In literature one often may find the wave number defined as k, but for consistency in this thesis k will be the turbulent kinetic energy and l wave number of an eddy and thus related to its characteristic size.

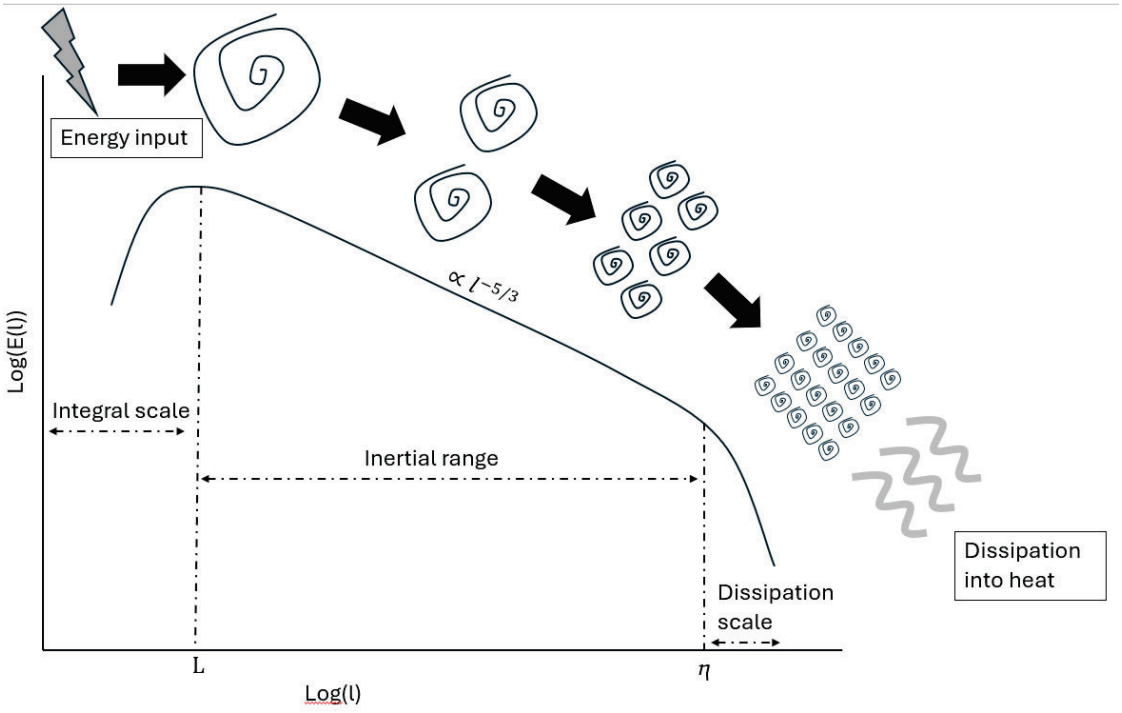

Figure 5: *Turbulent energy cascade. The eddies transfer most energy from the larger to smaller until dissipated into heat. Source: own elaboration.*

The size of the smallest eddies present in a system decrease with increasing Reynolds number. That is, the more turbulent is the system, the smaller the eddies that this system can produce, (Eq. 14):

$$\eta \approx \frac{L}{Re^{\frac{3}{4}}} \tag{14}$$

Where L is the characteristic length of the system and η is the size of the smallest eddy, also called Kolmogorov scale.

This means that if a numerical method is to be used, the physical discretization must be able to reproduce such small scales in order to be able to solve the Navier-Stokes equations (equations 12). Such method of solving these problems is only viable for small Reynolds numbers and 2 dimensional cases, as the amount of discretization cells grows rapidly with Re, becoming impossible to compute 3D cases with Reynolds above 10000 even with the most powerful computers nowadays available in the world.

1.2.1.Navier Stokes solution techniques

As stated earlier, analytical solutions can be found only for very simple situations and numerical methods are required in most cases. These methods require the spatial discretization of the domain to transform the Navier Stokes (NS) equations into algebraic equations. Three methods are the most notable and used for these tasks: finite difference methods, finite volume methods, and finite element methods.

1.2.1.1. Finite Difference Methods

Finite Difference Methods is based on approximating the derivatives in the Navier-Stokes equations with the slope of the line between adjacent points. The domain is discretized into a grid, where the values of the flow variables (e.g., velocity, pressure) are computed at each grid point.

Considering the 2D Navier-Stokes equations in a Cartesian coordinate system (Eqs. 15-16):

$$\frac{\partial \mathrm{u}}{\partial \mathrm{t}} + \mathrm{u}\frac{\partial \mathrm{u}}{\partial \mathrm{x}} + v\frac{\partial \mathrm{u}}{\partial \mathrm{y}} = -\frac{1}{\rho}\frac{\partial \mathrm{P}}{\partial \mathrm{x}} + \frac{\mu}{\rho}\left(\frac{\partial^2 u}{\partial x^2} + \frac{\partial^2 u}{\partial y^2}\right) \tag{15}$$

$$\frac{\partial v}{\partial \mathrm{t}} + v\frac{\partial v}{\partial \mathrm{y}} + u\frac{\partial v}{\partial \mathrm{x}} = -\frac{1}{\rho}\frac{\partial \mathrm{P}}{\partial \mathrm{y}} + \frac{\mu}{\rho}\left(\frac{\partial^2 v}{\partial x^2} + \frac{\partial^2 v}{\partial y^2}\right) \tag{16}$$

Each spatial derivative is substituted by finite differences. In the case of second order accuracy, the symmetric difference quotient can be used (Eq. 17):

$$\frac{\partial \mathrm{u}}{\partial \mathrm{x}} \approx \frac{u_{i+1,j} - u_{i-1,j}}{2\Delta x} \tag{17}$$

Where $u_{i,j}$is the velocity component at the grid point (i,j) and Δx is the grid spacing in the x-direction.

This method is easy to implement and computationally efficient for structured grids, but it is only useful for such structured grids and therefore is mostly used for simple geometries. The method also fails to solve the Navier Stokes equations when the advective term is present. In this case, the method does not inherently imply mass conservation, which leads to divergence problems.

1.2.1.2. Finite Volume Methods

Finite Volume Methods are one of the most popular choices for the discretization of NS equations in commercial CFD software. Finite Volume Methods integrate the Navier-Stokes equations over control volumes (discrete regions of the domain). This methodology takes the conservation laws from which the Navier Stokes equations are derived and discretizes them into control volumes (discrete regions of the domain). The fluxes of the different transport magnitudes (mass, momenta, energy…) across the boundaries of these control volumes are computed, ensuring that conservation laws are satisfied for each volume.

For instance, the integral form of the generalized transport equations for a control volume V with surface S is (Eq. 18):

$$\int_V \frac{\mathrm{D}\,\rho\varphi}{\partial \mathrm{t}}\,dV + \int_S \rho\vec{u}\varphi\cdot\vec{n}\,dS = \int_S \Gamma_\varphi \nabla\varphi\cdot\vec{n}\,dS + \int_V S_\varphi dV \qquad (18)$$

Where φ is the magnitude (mass, velocity…), ρ is the density, Γ_φ is the diffusion coefficient of said magnitude, and n is the outward normal vector of the surface S.

Equation 14 applied to a polyhedral control volume gives (Eq. 19):

$$\frac{\partial\rho\varphi}{\partial \mathrm{t}}\,\mathrm{V} + \sum_{f}^{N\,faces} \rho_f\vec{u}_f\varphi_f\cdot\vec{A}_f = \sum_{f}^{N\,faces} \Gamma_\varphi\nabla\varphi_f\cdot\vec{A}_f + S_\varphi V \qquad (19)$$

Where φ_f is the value of φ convected through face f, $\vec{A}_f$ is the area vector of face f, $\nabla\varphi_f$ is the gradient of φ at face f and N faces is the number of faces of the polyhedral cell. (ANSYS Fluent Theory Guide, 2024)

These methods naturally conserve mass momenta and energy and can be used for structured and unstructured grids, although it is more complex to implement and usually more computationally expensive. This method is the preferred method used by Ansys Fluent and the one that will be used throughout this thesis.

1.2.1.3. Finite Element Methods

In Finite Element Methods, interpolation functions are used to determine the flow variables once the fluid domain has been partitioned into smaller parts. The NS equations are multiplied by a test function and integrated over the domain. For a test function ϕ, the Navier-Stokes equations in weak form are expressed as follows (Eq. 20):

$$\int_V \left(\frac{\partial \mathrm{u}}{\partial \mathrm{t}} + \mathrm{u}\frac{\partial \mathrm{u}}{\partial \mathrm{x}} + v\frac{\partial \mathrm{u}}{\partial \mathrm{y}}\right)\phi\,dV = \int_V \left(-\frac{1}{\rho}\frac{\partial \mathrm{P}}{\partial \mathrm{x}}\right)\phi\,dV + \int_V \left(\frac{\mu}{\rho}\left(\frac{\partial^2 u}{\partial x^2} + \frac{\partial^2 u}{\partial y^2}\right)\right)\phi\,dV \qquad (20)$$

Interpolation functions, which are frequently polynomials, are used in each element to estimate the solution for the velocity u and pressure p fields. For example, the velocity component u of a triangle element can be represented as follows (Eq. 21):

$$u(x,y) = \sum_{i=1}^{n} N_i(x,y)u_i \tag{21}$$

Where Ni(x,y) are the shape functions associated with each node i of the element and u_i is the nodal value of the velocity components at node i.

Finite Element Methods methods can provide highly accurate solutions with appropriate meshing but are computationally intensive for 3D problems and are far more challenging to implement than Finite Volume Methods.

1.2.2. Turbulence modelling

Turbulence is a prominent example of chaos theory, which makes it seemingly random and highly dependent on initial conditions. In cases where turbulence is present, the "weak" computing capabilities that the world possesses force researchers to study it from a statistical point of view. Nevertheless, there are cases where the Reynolds number is low enough (like transitional cases), or cases where the simplifications made to the problem (like studying it in 2D or making symmetry assumptions) make possible the study and resolution of the Navier-Stokes equations directly with the computational resources that we possess. This technique is called Direct Numerical Simulation (DNS) and could theoretically be used in all the systems, but its limitation is the amount of computational time required. Here no turbulence modelling is required, and high accuracy can be achieved at the expense of computational resources. The sole requirement of these simulations is that the size of each cell in the domain must be smaller than the Kolmogorov length scale η and that the time step satisfies the Courant-Friedrichs-Levy number smaller than 1 (Eq. 22):

$$CFL = \frac{u\,\Delta t}{\Delta x} < 1 \tag{22}$$

Where Δt is the time step of the simulation and Δx is the cell size in the direction of the flow and CFL is the Courant number. This equation is used for ensuring the convergence of Partial Differential Equations such as the NS equations and is commonly used for Finite Difference Methods.

The use of this technique is constrained by the Reynolds number and the computing power available. The Navier-Stokes equations are resolved in their traditional form although some linearization is required to speed up computations in most cases. Practically, this approach is used only for studying fluids the microscale, like bacteria movement and distribution (Aparicio Medrano et al., 2016), or by those interested in mathematical beauty of the NS equations. If the fluid structures of larger systems in turbulent regime are to be understood, like those present in most engineering problems, DNS is not a suitable tool. By going a step further, the NS equations can be treated by mathematical operations to smooth the turbulence and avoid such small-scale resolution.

One of such mathematical operation is the spatial filtering that gives birth to the Large Eddy Simulation model.

1.2.2.1. Large Eddy Simulation

Large Eddy Simulation (LES) uses a spatial filter that allows for the reduction in computational cost present in DNS by ignoring or smoothing out the smallest features (eddies) of the flow. This filter is similar to the ones used for noise signal cancelation. Applying one such filter to the NS equations leads to the filtered Navier-Stokes equations (Eq. 23):

$$\frac{\partial \hat{u}_i}{\partial t} + \frac{\partial \hat{u}_i \hat{u}_j}{\partial x_j} = -\frac{1}{\rho}\frac{\partial \hat{P}}{\partial \mathrm{x}} + 2\frac{\mu}{\rho}\frac{\partial}{\partial x_j}\hat{S}_{ij} - \frac{\partial \tau_{ij}}{\partial x_j} \tag{23}$$

Where $\hat{u}_i$ is the filtered u value in the i direction, τ_{ij} is the residual stress tensor that includes all the unclosed terms and must be modelled. $\bar{S}_{ij}$ is the filtered rate of strain tensor (Eq. 24):

$$\hat{S}_{ij} = \frac{1}{2}\left(\frac{\partial \hat{u}_i}{\partial x_j} + \frac{\partial \hat{u}_j}{\partial x_i}\right) \tag{24}$$

By using this technique, the smaller eddies are filtered out up to Δ_{LES}, the minimum eddy size at which the turbulence is resolved, not modelled. Δ_{LES} is then the chosen mesh size of the system. The choice of Δ_{LES} is made so that at least 80% of the turbulent kinetic energy of the system is resolved. If $\Delta_{LES} \approx \eta$ then the method will resemble a DNS resolution. On the other hand, when $\Delta_{LES} \approx L$, where L is the characteristic length of the system, this method will be closer to a Reynolds Averaged Navier-Stokes (RANS) approach, which is discussed in the next section. Therefore, it is advisable to keep Δ_{LES} between those two values to avoid losing precision or an abrupt increase in computational requirements. Below Δ_{LES}, e.g. the region between the mesh nodes, the turbulence is modelled using sub-grid scale turbulence models like the Smargonsky-Lilly model, (Lilly, 1966), (Smargonsky, 1963). Here the deviatoric part of the stress tensor is modelled as (Eq. 25):

$$\tau^r{}_{ij} = -2\nu_t \hat{S}_{ij} \tag{25}$$

Where ν_t is the turbulent eddy viscosity, a recurrent scalar in turbulence modelling. In the Smargonsky-Lilly model it is modelled as (Eq. 26):

$$\nu_t = C\,\Delta_{LES}\sqrt{2\hat{S}_{ij}\hat{S}_{ij}} = C\Delta_{LES}{}^2\left|\hat{S}\right| \tag{26}$$

Where C is a constant.

Several more models have been created in the past years and it is research that is still going on. Although very popular among for several applications involving low Reynolds flows, LES has several issues when the Reynolds number becomes higher than 10^5, namely because the computational cost increase with the Reynolds number, similarly as what happened with DNS but not at the same rate. To solve these issues engineers have

designed a tool that is not so dependent on the Reynolds number, not requiring higher resolutions as such number increases. This technique is the Reynolds Averaged Navier Stokes equations or RANS modelling.

1.2.2.2. Reynolds Averaged Navier Stokes (RANS)

RANS modelling is based on time averaging or Reynolds averaging the Navier Stokes equations to obtain, dividing the velocity term into two terms, the time averaged value of the velocity $\bar{u}$ and the fluctuations of such velocity due to turbulence, u' (Eq. 27):

$$u(x,t) = \bar{u}(x) + u'(x,t) \tag{27}$$

Note that $\bar{u}$ does not depend on time, and as such the value obtained when solving these equations will be an averaged one. This is useful for multiple engineering applications, as the global averaged variables are the ones that are often of engineering interest, e.g. the time averaged pressure drop of a pipe is a relevant design parameter while the instantaneous pressure fluctuations might not be as relevant as long as they are within an acceptable range.

By substituting equation 27 into the NS equations and with a few extra mathematical considerations that can be found in great detail in literature (Warsi, 2005), the averaged NS equations are obtained (Eq. 28):

$$\frac{\partial \bar{u}_i}{\partial t} + \bar{u_j}\frac{\partial \bar{u_\iota}}{\partial x_j} = -\frac{1}{\rho}\frac{\partial \bar{P}}{\partial \mathrm{x}} + 2\frac{\mu}{\rho}\frac{\partial}{\partial x_j}\bar{S}_{ij} - \frac{\partial \overline{u_\iota' u_j'}}{\partial x_j} \tag{28}$$

Where $\bar{S}_{ij}$ is the time averaged strain rate tensor $\bar{S}_{ij} = \frac{1}{2}\left(\frac{\partial \bar{u}_i}{\partial x_j} + \frac{\partial \bar{u}_j}{\partial x_i}\right)$ and $\overline{u_\iota' u_j'}$ is the averaged product of the fluctuations also called Reynolds stress or τ_{ij}''. If the density is included, then (Eq. 29):

$$\tau_{ij}' = \rho\,\overline{u_\iota' u_j'} = R_{ij} \tag{29}$$

This is the term that must be modelled and here is where all the RANS turbulence modelling arises. One of the simplest modelling techniques is the Boussinesq hypothesis (Boussinesq, 1903), where the turbulent shear stress is modelled in a similar manner as the viscous shear stress. Therefore, from the viscous shear stress equation (Eq. 30):

$$\tau = \mu\frac{\partial u}{\partial y} \tag{30}$$

Follows the turbulent shear stress or Reynolds stress (Eq. 31):

$$\rho\,\overline{u'v'} = -\mu_t\frac{\partial \bar{u}}{\partial y} \tag{31}$$

Here μ_t is called turbulent viscosity or eddy viscosity. The goal of such called eddy viscosity models, is to find a good model for the turbulent viscosity term. Expanding and generalizing this equation we obtain (Eq. 32):

$$\rho\,\overline{u_\iota{}'u_j{}'} = \frac{2}{3}\rho\,k\delta_{ij} - \mu_t\left(\frac{\partial\bar{u}_i}{\partial x_j} + \frac{\partial\bar{u}_j}{\partial x_i}\right) \tag{32}$$

Where δ_{ij} is the Kronecker delta and k is defined as the turbulent kinetic energy (Eq. 33):

$$k = \frac{\overline{u'_\iota{}^2}}{2} \tag{33}$$

Several models have been developed over the years, and they are often classified by how many additional transport equations they require. Increasing the model complexity often means increasing the accuracy or applicability range of the simulations but this also comes increased computational costs. Zero equation models like Prandtl mixing length and one equation models like the Spalart-Allmaras (Spalart & Allmaras, 1992) are efficient computationally but can only be used reliably specific cases. For instance, the latter is only recommended for 2D cases where only the boundary layer flow is of interest. Two equation models like k-ε or k-ω are widely used in a lot of engineering applications, as they combine accuracy with adaptability to the studied case. These models developed by Launder and Spalding (Launder & Spalding, 1974) and Wilcox (Wilcox, 1988) are now industry standards.

There are models that do not follow the Boussinesq hypothesis and venture into the modelling of the Stress tensor without this simplification. The Reynolds Stress Models (RSM) try to model a transport equation for each term in the developed transport equation for the Reynolds Stress tensor. This implies that, unlike Boussinesq hypothesis models where the tensor is symmetric, RSM models can create anisotropic turbulence, that is, non-spherical eddies.

1.2.2.3. Turbulent model selection

All turbulence models have strengths and limitations due to the nature of the modelling assumptions. There is no single model that can be readily applied to all turbulent flows without a degree of adjustment and experience in selecting the most appropriate model. In addition, tuning the model coefficients is of utmost importance to obtain accurate, consistent and robust simulations. The selection of turbulent model comes down to the objectives of the simulation, the accuracy required and the computational power or time available. When overall variables are to be extracted from a system, RANS modelling offers the benefit of providing time averaged results, while variables extracted with LES must be probed and averaged. DNS will produce more reliable results, as it does not depend on modelling. LES does depend on modelling but only on the small scales. In this sense, LES is more reliable than RANS, which models all turbulent scales. Finally, if computational power is a limiting factor, RANS is the best option, as it requires less computational costs. The simulations performed in this thesis will be performed mostly by using different types of RANS modelling, as for chemical engineering the variables of interest are almost always global and time averaged. Moreover, RANS provides sufficient accuracy and with reduced computational costs. Figure 6 shows a schematic

representation of the different turbulent model tendencies. URANS stands for Unsteady RANS, a model that allows RANS equations to model time advancement and to obtain non-timely-averaged values.

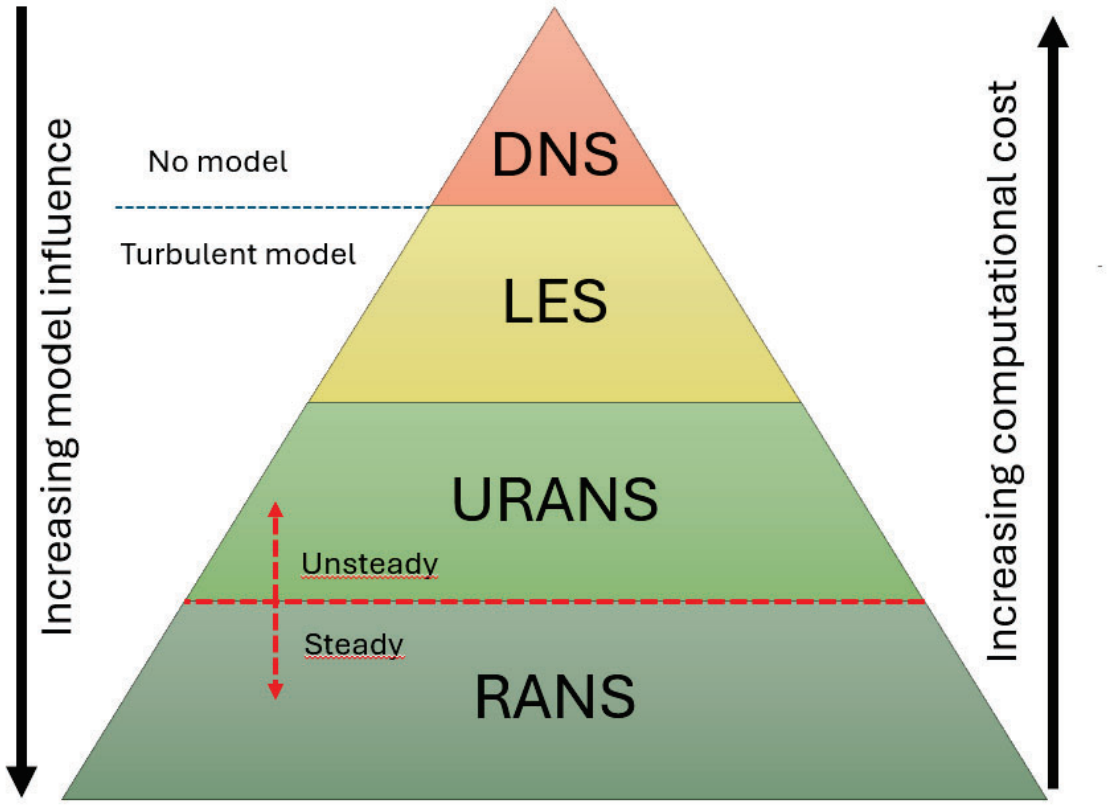

Figure 6: *Scheme of the different types of CFD simulations depending on the model influence and computational time.*

Similar concepts are summarized in Table 2, where the applications and requirements of each method are described in more detail.

Table 2: *Summary of the different turbulent models*

	DNS	**LES**	**RANS**
Model dependence	Null	Low	High
Grid requirement	$Re^{9/4}$	$Re^{9/5}$	Log (Re)
Applications	Simple flow low Re	Simple flow low Re	Wide range

1.3. Heat transfer in chemical engineering

One of the transport phenomena topics covered by this thesis is heat transfer. Heat transfer processes are extremely important in chemical engineering, and for their study, heat exchangers are taken as a clear example of this phenomenon.

Heat exchangers are present in most industries as they enable the recovery of thermal energy, making processes more profitable and environmentally sustainable. The design of classical heat exchangers is performed based on well-established semi-empirical equations, e.g. Double Pipe Heat Exchangers. These semi-empirical equations are very susceptible to geometry changes, as well as flow conditions at the entrance of the heat exchangers. Semi-empirical correlations are based on simplifying assumptions such as constant fluid properties along the heat exchanger. Moreover, such correlations are only valid for limited Reynolds and Prandtl ranges and are not valid in all situations. A design solution to this issue is Computational Fluid Dynamics (CFD), which is widely used for the design of novel heat exchanger geometries saving experimentation time and cost.

From the reviewed literature, some authors compare CFD results with novel heat exchangers configuration experimental results, but for classical Double Pipe Heat Exchangers the CFD results are blindly trusted or directly rely on the well-established semi-empirical handbook equations. CFD simulations are based on numerically solving microscopic mass and energy balances (conservation principles) together with a turbulent viscosity model, the uncertainty of the results mainly is caused by the eddy viscosity models. There are some studies that check which is the most suitable viscosity model for different units but not for Double Pipe Heat Exchangers. For example, different viscosity models are tested by Ajmi et al. (2020) when investigating the heat transfer enhancement of an inclined heated offset jet. Their results show that the SST k-ω model is the one that better predicts the Nusselt number. Abbasian Arani & Uosofvand (2021)found good agreements between their results using the k-ε model and analytical methods when studying single and double-pass tube with helical and segmental baffles. Gadave & Kothmire (2019) studied shell and tube heat exchangers with Realizable k-ε model and found up to 19.44 % difference in heat transfer and 13.31 % difference in pressure drop with respect to analytical methods. Petrik & Szepesi (2018) used the Realizable k-ε model to compare empirical and CFD results in the shell side of a Shell-and-Tube Heat Exchanger. Their results found errors in heat transfer that ranged from 2.84 % to 18.47 % depending on the case studied. Sruthi et al. (2021) used the k-ε model to model a Double Pipe Heat Exchanger with corrugations, obtaining discrepancies with experimental studies of up to 8.42%. Pal et al. (2016) tested different turbulence models with different heat exchanger configurations, founding that Standard k-ε model was the one that fits better the experimental results (±20 % error) with less computational time compared. Their research, however, did not consider different wall treatments for the turbulence models, nor their combination between themselves. With all this literature reviewed, one of the objectives of this chapter is fill the research gap of finding which

model better represents the reality of a heat exchanger, including heat transfer and pressure drop.

CFD also allows for the design of new and more complex geometries such as tubes with inserts or extended surfaces. These modifications are called heat transfer enhancement methods and there are of many types. Complex solutions in this category are not well documented experimentally, and not enough data is present to accurately describe the combinations of different heat enhancement methods and their interactions.

1.3.1. Heat transfer enhancement methods

Heat exchangers can be as simple as Double Pipe Heat Exchangers, but for efficiency purposes, they are often modified to enhance the transferred heat. These modifications called heat transfer enhancement methods fall into two categories: active and passive methods. Active methods require the use of energy by an external source to enhance the heat transfer. Such implementations may include surface or fluid vibration, use of electric fields, spraying with atomizers and many more. This thesis, however, focuses on passive heat transfer enhancement methods, those which do not require external energy. These are usually of the form of extended surface or turbulence inducing inserts. The bibliography on this topic is extensive, combining experimental and numerical research. Nusselt number (Nu) and TPF (Thermal Performance Factor) are the two major variables that are to be optimised, as the first is directly related to the amount of transferred heat and the second describes the energetical efficiency of the process in terms of heat transfer and pressure drop, Eqs. 34-35:

$$\mathrm{Nu} = \frac{\mathrm{h\,D}}{\mathrm{k}} \tag{34}$$

$$\mathrm{TPF} = \frac{{}^{Nu}/_{Nu_o}}{({}^{f}/_{f_o})^{1/3}} \tag{35}$$

Where Nu and $\mathrm{Nu_o}$ are the Nusselt number for the modified tube and the plain tube respectively. Accordingly, the variables of f and $\mathrm{f_o}$ refer to the friction factors of the modified tube and the plain tube respectively. TPF then directly compares the performance of the studied unit with the plain tube heat exchanger at the same Reynolds (with Nusselt Nu_o and friction factor f_o).

Research performed by Liao (2000) combined the use of twisted tapes (TT) with extended 3D surfaces inside the tubing, finding improvement with respect with plain tubes. This improvement, however, is only relevant outside the turbulent regime, for highly viscous fluids. Chang et al. (2007) correlated pressure drop and Nusselt number. Eiamsa-ard et al. (2009) tested twisted tapes of different length with plain tubes. They found up to 15.3% increase in heat transfer when full length twisted tapes where used. Later, Eiamsa-ard et al. (2010) compared the effects of single and dual twisted tapes (two parallel twisted tapes). While doing so, very useful correlations were also provided for twisted tapes in

the range of study. TT inserts increase from 36% to 48% the transferred heat due to the centrifugal forces induced by the spiral motion in the fluid (Naga Sarada et al., 2012).

Some experimental studies combine TT with other sorts of inserts. Hasanpour et al. (2016) analysed the combination of helical corrugated tubes and perforated TT and concluded that the combination of TT and corrugated tubes increased the Nu more than corrugated tubes alone. Chu et al. (2020) studied different v-cut TT shapes at the turbulent transition zone. The results obtained shows TPF of 1.18-1.23 for the obtuse v-cut TT which is the one that gave better results. Wang et al. (2020) compared the use of TT and HC (Helical Coils) and the presence of both inserts at the same time. It was found that helical coils (HC) alone improved heat transfer more than TT but resulted in a substantial increase in pressure drop. The resulting TPF was highest when both TT and HC were together, followed by the use of TT and HC, which produced overly high pressure drop for the heat enhancement yielded. There is an interest in studying complex configurations, as they increase Nu and TPF.

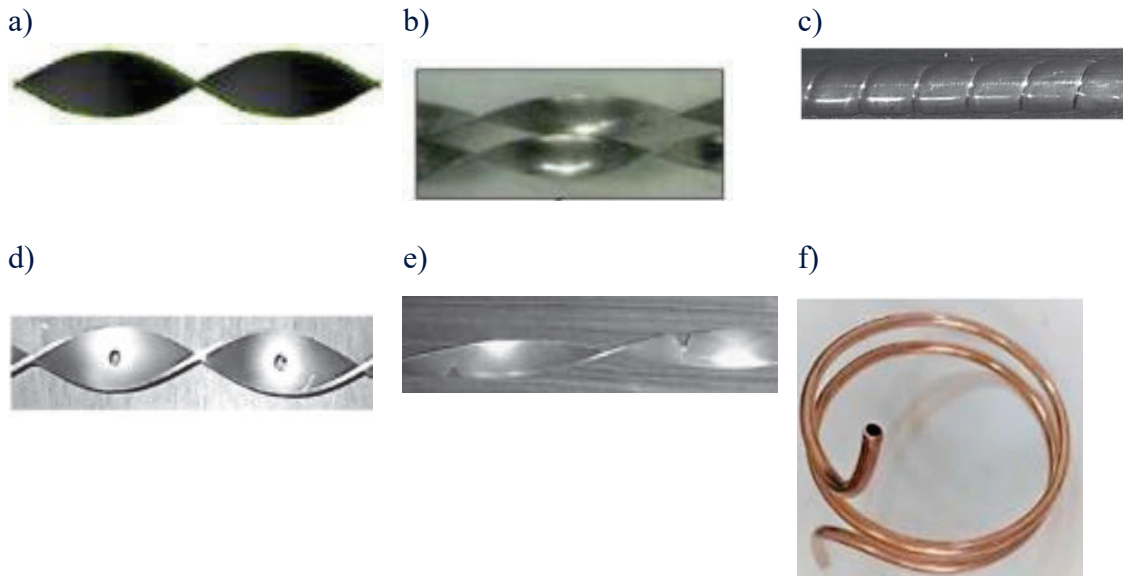

Figure 7: Different shapes of passive heat transfer enhancement techniques. a) Simple Twisted tape, b) Dual twisted tapes (Eiamsa-ard et al., 2010), c) Helically corrugated tube (Hasanpour et al., 2016) d) Perforated twisted tapes (Hasanpour et al., 2016) e) V-cut twisted tapes (Hasanpour et al., 2016a) f) Helical coil (Abdullah & Hussein, 2023).

More experimental research is being developed constantly, but CFD models are more and more frequently used in this field of research, often alongside experimental data. They offer tools to model these units efficiently and bring the opportunity of reducing experimental costs by finding optimal values for the geometrical and the input parameters of the heat exchangers. Shabanian et al. (2011) used CFD modelling to predict turbulence effects and explain experimental observations in an air cooler equipped with different tube inserts. The difference between experimental and CFD results ranged from 3.5% to 7.3% for Nusselt number and friction factor. The amount of passive heat enhancement methods related research that is developed with CFD should be enough proof to label

them as viable for these studies. Natarajan et al. (2020) et al. studied both experimentally and with CFD the effect of enhancement in heat transfer that the combination of different twisted tapes with different twist ratios and a working fluid composed of water and SiC nanoparticles. Both horizontal wings twisted tapes and plain twisted tapes were used for this work with the first giving more promising results. The error difference between the CFD study and the experimental case was between 5% and 9 % for Nusselt number and friction factor. Sharma and Kumar Patel (2020) studied different twist ratios and different Reynolds numbers in a counter flow heat exchanger. One twisted tape had alternating clockwise and counterclockwise twists while the other had semi-circular notches every two twists. In this research, the RANS model that fits the best this kind of simulation is RSM (Reynolds Stress model) and proved that CFD is in close agreement with experimental studies.

CFD models are often used for optimising geometries like the work developed by Noorbakhsh et al. (2020) who explored the effects of enhancement when both tubes (internal and external) are suited with twisted tapes. Hollows were also created with different aspect ratios in the twisted tapes. The results show that creating the hollows with an aspect ratio of one on the twisted tape leads to higher coefficient of performance. He et al. (2020) considered the effect of adding an additional TT insert and compared it to the use of a unique TT. CuO-water nanofluid at different concentrations was also used. The results proved that the use of two TT increased the Nu significantly more than the sole TT but the pressure drop masks the heat transfer enhancement yielding Thermal Performance Factor (TPF) values under those found with single TT. Nakhchi and Esfahani (2020) performed a CFD analysis of CuO nanofluid flowing on tubes with louvered strip inserts, proving that TPF could raise to 1.99 when the angle of the strips is 25o and there are perforations on each of them. Tiwari et al. (2021) analysed the thermal performance of a triple tube heat exchanger both experimentally and with CFD. The fluid used was WO3/ Water nanofluid and there were inserts inside the middle tube. In this case, rib inserts performed better than porous or TT inserts, although all of them showed improvement with respect to a plain tube. Zaboli et al. (2022) studied the combination of a corrugate coil tube with a spiral twisted tape. Five lobe corrugated tubes showed the best thermal performance, with an improvement of Nu of 30.7% and an increase in pressure drop of 37.1%. The TPF for these configurations was found to be 1.20-1.21. CFD models are even used to create correlations, which can mitigate the major downside of CFD: the computational time and cost that some cases require.

CFD tools are currently used for optimizing or providing correlations. Pourfattah et al. (2021) combined two powerful computational tools: Genetic Algorithms and CFD. In this way, the optimization of a twisted tape heat exchanger with five design points was achieved and found a 265% increase in heat transfer with respect to the plain tube. Oni (2021) used Ansys Fluent® to simulate different twisted tape shapes and inserts, finding correlations for the friction factor (f) and the Nusselt number (Nu) with Reynolds number, Prandtl number, tape's width, tape's pitch, and tape's perimeter of opening. Among the shapes studied, tapes with intersected axes and triangle-shaped openings were found to give best results for laminar flow.

The cases mentioned previously often lack realistic comparison between CFD results and experimental data or between different turbulent models and/or wall treatment methods. When it comes to choosing a turbulent model, most authors rely on previous studies with similar conditions. Sometimes it is just assumed that if for a geometry and settings a turbulent method predicts results accurately, it must be reliable for any other case. Scarce sources are found in which research is performed to compare different turbulent models and often the exact model or the wall treatment used is omitted. This section is focused on testing how reliable different turbulent models and wall treatments are when studying twisted tapes inserts. Different turbulent models are compared against correlations extracted from experimental data on twisted tapes. Different geometries and Reynolds numbers are tested to prove whether the accuracy of these models has a dependency of the case studied, and if so, which is the best model for every situation. An optimization is later performed once the reliability of the model is confirmed, to search for optimal geometrical parameters. The methodology for this chapter can be found in section 4.1. and the results and discussion in section 5.

1.4. Dispersion from continuous sources

When aiming at studying mass transfer of different chemical species, a wide range of processes are compatible with this topic. A few examples are membranes, mixers, reactors, adsorption beds among many more. A highly disregarded topic which is present in most industrial cases is the disposal of gases, or the consequences of their accidental release. Gas dispersion will then be used in this thesis as a case study for mass transfer.

Gas dispersion is a highly studied topic due to its great relevance, whether in unit operations, safety and risk assessment issues, or in determining the possible environmental or human health impact. The atmospheric gas dispersion is particularly important for assessing pollutant concentrations at a specific point location under given conditions and estimating any potential effects on human health. Pollution and air quality are two very pressing concerns in society. In fact, these concepts appear under different targets in the Sustainable Development Goals pleading for decreasing cities' environmental effects, with a focus on air quality (United Nations Development Programme, n.d.). The investigation of the atmospheric dispersion of a pollutant arose some time ago with the use of flues to dilute pollutants. Nowadays it is also important to be able to foresee the effects of accidental emissions of polluting substances. However, it is a subject that is still being studied because of its immense complexity and the fact that there are many variables to consider (Leelőssy et al., 2014), for example the wind velocity, temperature, or solar radiation, among others. Due to its relevance, many experiments have been carried out since the 1950s (J. C. Chang & Hanna, n.d.). As a result, a significant amount of data is available for diverse climatic conditions, terrains, and substances. Dipole Pride 26's experiments study instantaneous and continuous SF_6 discharges at ground level. The measurements are taken in arcs about one, five, and

twenty kilometres downwind of the source. Various surface, radiosonde, and pilot balloon (pibal) stations are used to gather meteorological data (George Mason University., n.d.). FLADIS investigate continuous NH_3 dispersion: the gas emissions are about 0.5 kg NH_3/s for 20 min. Concentration measurements were taken using sensors located in arcs at 20 m, 70 m, and 240 m intervals (George Mason University., n.d.). Semi-empirical models were developed from the collected data, such as data from the Prairie Grass Project (J. C. Chang & Hanna, n.d.). One such model is the Gaussian Plume Model (GPM) upon which various software packages are based.

1.4.1. Gaussian dispersion model (GPM) and other semiempirical models

The Gaussian plume model (GPM), Eq. 36:

$$c(x,y,z) = \frac{w}{2 \cdot \pi \cdot v_w \cdot \sigma_y \cdot \sigma_z} \cdot e^{\frac{-y^2}{2 \cdot \sigma_y^2}} \cdot \left[e^{\frac{-(z-h)^2}{2 \cdot \sigma_z^2}} + e^{\frac{-(z+h)^2}{2 \cdot \sigma_z^2}} \right] \tag{36}$$

This equation describes the concentration $c(x,y,z)$ as a function of the distance from the emission source: the wind direction distance (x), the perpendicular distance to the wind direction (y) and height from ground (z). The wind velocity (v_w), the leakage flow rate (w) and its heights (h). The horizontal (σ_y) and vertical (σ_z) dispersion coefficients are also called standard deviations. There are several ways to estimate these coefficients. In this case, the Martin's formulas (Martin, 1976) are used, Eqs. 37 and 38.

$$\sigma_y = a \cdot x^b \tag{37}$$

$$\sigma_z = c \cdot x^d + f \tag{38}$$

Where σ_y and σ_z are in [m], the downwind distance from the source (x [km]) and the empirical parameters a, b, c, d, and f described the dispersion coefficients.

These parameter's values depend on the atmospheric stability class (Table 2). This classification goes from A to F, being A an extremely unstable conditions and F extremely stable (Martin, 1976).

Table 3. *Coefficient values for distances under 1 km (Martin, 1976)*

Stability Class	***a***	***b***	***c***	***d***	***f***
A	213	0.894	440.8	1.941	9.27
B	156	0.894	106.5	1.149	3.3
C	104	0.894	61.0	0.911	0
D	68	0.894	33.2	0.725	-1.7
E	50.5	0.894	22.8	0.678	-1.3
F	34	0.894	14.35	0.74	-0.35

The stability class is depending on the release time (day or night), the sunlight intensity, the cloud cover, and the wind speed (Table 3). Knowing the atmospheric conditions allows calculating the dispersion coefficients. Then, the concentration at any point is estimated.

Table 4. *A Classification of the atmospheric stability (Air Resources Laboratory, n.d.)*

Wind speed	Day (sunlight intensity)			Night (cloud cover)	
[m/s]	**Strong**	**Moderate**	**Slight**	**Cloudy**	**Clear**
< 2	A	A – B	B	F	F
2 - 3	A – B	B	C	E	F
3 – 4	B	B – C	C	D	E
4 - 6	C	C – D	D	D	D
> 6	C	D	D	D	D

Most semiempirical models follow in some degree these equations, with different parameters or correction factors. These models are commonly used to authorize industrial sources and assess the risk of hazardous leaks in legal situations (Venkatram & Thé, 2003). Moreover, prevention of public safety and security can be enhanced by modelling and understanding the repercussions of a failure, such as a natural gas pipeline breakdown (Ahmed et al., 2022). Given the necessity for highly dependable estimations, these models have been refined throughout the years. Besides, some software appeared to make the calculations easier to manage. One software based on GPM is Areal Location of Hazardous Atmosphere (ALOHA) (*ALOHA Software | US EPA*, n.d.-a; National Oceanic and Atmospheric Administration (NOAA), 2013), which is especially famous for modelling accidents like atmospheric gas releases (Terzioglu & Iskender, 2021). However, these semi-empirical models do not consider the particularities of the scenario, for instance the mitigation effect that a line of trees between the emission and target points have in the dispersion of the gas. The following paragraph presents some cases where the semi-empirical models have been applied and, the next one presents some cases where Computation Fluid Dynamics are required.

Pakchotanon et al. (2022) study the consequences of an accidental amine leak in the carbon capture and storage (CCS) system of a coal-fired power plant located in Saskatchewan, Canada. In particular, the CALPUFF model (a Gaussian dispersion model) is used to find the concentration at ground level. Because air speed and velocity vary throughout the year, various simulated concentration distributions are seen depending on the season. Iskender (2021) was concerned about the industrial utilization risks of acetone, a very common chemical. Therefore, a storage tank release was carried out with ALOHA obtaining risk distribution zones. Ahmad et al. (2022) investigate the best location to build the methanol plant's reactor, minimizing the probability of deaths in the surrounding area in case of an accident. HYSYS software is used to characterize the chemical mixture release before calculating the effect with ALOHA. The inverse problem is likewise addressed: the acquired data indicates a release, but its location is unclear. Sánchez-Pérez et al. (2022) forecast the position, release time, and mass release rate of an unknown gas emission using ALOHA software and Matlab programming.

Mouilleau & Champassith (2009) discuss the validation of discharge and subsequent atmospheric dispersion for both unpressurised and pressurised carbon dioxide releases using the consequence modelling package PHAST. Shojaee Barjoee et al. (2022) reflect the need to compare the different models to determine which is most appropriate for each case. Particularly, ALOHA and PHAST are compared, and the results show that PHAST is more conservative. Other studied cases, like the study of empirical results of a LNG road tank discharge under class B atmospheric conditions, show a similar gas propagation to that obtained using the Gaussian gas model of EFFECTS software (Węsierski et al., 2021). It should be noted that standard software either neglects humidity and topography or is relatively insensitive to variations in them therefore requiring CFD modelling (Bernatik et al., 2008).

Despite their widespread use, these models contain scenarios in which the estimation of concentration is inaccurate, for example in complex terrain, in the presence of obstacles, with chemical reactions like combustion (Z. Zhang et al., 2022), or with very low wind speeds, among others. In these cases, there is a tendency to resort to wind tunnel experiments or Computational Fluid Dynamics (CFD) simulations (New Zealand. Ministry for the Environment. et al., 2004).

1.4.2. CFD applications to pollutant dispersion

In recent years researchers have used CFD as a tool for studying pollutant dispersion. This fact does not come without challenges, as CFD is a computationally expensive tool that has to compete with already established empirical models and empirical-based software. Gant & Tucker (2018) reviewed the challenges of CFD dispersion modelling, which include reliable representation of atmospheric boundary layers, suitable grid resolution and model variability. But according to X. Wang et al. (2019), CFD software is able to simulate and visualize plume drift more precisely than a Gaussian diffusion model or wind tunnel tests. In this sense, CFD programs like Ansys Fluent® (*Ansys. Engineering Simulation Software*, n.d.) can be the solution to evaluate those scenarios but being necessary a mesh capable to adapt itself to the terrain characteristics. Gianfelice et al. (2022) accurately predict the wind conditions in a complex terrain such as the Toronto city. They find that CFD can provide real-time estimations of the wind field with high precision. Oliver et al. (2013) highlights this crucial aspect of simulating when modelling the gas dispersion over La Palma Island. Shen et al. (2022) highlight the importance of the presence, number and location of inlet boundary conditions for gas dispersion cases, as they greatly impact turbulence and wind speed in the domain. The unstructured hexahedron mesh included by default in ANSYS Fluent® appears to be more suited for scenarios when barriers and mountainous terrain must be simulated (Vitali et al., 2021). These reviewed articles show the importance that the mesh generation and boundary conditions have on accuracy of the results.

Since there are many different cases and a lot of variables involved, more experimental data is needed to validate CFD studies ensuring good approaches (Schleder & Martins,

2016). Lateb et al. (2016) review wind flow studies around buildings because a correct simulation highly depends on an accurate modelling of the wind flow. CFD was more widely used in aerospace engineering than in any other field. Escarti-Guillem et al. (2019) predict the unsteady plume resulting from a rocket by using OpenFOAM. Synylo et al. (2020) analyse, using the OpenFOAM CFD code, the pollutant plumes produced by aircraft near airports to improve air quality. Alqallaf & Teixeira (2022) study the particle dispersion and erosion on a NASA compressor. They find good agreement between fan design parameters and CFD. These authors' research shows that CFD is a useful tool for predicting gas dispersion, but one of the main issues that it faces its use on large systems due to the computational power required for the simulations.

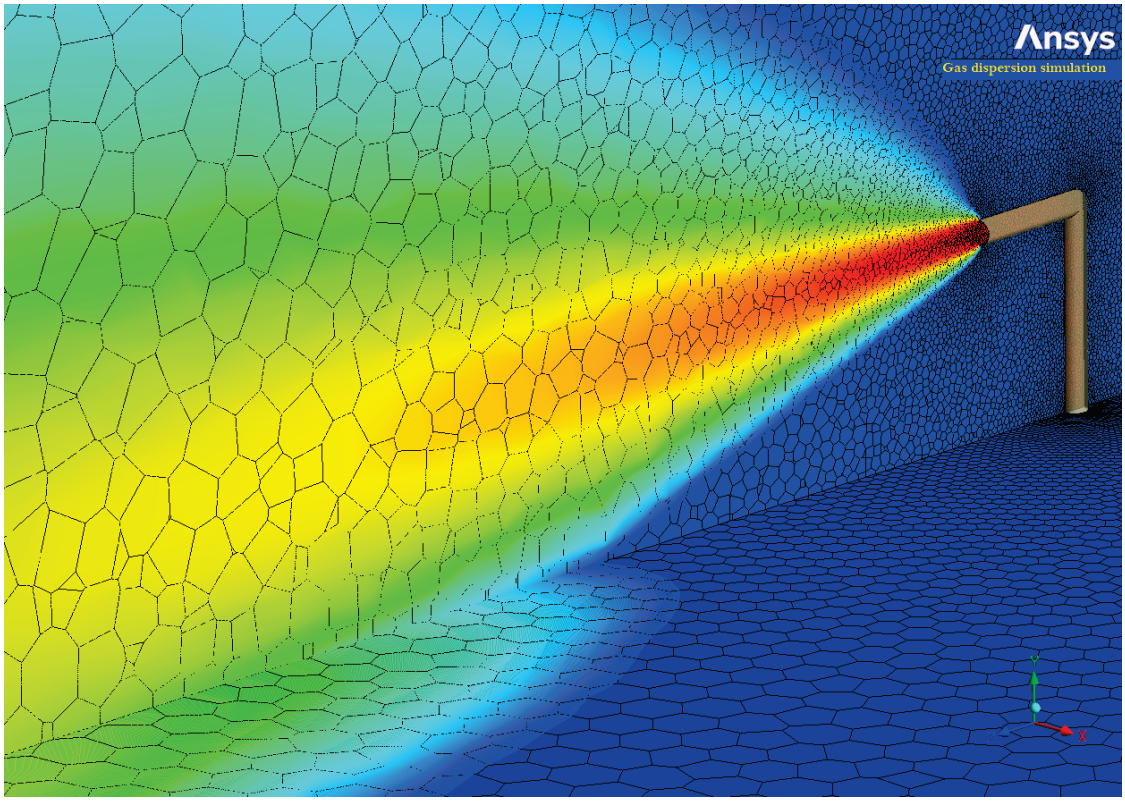

Figure 8: *CFD simulation of a pollutant dispersion with an elbow nozzle.*

In recent years CFD has seen an increase in its usage for safety and environmental problems. Nie et al. (2023) use Fluent to perform numerical simulations on spray nozzles dedicated to coal dust removal in ventilated environments. They find optimal parameters by combining experimental and CFD simulations. San José et al. (2018) use CFD modelling to infer the effects of climate change on temperature and air pollution of urban areas. They then estimate the cost on human health that climate change will have on the next 10 to 80 years. Hanjalić & Kenjereš (2005) simulate the pollutant accumulation in a town when the atmosphere is capped by an inversion layer, which is a weather condition that prevents the pollutant from leaving the region. Wójtowicz-Wróbel et al. (2023) recreate a typical urban domain in non-central areas and numerically investigate the dispersion of gases produced by a thermal waste treatment plant in various wind directions. Xin et al. (2021) studied dispersion on uneven mountain terrain over various kilometres. They find how the rough terrain greatly impacts the diffusion mechanisms.

Mehdi & Panin (2021) studied the gas dispersion in complex terrain, concluding that RANS turbulence models, particularly the k-Ɛ model, are adequate for such situations. Akhter et al. (2021) simulate the pollutant dispersion in urban areas with a k-Ɛ model and conclude that the building height has a high impact on dispersing pollutants. da Silva et al. (2022) confirmed the SST turbulence model with results obtained from a wind tunnel and then analysed the breathability in a city. Determining the most likely location of an unknown pollutant release is also possible with CFD. Particularly, Sharma & Kumar Patel (2020) provide a quick, accurate, and efficient approach for determining the location of contamination sources in real time.

Semiempirical models, which are based on the classical Gaussian Plume Model, are widely used and have been implemented in specialized software such as ALOHA. Nevertheless, when the terrain has some particularities that differ from the original conditions where the semiempirical model parameters were regressed, e.g., the presence of any obstacles, then CFD simulation is applied. CFD has been increasingly applied to atmospheric gas dispersion problems, especially for scenarios where GPM or ALOHA are considered not suitable or reliable. However, CFD also has some challenges and limitations, such as the need for validation with experimental data, the choice of appropriate turbulence models and boundary conditions, the computational cost and time, and the uncertainty quantification.

As stated in the paragraph above, several papers compare Gaussian models to one another or assess the differences between one of these models and CFD, but never have been compared all together experimental data, a Gaussian model, and CFD at our knowledge. The aim of this section is to apply the CFD to a scenario where experimental data is available to validate the CFD's reliability when it comes to gas dispersion and compare the results with those from ALOHA, which is a Gaussian Plume Model software. The strengths and weaknesses of the proposed model found in this thesis can be then considered by future research on this topic, providing insights into the accuracy and reliability of CFD simulations and helping to improve the prediction of long-term pollutant emissions. The methodology for this chapter can be found in chapter 4.2. and the results and discussion in chapter 6.

1.5. Hydrodynamics in stirred tanks

In chemical engineering operations, momentum transfer is almost always present. Fluids in unit operations tend to have some movement and therefore transfer momentum between them and their surroundings. Nevertheless, this momentum transfer is not always the most relevant factor in unit operations and can sometimes modelled macroscopically by using the balance of mechanical energy with the proper friction factors. There are, though, many cases where the internal hydrodynamics of a unit have a big impact on the efficiency, safety and viability of the process. One such example is stirred tanks or

reactors, where depending on the involved compounds and their properties, a proper agitation makes the difference between ruining a batch or obtaining the desired product.

Computational Fluid Dynamics (CFD) simulations are becoming a popular method for studying and optimizing mixing operations and agitation processes. Using CFD, multiple scenarios can be tested rapidly compared to physical setups without the need to consume large quantities of materials. By creating a virtual model of the stirred reactor and simulating fluid flow with different geometric characteristics, one can study the influence of these parameters on the fluid flow characteristics. For these reasons CFD is an attractive and cost-saving tool to study stirred tanks.

The problem that will be tackled is the agitation of highly viscous fluids such as polymers. Agitation quality plays a crucial role in heat transfer between the fluid and the tank wall during polymerization processes, especially with high viscosity polymers. Most polymerizations are exothermic processes that must occur at a constant reaction temperature. At times, the exothermicity of the reaction is insufficient to reach the specific temperature and requires heating the product. With other products, it is necessary to cool the fluid to maintain the desired reaction temperature. Once the reaction is completed, the product must be cooled to a temperature close to ambient, which consumes a significant portion of the process time. The final product often has high viscosity and a thick laminar flow film near the tank wall is formed, which hinders convective heat transfer. Stirred tanks intended for polymerization processes must be designed and operated in such a way that it ensures a minimum degree of heat transfer at the tank wall.

Energy consumption in agitation processes with high viscosity fluids is another variable to consider. High viscosity fluids require high energy consumptions for efficient heat transfer and short mixing time. In recent years, energy efficiency has become a worldwide concern, and modern industries must adapt their equipment if they want to compete in global market.

Impeller geometric parameters play a paramount role in agitation processes within stirred tank reactors. The angle of the blades determines the flow pattern within the reactor. Vertical blades (90º) push the liquid radially, with practically no axial movement. As the angle relative to the horizontal decreases, axial flow is promoted. When determining the optimal blade angle, power consumption and heat transfer at the tank wall are relevant factors to be considered. However, other parameters that have not been determined in this study such as the mixing time must be considered too. Kumaresan & Joshi (2006) studied the effect of blade angle on various fluid flow characteristics and concluded that as blade angle increases, power number (NP) and flow number (NQ) increase, while the mixing time is reduced. The study was conducted using a physical setup and CFD, and the simulation results demonstrated a high degree of concordance with the experimental data. Yang & Takahashi (2010) studied the influence of the blade pitch angle on the flow and energy dissipation in horizontal and vertical stirred vessels. Measurements for the two types of stirred vessels were carried out by experiments and numerical simulations using computational fluid dynamics (CFD). The results suggested that with an increase in the pitch angle, the flow pattern changed and the NP increased gradually in the horizontal

vessel and sharply in the vertical vessel. Nouri & Hockey (1998) studied the power characteristics of an impeller with six blades, each at 60º to the direction of rotation, in a fully baffled vessel as a function of Reynolds number. The results obtained showed that NP decreased rapidly by 12% at a Reynolds number of 191 and was constant at 0.057 ± 0.001 at high Reynolds numbers. The comparison with a Rushton impeller of the same size showed that the pumping efficiency of the pitched blade impeller is some 2.5 times higher and that it dissipates less power within the impeller. The methodology for this chapter can be found in chapter 4.3. and the results and discussion in chapter 7.

1.6. Study of partially full pipes

The presence of different phases is common in various chemical engineering processes. These different phase interactions can also be studied with CFD codes. Perhaps the simplest and often most forgotten case of different phases in a system is the open channel flow of partially full pipes.

Partially full pipes calculations are ruled by open channel hydraulics. Rigorously, the open channel hydraulics dictate that problems have to be solved by means of mass and momentum equations (continuity and Navier-Stokes). Traditionally, however, empirical equations like the Manning equation have been used due to the lack of enough calculation power. In the last fifty years, thanks to the technological advances in computation a brand-new branch has surged in fluid mechanics: CFD (Computational Fluid Dynamics). It allows to perform numerical calculations for a huge number of nodes simultaneously for the discretized equations of mass and momentum. ANSYS Fluent is a software that allows CFD simulations for a wide range of fluids and geometries in a relatively user-friendly interface.

1.6.1. The Manning equation

The Manning equation has been used for over a century to solve steady state, uniform flow open channel problems. The formula was proposed in 1889 by the Irish engineer Robert Manning (1891) as an evolution of the Chézy formula, based on the work on outdoor experimental canals done by numerous researchers of the time (Fischen, 2000). The Manning equation is expressed in Eq 39:

$$v = \frac{K_n}{n} * R_h^{\frac{2}{3}} * S^{\frac{1}{2}} \tag{39}$$

where v is the mean cross-sectional velocity, Rh is the hydraulic radius, S is the slope of the channel and n is the Manning number, which depends on the nature of the surface roughness of the canal boundaries. Kn is a coefficient whose value depends on the units of the velocity and the hydraulic radius, if it is expressed in [m/s] and [m] respectively its value is 1.

When it is taken in consideration that the mean cross-sectional velocity is the ratio of the volume flow and the cross-sectional area, and that the units are expressed in the metric system, the Manning formula is expressed as:

$$Q = \frac{A}{n} * R_h^{\frac{2}{3}} * S^{\frac{1}{2}} \tag{40}$$

where Q is the volume flow in [m/s], A is the cross-sectional area in [m] and the rest of the variables are the same as the ones of Eq. 39 in metric system.

The algorithm for resolving this equation is the one proposed in Figure 9. It starts by supposing a flow depth (h) value and calculating the volume flow Q. This process can be performed with the Solver tool from Excel.

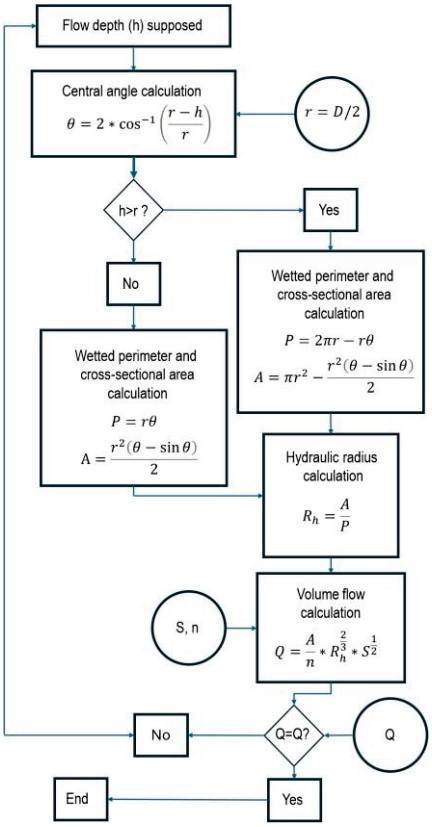

Figure 9: *Resolution iterative process for solving the manning equation.*

1.6.2. Modelling for multiphase flow

The models used for modelling the turbulence inside the partially full pipes are the same as the ones used for other applications like heat transfer. The k-ω SST model proved accuracy in a variety of cases and here is the model of choice. Apart from turbulence modelling, multiphase modelling is also required, a subject that has not been discussed before. There are two main approaches when it comes to modelling a multiphase flow. The Euler- Lagrange approach treats the fluid phase as a continuum by solving the Navier-Stokes equations, while the dispersed phase is solved by tracking many particles, bubbles, or droplets through the calculated flow field. The Euler-Euler approach treats each phase as interpenetrating continua. The volume fractions of the problem volume occupied by each phase are assumed to be continuous functions of space and time and

their sum is equal to one. Thus, there are equations of similar structure for each phase. The Euler-Euler Approach suits better the particularities of an open channel flow, as it is centered in the definition of the space that each phase occupies. ANSYS Fluent has three Euler-Euler approach models, the Volume of Fluid (VOF) Model, the Mixture Model and the Eulerian Model. The Eulerian Model is focused on fluid-solid and fluid-fluid problems. The Mixture Model allows gas-liquid problems and solves the mixture momentum equation and prescribes relative velocities between each phase to describe the dispersed phases. The VOF Model allows gas-liquid problems as well and is designed to track the position of the interface of both fluids. The VOF Model is the most appropriate multiphase model for open channel flows simulations since focuses on defining the depth of flow, which defines the mean cross-sectional velocity (ANSYS Fluent Theory Guide, 2024).

To track the interface of each phase the VOF model adds volume fraction continuity equations. For each new phase that is added one extra equation is appended to the to the solution algorithm. The number of volume fraction equations is the number of phases minus one, as the volume fraction equation is not solved for the primary phase. For open channel problems where there are two phases there is only one volume fraction equation. For the qth phase, Eq. 41 has the following form:

$$\frac{1}{\rho_q}[\frac{\partial}{\partial t}(\alpha_q \rho_q) + \nabla * (\alpha_q \rho_q \vec{v}_q) = S_{\alpha q} + \sum_{p=1}^{n} \dot{m}_{pq} - \dot{m}_{qp}] \quad (41)$$

Where $\alpha_{q}$is the q[th] phase fluid's volume fraction, m_{qp} is the mass transfer from phase q to phase p and $\dot{m}_{pq}$ is the mass transfer from phase p to phase q. By default, $S_{\alpha q}$ is zero, but it can be specified a constant or user-defined mass source for each phase.

The primary primary-phase volume fraction is computed based on Eq 42:

$$\sum_{q=1}^{n} \alpha_q = 1 \quad (42)$$

1.6.3. Engineering of open channel hydraulics

Open channel hydraulics has seen two research lines in the last fifty years. The first one intends to find better ways to model open channel flows by means of empirical equations. The second one focuses on taking advantage of the new technologies and uses CFD simulations to predict the behavior of free surface flows.

Regarding the first research branch, it is focused on getting a both rapid and accurate solution for problems that can be considered uniform and steady state due to their smooth variations under normal conditions, like rivers or sewers. Camp noted the dependence of the Manning number with the depth of flow. By changing the constant "n" for a variable "n" the accuracy improved (Camp, 1946). Saatci (1990) proposed a new equation that intended to remove the iterative process in the calculation of uniform, steady state free

surface flows by offering an explicit solution that allows to directly estimate the value of the depth of flow. However, this study branch is quite limited to mainly steady state uniform flows, with less research on transient cases or non-uniform.

Regarding the second research branch, it is focused more on resolving a wide range of problems that are more difficult to model empirically, mainly in transient state. Wu et al. (2000) presented a model for calculating flow and sediment transport in open channels. Olsen (2003) showed a three-dimensional CFD model was used to compute the formation of the meandering pattern in an initially straight alluvial channel.

Finally, in respect of partially full pipes as a special case of open channel flows, the research is very focused in experimenting with air entrapped pockets in the tubes. Bousso & Fuamba (2014) carried out experimental analysis to validate the numerical model they proposed. The methodology for this chapter can be found in chapter 4.4. and the results and discussion in chapter 8.

1.7. Simulations for materials engineering

Materials Engineering has been historically closely related to chemical engineering. Once the same field, they are now two separate fields but still share a lot of key features. The study of some processes like milling or mixing of solids is shared between the two areas of research. Consequently, some simulations are also performed for material design and process improvement in the scope of the Thermodust project. These simulations range from large scale, where the process is studied at a macroscopic level using Discrete Element Methods (DEM), to the atomic scale, where Density Functional Theory (DFT) or Molecular Dynamics (MD) methods are used. Between these two scales we find Finite Element Analysis, also used in the scope of the project. Starting from larger to smaller scales these methods are briefly described in the following sections. The specific methodology for each method can be found in chapter 4.5 while the results are discussed in chapter 9.

1.7.1. Discrete Element Methods

The Discrete Element Method (DEM) is a numerical technique for modelling the behaviour of systems composed of discrete, interacting bodies. It was originally created by Peter A. Cundall and Otto D. Strack in 1979 for simulating granular materials. Its uses extend from pharmaceutical applications to agriculture, chemical or mineral processing industries among others.

DEM simulates the motion of individual particles and their interaction between them. Such particles can vary in size from asteroids or planets with self-gravitating DEM like

the research performed by Sánchez & Scheeres (2011), to large rocks or fine powders for industrial applications or even to atoms in case of Molecular Dynamics simulations (MD), for which the principle is very similar. The method is based on solving Newton's second law of motion for a large set of particles:

$$m\frac{d^2x}{dt^2} = \sum F \tag{42}$$

Where m is the mass of the particle x is its position and ΣF is the sum of forces acting on such particle.

The key aspect of DEM resides in the ΣF calculation. In this term, forces can be self-gravitation, elastic or inelastic collisions, electrostatic etc. making this method applicable for a wide range of problems. In our case, the interest is in collisions between particles inside a mill, so the forces involved will be derived from collisions, which transfer translational and rotational momenta, and gravity.

The normal contact equations are from the Hysteretic linear spring model based on the Walton Braun theory (Walton & Braun, 1986). Rocky DEM is the software used to solve these simulations describes this model in Eq. 43 (Rocky DEM, 2020):

$$F_n^t = \begin{cases} \min\left(K_{nl}s_{nl}, F_n^{t-\Delta t} + K_{nu}\Delta s_n\right) & if\ \ \Delta s_n > 0 \\ \max\left(\lambda\, K_{nl}s_n^t, F_n^{t-\Delta t} + K_{nu}\Delta s_n\right) & if\ \ \Delta s_n < 0 \end{cases} \tag{43}$$

Where $F_n^{t-\Delta t}$ and F_n^t are the normal contact forces in previous and currents timesteps respectively, Δs_n is the change in contact normal overlap at current time. It is positive when particles approach each other and negative otherwise. Is defined as $\Delta s_n = s_n^t - s_n^{t-\Delta t}$ where s_n^t is the normal overlap value at time t. K_{nu} and K_{nl} are the values for unloading and loading contact stiffness (derived form the Young's modulus and particle size at each collision) and λ is a dimensionless constant assumed to be 0.001.

Tangential forces are estimated by using the linear Coulomb limit model. Described in Eq. 44:

$$F_{\tau,e}^t = F_\tau^{t-\Delta t} - K_\tau \Delta s_\tau \tag{44}$$

Where $F_{\tau,e}^t$ is the tangential force at time step t, K_τ is the tangential stiffness and Δs_τ the tangential relative displacement. This model assumes that the tangential forces cannot exceed the coulomb limit, thus the final force is calculated, Eq. 45:

$$F_\tau^t = \min\left(\left|F_{\tau,e}^t\right|, \mu_f F_n^t\right) \tag{45}$$

Note that here μ_f is the friction coefficient between the two materials.

Collision statistics are collected and account for three different types of work: dissipation work, impact work and shear work. Dissipation work is the amount of mechanical energy that is transformed irreversibly into other forms of energy. Impact work refers to the maximum amount of work transferred during a collision. It is the one that can lead to breakage of particles, and it is defined as the integral during the loading stage of the collision of the normal contact force F_n over the overlapping distance s_n:

$$W_{imp} = \int_{loading} F_n ds_n \tag{46}$$

Shear work is defined mathematically in a similar manner but with tangential forces F_τ and over the sliding distance ds_τ. The collision statistics then translate to obtaining the energy spectra of collisions. This energy spectra data correlates different collision energy ranges with the occurring frequency of such collisions e.g. with some given milling conditions produce 1000 collisions per second of an energy between 1 J- 2 J, 10^4 collisions of energy between 0.5 J and 1 J and so on. This energy spectra is directly correlated to the breakage and interactions between the particles, so a model can be created to fit the Particle Size Distribution (PSD) data obtained experimentally with the DEM energy spectra.

1.7.2. Finite Element Analysis

The basic equation in Finite Element Analysis for structural analysis is shown in Eq. 47:

$$K\,u = F \tag{47}$$

Where K is the global stiffness matrix, u is the global displacement vector and F is the global force vector. This global formula is extracted from Hooke's Law, Eq. 48:

$$\sigma = D\epsilon \tag{48}$$

Where σ is the stress vector, D the material property matrix (elastic modulus) and ϵ the strain vector. Equation 48 is applied to a discretized domain divided in individual element contributions. Between each element a virtual spring is placed that replicates the interaction between the different nodes of the system. Figure 10 showcases this discretization process.

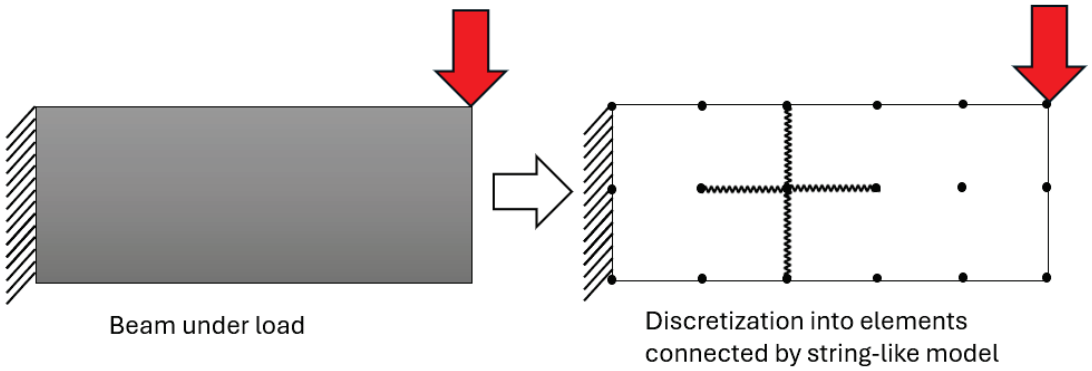

Figure 10: *Discretization of a 2D beam into spring-connected individual elements.*

These simulations can account for phenomena like elasticity, plastic deformation under load and failure of materials among others.

1.7.3. Molecular dynamics simulations

Complex interactions are present between different types of nanomaterials inside the mill. Namely copper and carbon atoms exhibit adhesion between themselves and the mechanisms at which these interactions occur have to be studied at an atomic level. Molecular dynamics are closely related to DEM in the sense that they simulate a set of particles, in this case atoms, and apply a force field to mimic the atomic interactions between them. These interactions go from electronic attraction or repulsion, to bonding, Van der Waals forces or quantum effects. This makes MD a powerful tool to estimate large sets of atoms where properties arise from multiple atomic interactions like crystallization, melting, membrane separation etc.

The most common (and one of the simplest) forms of force fields is the Lennard-Jones potential, Eq. 49:

$$V_{LJ}(r) = 4\,\varepsilon\left[\left(\frac{\sigma}{r}\right)^{12} - \left(\frac{\sigma}{r}\right)^{6}\right] \tag{49}$$

Where $V_{LJ}(r)$ is the Lennard-Jones potential, r is the distance between the two atoms, ε is the depth of the potential well and σ is the interatomic distance r at which the potential is zero.

This interaction is for two unbounded particles without charge, those particles can be atoms with repulsive and attractive Van der Waals interactions (Dzyaloshinskii et al., 1961). At short distances the repulsive term is stronger while at larger distances the attractive term is larger. In the middle there's a point where the potential is minimal and therefore the force is zero, an equilibrium point where the particles are most stable, although due to thermal agitation they can escape this potential well, Figure 11.

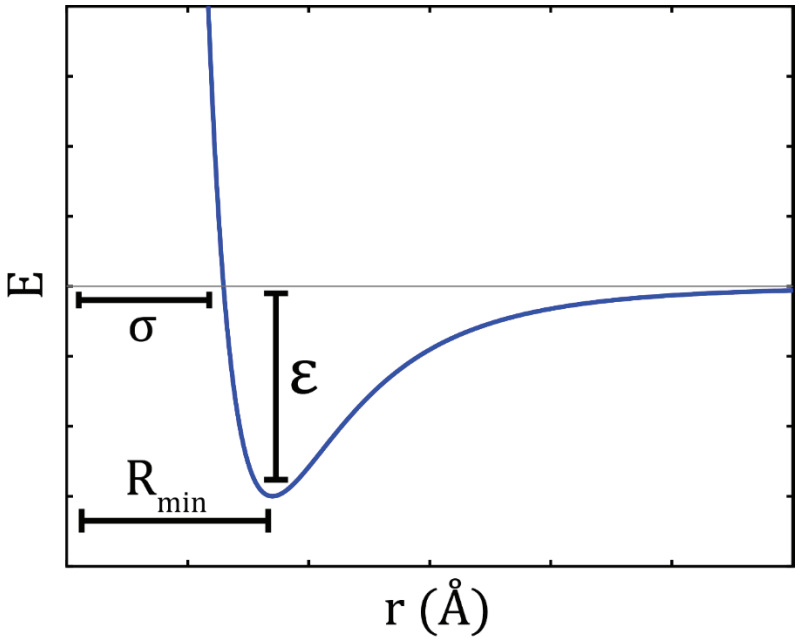

Figure 11: *Scheme of Lennard-Jones potential. Credits to Christophe Rowley, https://commons.wikimedia.org/wiki/File:Schematic_of_the_Lennard-Jones_6-12_Potential.png*

The force term is then computed as, Eq. 50:

$$F = -\nabla V \tag{50}$$

Where F is the force and ∇V is the gradient of potential with respect to position. Each atom contributes to the potential of its surroundings making for a total potential field upon which forces are calculated. Additional to Van der Waals forces, the potential term may include atomic bonding, electrostatic interactions, bonding angle or dihedrals, as seen in Eq. 51:

$$V = V_{bond} + V_{angle} + V_{dihedral} + V_{LJ} + V_{electrostatics} \tag{51}$$

Each of those terms may be modelled with different equations but generally the equation above is substituted for Eq. 52:

$$\begin{aligned} V(r) = & \sum_{bonds} k_i^{bond}(r_i - r_0)^2 + \sum_{angles} k_i^{angles}(\theta_i - \theta_0)^2 \\ & + \sum_{dihedrals} k_i^{dihe}[1 + \cos(n_i\phi_i + \delta_i)] + \sum_i \sum_{j \neq i} 4\,\varepsilon_{ij}\left[\left(\frac{\sigma_{ij}}{r_{ij}}\right)^{12} - \left(\frac{\sigma_{ij}}{r_{ij}}\right)^{6}\right] \\ & + \sum_i \sum_{j \neq i} \frac{q_i q_j}{4\pi\, D\, r_{ij}} \end{aligned} \tag{52}$$

In practice, for complex systems, force fields are hard to find and implement in various scenarios, which means that they have to be extracted from quantum simulations like DFT (Density Functional Theory) methods. These methods are based on the Kohn-Sham equations (Kohn & Sham, 1965) designed for simplifying and numerically resolving the Schrödinger equation.

1.7.4. Density Functional Theory

The basic equation that is to be solved when using this method is the Schrödinger equation for a set of atoms formed by nuclei interacting with its electrons, Eq. 53:

$$i\hbar \frac{\partial}{\partial t}\Psi(r,t) = \widehat{H}\Psi(r,t) \tag{53}$$

Where i is $\sqrt{-1}$, ħ is the reduced plank constant, $\Psi(r,t)$ is the wave function that describes the physical state of the system (usually the time is omitted to consider only stationary electronic state solutions), $\widehat{H}$ is the Hamiltonian operator that depends on the phenomena considered. This equation by itself is too computationally demanding to be numerically solved for systems larger than a few atoms, as the algorithm scales with 2^n, where n is the number of electrons. This resolution is the one used in the Hartree-Fock method. Some considerations are made to transform this kind of computational hazard into a system that is easier to solve, at least up to systems up to a few hundred atoms.

A useful consideration is the Born-Oppenheimer approximation that, based on the basis that electrons are much smaller and faster than the nucleus, assumes that the electrons adapt instantly to changes in position of the nuclei. Electrons are perceived by the nucleus as an electronic cloud, while for the electrons the nucleus is static. This approximation allows to consider the atomic nucleus as fixed charged points in space, enormously

speeding up the computational process. A final simplification is the one made in DFT, where electronic density is assumed to be responsible of the emerging properties of materials and their interactions and therefore obtaining such electron density is the objective of DFT. This electron density is defined by Eq. 54 for a set of noninteracting orbitals ϕ:

$$\rho_e(r) = \sum_i |\phi_i(r)|^2 \qquad (54)$$

Where r is the 3 dimensional position (x,y,z), ρ_e is the electron density and $\phi_i(r)$ is the ith occupied orbital present in the system. With these and many more considerations detailed in (Kohn & Sham, 1965) are the basis of the Kohn Sham equations which DFT attempts to solve numerically.

The basis of DFT calculations has been summarized but its applications in the scope of this research are to be explained. DFT is a widely accepted method for its accuracy and reliably, especially compared to molecular dynamics simulations. Its complexity prevents us to perform simulations involving more than a few hundred atoms. Here is where Neural Networks come into play. Neural networks are designed to fit nonlinear high-dimensional data. DFT calculations are used to train a High-Dimensional Neural Network Potential (HDNNP) which uses atoms positions and their interactions (such as bonding) as input and outputs a force field that can be used for MD calculations. Thanks to this procedure DFT accuracy can be exported to MD providing reliable predictions of the materials behaviours and interactions.

2. Research scope

Chemical Engineering has typically benefited from computational tools based on macroscopic balance along the various units that can be present in a chemical process. These simulations rely on semiempirical models and correlations to describe the complexity of each unit operation.

Microscopical balance calculations are widely used in other engineering fields to evaluate and/or optimize various key components. For instance, in aeronautical engineering the drag and lift of a wing is estimated with Computational Fluid Dynamics (CFD) calculations. Mechanical engineering often relies on Finite Element Analysis to discern how close are certain structures to failure. Although being present in some areas, these tools have not yet taken a significant role in the chemical engineer's day to day basis.

The purpose of this thesis is to test these computational tools applied to various chemical engineering units and processes, to evaluate its accuracy, precision and utility when applied to this field. These tools will be, in the following sections, compared against classical correlations and engineering tools to test their capabilities. Optimizations that could only be obtained by experimental process will also be performed virtually, providing a good sense on how these tools can be used. Their utility is tested in real case scenarios where their performance is evaluated. In order to answer this general question, more specific issues and questions are proposed, based on different the transport phenomena equations (momentum transfer, heat transfer and species transfer) and on common cases studied in chemical engineering. For the cases studied, the first questions are about the consistency, accuracy and validity of the CFD models. Once validated other questions arise trying to optimize/improve the studied processes.

For heat transfer, the specific questions are based on the study of heat exchangers:

- How is the accuracy of CFD tools compared to traditional semiempirical correlations?
- Do they perform well when used in more complex geometries like heat exchangers with twisted tapes?
- Which is the best turbulent model to simulate those cases?
- What are the optimal parameters of a novel geometry consisting of a corrugated tube with twisted tape inserts?

For species transfer these questions are based on the study of pollutant dispersion:

- How do CFD tools compare in accuracy with other semiempirical methods and well-established software?
- How do these tools perform in the presence of obstacles?

For momentum transfer, two unit are studied via CFD, a stirred tank reactor and open channel flow in partially full pipes. For these cases, the following questions are provided:

- What is the best blade angle to obtain optimal agitation in a stirred tank reactor?
- How does the Reynolds number impact the heat transfer in such unit?

- Do CFD tools provide similar results as the semiempirical correlations found by Manning for open channel flow?
- How does a geometry like an elbow affect the fluid flow in an open channel?

Finally, simulations in the scope of the Thermodust project are performed, an European project that uses ball milling to produce powders with specific properties. Following questions are to be answered:

- Are Discrete Element Method simulations able to reliably describe the dynamics of a planetary mill process?
- What are the best conditions to produce the desired products?
- Can other computational tools (like DFT or MD) provide useful additional information on the interactions of different nanoparticles?

3. Objectives

This research is focused on covering various main topics in chemical engineering: Heat transfer, mass transfer, fluid dynamics and solid treatment. For doing so, this thesis is divided into various sections, each covering extensively one or more of the topics.

For heat transfer, different turbulent models are tested for simulating a double pipe heat exchanger and their accuracy is compared against semiempirical correlations. Similar work is done for a heat transfer enhancement tool like the twisted tape, that poses the additional complexity of an abrupt geometry and induced turbulence. Finally, a novel geometry is optimized with CFD, providing optimal operational conditions in various scenarios.

The topic of mass transfer is studied via a pollutant dispersion study, where a toxic release is simulated, and its range and possible damage are evaluated in various scenarios. Firstly, experimental results, classical correlations and CFD are compared for a wide range of experiments and atmospheric conditions. Then a study on how the presence of obstacles affects the pollutant dispersion is performed both with CFD and non-CFD tools.

Both previous topics contain fluid movement and therefore momentum transfer, but these are also studied in detail in the two following sections: hydrodynamics in stirred tanks and the study of partially full pipes. In the first case, an industrial sized stirred polymerization reactor is studied. Here, the angle of the agitation blades will be simulated for various Reynolds numbers. The second case will study open channel flow and compare the results with empirical data. Other open channel geometries are also studied, like a 90^{o} elbow case. In these two cases, validity of these computational tools is assessed for very simple but extremely important for chemical engineers, fluid dynamics cases.

Finally, a collaboration with the European Project Thermodust in the production of novel nanomaterials allowed for the application of computational tools focused on materials engineering to be tested in a real project and with live experimental feedback. Discrete Element Method is used for simulating the milling of the nanoparticles. Other tools like DFT, MD and Finite Element Analysis are used to understand in detail the collisions and interactions of these particles inside the mill.

4. Materials and methodology

All simulations are performed using Ansys® Software. The geometry is designed in programs such as SpaceClaim®, DesignModeler® or Autocad®. The meshing process was divided depending on the specific needs between the Ansys® mesh and Fluent® mesh. Finally, all fluid simulations are performed with Ansys Fluent®.

4.1. Heat exchange simulations

For the different heat exchange case studies different methods have been used. Three cases are studied of increased complexity. Firstly, a Double Pipe Heat Exchanger in parallel disposition, then a tube with constant temperature at the walls and a twisted tape insert and finally the combination of twisted tape and corrugated tube. In the first two cases, the goal is to find which turbulent model fits the empirical data found in literature. For the third case, no empirical data is available, so the models validated earlier are considered valid for the case. The goal is then to optimize the geometry to obtain the highest value of TPF.

a)

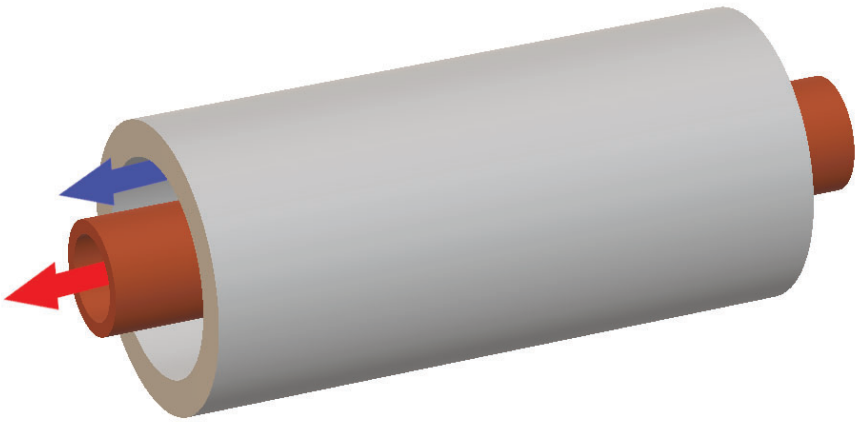

b)

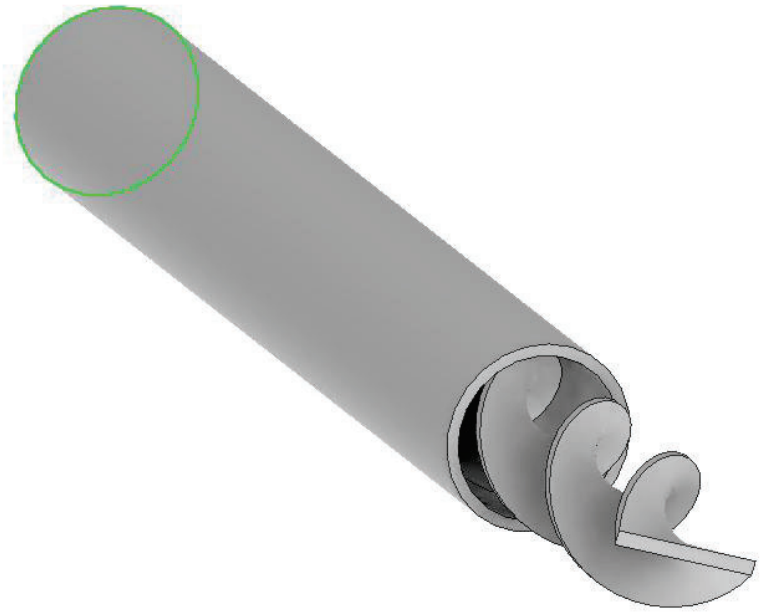

c)

Figure 12: *Three different geometric cases studied. a) Double pipe heat exchanger in parallel setup. b) Plain tube with twisted tape insert. The temperature at the external wall is constant. b) Corrugated tube with twisted tape insert. The external wall is treated similarly as in case b).*

4.1.1. Double pipe heat exchanger methodology

The double pipe heat exchanger is compared against extensive available experimental data extracted from various handbooks such as Serth, Levenspiel and Sinnot. For this comparison to be performed adequately, the ranges at which these correlations are

obtained must be preserved, so a simulation is designed to fit such ranges. Those correlation methods take into account the hydraulic diameter of the annular tube (outer tube of the heat exchanger) for the estimation of its pressure drop. Rothfus et al. (1950) proved that these methods tend to underestimate the Fanning Friction Factor of the system and proposed the use of a correction factor, Eq. 55:

$$f_2 = \frac{R_i^2 - r_m^2}{R_i(R_i - r_o)} f \tag{55}$$

where r_m is the radius at which the velocity is maximal.

4.1.1.1. Geometry and input conditions

As seen in Figure 13, the geometry consists of two concentric pipes where hot and cold fluid travel. Both fluids are water. The hot fluid travels inside the inner pipe as seen in Figure 13. The chosen length is set to be sufficient to ensure profile stabilization although some techniques are later used to ensure that the flow is stabilized from inlet to outlet. In order to account for the difference in temperature that the fluids (water in both pipes) experiences, all properties except thermal capacity (which is fairly constant in the range of study) are fitted to polynomials of temperature.

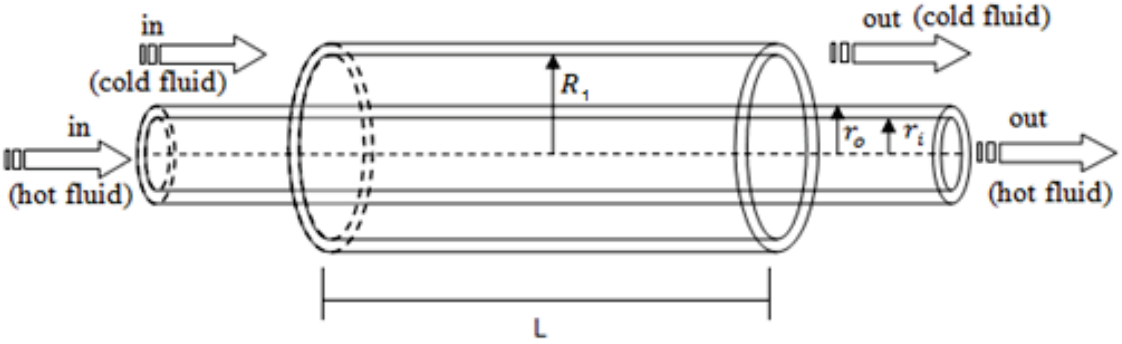

Figure 13: *Simulated domain of the Double Pipe Heat Exchanger.*

The simulations will include the copper solid inner pipe where heat transfer occurs. The dimensions and operating conditions of the pipe are shown below in Tables 5 and 6.

Table 5: *Dimensions of the pipe*

	Parameter	Value (cm)
Inner pipe	Inside radius (r_i)	1.42
	Outside radius (r_o)	1.51
Outer pipe	Inside radius (R_i)	2.11
	Outside radius (R_o)	2.22
Pipe Length	(L)	100

Table 6: *Input values at the boundary conditions*

	Parameter	Value
Inner pipe	Inlet velocity	0.5 m/s
	Inlet temperature	363.15 K
Outer pipe	Inlet velocity	0.5 m/s
	Inlet temperature	288.15 K

To ensure fully developed profiles, some iterations of the same tube are performed by replacing the inlet velocity value (given only in the first iteration) with the velocity profile obtained at the output of the pipe. The same procedure is performed at the outlet, where the pressure profile found in the inlet is then exported for the pressure outlet. This process is repeated until the input profiles in the inlets are indistinguishable from those found at the outlet, that is the flow is stable and fully developed. This procedure only takes about three iterations. The values of pressure drop are then estimated by area-averaging the pressure at inlet and outlet and making the difference. There's no need to stabilize the temperature profiles as the fluid will not start to transfer heat until it arrives at the heat exchanger wall, contrarily to momentum, which is surely developed upon arrival at the heat exchanger.

4.1.1.2. Turbulence models considered

The main goal of these simulations is to compare the predictive power of the various turbulent models available in Ansys Fluent ®. Each turbulence model is tested with each wall treatment inside the same family. Some wall treatments are avoided for the k-ε such as Standard Wall Functions or Enhanced Wall Treatment, the first for not being a Mesh insensitive treatment and the second for causing solution instability when the turbulent Reynolds number is around 200 at the boundary layer (Ansys, 2021). All simulations are tightly converged to a continuity and other residual values of at least 10^{-5} except for the mesh optimization test with fewer nodes, that are impossible to converge and stabilized around values of $2\sim4 \cdot 10^{-5}$.

Table 7 shows that for this case only two equation viscosity models are selected. It is considered that this is a simple case and with a high enough Reynolds number (well above the laminar-turbulent transition zone) allows us to employ RANS. The use of RSM (Reynolds Stress Models) seem to only provide significant advantages when the conditions produce highly swirling flows or flows with strong curvature. As such they should not make any improvements to these particular settings. Finally, one-equation eddy viscosity models are not suitable for free-shear flow, which is of great importance in our case study. Therefore, this work is focused on two equation eddy viscosity models, k-ε and k-ω. The 3 different versions of the k- ε models that are used are combined with

two types of wall treatment, Scalable Wall functions and Menther-Lechner. As for k- ω models, SST (shear stress transport) avoids free shear flow errors, and this option is used alongside its default wall modelling and Low-Reynolds corrections.

Table 7: *Different turbulence modelling employed. Each Turbulence model is combined with each associated wall treatment*

Family	Turbulence model	Wall treatment
k-ε	Standard	Scalable Wall Functions
	RNG	Menther-Lechner
	Realizable	
k-ω	SST	Default treatment
		Low-Re corrections

4.1.1.3. Mesh

The mesh created covers the three simulated zones: inner tube, outer tube, and solid wall. Different meshes are created according to the y+ necessities of each model. Wall modelling turbulence models such as k-ω require values of $y+\approx 1$ so an inflation is created at the wall of the tube. Figure 14: depicts the mesh generated for such case where y+ needs to be that low.

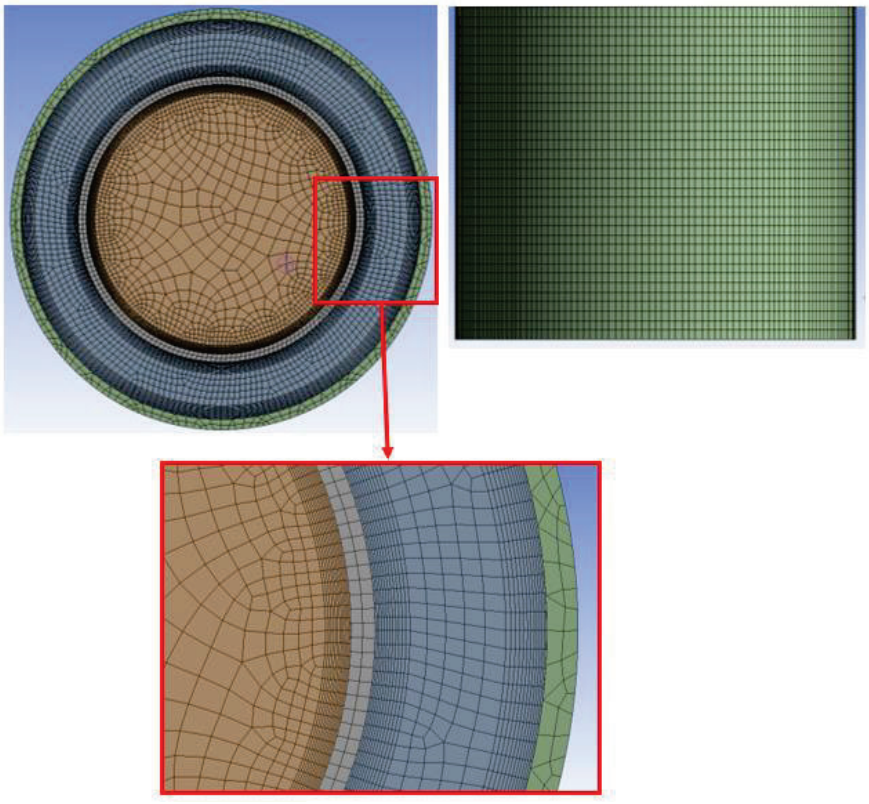

Figure 14: *Meshing for double pipe heat exchangers.*

Table 8 shows the different meshes tested for the k-ε model, similar configurations are tested for the k-ω model. The computational time has to be taken into consideration when selecting the mesh. The final mesh obtained is the one providing more accuracy with the fewer number of nodes possible. After performing the simulations, the clue values such as pressure drop, and Output Temperature are extracted and compared.

Table 8: *Mesh configurations tested for the k-ε model*

Number of radial divisions	Element size (m)	Inflation Layers	Growth Rate	Number of Nodes
50	0.006	5	1.2	**1 003 879**
150	0.003	5	1.1	**2 322 692**
200	0.002	5	1.1	**3 974 133**
200	0.002	10	1.1	**5 402 484**
200	0.002	12	1.1	6 669 440
235	0.00175	10	1.1	**7 073 405**
200	0.002	15	1.1	**7 710 581**
250	**0.0015**	**10**	**1.1**	**8 583 650**

With the data obtained from the mesh optimization (Table 8), it has been concluded that 200 divisions, element size of 0.002, 12 inflation layers and growth rate of 1.1 are sufficient for the set purpose. The considered mesh for the following simulations is the one with $6.7 \cdot 10^6$ nodes highlighted in Table 8.

4.1.2. Plain tube with twisted tape inserts methodology

In the previous section the validity of the different turbulent models is tested for simple Double Pipe Heat Exchangers. In the following section, a similar study is conducted on pipes with twisted tape inserts, studying the Nu and friction factor and comparing it to empirical data on these systems. The turbulence induced by the twisted tape offers an additional challenge for these models, which by assuming isotropic turbulence, they can create an additional source of error.

In order to test consistently different models and wall treatments, every other source of error has to be reduced to the minimum possible values. According to Ansys Fluent

(Oswald, 2015) there are five sources of error: Round-off, iteration, discretization, model and systematic. Round-off errors are produced when the numerical precision of the computer is not enough. To avoid this kind of errors, all CFD simulations in this project are performed with double precision variables. Iteration errors occur when solutions are not fully converged, or the solution oscillates between values. This error is often mitigated with sufficient iterations to ensure convergence. In some cases, the model or the mesh can cause numerical instability which can affect the convergence. Discretization errors occur when the mesh is not fine or has not enough quality, often misrepresenting the geometry or not allowing sufficient representation of the gradients present in the problem. While tetrahedrons meshes can cover extreme geometries, they often come with errors such as numerical diffusion. Prism meshes on the other hand, usually avoid this type of errors, and are used in this research for all the models. Mesh optimization is key to avoid these errors. The model error is what this research seeks for. Different models can lead to different results, as their formulation and constants differ from one to another. Most models require specific conditions to operate optimally. That is, models such as k-ω require that the first node located at a fluid region is at a distance y+≈1. Wall function methods often ask for a coarser mesh, requiring meshes at a y+>30 to give proper results. When using wall functions, this research will focus on wall functions insensitive to y+. Different meshes are designed according to the different requirements of each model. For k-ε, the mesh is optimised according only to the cell size, as all the wall treatments used are said to be y+ insensitive. For k-ω models, the cell size is optimised and then a mesh adaptation is performed to ensure that all the nodes in the domain have at least y+≈1 at the first node near the wall (ANSYS Fluent Theory Guide, 2024).

4.1.2.1. Problem description

Simulations are conducted so that they emulate the conditions present in Eiamsa-ard et al. (2010) experimental procedures. The setup consists of a single tube with a twisted tape insert and surrounded by an electrical heater. For emulating a phase changing vapour, temperature will be assumed to be constant at the outer wall of the pipe. Different twist ratios (TR, defined as y/d) and Reynolds numbers are tested. Figure 15 describes the different variables in the domain.

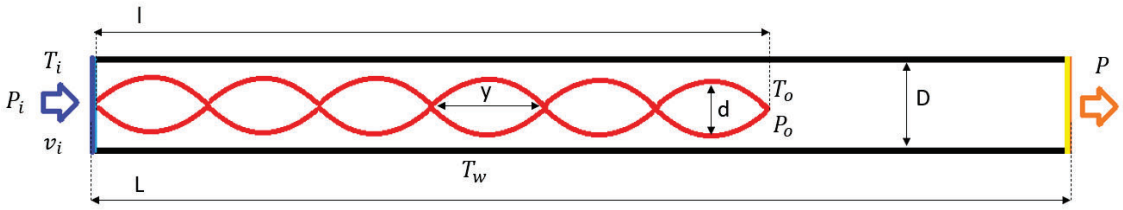

Figure 15: *Outline of the problem with its domain variables. In blue is depicted the velocity inlet and in orange the pressure outlet*

Here, the input variables are the inlet temperature T_i ; the wall temperature T_w ; the inlet velocity v_i , the outlet pressure P, which is set to atmospheric pressure; and the different geometrical parameters. As for the output parameters, P_i is set to be the pressure at the inlet, which is compared against P_o, the pressure at the end of the TT, which is the relevant section of the simulation. Temperature T_o is also taken at the end of the TT. The reasoning behind the twisted tape not covering the full length of the pipe is that pressure outlets near obstacles can produce backflow errors, leading to poor convergence. By extending the pipe, it is guaranteed that the flow at the outlet flows in the same direction, thus avoiding this issue. The average pressure and temperature are also monitored in various lengths along the tube to test whether the profiles have stabilized and if the entrance effects are relevant in this scheme. If these effects are large enough, the comparative values of pressure and temperature are then taken from a point where the profile is already stable. Table 9 describes the different input parameters of the system, similar to those found in Eiamsa-ard et al (2010).

Table 9: *Values for different variables*

Parameter	**Value(s)**
Inlet velocity (v_i)	4, 6, 8, 10, 12 m/s
Inlet temperature (T_i)	300 K
Reynolds number (Re)	From 4 000 to 19 000
Tube length (L)	1.75 m
TT length (l)	1.25 m
Tape pitch length (y)	138, 184, 230 mm
Twist ratio (TR= y/d)	3, 4, 5
Tube diameter (D)	47 mm
Tape width (d)	46 mm
Tape thickness	0.8 mm
Outer wall temperature (T_w)	363 K

The working fluid is air, whose physical properties such as thermal conductivity (k), specific heat (cp) and viscosity (μ) are temperature dependent. Ideal gas model is selected for estimating the air density in this case, as air is compressible and pressure is low enough.

4.1.2.2. Empirical correlations

Several correlations that proceed from experimental results are found in the literature. It is often the case that the range for which those correlations are designed does not match exactly the range of the simulations performed. Eqs. 56 and 57 are found in Eiamsa-ard et al. (2010), valid for all the range of simulations.

$$Nu = 0.06\, Re^{0.75} Pr^{0.4}\, TR^{-0.26} \tag{56}$$

$$f = 10.02\, Re^{-0.46}\, TR^{-0.48} \tag{57}$$

where Re is the Reynolds number, Pr is the Prandtl number and TR is the twist ratio. Other correlations are found in Chang et al. (2007), where the range of TR goes from 1.56 to 2.81. Their results should be at least suitable for our simulations with TR =3, as for higher twist ratios the extrapolation of the equations could lead to errors. Functions generated by Manglik et al. (1992) are used to estimate Nusselt numbers. Date (1974) also found correlations for laminar and turbulent flows with a range of $Re/Tr \geq 100$ also valid in this research, useful for estimating friction factors. The previously mentioned studies are widely used and accepted, being also validated by other studies such as Kumar (2000).

4.1.2.3. Turbulent models

In this section the turbulent models and wall treatments are classified without entering in much detail of the equations used by all the models and focussing more on its general usage and recommendations. From the turbulent models available, this research is focused on RANS (Reynolds Averaged Navier-Stokes) models, more specifically in two-equation Eddy viscosity models and Reynolds Stress Models (RSM). LES (Large Eddy Simulations) and other similar models which require Subgrid-Scale turbulent models are discarded due to the high computational costs and time that they require as well as the long flowtime required to obtain reliable engineering values. Two-equation Eddy viscosity models and RSM are the ones that are currently most used for modelling these units, as they offer a fair trade between accuracy and computational requirements. They are time-averaged, which means the variables extracted from the models can be of engineering interest, as they are not time-dependant. Two of the most relevant RANS models nowadays are k-ε and k-ω based models and their variants. The main difference between them lays in how those models behave in free shear flow situations and wall bounded ones. K-ε models are more reliable away from boundaries, where free shear flows are present. As such, they require additional equations for modelling the domain close to boundaries, that may come in form of wall functions or additional models. As a counterpart, k-ω is a low Reynolds model, which means that is better suited for wall bounded flows, decreasing in accuracy for free-shear flows. These reasons lead to models like k-ω SST to be a combination of k-ω and k-ε each applied at the region where they are more accurate by using a blending function. RSM models require more computational

time, but unlike two-equation models, they do not rely on the Boussinesq approach which assumes that the turbulent viscosity (μ_t) is isotropic (Hinze, 1975). Seven additional transport equations are required by RSM to compute μ_t which create anisotropy in the turbulence. In cases with swirling flows such as this one RSM can yield better results as two-equation models (ANSYS Fluent Theory Guide, 2021).

Table 10: *Different models and wall treatments*

Turbulent model	***Variants***	***Wall treatments***
k-ε	Standard RNG Realizable	Scalable Wall Functions (SWF) Non-equilibrium wall functions (NEWF) Enhanced Wall Treatment (EWT) Menther-Lechner (ML)
k-ω	SST	Default k-ω modelling Low-Reynolds corrections
RSM	k-ε based: Linear Pressure Strain Quadratic Pressure Strain	Scalable Wall Functions (SWF) Non-equilibrium wall functions (NEWF) Enhanced Wall Treatment* (EWT)
	k-ω based: Stress Omega ** Stress BSL	Default k-ω modelling

**Only available for Linear Pressure Strain **With shear flow corrections*

Table 10 shows each turbulent model variant combined with each wall treatment, generating a total of 19 combinations tested in the present study. For k-ε models (both k-ε and k-ε based RSM) wall functions are implemented as well as wall modelling methods such as Enhanced Wall Treatment (EWT) and Menther-Lechner (ML), all of which are y+ insensitive. EWT treatment is selected with the additional option of pressure gradient effects and thermal, which would consider the presence of large pressure or temperature gradients near the walls if there were any. K-ω based models are all suited with free shear flow improvements by using blending functions with k-ε (SST and Stress BSL) or the shear flow corrections of the Stress Omega model.

4.1.2.4. Mesh optimization

As stated before, the mesh optimization is different for k-ε based models and for k-ω based models. For k-ε models, the relevant mesh optimization is performed only for the cell size, as all the wall treatments are insensitive to y+. Inflation layers are also tested with these models and the results show that the influence on the results of decreasing y+ is minimal. Different node distance values are tested, and the most relevant variables are then extracted: pressure drop and temperature.

4.1.2.5. Convergence

To ensure convergence it is not sufficient to track residuals, which are dependent on how close from the solution are the initialization values. Two additional variables are tracked: area-weighted average pressure at the inlet and area-weighted average temperature at the outlet. These are relevant variables which must be converged to validate the results. All residuals in the simulations are converged to at least 10^{-5}. As for the tracked variables, it is ensured that they have not varied in more than 10^{-5} for the last 30 iterations. For most models though, the convergence criteria is much more strict, making almost all the simulations converge to 10^{-7} for residuals and tracked variables, as seen in Figure 16, where the k-ω SST model is converged to a continuity value of 10^{-7}.

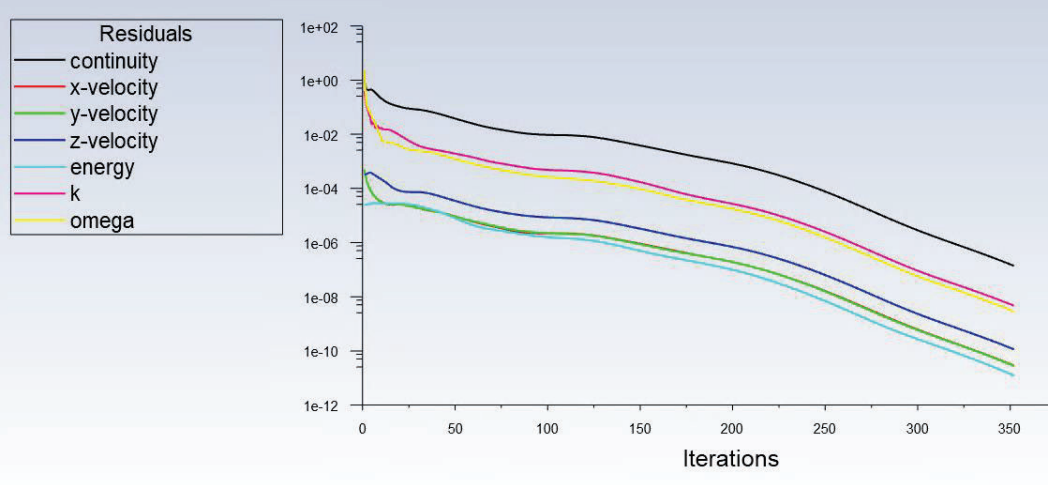

Figure 16: *Example of convergence in a k-omega model.*

4.1.3. Corrugated tube with twisted tape inserts methodology

The methodology used for the optimization of the corrugated tube with twisted tape insert is like the one followed for the simple twisted tapes. Here the goal is not to validate the turbulent models, as there is not enough experimental data available on this specific system, but to optimize the geometrical parameters involved. The geometry consists of various parameters as seen in Figure 17:

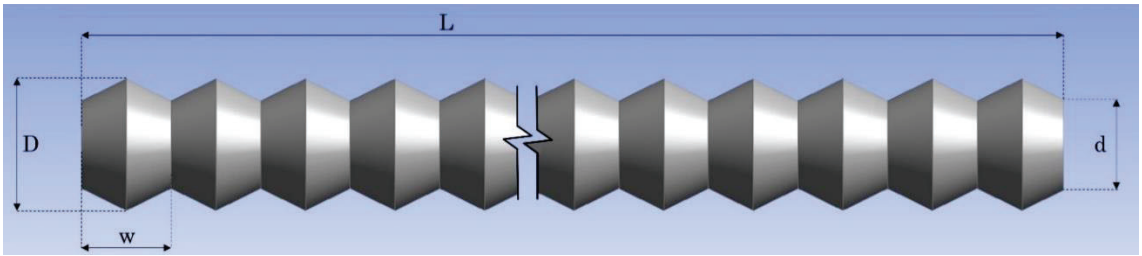

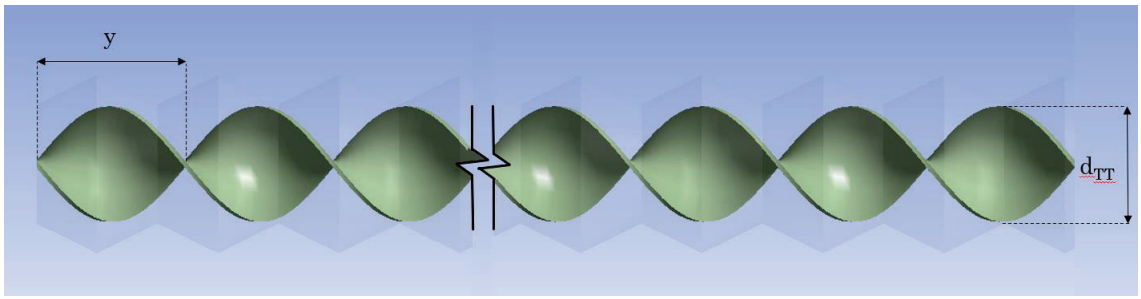

Figure 17: Corrugated tube with twisted tape inserts geometry scheme.

As the goal is to optimize the geometry, by dimensional analysis 3 geometrical parameters are obtained, Eqs. 58:

$$N_1 = \frac{D}{d}; \quad N_2 = \frac{y}{d}; \quad N_3 = \frac{w}{d} \tag{58}$$

Where N_1, N_2 and N_3 are the geometrical dimensionless parameters d and D are the inner and outer the outer diameters of the corrugated tube, y is the twisted tape pitch length (length that it takes to turn 180º and w is the distance between the different valleys of the corrugated tube and w is the distance between crests. Therefore, N1 relates to the width of the corrugated tube, N2 is also interpreted as TR (Twist Ratio from literature) and N3 relates to the spacing between the corrugated crests. These three parameters are optimized in the ranges described in Table 11. The inner diameter is fixed for all the simulations to be 35cm, while the outer varies depending on N1.

Table 11: *Geometrical parameters range in the optimization*

Name	***Lower Bound***	***Upper Bound***
N_1	1.01	2.5
N_2	0.5	5
N_3	0.2	2

The meshing is performed to ensure an y+~1 even in the highest velocity case. For doing so, 25 layers of inflation are positioned in the corrugated and the twisted tape wall, Figure 18 a. The mesh is optimized and an element size of 1mm, Figures 18 b and c, is selected for the domain, resulting in cases that range from 15M to 24M cells depending on the geometry of each case.

Because the interest is on the stabilized profile and thermal properties of the pipe, the length is not a variable, instead a long enough pipe is selected of 1.5m to ensure that both temperature and velocity profiles are stabilized when sampling. To avoid entrance and outlet effects, samples are taken from the last third of the corrugated pipe and an

additional 10 cm pipe with an adiabatic wall is positioned at the end of the domain to avoid reverse backflow and other undesirable outlet effects. The value of the inner diameter d is set constant to 35 mm and the twisted tape width and thickness are both 34 mm and 2 mm.

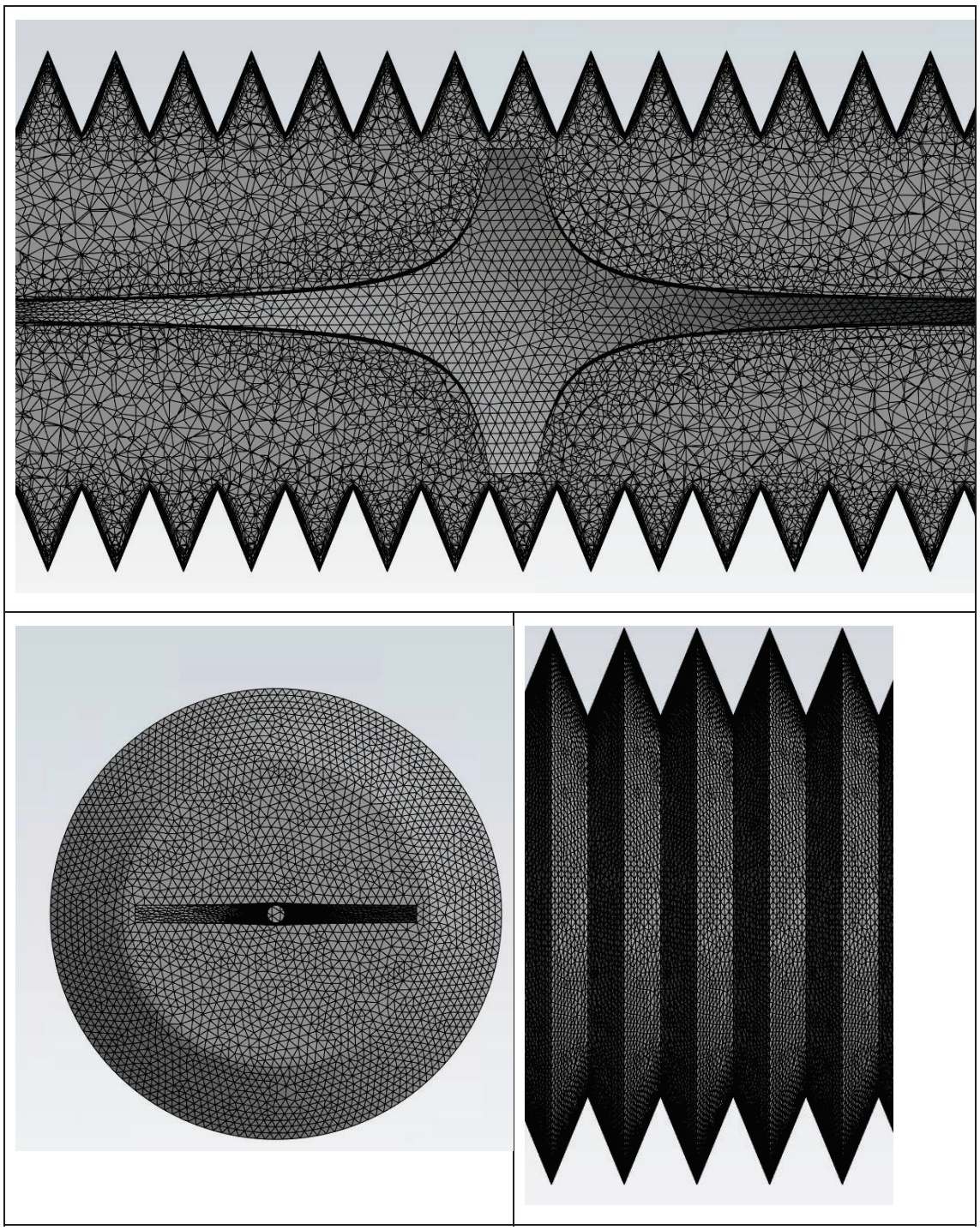

Figure 18: *Meshing of the corrugated tube with twisted tape insert. a) Side section cut of the mesh b) Meshing at the inlet c) Meshing at the corrugated exterior wall*

The meshing selection is similar to the one described in the previous section. For the setup, the fluid is air, whose properties are temperature dependent and are adjusted to a 3rd order polynomial. The corrugated wall is set to be at constant temperature, emulating a phase-changing vapour. The inlet is set as velocity inlet and the outlet is a pressure outlet. The wall temperature is set to 373.15 K and the inlet temperature to 300 K. The domain is optimized for different operational velocities: 10 m/s, 15 m/s and 25 m/s.

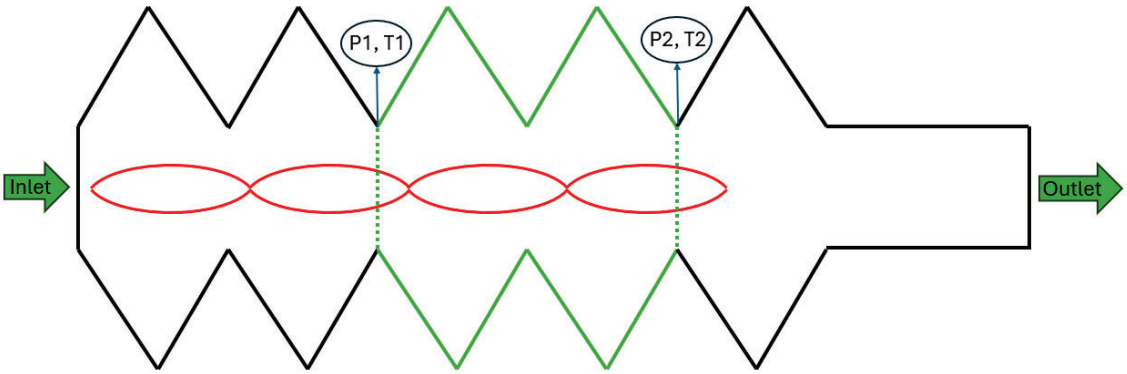

Figure 19: *Schematic of the sampling process, always centred at the lowest point of the tube crests. The sampling is away from the outlet, and far enough from the inlet to have a stabilized profile.*

The pressure and temperature values sampled to later calculate the Nusselt and friction factors are computed always at the valleys of the corrugated points. Additionally, the samples are taken far enough of the outlet to ensure stabilization of temperature and velocity profiles. The last crests are also omitted to avoid the unrealistic effects that the outlet can induce in those values, Figure 19.

4.1.3.1. Thermal performance factor optimization

The TPF is optimized as a function of the geometrical parameters N_1, N_2 and N_3. The calculation of the Nusselt number of the modified pipe is as follows, Eq. 59:

$$\mathrm{Q} = \mathrm{w}\, c_p(T_2 - T_1) \rightarrow \mathrm{Q} = \mathrm{h}\, \mathrm{A}\, \Delta T_{ml} \rightarrow \mathrm{Nu} = \frac{\mathrm{h}\, \mathrm{D}_h}{\mathrm{k}} \tag{59}$$

Where Q is the transferred heat inside the sampled area, A is the external wall area of the corrugated tube, T_2 and T_1 are the temperatures at the two sample points in the simulation (taken as the mass weighted average of the temperature at the cross sectional area), h is the heat transfer coefficient, ΔT_{ml} is the logarithmic average of the temperature difference between the wall and the two sampled points, k and c_p are average thermal conductivity and heat capacity respectively inside the sampled volume. Finally, the hydraulic diameter D_h is calculated as $\mathrm{D}_h = \frac{4V}{S}$ with V being the volume of fluid inside the tube and S the wetted surface, including the twisted tape.

The Darcy friction factor is found by the Darcy-Weisbach equation applied to our system, Eq. 60:

$$\frac{P_1 - P_2}{L} = f\,\frac{\rho\, v^2}{2\,\mathrm{D}_h} \tag{60}$$

With L being the distance between the sample points, f the Darcy friction factor, P_1 and P_2 the sampled pressures, and ρ and v the volume average density and velocity inside the sampled volume.

For estimating the Nusselt and friction factors of the smooth pipe, the Gnielinski correlation is used for the Nu and Petrukov's correlation for the friction factor, Eqs. 61 and 62:

$$Nu = \frac{\left(f/8\right)\,(Re - 1000)Pr}{1 + 12.7\,\left(f/8\right)^{1/2}\left(Pr^{2/3} - 1\right)} \tag{61}$$

$$f = (0.79\,\ln(Re) - 1.64)^{-2} \tag{62}$$

Here the Prandt number (Pr) is estimated to be the average Prandt number inside the sampled volume and the Reynolds number is supposed to be the Reynolds number of a pipe with similar mass flow as the one in the modified pipe and the same external diameter, that occupies the same space as the modified pipe, Eq. 63:

$$Re = \frac{4\,w}{\mu\,\mathrm{D}_h} \tag{63}$$

4.2. Continuous source dispersion simulations methodology

The material and methods described here are used to check the reliability of CFD as a tool for predicting an atmospheric dispersion of a gas. Several experiments are simulated and then compared to empirical data to check its accuracy. Concentration is also predicted with the widely used and accepted Gaussian Plume Model (GPM) and ALOHA and critically compared with CFD results.

4.2.1. Material

The material used in this investigation is a computer with an Intel(R) Core (TM) i9-10940X processor and a NVIDIA Quadro RTX 5000 graphics card. On this computer, the simulation requires around six computing hours per studied case.

4.2.2. Simulation set up

The simulation domain is a rectangular base prism with a release column at 50 m away from the prism base (Figure 20). It is made up of two inlets (air and emission), an outlet, and 4 walls (top, bottom, right and left side). The bottom wall is defined as a no-slip boundary condition. The other walls are set to have zero shear stress, as if the air flowing outside the domain had the same velocity as the air flowing by the wall, or in other words, zero velocity gradient towards the wall.

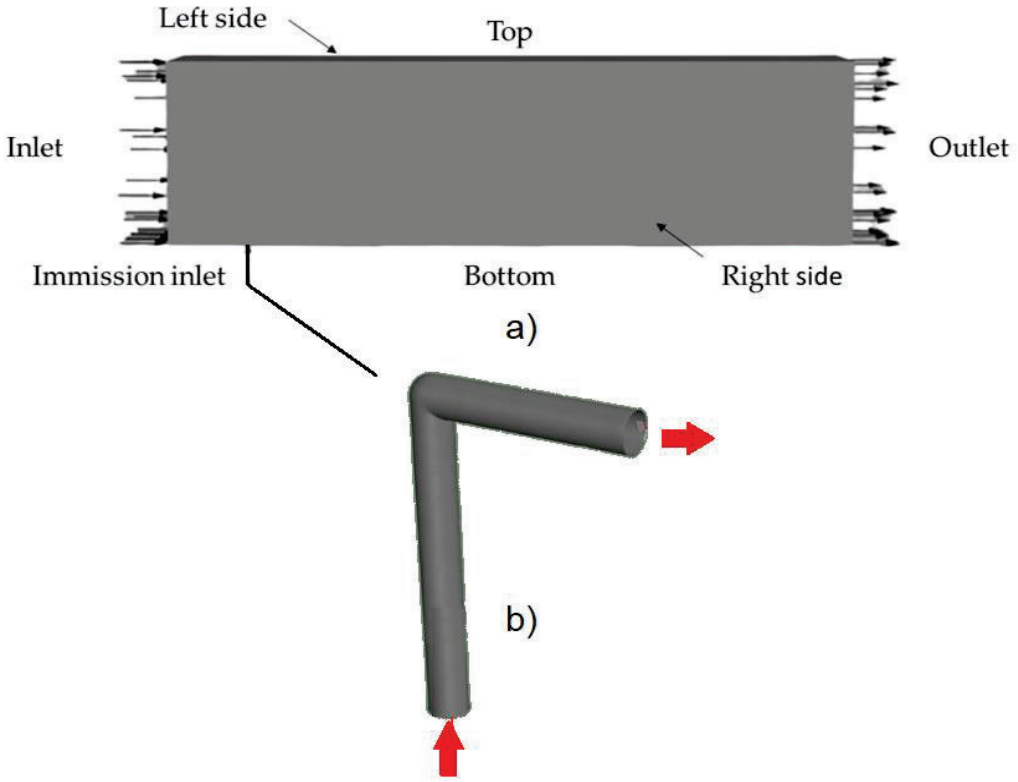

Figure 20: *a) Boundaries in the simulation domain. b) Elbow emission flue geometry.*

The domain dimensions to simulate the atmospheric gas dispersion, which are shown in Table 12, are chosen based on:

Validation based on the experimental data collected from Prairie Grass Project (Morton L. Barad, 1958):

The computational time and cost.

The first criterion is met by mimicking the experiment. That means using the same emission structure and fixing the dimensions down to at least the measurement points. The empirical experiment takes place near O'Neill, Nebraska, during the summer of 1956. The sampling array is made up of five arcs located from 50 to 800 meters from the release. But due to the computational cost, the 800 m measurements are not analysed. Furthermore, crosswind dispersion is not compared, so the domain width should only

ensure that pollutant accumulation does not occur (top, bottom, right and left sides are set as walls). The pollutant accumulation will start by the time a significant pollutant concentration reaches the side and top walls. Due to the computational cost and time, a maximum concentration of 0.5 mg/m^3 is settled to be a threshold of accumulation at the walls. Series of simulations are performed to ensure that with the given dimensions this threshold is not surpassed.

To ensure that the air velocity profile is stabilized, and that the outlet boundary has no effect on the 400-m measurement, the domain is lengthened by 50 m. Considering the aforementioned, the final dimensions of the domain are summarized in Table 1. The selected dimensions are similar to those found in B. Zhang & Chen (2010), where a risk analysis of toxic gas leakage is performed with CFD for a real gas gathering station of H_2S.

Table 12: *Domain's dimensions*

	Parameter	***Value***	***Unit***
Domain	Length	500	m
	Width	250	m
	Height	50	m
Prairie Grass Project emitter column (Barad M. L., 1958)	Height	0.46	m
	Diameter	0.0508	m

All geometries and simulations are created and performed in ANSYS 2022 R1. The turbulence model, the energy equation and the species transport equation used are implemented in this software. In particular, the selected model has been the SST k-ω, as it smoothly blends wall resolving k-ω equations for near-the-ground phenomena and k-ε model for bulk-free shear air flow in upper layers. Further details on this model can be found in ANSYS Fluent Theory Guide (2024). The specified gas mixture contains air and the studied species, which in case of Prairie Grass Project is sulphur dioxide (SO_2) (Barad M. L., 1958). Pure SO_2 (40.61 mol/m^3) is fed in the emission inlet at the same ratio as done in experimental. Different meshes are created to determine the configuration that allows the minimum cell number and do not affect the results (mesh independence test). The influence of a mesh correction function, Eq. 64, is also evaluated.

$$f_{MeshCorrection} = \left|\nabla X_p\right| \cdot 2^{-3 \cdot CRL} \tag{64}$$

where X_p is the molar fraction of the pollutant and CRL (Cell Refine Level) is the number of times a cell has been refined.

As the magnitude of the SO_2 molar fraction gradient increases in a cell, such cell is refined further to properly represent the concentration curve. The right term ensures no excessive

refinement, avoiding extra computational costs. Only the high gradient cells are refined further. This function is evaluated in all cells, and those whose value is over the refinement criteria are further refined. The refinement is performed 6 times every 50 iterations. The selected solution algorithm to resolve the simulations is Coupled.

Ideal gas model is used for estimating the density of the gases involved. The other air properties are kept constant. For sulphur dioxide, the specific heat is set as piecewise polynomial, and the thermal conductivity and viscosity are calculated with the kinetic theory. Mixture properties are evaluated using the mixing law approximation, except for the mass diffusivity, where kinetic theory is applied. The solar radiation intensity generates a temperature gradient between heights. A heat flux at the ground surface is used to simulate this phenomenon, assuming the radiation bounces off the ground in the form of heat and is not absorbed by chemical compounds of the domain. The side walls are adiabatic. The accumulation of thermal energy is prevented by restricting the top side to the same heat flow as the bottom.

The air inlet is defined with three formulas: the velocity profile regarding the height, the turbulent kinetic energy (k), and the dissipation rate (ω) (*OpenFOAM: User Guide: AtmBoundaryLayer*, n.d.). The temperature and the mass fraction are also indicated. For describing the emission inlet, the mass flow is required, which is selected according to the experimental data used.

4.2.3. Aloha

ALOHA is the hazard modelling tool for the Computer-Aided Management of Emergency Operations (CAMEO) software package, which is used to prepare for and respond to chemical crises (*ALOHA Software | US EPA*, n.d.-b). ALOHA simulates hazardous gas clouds, flammable gas clouds, Boiling Liquid Expanding Vapor Explosions (BLEVE), jet fires, pool fires, and vapour cloud explosions (VCE) This software inputs for studying gas dispersion are similar to those for the Gaussian Plume Model, but there is no need to perform any calculations or search for a number in any table; everything is ready implemented in the software and done automatically. The building parameters are “single storied building” with “unsheltered surroundings”. Then the data and time of the sulphur dioxide tracer emission is specified. In the atmospheric options, the weather conditions of each experiment are introduced one by one, e.g., wind speed, temperature, etc. The release emission must then be defined, including the amount of pollutant entering the atmosphere and indicating that for the studied case it is a continuous source that lasts for 10 minutes. The software has two models available: Heavy gas and Gaussian dispersion. When estimating concentrations, the program suggests using Heavy gas model for the selected compound.

4.2.4. Mesh independency

The mesh independence study is made with the following parameters: the element size, the ground surface sizing, the inflation layers, the use or not of a mesh adaptation function, and the refinement criteria. This analysis has accomplished obtaining a mesh that does not affect the results using a reasonable number of nodes. In other words, there is no appreciable results difference in further increasing the nodes. The tested meshes characteristics are summarized in Table 13.

Table 13: *Mesh characteristics*

Mesh name	***Max Sizing [m]***	***Ground Surface Sizing [m]***	***Inflation layers***	***Refinement criteria***	***Nodes (10^6)***
Mesh 1	5	5	-	-	1.1
Mesh 2	3	3	-	-	4.3
Mesh 3	3	3	-	10^{-6}	4.6
Mesh 4	2.56	1	5	-	13.7
Mesh 5	2.56	1	10	-	16.5
Mesh 6	2.56	1	20	-	22.3
Mesh 7	2.56	1	10	10^{-7}	35.6
Mesh 8	2.56	0.5	10	-	51.7
Mesh 9	2.56	0.5	10	10^{-6}	66.0
Mesh 10	2.56	0.5	10	10^{-7}	128.7

Mesh 7 is the chosen option, as discussed in the following paragraphs that compare the different options and parameters and their significance. The comparison of each parameter is done by grouping similar meshes. For example, the only difference between Mesh 9 and 10 is the refinement criteria. Comparing both results allows us to interpret the significance of this parameter. Therefore, the concentration and node ratios are plotted (Figure 21). The concentration ratio (r_c) is the relation between the concentration results at 50m downwind of a mesh and the mesh with more nodes. Similarly, the node ratio (r_n) indicates the fraction of mesh nodes under maximum mesh nodes.

The mesh number 10 is used as a reference (it is assumed close to the true solution of the model) due to its large number of nodes. Mesh 7 is used to run the simulations as it proves to provide good balance between accuracy and computational time (Figure 22). Further tests are performed to prove whether y+ values in the bottom wall have significant impact on the results. From the later mesh optimization and the tests, it is proven that for this

case y+ values ranging from 30 to 1000 do not present significantly different results. This can be due to the scarce presence of obstacles and the plain geometry of the system added to the fact that the relevant transport phenomena occurs far from the walls.

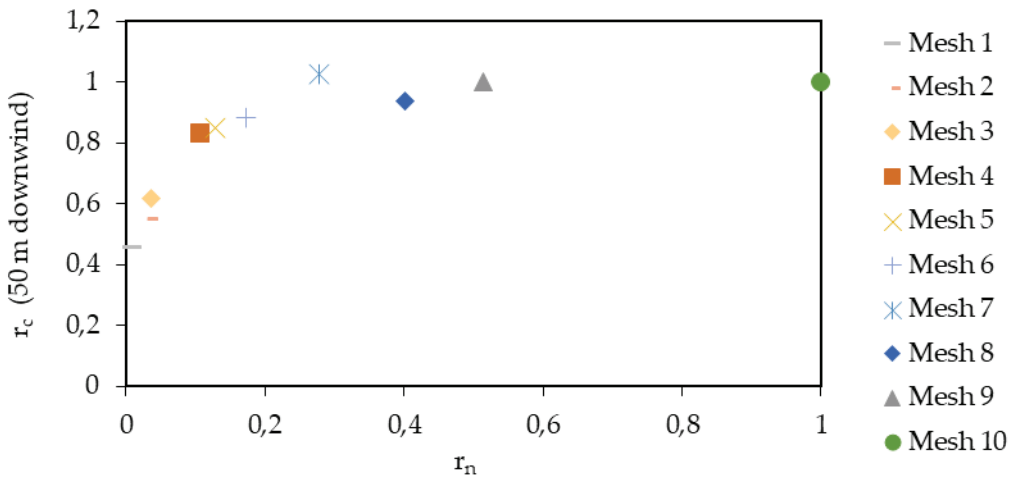

Figure 21: *Mesh independency study results for concentrations at 50 m downwind from the source*

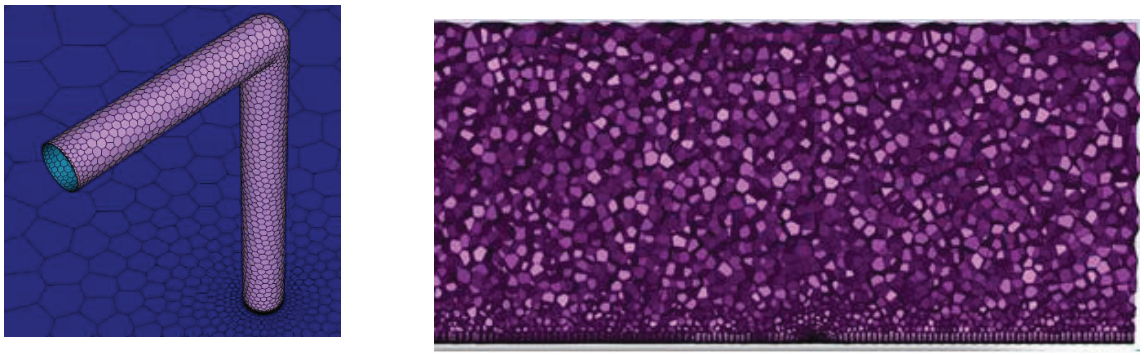

a) b)

Figure 22. *Resulting mesh. (a) Surface mesh around the emission nozzle, an exact reproduction of the one used in the experimental (Barad M. L., 1958); (b) Side view of a cut mesh in the downwind plane.*

4.2.5. Convergence analysis

The continuity equation criteria is set to 10^{-5}. All other residuals are set to converge to at least 10^{-6} to become acceptable. Figure 23a shows the evolution of those residuals in a simulation: The spikes in convergence correspond to the instances where the mesh is refined. Tracking is also performed in critical zones like the sampling points, where the SO_2 concentration is plotted in each iteration to make sure it does not oscillate

significantly at the end of the simulation (Figure 23b). From Figure 23, the mesh refinement has a significant effect on the results.

a)

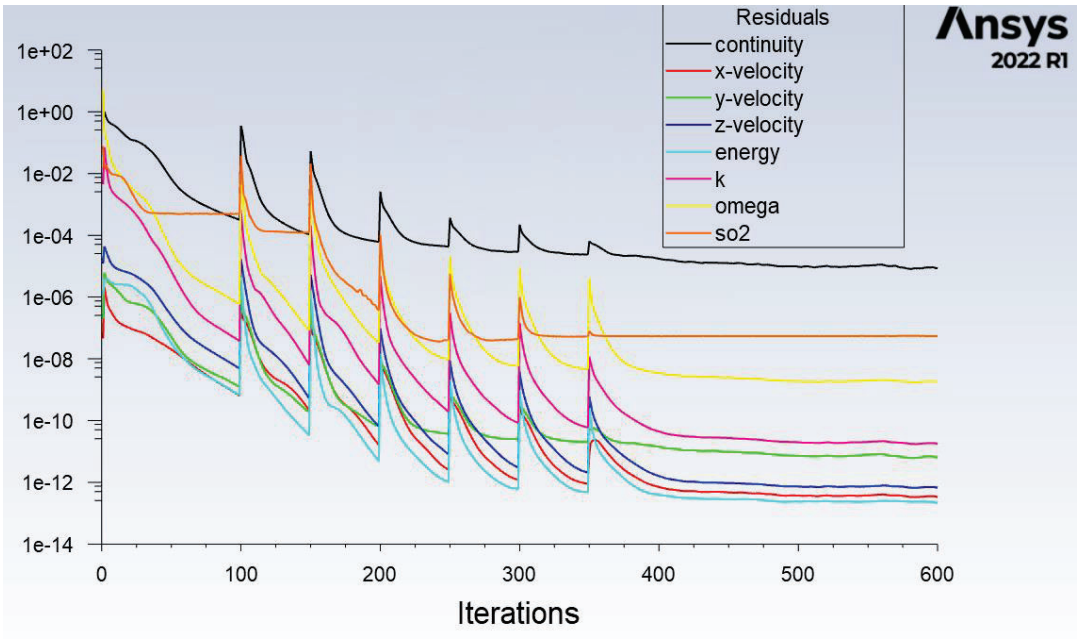

b)

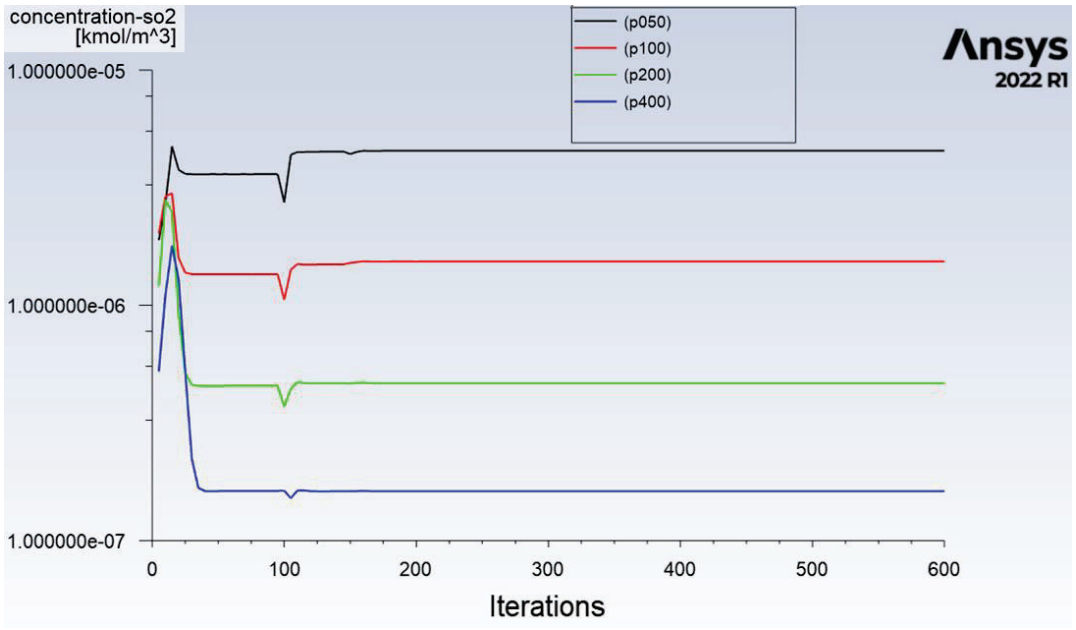

Figure 23: *Convergence analysis. (a) Residuals of a typical simulation with mesh refinement; (b) Tracking of SO_2 concentration at various distances from emission at each of the 600 iterations*

4.2.6. Obstacle dispersion comparison methodology

To test Aloha and CFD, a similar case is studied with the presence of obstacles. It is often assumed that Aloha and other GPM based methods do not estimate properly dispersion in the presence of irregular terrain, and that is one of the main advantages of CFD codes.

In Aloha the only way to input the presence of obstacle is by estimating the terrain roughness. A common way to do this is via the Center Line Average equation:

$$R_o = \frac{1}{L}\int_0^L |y|\, dx \tag{65}$$

Where R_o is the roughness value, L is the total distance along the longitudinal axis parallel to fluid motion (the z axis with L = 500 m in Figure 24) and y is the elevation from the terrain of the obstacles.

The geometry is like the previous cases with regards to general domain dimensions and the emission nozzle, but contains four rectangular-shaped bumps that are 10 m tall and 25 m wide with a separation between the of 36 m. The dimensions are chosen to be like a set of streets separated by rows of houses.

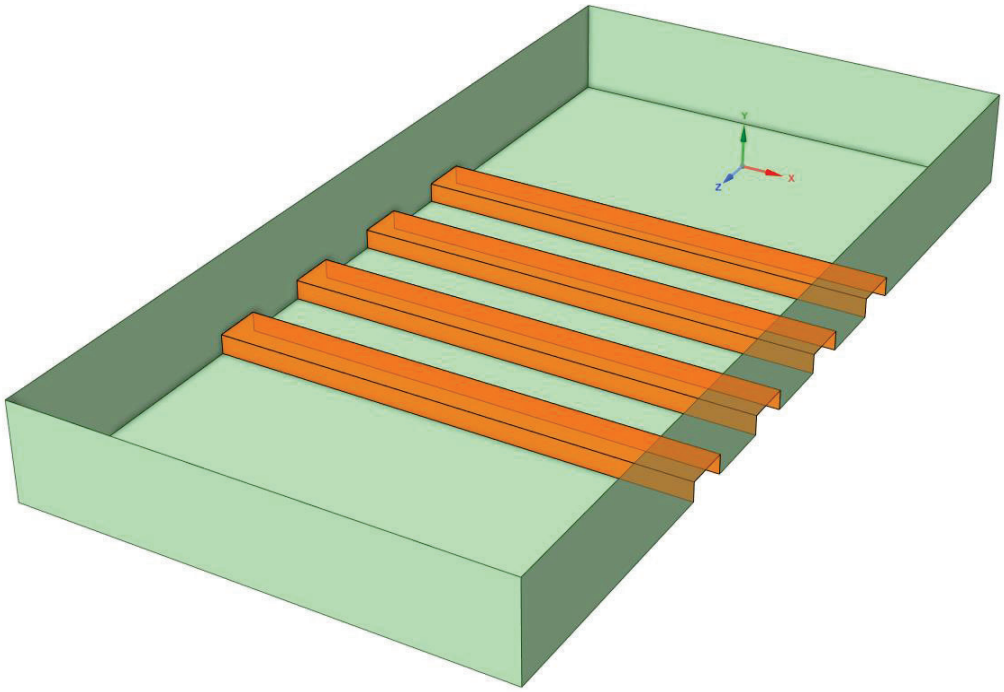

Figure 24. *Domain with obstacles (orange). The emission is produced in the location of the coordinate axis*

It is no coincidence that the roughness value calculated using equation 65 for this domain is R_o= 2 m, which is the maximum value admissible by the Aloha software. The value typically used by Aloha in urban environments is 1 m, which are also tested giving identical results. Aloha has two estimation methods available for this case: heavy gas and gaussian, both which are compared against the simulation. The meshing is performed using a similar sizing as the one described in section 3.2.4.

4.3. Methodology for the study of a stirred tank

4.3.1. Problem description and geometry

Simulations are conducted so that they emulate the conditions present in Stahl Iberica S.L production plant resource. The setup consists of a batch stirred baffled reactor equipped with a paddle agitator. The agitator has four levels of blades and a semi-anchor at the bottom. The reactor geometry was generated using AutoCAD 3D 2024, which is a software application used for creating three dimensional models and designs. The 3D geometry of both the baffled tank and the blades agitator were created from the 2D blueprints of the equipment provided by Stahl Iberica S.L. First the solid parts of the geometry were generated, then the fluid zones were created, and finally, the solid parts were subtracted to remain only with the fluid domain. The reactor specifications used for the model simulations are tabulated in Table 14.

Table 14: *Reactor specifications*

Parameter	*Value*
Tank external diameter	2.40 m
Liquid level	3.03 m
No. of impeller levels	4
No. of blades /level	2
No. of baffles	4
Impeller diameter	1.68 m
Impeller elevation	0.14 m
Impeller type	Pitched blades (30 º)

The original impeller geometry is modified to study the effect of blade angle on the required power consumption and heat transfer efficiency. For each geometry, different Reynolds numbers are tested from 1 to 10^7 to cover all flow regimes. Different blade angles from 0º to 90º shown in Figure 25 are tested (0º,15º, 30º, 45º, 60º, 75 º, 90º).

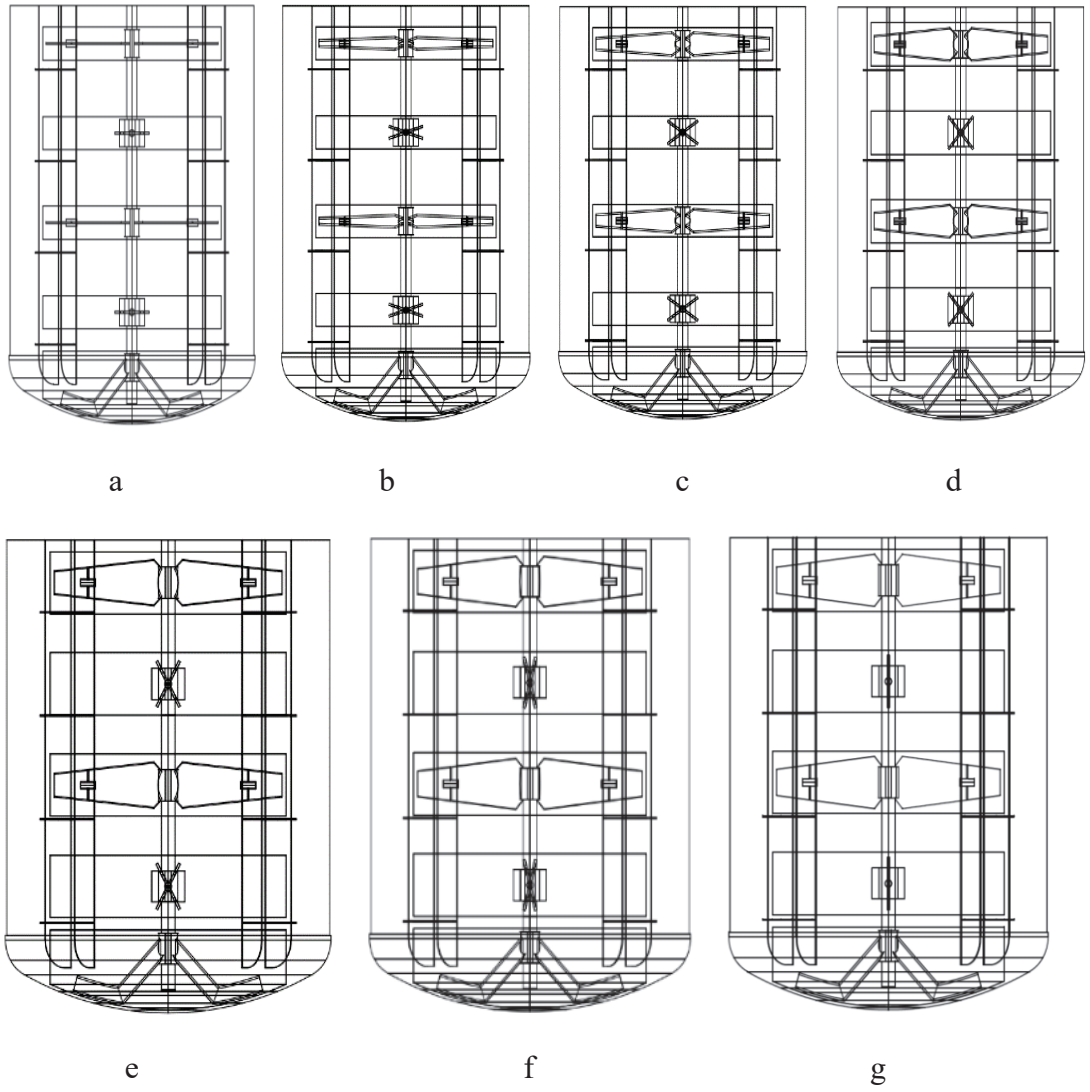

Figure 25: *Blade angles tested: 0º (a) 15º (b), 30º (c), 45º (d), 60º (e), 75º (f) and 90º (g)*

The impeller rotational speed is kept constant at 50 rpm in all simulations. The fluid dynamic viscosity (μ) is the input parameter varied from 1.47 cP to $1.47 \cdot 10^7$ cP to simulate different turbulence intensities. The torque (T) at the agitator and the area weighted-average wall shear stress (τ_w) at the tank wall are the output parameters of interest. The rest of the working fluid properties such as density (ρ) are equal as those of liquid water.

4.3.2. Reynolds number and power number

To work properly, the agitator of a tank needs to circulate enough fluid volume to carry currents to the farthest reaches of the tank. Circulatory movement of the fluid is not the only, nor even the most important, aspect in mixing operations; turbulence in the flow frequently determines how effective the procedure is. When currents flow through a liquid in the right direction and create noticeable velocity gradients, turbulence results. Certain agitation tasks require high average velocities or high flow rates, while other challenges

require strong turbulence or concentrated power dissipation. The choice of agitator geometry affects the relative values of flow velocity and power dissipation, even though both variables rise with agitator speed.

Both circulation and turbulence generation consume energy. Consequently, a crucial aspect in the design of stirred tanks is the power required to drive the impeller. The power consumption can be approximated by the product of the flow rate (q) generated by the impeller and the kinetic energy (E_k) per unit volume of fluid, Eqs. 66 and 67:

$$q = n\, D^3 N_Q \tag{66}$$

$$E_k = \frac{\rho\,(V\prime_2)^2}{2} \tag{67}$$

Where V'_2 is the fluid velocity at the blade tip, n is the revolution speed, D is the blade diameter and N_Q is the flow number. If the velocity of the blade at its tip is proportional to the fluid velocity with a proportionality constant α, then $V'_2 = \alpha\, \pi n\, D$ and the required power, Eq. 68:

$$P = n\, D^3 N_Q\, \frac{\rho}{2}\, (\alpha\, \pi n\, D)^2 = \rho\, n^3\, D^5 \left(\frac{\alpha^2\, \pi^2}{2} N_Q\right) = T\, 2\, \pi\, n \tag{68}$$

In a dimensionless form, Eq. 69:

$$\frac{P}{\rho\, n^3\, D^5} = \frac{\alpha^2\, \pi^2}{2} N_Q \tag{69}$$

The first term of Equation (3) is the power number, N_P. It is proportional to the ratio between the frictional force acting on a unit area of the impeller and the inertial force. The inertial force, in turn, is related to the momentum flux corresponding to the global motion of the fluid. The power number is defined by:

$$N_P = \frac{P}{\rho\, n^3\, D^5} \tag{70}$$

Accurately estimating the power required to rotate an impeller at a specified speed is crucial for operating stirred tanks efficiently. This estimation relies on empirical correlations that relate power (or power number) to other system variables. Dimensional analysis provides a systematic method to derive such correlations. It involves identifying the relevant physical quantities and their dimensions and then expressing the relationships between them in dimensionless terms. The key variables involved in the dimensional analysis for power estimation in stirred tanks include geometric parameters (tank dimensions and impeller characteristics), fluid properties (fluid viscosity and density) and operating conditions (impeller rotational speed and gravitational acceleration). Vortex formation at the liquid surface cause the elevation of liquid above the tank surface level and requires overcoming the gravitational force. Hence, the acceleration due to gravity (g) is introduced as a factor in the analysis. In this specific case, the baffles prevent the

formation of the vortex, therefore g can be excluded from the relevant list to simplify the analysis.

Geometric dimensions can be converted into dimensionless ratios, or shape factors. When shape factors are ignored the power (P) becomes a function of the remaining variables, which can be expressed as

$$P = f(n, D, \mu, \rho) \tag{71}$$

Once the relevant variables involved in the problem are identified the fundamental dimensions are determined

- Impeller rotational speed, n: [T^{-1}]
- Impeller diameter, D: [L]
- Fluid dynamic viscosity, μ: [M L^{-1} T^{-1}]
- Fluid density, ρ: [M L^{-3}]
- Power, P: [M L^2 T^{-3}]

According to Buckingham Pi theorem, a physical problem with n dimensional variables and k fundamental dimensions can be reduced to n-k dimensionless parameters.

Table 15: *Dimensional analysis of the power of a stirred tank*

	D	n	ρ	P	μ
L	1	0	-3	2	-1
T	0	-1	0	-3	-1
M	0	0	1	1	1

	D	n	ρ	P	μ
L+3M	1	0	0	5	2
-T	0	1	0	3	1
M	0	0	1	1	1

The obtained dimensionless parameters are then: $\pi_1 = \mu / (n\, D^2 \rho) = Re^{-1}$ and $\pi_2 = P/(\rho\, n^3\, D^5) = N_P$, therefore, it is obtained, Eq. 72:

$$\frac{P}{\rho\, n^3\, D^5} = f\left(\frac{n\, D^2 \rho}{\mu}\right) \tag{72}$$

The first nondimensional group of the Equation (7) is the power number (N_P). The second nondimensional group is the Reynolds number (Re).

4.3.3. Wall shear stress and viscous sublayer thickness

Film theory is a simplified model that is used to describe heat transfer processes at the interfaces (in this case liquid-solid) where various phases meet. It assumes the existence

of a thermal film or boundary layer close the interface where temperature gradient is noticeable. This film is where the resistance to heat transfer is mostly found, since the bulk phase is considered to generate negligible resistance.

On the other hand, the viscous sublayer is the area close to a solid boundary such as a tank wall, where fluid velocity gradient is significant. Because of the no-slip condition of the wall, the fluid velocity goes from zero to the free stream fluid velocity. Viscous forces dominate in this layer and the fluid's velocity profile is laminar.

The thickness of the viscous sublayer has an influence on the heat transfer coefficient (h) at the tank wall. A thinner viscous boundary layer usually results in a thinner thermal boundary layer, which increases the heat transfer rate. On the other hand, a thicker boundary layer lowers the temperature gradient at the wall, which lowers the rate of convective heat transfer. Viscous sublayer thickness can be estimated from the shear stress at the tank wall using the non-dimensional wall distance (y^+) definition. The y^+ is used to describe the behaviour of the fluid near the wall and is defined by, Eq. 73:

$$y^+ = \frac{\rho\, y\, u_\tau}{\mu} \tag{73}$$

where y is the distance from the wall and u_τ is the friction velocity. The latter is expressed by Eq.74:

$$u_\tau = \sqrt{\frac{\tau_w}{\rho}} \tag{74}$$

where τ_w is the shear stress at the wall, which is the tangential force produced by the fluid on the wall and can be determined with the product of the fluid dynamic viscosity (μ) and the velocity gradient perpendicular to the wall at the wall $(\partial u/\partial y)_{y=0}$, Eq. 75:

$$\tau_w = \mu \left(\frac{\partial u}{\partial y}\right)_{y=0} \tag{75}$$

Laminar sublayer is associated with the y+ range between 0-5, Figure 26 (Wilcox, 1993). If y+ = 5 is considered the upper limit of the viscous sublayer, its thickness can be estimated from the shear stress at the tank wall combining Eq. 73 and Eq. 74:

$$\delta = \frac{5\,\mu}{\sqrt{\rho \tau_w}} \tag{76}$$

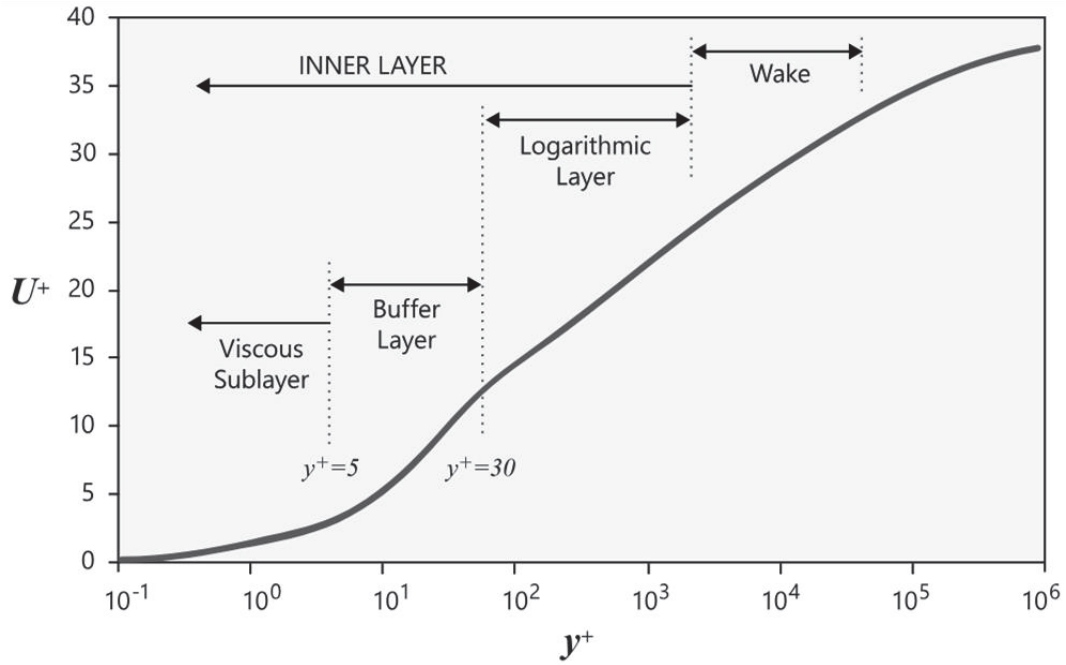

Figure 26: *Non-dimensional wall distance (y+) and non-dimensional velocity (U+) of the near-wall layers, (Wilcox, 1993)*

For polymerization operations, it can be useful to estimate the laminar sublayer at the tank wall at a certain speed in order to operate agitated tanks efficiently. This estimate could be found through empirical correlations between other relevant system variables and viscous sublayer thickness at the tank wall (δ).

The Buckingham Pi theorem can be used to determine a relationship between dimensionless groups in a similar manner to that which is done with the agitator's required power. The geometric factors (tank dimensions and impeller characteristics), fluid properties (fluid dynamic viscosity and density), and operating conditions (impeller rotational speed) are the main variables in the dimensional analysis for viscous sublayer estimation in agitated tanks. The viscous sublayer thickness (δ) at the tank wall is dependent on the remaining variables when shape considerations are not taken into account. These variables can be stated as:

$$\delta = f(n, D, \mu, \rho) \tag{77}$$

The fundamental dimensions of the problem are ascertained once the pertinent variables are identified.

- Impeller rotational speed, n: $[T^{-1}]$
- Impeller diameter, D: [L]
- Fluid dynamic viscosity, μ: $[M\ L^{-1}\ T^{-1}]$
- Fluid density, ρ: $[M\ L^{-3}]$
- Viscous sublayer thickness, δ: [L]

Table 16: *Dimensional analysis of the viscous sublayer in a stirred tank*

	D	n	ρ	δ	μ
L	1	0	-3	1	-1
T	0	-1	0	0	-1
M	0	0	1	0	1

	D	n	ρ	δ	μ
L+3M	1	0	0	1	2
-T	0	1	0	0	1
M	0	0	1	0	1

The obtained dimensionless parameters are then: $\pi_1 = \mu/\left(n\,D^2\rho\right) = Re^{-1}$ and $\pi_2 = \delta/D = N_P$, therefore, it is obtained, Eq. 78:

$$\frac{\delta}{D} = f\left(\frac{n\,D^2\rho}{\mu}\right) \tag{78}$$

where the second nondimensional group is the Reynolds number (Re). Another possible approach is to estimate the wall shear stress using an empirical correlation between dimensionless numbers. Once obtained, the thickness of the viscous sublayer can be calculated using Equation 11. If it is assumed that the wall shear stress depends on the same list of dimensional variables as the thickness of the viscous sublayer, Eq. 79:

$$\tau_w = f(n, D, \mu, \rho) \tag{79}$$

applying the Buckingham Pi theorem, the following relationship between dimensionless numbers is obtained, Eq. 80:

$$\frac{\tau_w}{n^2D^2\rho} = C_f = f\left(\frac{n\,D^2\rho}{\mu}\right) \tag{80}$$

where the first nondimensional group is a friction coefficient (C_f) at the stirred tank wall. This dimensionless measure relates the frictional force to the inertial force of the flow near the tank wall. The second nondimensional group is the Reynolds number (Re).

4.3.4. Mesh generation

Meshing involves dividing space into a grid composed of a finite number of elements to discretize the system and apply a mathematical model to each element. Each vertex of the resulting grid or mesh is called a node. At each node in this mesh, the system of equations is solved using either a finite difference or finite volume numerical method.

In some cases, mesh can be a source of numerical instability which can affect the convergence. Discretization errors occur when the mesh is not fine enough or has not enough quality, often misrepresenting the geometry or not allowing sufficient representation of the gradients present in the problem. Tetrahedrons meshes can cover extreme geometries, but they often come with errors such as numerical diffusion. On the other hand, more complex elements such as polyhedrons and prisms tend to avoid these errors.

4.3.4.1. Surface mesh

The mesh was performed using ANSYS Fluent. A polyhedral volume mesh was generated without inflation layers. Instead, a conformal mesh was created, which is a connected surface mesh on all the objects. The surface mesh is used to read the geometry and identify the regions to be filled with the volume mesh. This is the first of a two-step process for creating a tetrahedral, hexcore, polyhedral, or hybrid mesh in meshing objects.

Surface mesh was generated with a minimum cell length of 0.001 m, a maximum cell length of 0.07 m and 2 cells per gap, which ensures that there are at least 2 cells between two boundary walls. The rest of the parameters were kept by default. Join and intersect operation was performed to remesh the geometry and create a conformal, connected surface mesh.

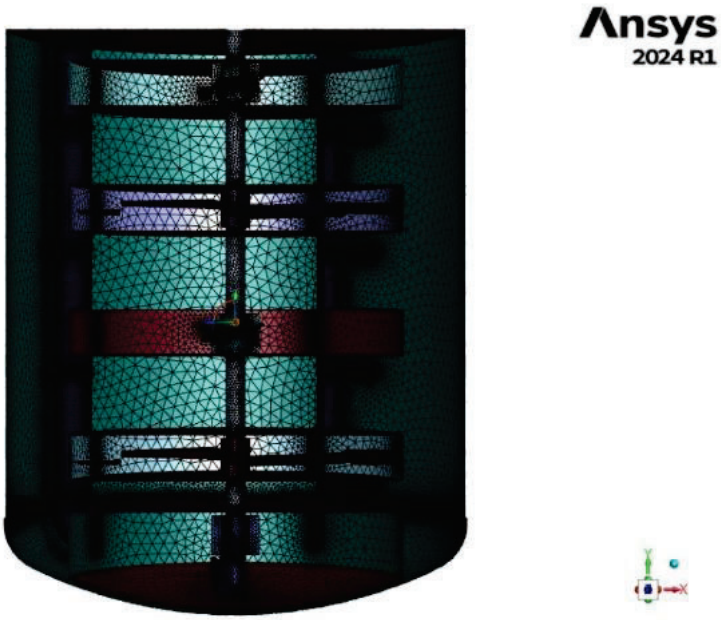

Figure 27: *Stirred tank reactor surface mesh*

4.3.4.2. Volume mesh

The volumetric regions were calculated from the conformal, connected surface mesh, and then filled with polyhedral mesh. This is the second of the two-step process for meshing objects. Maximum cell length was set at 0.07 m. The rest of the settings were kept by default. Figure 28 shows the internal hexacore meshing created for this unit, highlighting in different color the zones of impeller and fluid.

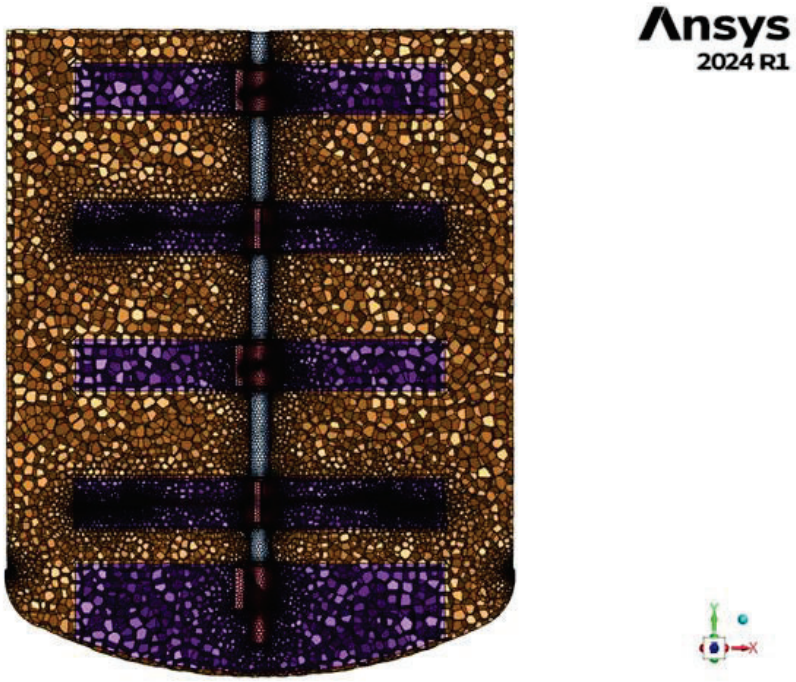

Figure 28: *Stirred tank reactor volume mesh*

4.3.4.3. Mesh statistics and quality

Several important parameters need to be considered to ensure that the mesh is of high quality and yields accurate and reliable results:

Skewness**:** determines the degree to which a cell deviates from a perfect shape, such as the degree to which it deviates from being equilateral. An equilateral cell (highest quality) has a value of 0, whereas a fully degenerate cell has a value of 1. Numerical diffusion and interpolation errors can result from high skewness. The range of skewness values and the accompanying cell quality are listed in Table 17.

Table 17 shows the statistics and quality of all the generated meshes including all the parameters mentioned above.

Table 17: *Quality of the generated meshes*

Geometry	***No. of cells***	***No. of nodes***	***Skewness (max/average)***	***Orthogonal quality (min/average)***
a	1 377 065	8 998 541	0.83/0.02	0.15/0.94
b	1 372 858	8 970 719	0.86/0.02	0.20/0.94
c	1 359 633	8 891 084	0.91/0.02	0.18/0.94
d	1 349 771	8 834 407	0.92/0.02	0.16/0.94
e	1 346 375	8 821 036	0.88/0.02	0.14/0.94
f	1 358 306	8 890 963	0.84/0.02	0.12/0.94

4.3.5. Model definition

The Navier-Stokes conservation equations can be approximated using Ansys Fluent, which discretizes them into algebraic equations for each node. The previously mentioned mass and momentum conservation equations are solved for all flows using Ansys Fluent. Apart from that, the viscous model is also defined. In this study, simulations with various degrees of turbulence are conducted to cover all flow regimes within the reactor. To obtain an accurate solution in all simulations, different viscous models are employed depending on the flow regime. For simulations where fluid flow inertial forces predominate over viscous forces, a model to capture the effect of turbulence is required. The turbulence intensity is evaluated using the agitation Reynolds number (Re):

$Re < 10^2$: to simulate low Reynolds numbers, laminar flow model is used.

$10^2 < Re < 10^4$: to capture transitional flow effects k-ω SST (Menter, 1994) model is used.

$Re > 10^4$: to simulate fully turbulent flows k-ε Realizable (Shih et al., 1995) M-L is used.

4.4. Methodology for partially full pipe simulations

4.4.1. Case selection

The research performed by Akgiray (2004) compared a newly proposed correction of the Manning equation with previous corrections and modifications of it, as well as the original equation. Several example cases were included in his research, and one of them has been chosen to be the basis upon which several first test simulations are carried out. Later, to optimize the simulation procedures and duration, some changes are made to that

example. The first set of verifications consists of varying the inlet velocity to test whether simulations can reproduce the results of the Manning equation. Table 18 describes the different conditions of this case. Note that all the parameters related to Manning's equation are constant, and therefore the theoretical mean velocity when stabilized should be the same regardless of the inlet velocity.

Table 18: *Manning equation related parameters and inlet conditions for first verification simulations*

Manning equation related parameters				**Inlet flow conditions**	
S [m/m]	*Kh [m]*	*D [m]*	*Q [m^3/s]*	*Inlet area [m^2]*	*Inlet velocity [m/s]*
0.0005	0.002247	0.5	0.0001	0.00050	0.2
0.0005	0.002247	0.5	0.0001	0.00033	0.3
0.0005	0.002247	0.5	0.0001	0.00100	0.1
0.0005	0.002247	0.5	0.0001	0.00001	10

Once this verification is performed, the diameter of the tube is varied to modify the hydraulic radius and check the resulting mean velocities inside the tube.

Table 19: *Manning equation related parameters and inlet conditions for second verification simulations*

Manning equation related parameters			
S [m/m]	*Kh [m]*	*D [m]*	*Q [m^3/s]*
0.0005	0.002247	0.5	0.0001
0.0005	0.002247	1	0.0001
0.0005	0.002247	0.75	0.0001
0.0005	0.002247	0.6	0.0001

Finally, the case of the 90° elbow partially full tube consists in a tube with a set of parameters (slope, roughness, diameter and volume flow) equal to the ones from the first simulation (first of Table 19). The difference is that instead of drawing a 10-meter tube, the tube to draw is composed of two identical tubes (in diameter, slope and roughness height *Kh*) of 2.5 and 3.5 meters connected by an elbow whose turn radius is equal to two times the radius of both tubes.

4.4.2. CFD setup

When designing each geometry, the diameter of each tube was according to the case (Table 19). For the length, as it is theoretically not involved in the problem, any value could initially seem appropriate. However, a tube with a length-diameter ratio too large will increase the number of nodes to the point that the simulation costs will make the calculations run too slow. The only way to control the number of nodes without compromising the element size of the mesh then is to make the tube as short as possible. But at the same time, a tube too short can lead to an erroneous result, as the flow may have not enough space to reach uniformity. Thus, enough length for a tube is the one that let the flow to reach uniformity while remaining as short as possible. Additionally, the inlet area, shape and position of each case is defined and drawn according to the volume flow and mean velocity desired in the inlet.

Figure 29: *Inlet zone of a pipe form this work in seen from SpaceClaim interface*

The slope value is considered with each gravity component in the input of the simulation.

As settings, VOF (Volume of Fluid) method is selected alongside open channel flow and implicit body force options. These options help improve convergence by accounting for the partial equilibrium of the pressure gradient and body forces in the momentum equations. The temperature is set to 293.15 K, and the surface tension at that temperature is 0.727 N/m [12], value which is introduced in the "Phase Interaction" options tab.

In the wall, the roughness height value in meters must be specified. This is very important as is the way the Manning number is introduced for the simulation. The conversion from Manning number to roughness height is defined by Eq. 81:

$$n = 0.042 * {k_h}^{1/6} \tag{81}$$

Where k_h is the roughness height in meters and n is the Manning number. As the Manning number used in the Manning equation iteration is 0.0152, the roughness height is 0.002247 m.

When initializing the solution, a sigmoid function is used to assign the volume fraction of water in each cell depending on its y position (or height). This function has to represent the evolution of the volume fraction throughout vertical axis of the tube (from the bottom to the top) in the steady state and must be continuous function. The approximate value of the steady state is taken from the depth of flow obtained via Manning's equations, and the continuous function chosen is as follows in Eq. 82:

$$v_f = 1 - e^{(-1*e^{(-6000*y+C_2)})} \tag{82}$$

Where v_f is the volume fraction of water inside the tube, y is the y-axis position in the tube and C_2 is a parameter that is adjusted in each case to make the volume fraction to change from 1 (full water phase) to 0 (full air phase) at the desired y (the depth of flow obtained via Manning's equation iterative process).

The rest of the parameters, like the residuals or the solution algorithm are set to ensure convergence and accuracy with the minimal computational cost possible. The under-relaxation factors (URF's) are lowered by a 30% to increase simulation stability and ensure arriving at a solution at the expense of computational time.

4.5. Methodology for materials engineering simulations

The main focus of the research described in this chapter is to aid in the simulation part of the European project "Thermodust". Its objective is centred around the discovery and application of new nanomaterials for thermal applications. More precisely, the main focus is the production of metal powders like copper, steel, or titanium covered with 2D nanomaterials for example graphene or hexagonal boron nitride (h-BN). When performed correctly, this procedure would enhance some properties of the powder for thermal or electronic applications.

4.5.1. Discrete Element Method methodology

The planetary ball mill is used in crucial aspects of the nanomaterial production process, and the mechanical interactions that are produced inside may be key to understand and improve powder production. Furthermore, this knowledge can be then applied to a scale up to the industrial production of the aforementioned nanomaterials.

Rocky DEM was acquired as simulating program for doing the simulations required by the project. To perform the simulations, the movement and geometry of the mill must be perfectly known. Planetary mills have two moving frames, they rotate around a central axis (sun wheel) and around the axis of the grinding container (planetary wheel).

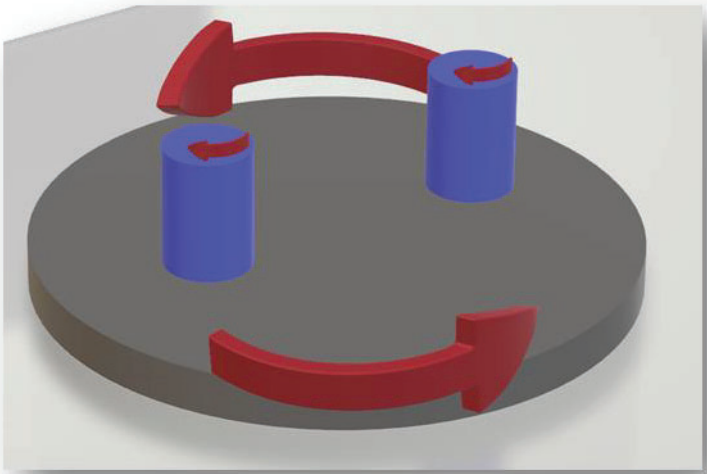

Figure 30: Planetary mil movement scheme.

The experimental apparatus to be simulated has the following operating conditions:

- The sun wheel rotating speed ranges from 0-290 rpm while the planetary wheel ranges from 0-580 rpm. The ratio at which the two wheels rotate is fixed and was measured via high-speed footage of the apparatus. It is found that the planetary mill is 2 times faster than the sun wheel, and they rotate opposite to each other.
- Grinding balls have a diameter of 0.5 cm, are made of steel and around 10-20 g of them are used in each grinding.

Two types of simulations are considered. Initially, only the milling balls and the cylindrical vessel are simulated and their interactions at different conditions, collecting information on the energy spectra (Chapter 1.7.1) of the ball-ball collisions and the ball-vessel collisions. Later simulations also include the grinded materials, to prove whether its presence is relevant to the energy spectra and therefore to the milling process.

The energy spectra is then related to the resulting PSD obtained from experimental results via modelling. The modelling parameters are tuned to match experimental. Different models are used to calculate the breakage present in the graphite milling or the adhesion present when in the Cu-Gr interactions.

Only one of the four vessels present in the experimental setup is simulated, as each vessel has the same dimensions and are symmetrical. The cylindrical vessel has 53 mm both in height and diameter. It is meshed so that the curvature is well depicted when estimating collisions.

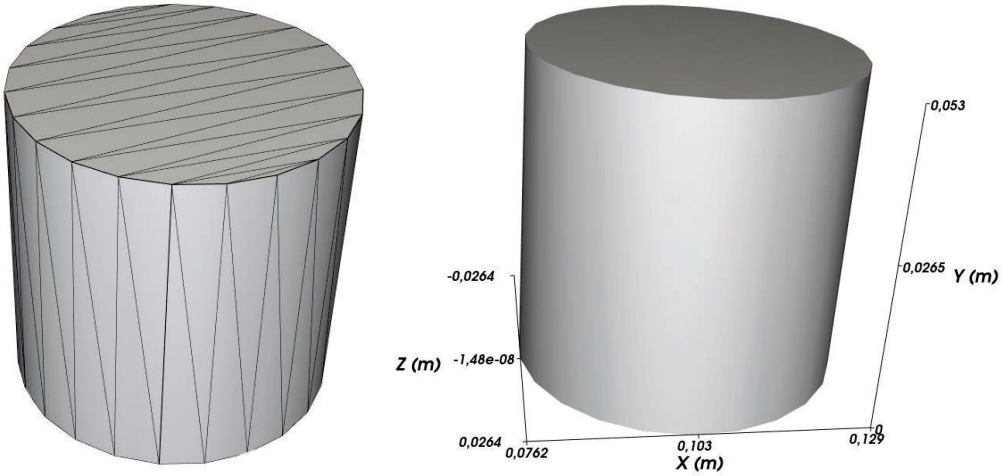

Figure 31: *a) Mesh of the cylindrical vessel. b) Vessel with measurements in 3D.*

Different simulations are run at all combinations of various ball diameters (3, 5, and 10 mm) and rotation speeds (100, 300, and 500 rpm), in order to match the model with experimentation. The simulations utilize a total mass of 10.2 g of steel balls, yielding a varying quantity of balls based on their dimensions. This translates to a 1% volume filling in each case. The tests are run for 10 seconds, which is enough to stabilize the motion of the balls inside the mill and obtain steady energy results.

Table 20: *Steel ball size and numbering for different diameters*

Diameter (mm)	3	5	10
Total number of particles	93	20	3
Mass per particle (g)	0,11	0,511	4,08
Total mass (g)	10,23	10,22	12,24

While there are various models that can relate energy spectra with particle breakage, no model describes accurately the differences between impact and shear energy, taking only impacts into account. The selection and design of the model can be even more challenging than the simulations.

To better understand the behaviour of materials inside the mill, a simulation has been performed with 10.2 g of 0.5 cm steel balls at 150, 300 400 and 500 rpm with 0.5 g of graphite material of 150 µm. The total number of graphite particles is 125196 and remains constant. This allows to compute statistics on the truly important collisions which happen against the graphite material particles. Simulations are run for 0.5 seconds and took over a week to complete with the current hardware. Simulations have been performed at 150,

300, 400 and 500 rpm to match experimental conditions. The goal is to predict the centripetal forces and particle collisions inside the mill to correlate them to the time that it takes to produce the graphene flakes. These simulations are referred in the results section 12.1.2. as the ones involving grinded particles.

4.5.2. Finite Element Analysis methodology

To understand the graphite breakage phenomena, single particle collisions are studied. With these simulations we will be able to discern which collisions and under what conditions cause breakage, delamination or other type of damage. Collisions are simulated at various speeds and impact angles and the stresses inside the particle are obtained. With this data the damage inflicted upon the particle can be derived. Finite Element simulations are performed with Ansys LS-DYNA software. The simulations involve steel and graphite to see the breakage of graphite. The graphite particle is of an hexagonal shape and the steel ball is spherical. With this methodology the energy that each particle is able to absorb can be correlated to the breakage or exfoliation of each particle. The tested cases ranged along various collision speeds that were seen from DEM simulations (from 0.1 to 5 m/s) and various angles of collision.

4.5.3. Molecular dynamics and Density Functional Theory methodology

Few studies have been found to simulate graphene with copper, and therefore the force field that describes their interaction is not easy to find or implement. Success was found when simple force field of Copper-Carbon interaction was found in literature allowing to produce the first set of simulations. LAMMPS software package is chosen for this task. In these simulations, temperature is increased from 5 K to 1200 K and then cooled down to 300 K in NVT ensemble. The simulations are initialized with gaussian distributed velocities with a mean temperature of 5 K. The simulation box is periodic in all coordinates which makes an infinite copper-graphene plane interaction. These simulations consider the carbon bonding of the graphene structure.

While the first set of MD simulations were performed in LAMMPS, CP2K is the software of choice for training a neural network with DFT data. Further MD simulations are also performed with CP2K for compatibility and simplicity. The High Dimensional Neural Network Potential (HDNNP) takes the atom position, type and bonding information as input and outputs the force field those atomic interaction would produce thanks to the DFT data that it has been trained with.

DFT calculations for the High Dimensional Neural Network Potential (HDNNP) training were performed with the CP2K software (VandeVondele et al., 2005), using Gaussian and plane waves (GPW) formalism (Lippert et al., 1997). The Perdew-Burke-Ernzerhof (PBE) of the generalized gradient approximation (GGA) was used for evaluating exchange correlation functional (Perdew et al., 1996), combining with the

Double Zeta Valence Plus polarization- Molecular Optimized (DZVP-Molopt) local basis sets and Geodecker-Teter-Hutter (GTH) pseudopotentials (VandeVondele & Hutter, 2007). Moreover, the DFT-D3 (Becke-Johnson, BJ) dispersion correction was included to account for long-range van der Waals interactions. The plane wave density cutoff and energy convergence criterion were set at 400 Ry and 1×10^{-6} Ha, respectively.

The High-Dimensional Neural Network Potential (HDNNP) consists of 2 hidden layers. Each hidden layer contains 10 nodes, allowing the model to capture complex, non-linear relationships in the input data. The architecture is designed to efficiently approximate the potential energy surface by learning the intricate interactions between atoms in the system. A cutoff radius of 14 Bohr was applied to limit the range of atomic interactions considered by the symmetry functions, ensuring computational efficiency while retaining accuracy. A total of 280 symmetry functions were employed to encode the local atomic environments. The DFT training data was generated using the minimum hopping method, considering various graphene/Cu(111) models. The dataset comprised a total of 12415 structures, including infinite graphene, as well as graphene nanosheets with and without defects. During the HDNNP fitting process, 90% of the data was allocated for training, while the remaining 10% was reserved for testing.

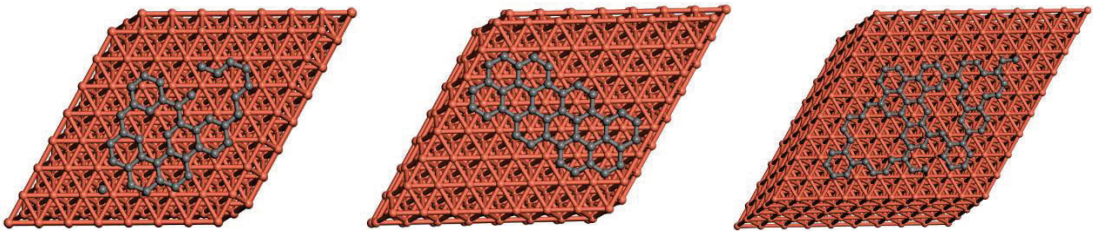

Figure 32: *Structure models of graphene/copper with defects*

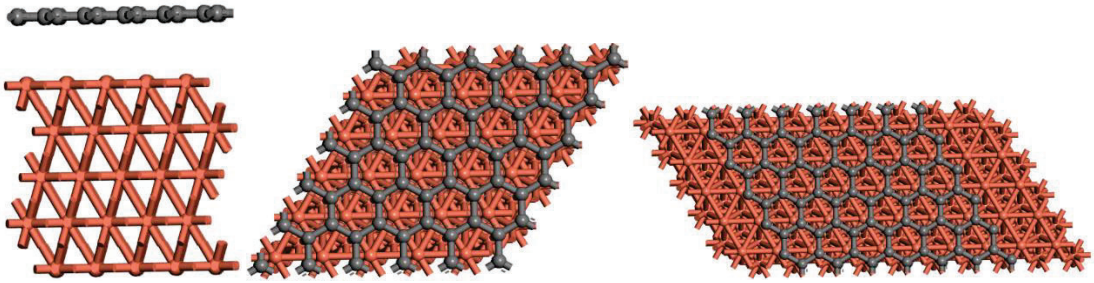

Figure 33: *Structure models of graphene/copper without defects*

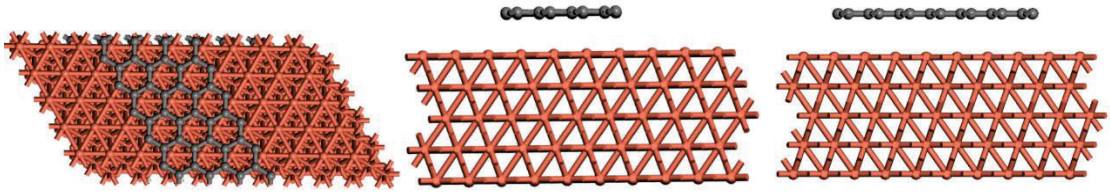

Figure 34: *Structure models of graphene/copper of graphene nanosheet*

Different graphene models are considered in the HDNNP. There are structure model of graphene/copper with and without defects, and structure model of graphene/copper of graphene nanosheet (Figures 32-34).

5. CFD applied to heat transfer units

The results obtained from the study of heat exchangers are presented in this section. First, the different models are evaluated and validated for two different geometric cases: a double pipe and a pipe with a twisted tape insert. For both these cases, empirical data are available from literature, and the different models are evaluated comparing against those empirical correlations.

The next part consists on the optimization of different geometrical parameters of a twisted tape inserted on a corrugated tube.

5.1. CFD validation for simple heat exchangers

When conducting the simulations, the temperature profile is assumed to develop rapidly along the tube, and that a constant temperature profile at the inlet should not have a great effect on the overall heat transfer coefficient (U). To prove this hypothesis, a series of simulations are performed, where fully developed temperature profiles extracted as a result from previous iterations are used as input values in the inlets of the simulations. Figure 2 shows the results comparing, three cases for the k-ε RNG with scalable wall functions: first simulation (1st) with constant profiles on inlets and outlet, second one (2nd) with fully developed profiles of velocity and pressure at the inlet and outlet, and the third (3rd) with fully developed temperature and velocity profiles at the inlet and pressure profile at the outlet. This analysis is performed to be able to reliably compare these results against the semiempirical correlations, which are obtained for fully developed profiles.

Results from the simulations show no improvement in the solutions when fully developed temperature profiles are used, rather the opposite. All simulations tend to overestimate the overall heat transfer coefficient (U) with respect to the empirical values with a relative error of up to 11.34 % with respect to the mean empirical value in 3rd case. As for pressure drops, this model seems to fall between the empirical correlations of Sinnot et al. (2012) and the estimation of the Fanning Factor by using Colebrook's equation. All in all, simulations provide good approximation if considering that empirical correlations differ from one to another with around 5 % of error for U values and 8~24 % for ΔP. With those results, the rest of the simulations are performed by using only fully developed velocity and pressure profiles. The comparison between the studied turbulence models and the semi- empirical results for pressure drop and overall heat transfer coefficient (U) are depicted in Figures 35 and 36.

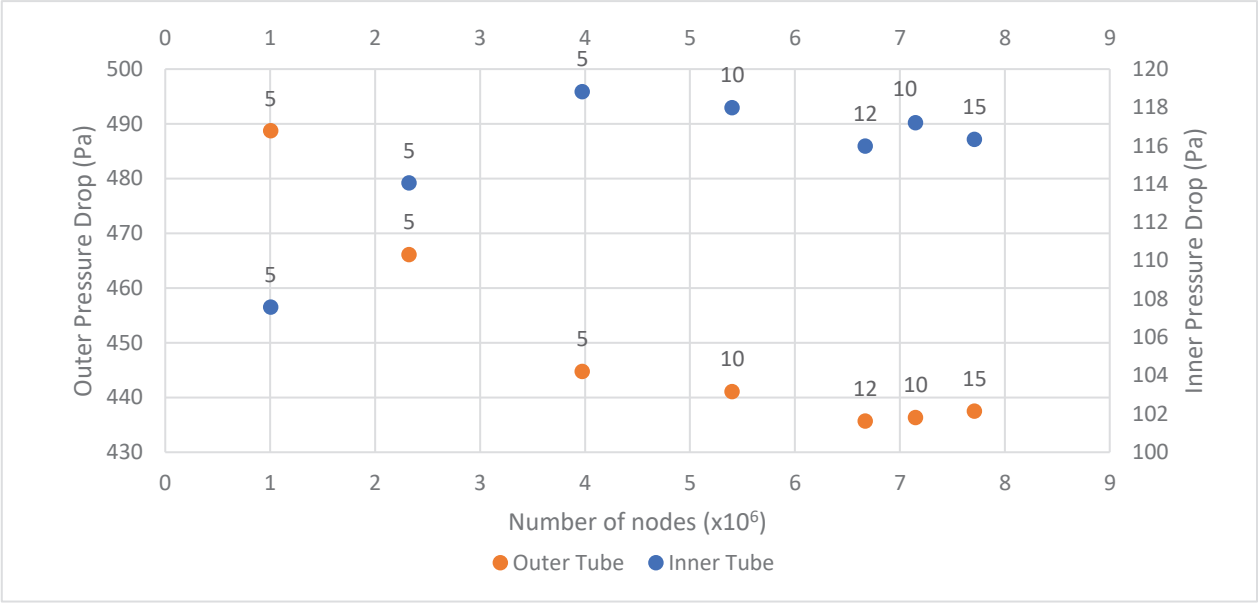

Figure 35: *Mesh optimization results for pressure drop at inner and outer pipes*

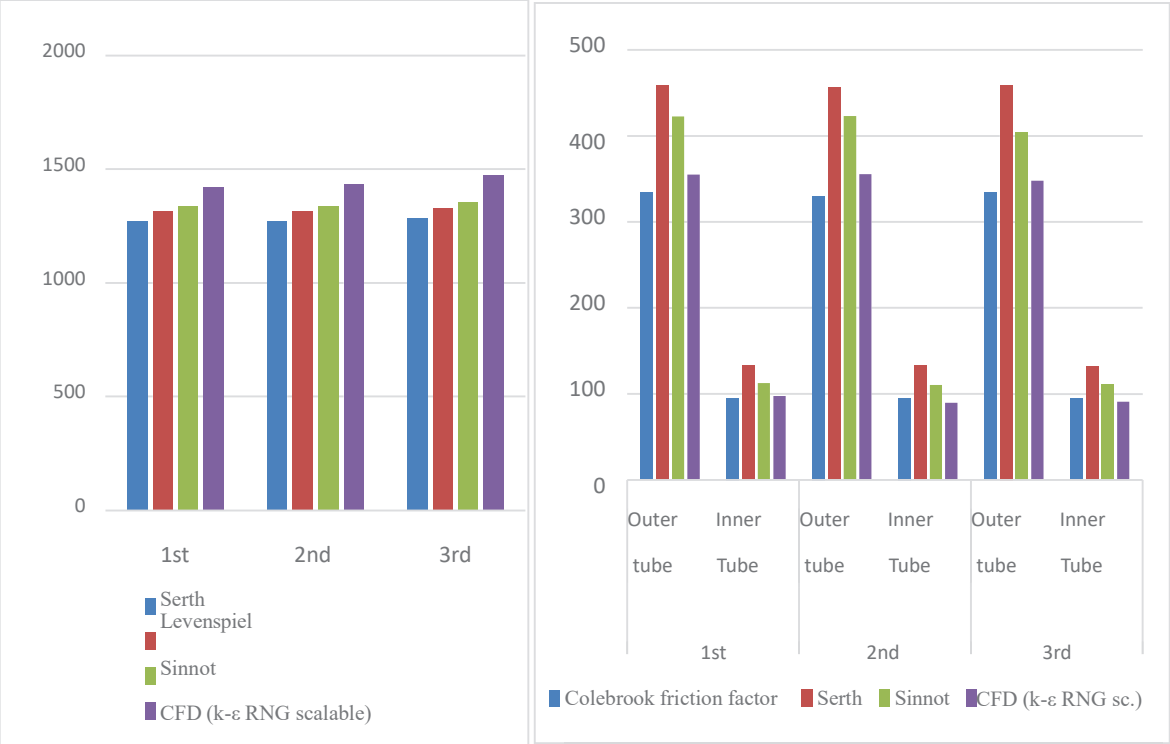

Figure 36: *Comparison between three simulations with different input profiles at the boundaries. a) overall heat transfer coefficient b) pressure drop*

In the case of the k-ε family, results show a major dependence on the wall treatment used that on the turbulence model itself. It also has to be taken into account that the classical equations used tend to overestimate pressure drop and underpredict the overall heat transfer coefficient for engineering purposes, as they use conservative coefficients for the estimates. Velocity profiles at the outer tube are found to match the form of those found by Rothfus et al. (1950) for annular tubes. For pressure drop, classical correlations differ from one to another significantly: 24 % in the case of Serth (2007) compared with the corrected Colebrook friction factor equation. Sinnot's (2012) results are more

conservative, differing with 7.8 % error from Serth's (2007) and 14 % from Colebrook's equation. With these considerations, it cannot be stated that there is a bad result for the CFD simulations, as each model follows one or other empirical correlation. Scalable Wall Functions are the ones that most differ from the mean value and tend to underestimate the pressure drop of both pipes, yielding results close to the ones found by the Colebrook equation corrected by Rothfus et al. (1950) in a non-isothermal regime. k-ω SST model seems to give intermediate results compared with other methods. Compared to the average semi-empirical value, k-ω SST with default settings has performed within a maximum of 16 % of relative error for the inner pipe and 2.4 % for the outer pipe. Low Re treatment for k-ω SST yields 11 % error in pressure drop with respect to the mean for both pipes.

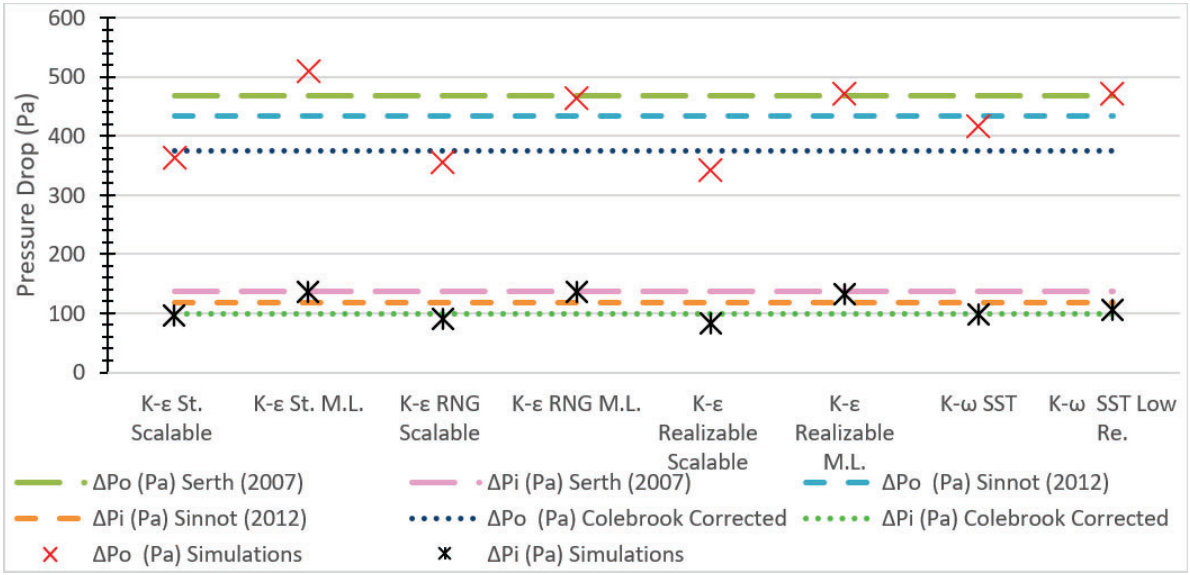

Figure 37: *Pressure drop comparison between empirical equations and CFD (ΔPo outer tube and ΔPi inner tube)*

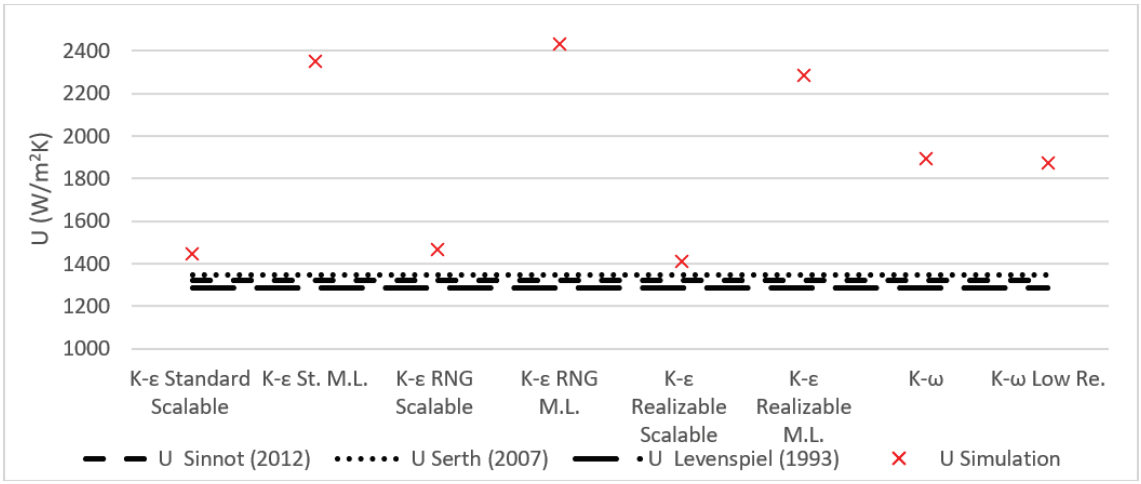

Figure 38: *Overall heat transfer coefficient comparison between empirical equations and simulations*

All CFD results for pressure drop are valid, as they all seem to follow empirical data: Scalable Wall functions reproduce Colebrook's equation for the friction factor with k-ε Standard being the one with less relative error (~4.1 %). Menther-Lechner treatment as well as Low Re k-ω SST follow Serth's (2007) correlations with up to 2.0 % relative error in the inner pipe and 0.87 % error in the outer one for the case of the k-ε RNG model. While being less accurate at predicting pressure drop (at least in the case where they are combined with the k-ε Realizable model), Scalable Wall Functions give a far superior performance than other methods when estimating heat transfer in these simple geometries: k-ε Standard had a 9.8 % error, k-ε RNG 11 % and the k-ε Realizable model predicted U values with an error of 7.1 %. Finally, SST k-ω models are found to be a good tradeoff in accuracy between pressure drop and heat transfer but further simulations with different velocity inlet values found a correction factor of ~0.7, for correctly estimating the U value.

5.2. Plain tube with twisted tape results

5.2.1. Mesh optimization results

The selected mesh is a polyhedral mesh with a cell size of 0.001m. The total number of nodes is around 27M. For k-ω based models, additional mesh adaptation is performed to ensure y+<1 at the boundaries. This optimization results in meshes of about 70M nodes. Figure 39 shows the resulting polyhedral mesh, where smaller cells are present near the gaps between the pipe and the twisted tape.

a) b)

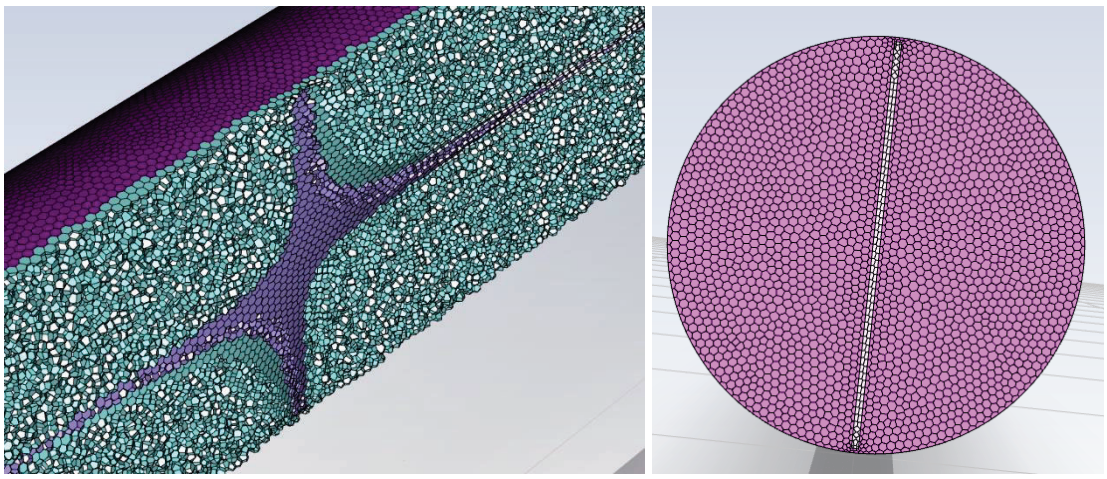

Figure 39: *Mesh results a) side view of the twisted tape, b) Mesh at the inlet face*

5.2.2. Correlation's deviation

In this section, literature correlation equations for twisted tape inserts are compared. The correlations in this research do not always yield similar results. Those correlations are obtained from different experimental conditions, such as Reynolds number and working

fluid, therefore their results differ significantly from one to another. Depending on Reynolds number and TR, different correlations vary in up to 56% for friction factor at low Reynolds numbers and up to 48% for Nusselt number among themselves. Correlations by Date (1974) and Eiamsa-ard et al. (2010) prove to be more consistent, as the deviation between them is low in most of the cases. Chang et al. (2007) correlations' have proven to have more deviation for this case as there are designed for lower TR than the ones presented. Turbulent models that can provide results close to the ones found in the first two correlations are regarded in the present work as better and more accurate. Figure 40 shows that correlations prove to be more consistent with each other as twist ratio increases. It can also be observed that Nusselt number deviation between correlations increases with Reynolds, whereas friction factor decreases.

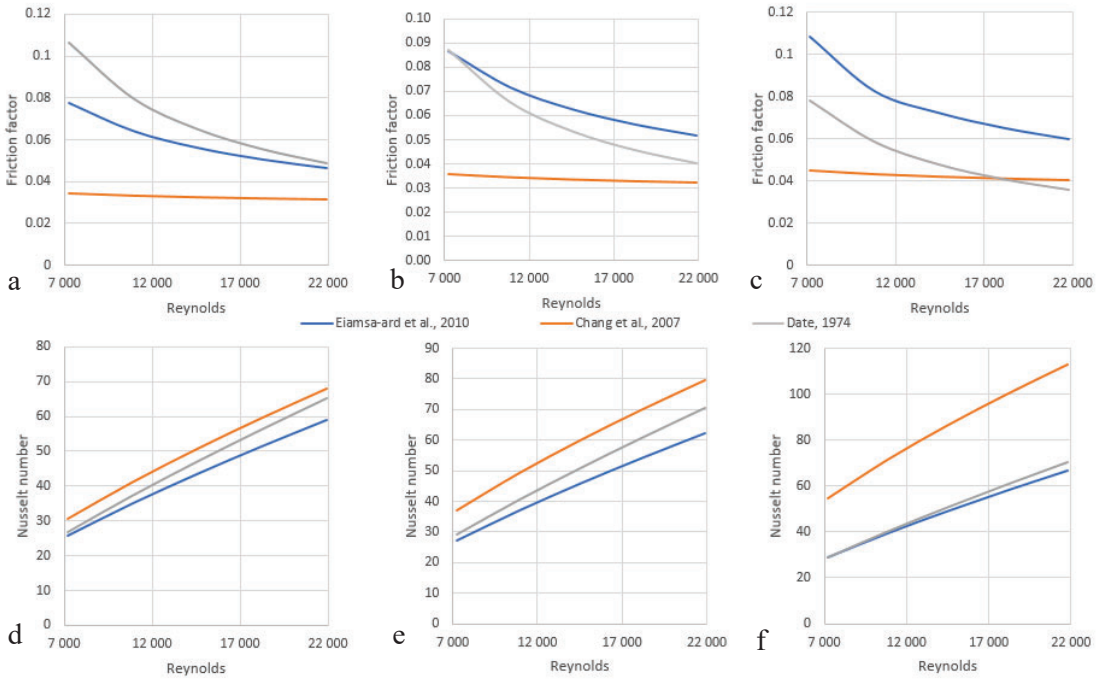

Figure 40: *Correlations comparison a) Friction factor from different correlations TR=5 b) Friction factor from different correlations TR=4, c) Friction factor from different correlations TR=3, d) Nusselt number from different correlations TR=5, e) Nusselt number TR=4 f) Nusselt number TR=3*

5.2.3. Stabilization profile results

Profile stabilization is a key element when comparing against correlations, as they assume fully developed profiles. To ensure that the results are in a fully developed form, only the parts of the pipe where the pressure and temperature profiles are linear are considered.

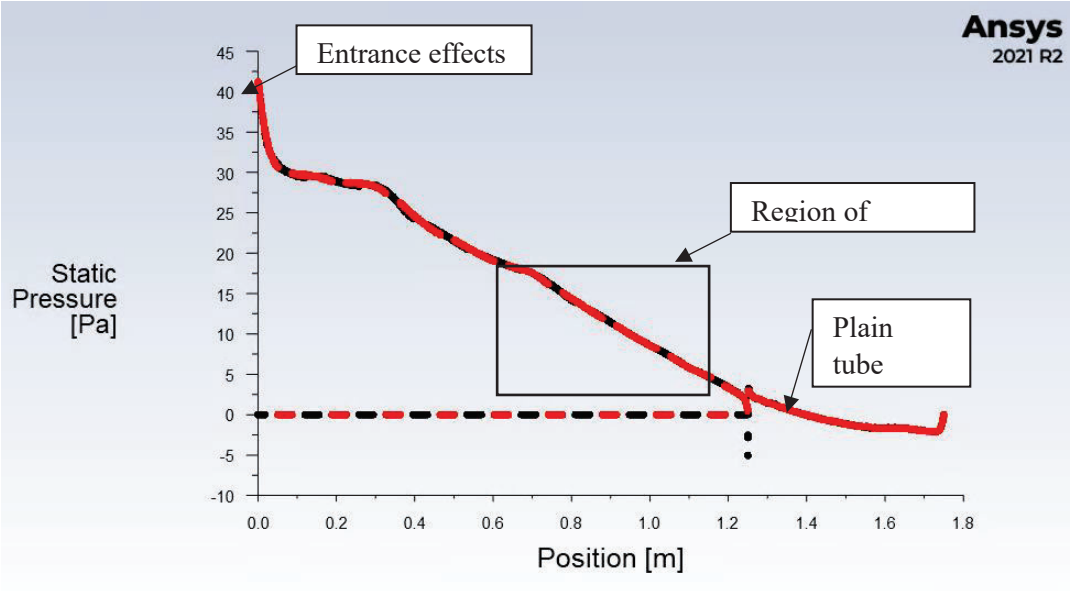

Figure 41: *Pressure profile along two lines parallel to the twisted tape (one in red and the other in black). TR=3, Re=10 000. Model: K-ε RNG SWF. Values are taken from the area between 0.75 m and 1.25 m, where the profile is linear.*

Generally, values between 0.75 m and 1.25 m from the inlet are considered. For some models profile stabilization occurs more rapidly than others, but from the 0.75 m mark, all do present a linear profile. Figure 41 shows that the profile starts to become linear and therefore stabilized at a distance 0.7 m from the inlet. The points where P=0 correspond to the presence of the twisted tape, that since it is a solid, the program takes its pressure as 0. Values such as velocity and temperature follow a similar trend but are too chaotic in the presence of a twisted tape to display them. Instead, the profile perpendicular to the motion of the fluid is displayed.

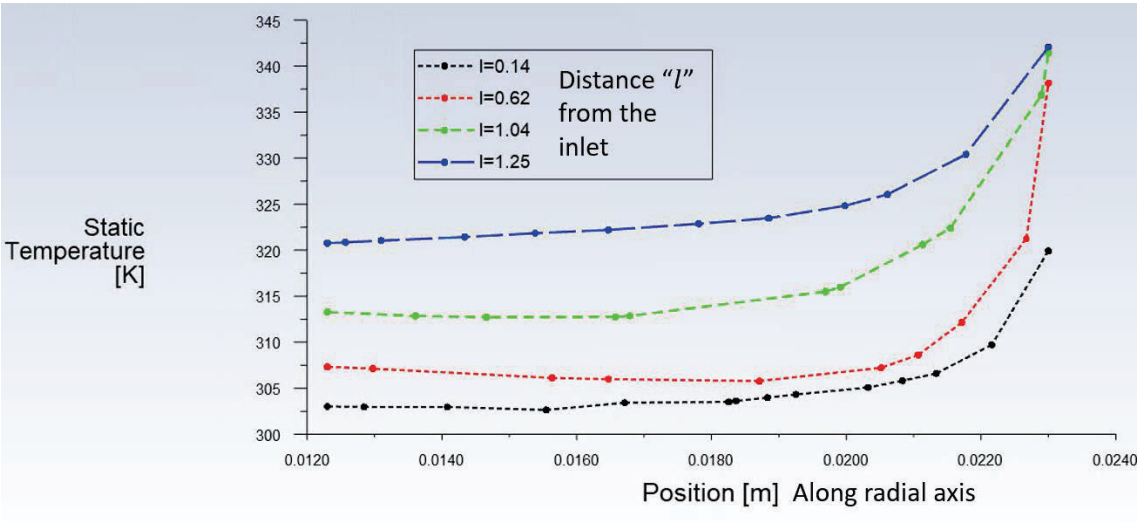

Figure 42: *Temperature profiles at different distances "**l**" from the inlet with respect to the radial position. TR=3, Re=10000. Model: K-ε RNG SWF.*

Figure 42 illustrates that temperature profiles develop early in the tube, as for lengths of 0.62 m from the inlet, the profile is stabilized. It is observed that the profile is unstable at $l = 0.14$ m, presenting a disruptive change in temperature at around 0.016 m of the centre. Despite this, values are again taken from the 0.75 m mark. This graph also shows which reference will be used for estimating the Nusselt number: $T_\infty = 322$ K in this case. T_∞ is estimated as the average bulk temperature in the middle of the interest zone: at 1 m from the inlet.

5.2.4. Turbulent model results

This section is divided in order to cover every model and wall treatment. Some models are showcased in Figures 43-46.

The Figures 43-46 show that all models may be suitable for the simulation of the heat exchanger, as their expected deviation will be similar to the ones found between correlations themselves. Figures 43-44 show how even at different TR values the different wall treatments of the k-ε standard model each follow a different experimental correlation. For Figures 45-46 it can be seen that k-ω based models are less accurate at high TR, but for a lower TR they yield values close to those of the empirical correlations. In order to decide which model better performed for this scenario, results are compared against the correlation found in Eiamsa-ard et al. (2010) as it is the one which was obtained with the same domain variables as the simulations performed in this work. These results do not mean that turbulent models with high deviation are not accurate as they most probably follow the trend of another correlation, as seen in Figures 43-46 where RSM Quadratic Scalable and K-ε Standard wt. Scalable Wall Functions followed correlations found in Chang et al. (2007), while other models lean towards the results found in Eiamsa-ard et al. (2010).

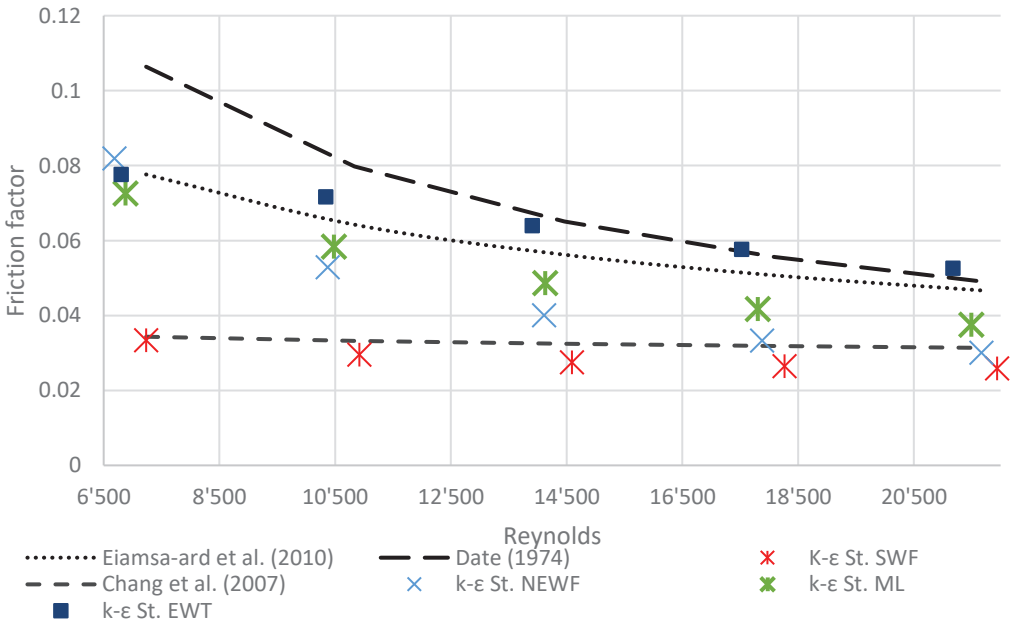

Figure 43: *Friction factor for some turbulent models (TR=5)*

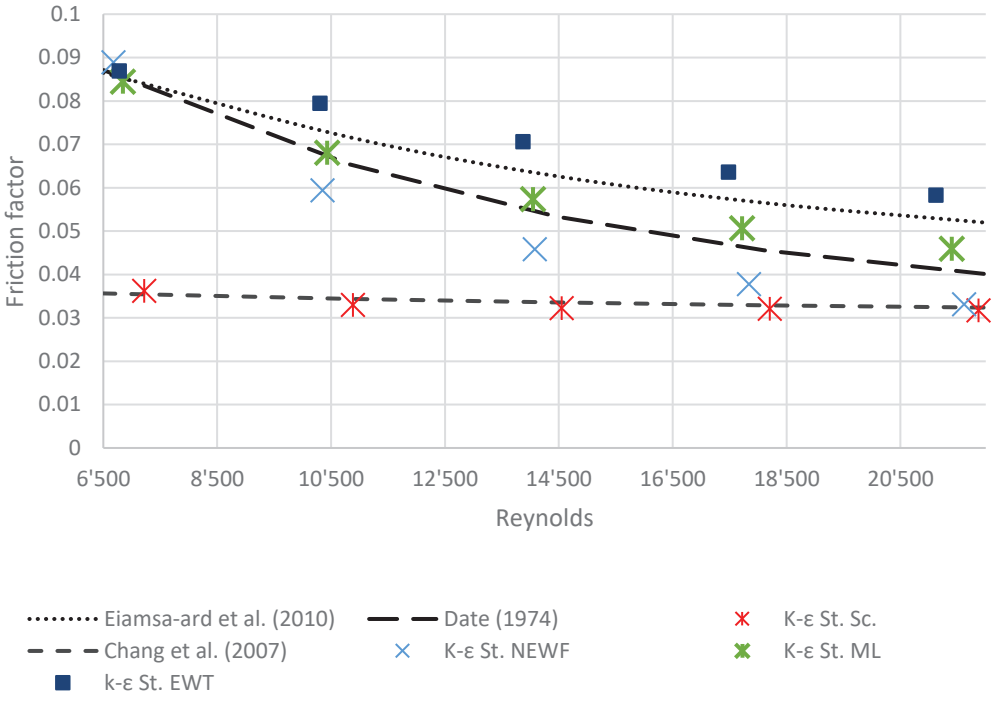

Figure 44: *Friction factor for some turbulent models (TR=4)*

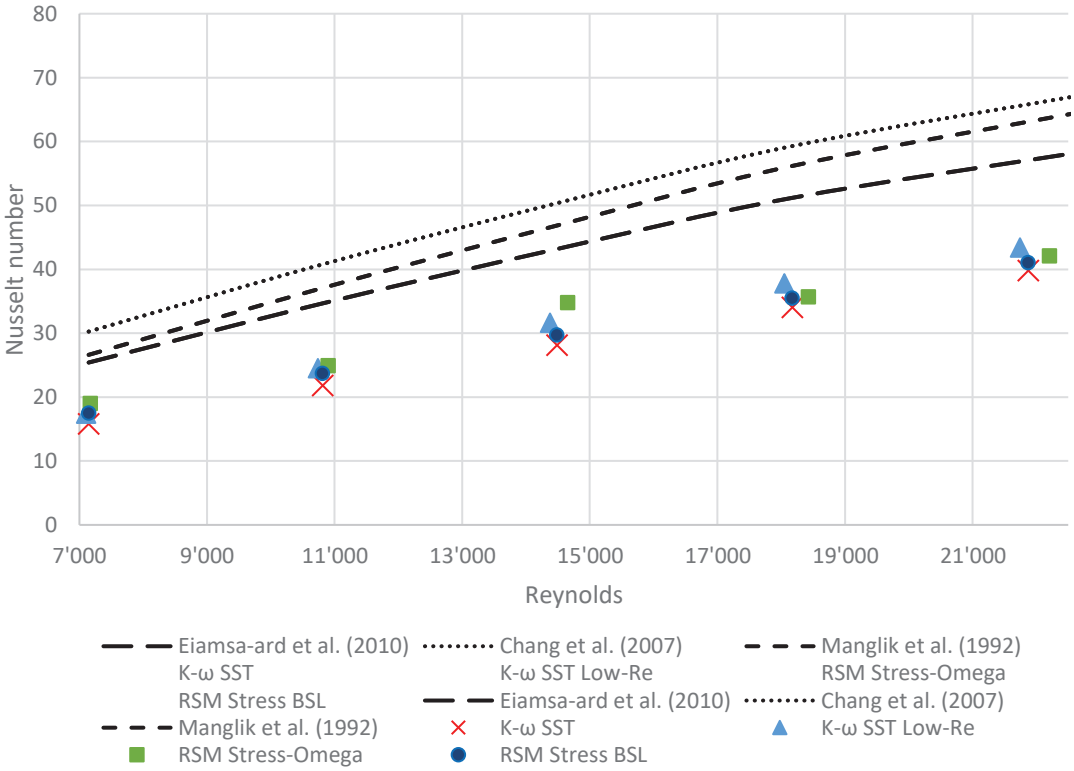

Figure 45: *Nusselt number CFD vs Correlations for K-ω based models (TR=5)*

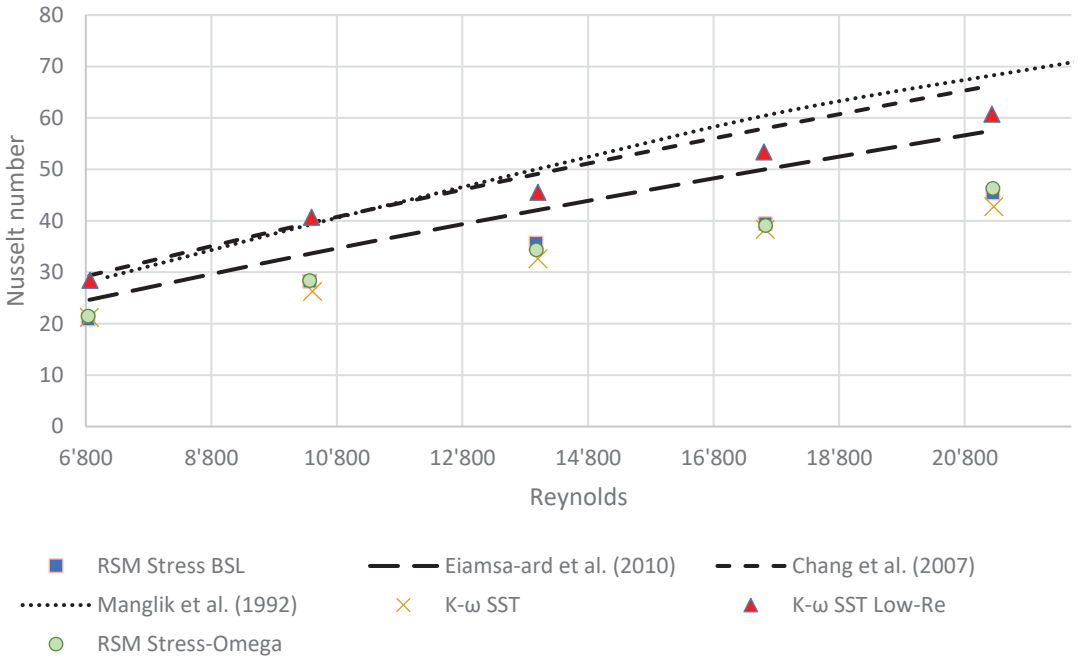

Figure 46: *Nusselt number CFD vs Correlations for K-ω based models (TR=3)*

The deviation between each turbulent model and the correlations described has a dependency on the geometry variables (in this case different TR) and the Reynolds number. A grid is generated testing all the combinations along the 5 different Reynolds numbers in that range from 7 000 to 21 000 and the 3 TR. In order to study how the TR affects the deviation of each model with respect to experimental correlations, the deviation value is averaged along all simulations with the same TR. Later, the deviation present in all simulations' results with the same Reynolds is averaged, in order to study the total deviation produced by different Reynolds numbers.

Table 21 shows the discrepancy or deviation between simulation results and those found using equations 1 and 2. The combination that gives a better performance is k-ε Realizable ML, which in average has the lowest deviation. The total average shows the expected deviation if a turbulent model and wall treatment is chosen randomly, showing how good the performance of these models are in average.

Table 21: *Averaged deviation of the different turbulent models at different twist ratios*

	TR=3		TR=4		TR=5	
	f (%)	Nu (%)	f (%)	Nu (%)	f (%)	Nu (%)
k-ε standard SWF	44.73	38.80	48.56	41.63	50.84	48.27
k-ε standard NEWF	21.29	25.14	23.64	27.13	24.37	30.66
k-ε standard ML	5.61	22.66	9.11	20.73	14.62	16.85
k-ε standard EWT	12.80	26.25	8.33	20.35	9.11	22.65
k-ε realizable SWF	47.10	42.35	51.43	45.41	53.72	52.06
k-ε realizable NEWF	24.63	21.00	29.36	23.45	30.67	25.61
k-ε realizable ML	4.73	23.33	8.73	20.97	14.20	16.91
k-ε realizable EWT	14.02	29.93	8.60	22.29	9.65	25.08
k-ε RNG SWF	45.39	39.58	49.08	41.67	51.07	47.74
k-ε RNG NEWF	21.34	29.23	24.89	27.59	25.86	32.45
k-ε RNG ML	6.68	23.03	9.42	20.76	14.91	16.77
k-ε RNG EWT	14.55	34.27	8.30	24.57	8.90	27.18
RSM linear SWF	47.16	42.77	11.35	18.09	55.26	53.60
RSM linear NEWF	24.72	30.21	51.55	44.66	33.34	32.93
RSM linear EWT	18.11	32.01	29.92	27.52	9.08	15.23
RSM quad. SWF	47.11	42.45	30.65	28.09	55.42	53.90
RSM quad. NEWF	25.40	30.21	52.04	45.61	33.97	32.42
k-ω SST	22.24	21.42	15.55	7.19	48.74	35.18
k-ω SST low-re	19.73	11.46	13.40	21.82	40.65	27.69
RSM stress-omega	20.31	17.49	17.50	24.67	64.12	46.34
RSM STRESS BSL	23.40	20.98	17.61	26.71	52.36	30.97
Average total	24.34	28.79	24.71	27.66	33.37	32.88

Clear relationships can be derived from the data collected. For k-ε models there is much more influence on the final results of the wall treatment used than the specific turbulent model selected. The wall treatments that better adjust the experimental correlations are Menther-Lechner and Enhanced Wall Treatment, both being designed to avoid the ideal assumptions present in wall functions. Menther-Lechner treatment is therefore advised when dealing with complex geometries such as this case. Simple models such as SWF prove to be inaccurate for this complex geometry, they underestimate friction factors and Nusselt number, which can lead to huge errors when calculating TFP. If wall functions are to be used, non- equilibrium wall functions are better suited for complex flows. When estimating Nusselt number, which is the major design interest in these problems, k-ω models prove to yield accurate and consistent results.

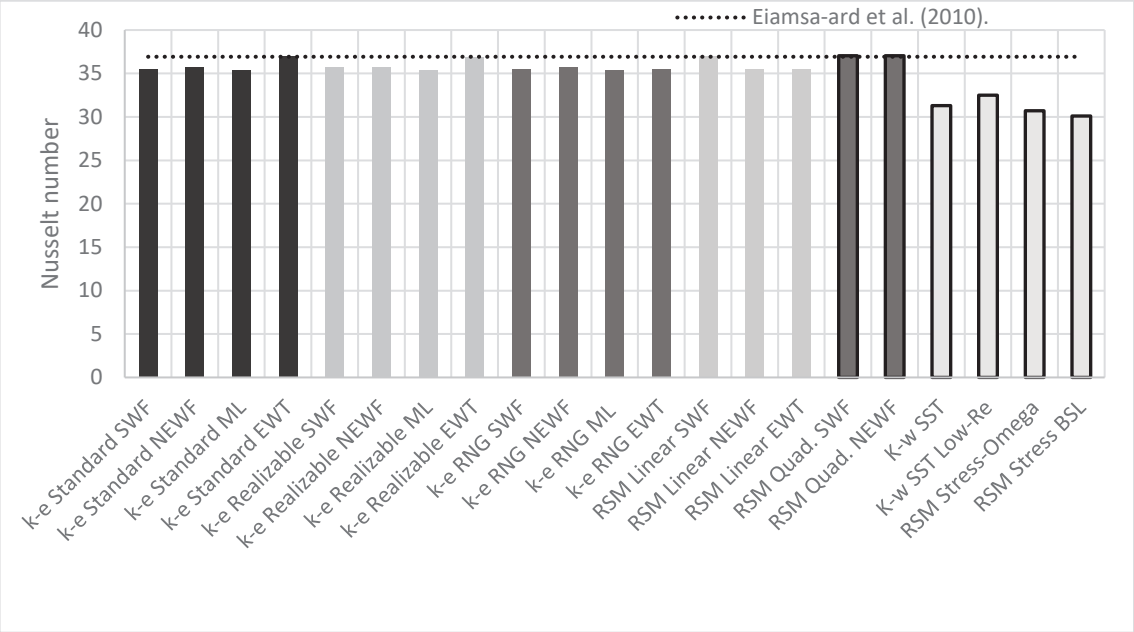

Figure 47: *Nusselt number comparison between different models (TR=4, Re=10 000)*

In Figures 47-48, the different values of friction factor (f) and Nusselt number (Nu) are compared to those obtained from Eiamsa-ard et al. (2010)'s equations. k-ε models and k-ω based models, seem to give similar results between themselves, both for f and Nu. k-ω based models have a low dependency on Low-Re treatment or if the RSM is selected.

In general, all models present a mean bias with respect to Eiamsa-ard et al. (2010)'s correlations that makes the consistently underestimate pressure drop by about 22%. In the case of Nu, they underestimate it by a 3% in average. Lowest bias was found in k-ε standard EWT for friction factor and k-ε Realizable NEWF, the later being accurate but not precise enough.

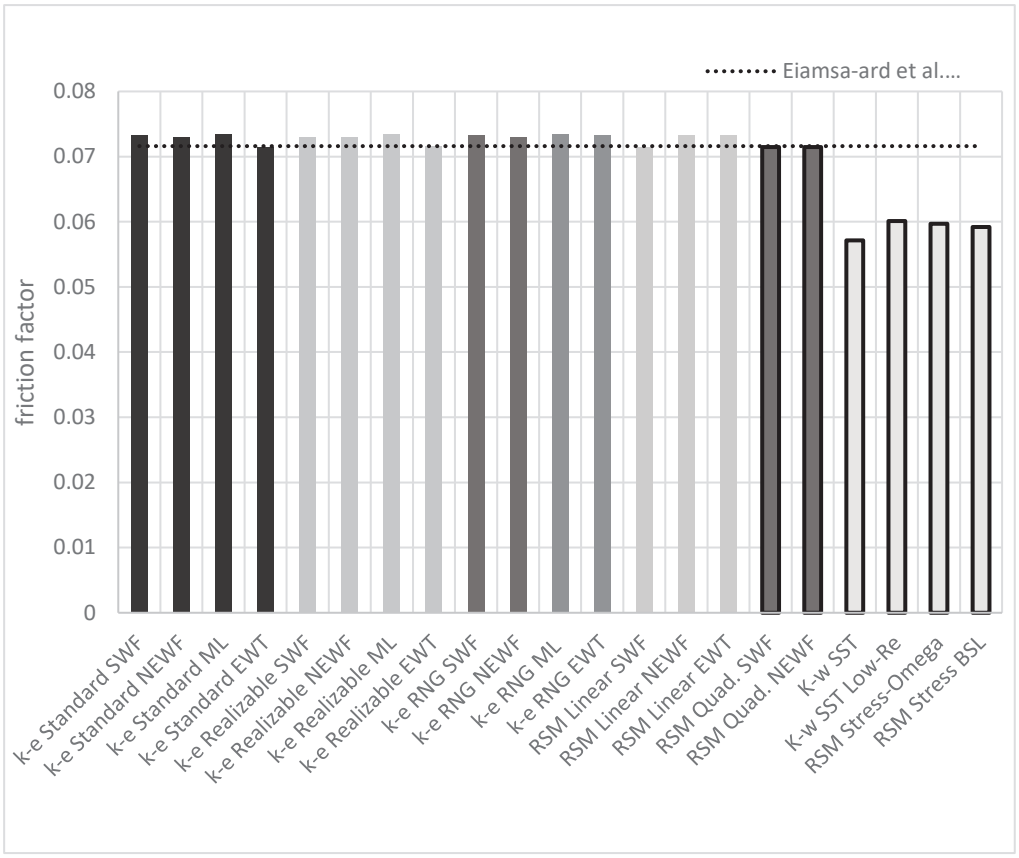

Figure 48: *Friction factor comparison between different models (TR=4, Re=10 000)*

Figure 49 presents the mean deviation with respect to equations (1) and (2) of each combination of model and wall treatment. There are combinations that work much better than others. k-ω based models gave good results, with k-ω SST Low-Re giving better results than the others. In general, RSM models did not give a better accuracy in validating experimental data. For k-ε based models, all of the models which include EWT or ML produced accurate and precise friction factors and Nusselt numbers. There seems to be little to no influence on how the combination of turbulent models and wall treatments affect the results, as the outputs seem to be the sum of the two influences independently.

All of the above conclusions are extracted solely by comparing the simulation results with the experimental correlations extracted from the same unit. Different conclusions can be extracted if results are compared with the average value of the three correlations reviewed. Chang et al. (2007) results are only considered in the TR=3 case, as in their experimental procedures the TR ranged from 1.56 to 2.81, not covering our region of interest. Total deviation is calculated in the following manner, Eq. 83:

$$dv = Abs\left(\frac{a_s}{\sum w_i\, a_{ci} / \sum w_i} - 1\right) \tag{83}$$

Where a_s is a simulation variable result, a_{ci} is the same variable extracted from the "ith" correlation and w_i is the weight or importance that is assigned to the correlation, in this case $w_i = 1$ for all the cases except for Chang et al. (2007)'s correlations in cases TR=4 and TR=5, where $w_i = 0$. By using this equation, the first comparison has $w_i = 1$ for Eiamsa-ard et al. (2010)'s correlations and $w_i = 0$ for the others.

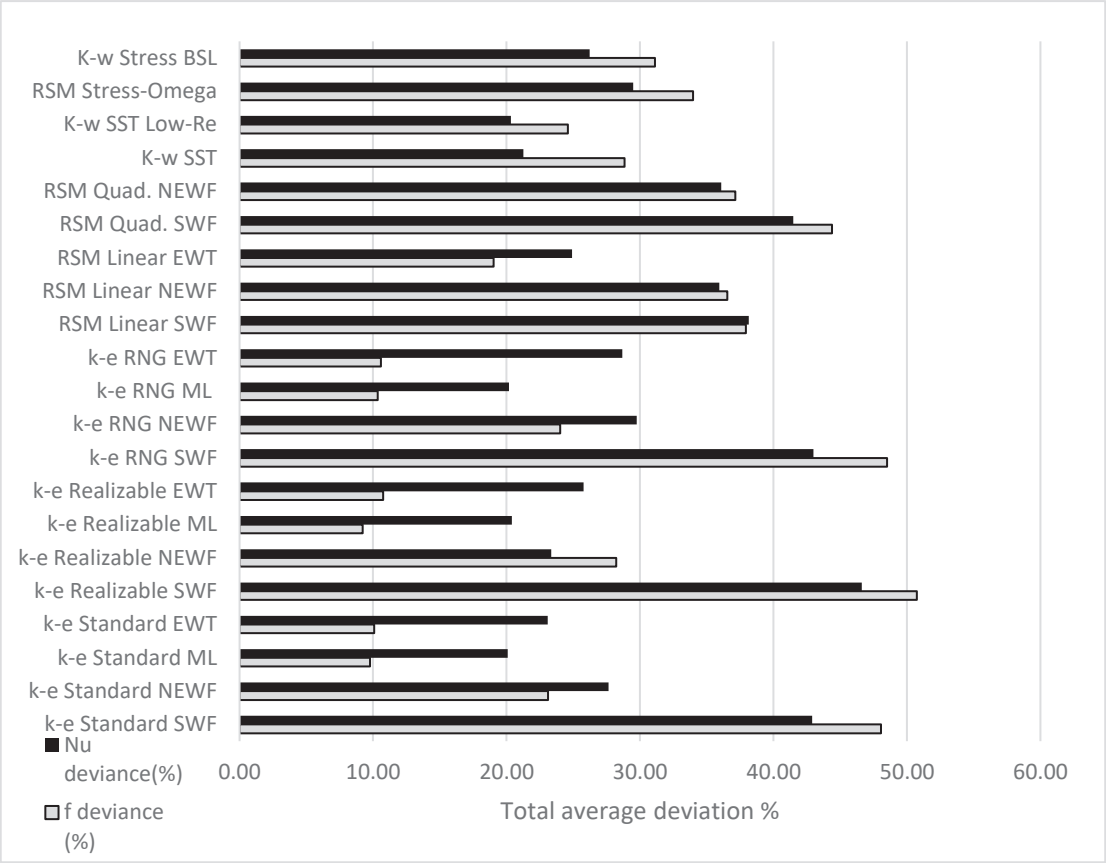

Figure 49: *Total average deviation of each model when compared against correlations in Eiamsa-ard et al. (2010). Deviation is averaged along Reynolds and TR to obtain the total expected deviation of each variable*

The results of using the second comparison method are displayed in Table 22, where values are compared against the mean correlation value. On the contrary of the first method, here the method that shows less discrepancy with experimental is the k-ω SST. Models that did not have high accuracy in the first method do not present it here either, like the case of SWF. Figure 50 illustrates the different average deviation from the mean experimental value for the models studied. It is noticeable how in this case the method with lower friction factor deviation is the k-ω SST.

Table 22: *Averaged deviation of the different turbulent models at different twist ratios. Deviation is averaged for the different Reynolds numbers*

	TR=3		***TR=4***		***TR=5***	
	f (%)	Nu (%)	f (%)	Nu (%)	f (%)	Nu (%)
k-ε Standard SWF	26.46	51.63	44.55	43.23	62.83	50.28
k-ε Standard NEWF	12.63	21.28	19.16	28.02	43.56	31.32
k-ε Standard ML	25.78	14.44	3.13	19.34	36.29	17.84
k-ε Standard EWT	50.29	2.87	16.05	17.42	19.13	18.50
k-ε Realizable SWF	29.62	54.43	47.61	46.91	64.98	53.93
k-ε Realizable NEWF	11.07	23.97	25.04	24.28	48.57	26.30
k-ε Realizable ML	26.95	12.72	2.72	19.55	35.99	17.91
k-ε Realizable EWT	51.92	4.02	16.34	19.31	18.54	20.46
k-ε RNG SWF	27.33	52.26	45.10	43.25	63.00	49.76
k-ε RNG NEWF	13.89	23.13	20.48	28.04	45.20	33.06
k-ε RNG ML	24.36	15.00	3.47	19.37	36.52	17.77
k-ε RNG EWT	52.64	7.27	16.01	21.55	19.24	22.49
RSM Linear SWF	29.71	54.76	18.79	15.68	66.07	55.42
RSM Linear NEWF	11.21	24.36	47.66	46.18	50.63	33.48
RSM Linear EWT	57.40	7.40	25.67	28.41	18.39	12.98
RSM Quad. SWF	29.63	54.50	26.44	28.96	66.18	55.71
RSM Quad. NEWF	10.90	24.47	48.20	47.10	51.08	32.99
K-ω SST	8.50	29.72	10.66	3.74	18.78	35.56
K-ω SST Low-Re	11.99	5.27	9.99	26.18	19.80	36.20
RSM Stress-Omega	11.19	26.16	8.93	28.95	28.95	37.14
RSM Stress BSL	10.96	26.14	9.05	30.85	26.70	36.47
Average Total	25.45	25.51	22.14	27.92	40.02	33.12

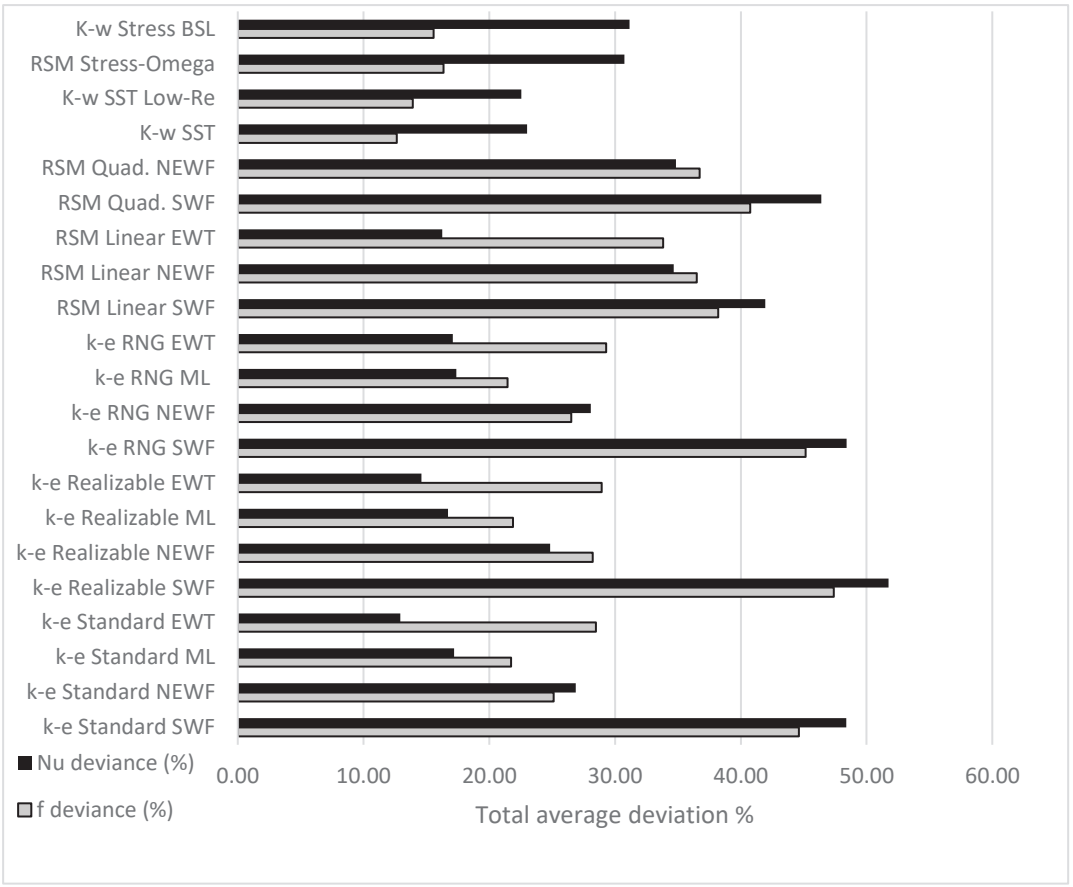

Figure 50: *Total average deviation of each model when compared against mean correlation values*

It is hard to decide which correlation is more reliable, which propagates to turbulent models and wall treatments. Still, most combinations of models and wall treatments provided similar deviations for both comparisons. The mean deviation result of the two comparative methods can be used, which is analogous to giving twice the weight when averaging to Eiamsa-ard et al. (2010)'s equations. In fact, during the averaging process, the weights can be adjusted to the needs or beliefs of the user on which correlation is better suited for the parameters of the domain. This research presents the two extreme cases: either the user considers all correlations equally, or only considers one is correct. Each other case falls between those two cases, as no correlation should be given more credit (and therefore more weight) than the one that has the same experimental setup as the simulations conducted. Even if the number of correlations used for averaging was large enough, the averaged result (while being free of experimental deviation) would capture the bias caused by the uneven and more popular experimental settings present in these correlations. If most of the researchers experimented with TR<2, the correlations would be really precise around those TR values but outside this range they would be unreliable and so would be the average correlation value ($\sum w_i \, a_{ci} / \sum w_i$).

When compared to the mean correlation's values, simulations have larger discrepancies than when they were compared against Eiamsa-ard et al. (2010)'s correlations. The total average deviation with the mentioned correlations is 28.63% while the total average deviation when compared with the mean correlation value is 29.03%. Total bias found by

using the mean correlation value shows that simulations underestimate f by 13% and Nu by 12%, so the accuracy has increased for f and decreased for Nu with respect to the first method. By contrasting simulations in this manner, k-ω models seem to give superior precision than k-ε based models. It is clear that no model can be easily catalogued as the best one for conducting these simulations, as its analysis depends on which empirical correlations are considered valid to compare against. As stated previously, these empirical correlations' results differ from each other significantly, so the same result is to be expected when simulations are compared against each other. In fact, simulations do have lower standard deviation between themselves than experimental correlations. While correlations have 44.4% of deviation for f and 16.7% for Nu, simulations grant 24.3% deviation for f and 24.4% for Nu, even though some models are not clearly suited for this case, such as SWF. If the 9 best models are considered, i.e. k-ε models with ML or EWT and k-ω SST models, their deviation is reduced: 17.2% for f and 17.7% for Nu. It is not coincidental that these models and wall treatments agree so much between themselves: ML and EWT are Near Wall y+ method that rely on near wall modelling (NWM) when y+ is sufficiently small, and with the exception of RSM Stress-Omega (which is used alongside shear flow corrections) all other k-ω based models employ k-ε formulation far from the walls and k-ω's NWM close to the walls.

Models that use wall functions are clearly outclassed by NWM for such complex geometries. RSM k-ε based models seem to only provide good results when EWT are used (which are only available for RSM Linear Pressure-Strain model), and even in this case they do not seem to give more accurate results than their simpler counterparts. Same is true for RSM k-ω models albeit to a lesser extent: they tend to differ slightly more from correlations than k-ω SST.

Models present different accuracies depending on the geometrical conditions of the simulations, in this case the TR. Lower twist ratios produce more swirling flows and more wall adjacent gradients, which are best modelled by any k-ω model and k-ε based models with ML. These models provide fewer promising results when TR=5, setup in which more shear flow is present in the domain. Contrarily, models which use EWT are more accurate for higher twist ratios than others, in shear dominated flows, where k-ε based models seem to provide better results, and are precise in all scenarios. This difference might be derived on how different wall treatments extend their boundary layer, based on their own different criteria. Figures 51-52 show the contours of velocity and temperature. The contours are taken at the end of the TT, a distance $l = 1.25$ from the inlet. The contours show a point symmetry around the centre of the TT. The fluid is in a counter clockwise swirling motion induced by the TT.

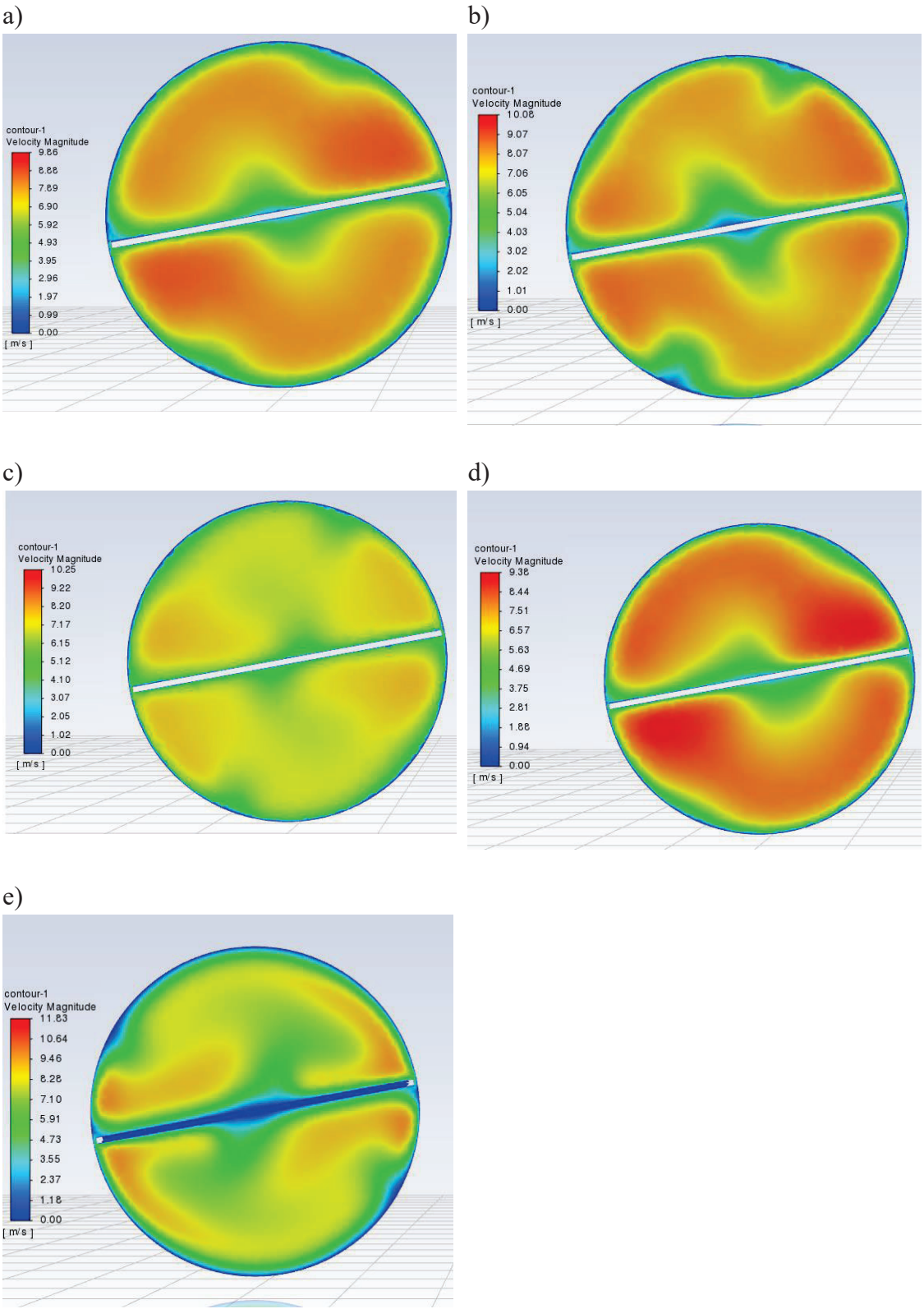

Figure 51: *Velocity magnitude contours, TR=3. Re=10 000. Velocity magnitude contours a) K-epsilon St. EWT, b) K-epsilon St. ML, c) K-epsilon St. NEWF d) K-epsilon St.SWF, e) K-omega SST*

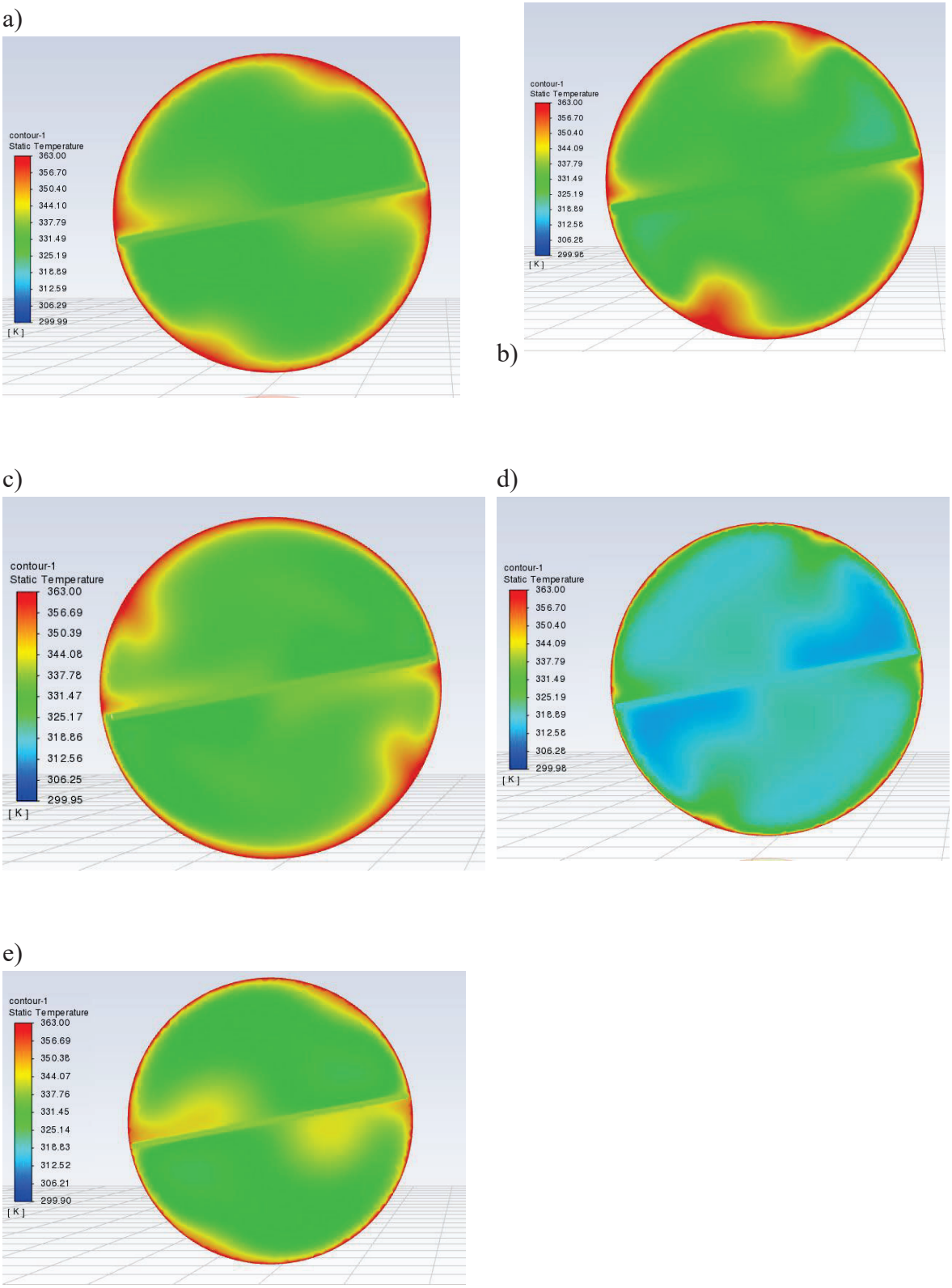

Figure 52: *Temperature contours, TR=3. Re=10 000. Velocity magnitude contours a) K-epsilon St. EWT, b) K-epsilon St. ML, c) K-epsilon St. NEWF d) K-epsilon St.SWF, e) K-omega SST*

Figures 51-52 show different contours of velocity and temperature for the same case and at the end of the twisted tape, at 1.25 m from the inlet for k-ε standard and k-ω SST models. As seen from Figure 51 different wall treatments calculate differently the thermal layer and the transition layer near the walls. Figures 51 a), b), and c) show the results in treatments such as EWT, NEWF or ML and how they capture the swirling flow correctly, having more velocity near the walls of the twisted tape where the flow rotates counterclockwise. ML method exhibits zones of low fluid velocity, which affect negatively the heat transfer, much less present in other methods (Figure 51 b). SWF seem to diffuse the swirling motion of the flow not capturing noticeable gradients in the domain (Figure 51 d). k-ω SST model displayed in Figure 51 e) captures more complex features, and low velocity zones, this time opposite of where ML method predicts them. Although having different profiles, both ML and k-ω SST agree with experimental data in the final pressure drop. But this is not propagated to the heat transfer, where both methods largely disagree on the final transferred heat. In Figure 52 different shapes and thickness of the thermal layers can be seen, which produce larger or smaller Nu numbers. It is also seen that the slow zones produced in some models caused by the induced swirling generate domains where the thermal boundary layer extends towards the middle of the tube such as the ones seen in Figures 52 a), b) and e), corresponding to EWT, ML and SST respectively. NEWF depicted in Figures 51 d) and 52 d) show a central low velocity zone that allows the entrance of hot fluid towards the middle of the pipe. From Figure 52 d), corresponding to SWF it can be seen that heat transfer is low, as the temperature near the centre is similar that the inlet temperature. All models exhibit thinner boundary thermal layers in zones where the velocity is higher, where most of the heat is transferred. The results obtained from the simulations from Figures 51-52 are shown in Figure 50. EWT, NEWF and ML exhibited similar thermal boundary shapes and gradients, thus providing similar Nu results. Although providing similar friction factor results, both ML and k-ω SST created very different velocity contours, making it difficult to decide which one provided a correct answer.

Deviation's dependency of every model on the Reynolds does not follow clear patterns and in most models the discrepancy with correlations seems to not be affected by Reynolds numbers. There are combinations of models though, that exhibit clear tendencies where the deviation increases or decreases smoothly with the Reynolds number. Nu and f deviation against Eiamsa-ard et al. (2010)'s correlations are averaged along all twist ratios and compared for every Reynolds number. K-ε RNG SWF, RSM Linear and both k-ω SST simulations show increase in friction factor accuracy with higher Reynolds. The opposite is true with K-ε RNG NEWF, who performed better at lower Reynolds. EWT and ML containing models see an increase in Nusselt number accuracy with increasing Reynolds while K-ε RNG NEWF and RSM Stress-Omega experienced higher correctness at low Reynolds.

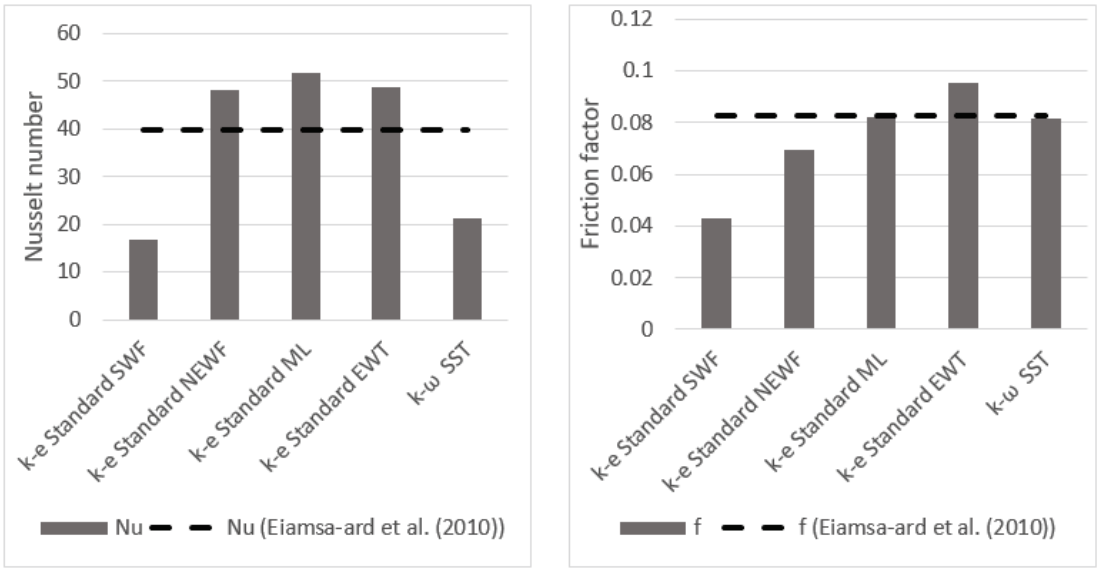

Figure 53: *Deviation with respect to Eiamsa-ard et al. (2010) for the case presented in Figures 51-52*

5.3. Optimization of a corrugated tube with twisted tape geometry

The optimization of the twisted tape geometry is based on finding the maximal TPF value by changing the geometrical parameters N1, N2 and N3. These values are bounded as expressed in table 23.

Table 23: *Geometrical parameters range*

NAME	LOWER BOUND	UPPER BOUND
N1	1.01	2.5
N2	0.5	5
N3	0.2	2

As remainder, N1 relates to the width of the corrugated tube, N2 is also interpreted as TR (Twist Ratio from literature) and N3 relates to the spacing between the corrugated crests. All those parameters are scaled to the diameter of the tube.

Within these parameter ranges, the results found are for inlet velocities ranging from 10-25 m/s (which result in Reynolds 16000~42000). As the studied cases have a Reynolds are over 16000 and a TR (or N2) value under 5, the selected turbulent model is the k-ω SST, as it was found the previous chapter that this model provides accuracy under these conditions.

The optimization algorithm is the Multi-Objective Genetic Algorithm (MOGA) available with Ansys Workbench, with 35 initial samples and 175 maximum number of points. The optimization for the 15 m/s (Re=24000) case created 148 points and found a maximal TPF of 1.43. In this case, N1= 1,90, N2=2,63 and N3=1,78. This optimal point has an increase in Nusselt number of 369.5% with respect to the plain tube (Case 128 in Annex 1). Higher values are found in other cases with lesser efficiency due to an additional increase in friction factors. The highest Nusselt number difference is 443.0%, and its associated thermal performance is 1.18, which is still better than a plain tube (Case 96 in Annex 1). With the volume of data found (Annex 1), choices can be made if the objective is to maximize heat transfer, maintain the balance provided by the TPF value, or try to reduce friction as much as possible without compromising heat transfer. The 1.43 TPF value relatively if other findings from literature are considered at similar Reynolds numbers extracted from a review byC. Zhang et al. (2016):

- At Re=30000, Promvonge et al. (2014) found a 1.2 TPF value for twisted tapes with winglet generators.
- At Re=35000 Bhuiya et al. (2013) obtained a TPF of around 1.4, similar to the findings obtained here.

Most of the comparisons found in literature for twisted tape inserts and various geometrical variations obtained TPF values at this Reynolds numbers that ranged from 1 to 1.2.

The following graphs (Figure 54) show the different variables and their associated TPF numbers. Notice that each variable is highly dependent on the other ones, and no clear trend arises it is the combination of the values the different variables which creates an optimal geometry.

a)

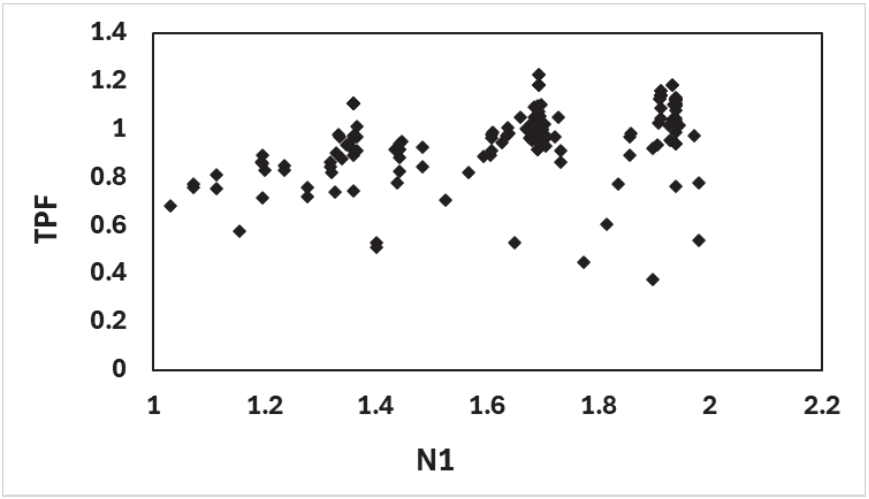

b)

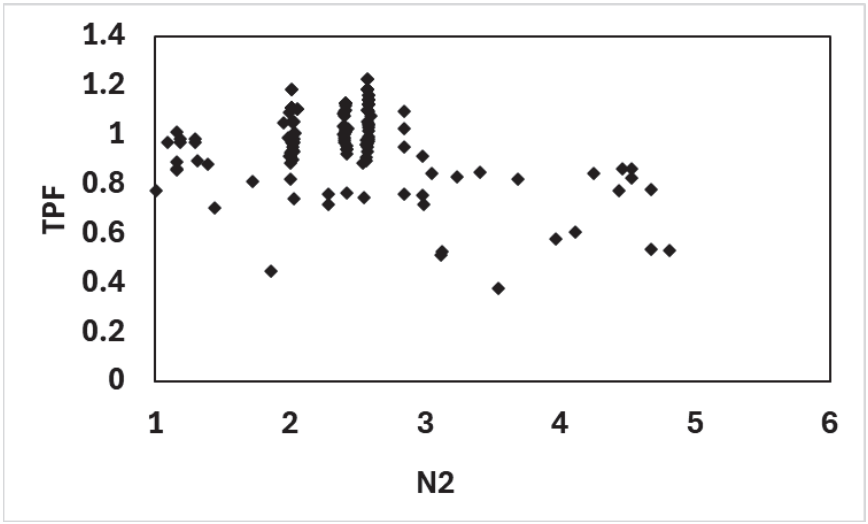

c)

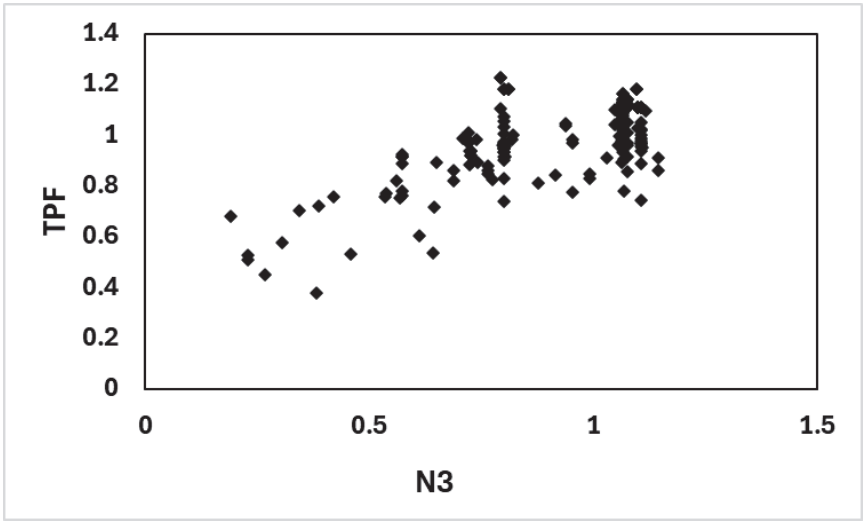

Figure 54: *Thermal Performance factor as a function of the different geometrical parameters at 15 m/s inlet conditions, Re~24000, a) TPF vs N1. With increased external radius, comes increased area of heat transfer and turbulence. This comes at the cost of higher friction. Consequentially, the TPF does not depend significantly on the N1 parameter, b) TPF vs N2, here twist ratio seems to depend on the other parameters at its optimal point, c) TPF vs N3, the increased spacing between the crests reduces friction and therefore increases TPF*

a)

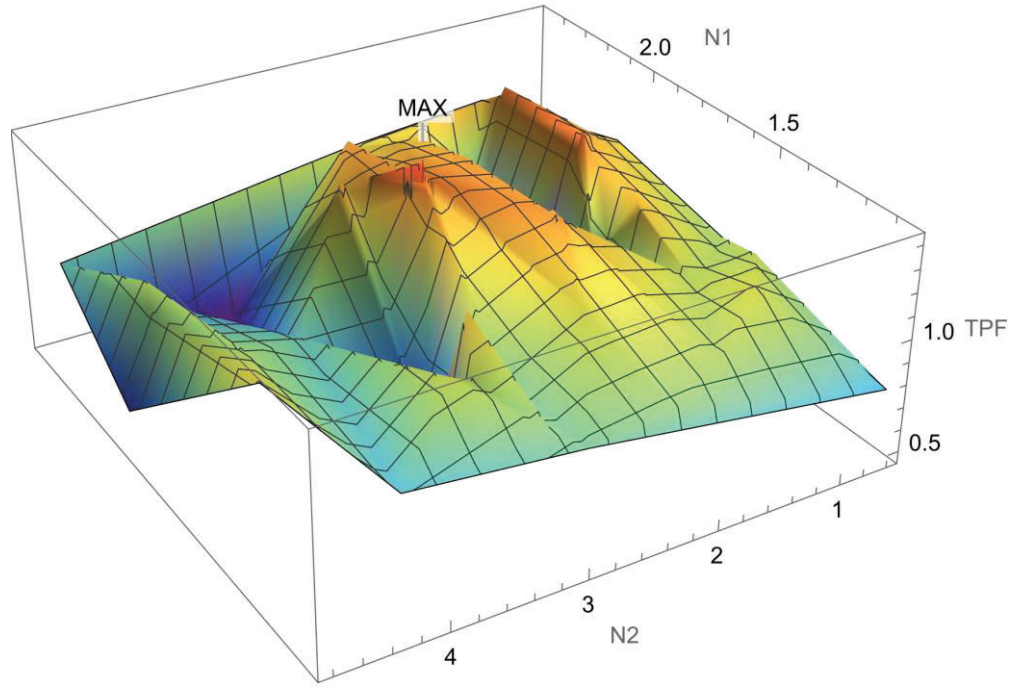

b)

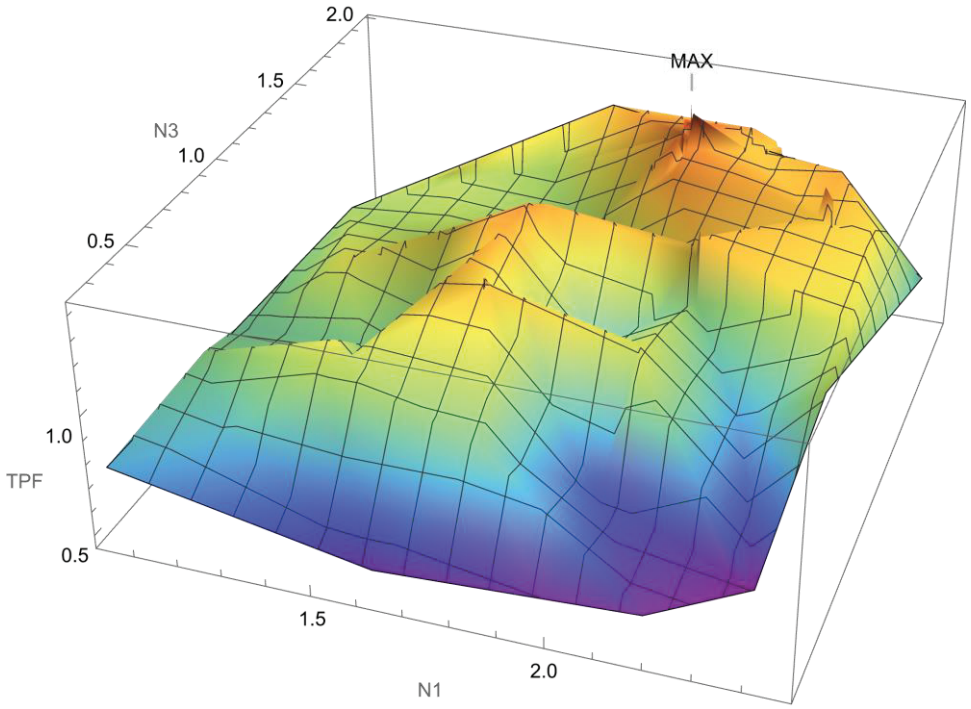

c)

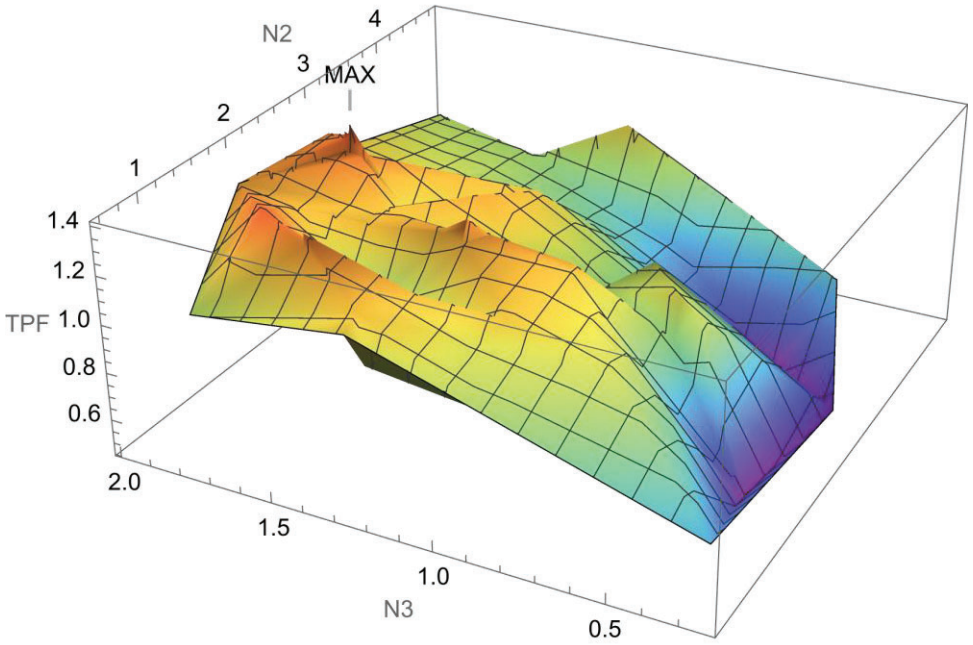

Figure 55: *Data surface of the optimization points and its associated TPF value for the different combinations of N1, N2 and N3, a) TPF vs N1 and N2, b) TPF vs N1 and N3, c) TPF vs N2 and N3*

It must be noted that an increase in Nusselt number with respect to the plain tube does not correlate directly to the same increase in heat transfer, as the contact surface is always greater for the case of the corrugated tube. Therefore, the increase in transferred heat can be estimated by the equation Eq. 84 depending on the geometrical parameters N1 and N3:

$$\frac{h}{h_o} \propto \frac{A\ Nu}{A_o\ Nu_o} = \frac{\left(1 + {N_1}^2\right) + (N_1 + 1)\sqrt{(N_1 - 1)^{\,2} + {N_3}^2}}{2\ N_1\ N_3} * \frac{Nu}{Nu_o} \tag{84}$$

Where h/h_o is the heat that the enhanced tube transfers divided by the heat of the plain tube, A/A_o is the area of the corrugated tube divided by the area of a plain tube with same length and diameter equal to the diameter of the crests (d*N1). The following term $Nu/\ Nu_o$ is the increase in Nusselt number. For the optimal case of N1= 1.90, N2=2.63, N3=1.78 and a diameter of 0.035m this tube would have 53.7% more area resulting in an increase of heat exchange of 567.8%. The TPF value, if it were to be calculated accounting this ratio increase, would be of 2.20.

It has been experimentally found that for low Reynolds number the value of the thermal performance factor is higher and as the Reynolds number increases the thermal performance factor decreases respectively (Kumar et al., 2016). Due to this fact, the expected case with the higher TPF should be the lower velocity one. Similar optimal points are obtained at lower and higher Reynolds numbers:

- At Re=16000, with an inlet velocity of 10 m/s the optimal parameters found were N1= 1.95, N2=2.54 and N3=1.92, with a TPF value of 1.50 (Annex I, Table 2, case 55).

– At Re=42000, which means an inlet velocity of 25 m/s the optimal parameters found were N1= 2.11, N2=2.98 and N3=1.83. They achieved a TPF of 1.27 (Annex I, Table 3, case 59).

Notice that the variation across all parameters at different Reynolds is less than ±10% for N1 and N2. N2 presents larger variations with values that have a ±23% variation. For the range studied these differences are small, and when testing one optimal point at other Reynolds number its performance is close to the optimal found, meaning that this geometrical configuration allows for some optimal conditions across different Reynolds numbers.

5.3.1. Flow and temperature analysis

This section analyses the different flow structures that the optimal case for 15 m/s and Re=29600. Figure 56 shows the contours of velocity magnitude for the optimal found at 15 m/s. In this contour the velocity oscillates depending on where the point sampled is with respect to the twisted tape. When the corrugation decreases the diameter of the tube it creates high velocity zones that appear at both sides of the twisted tape in a symmetrical pattern.

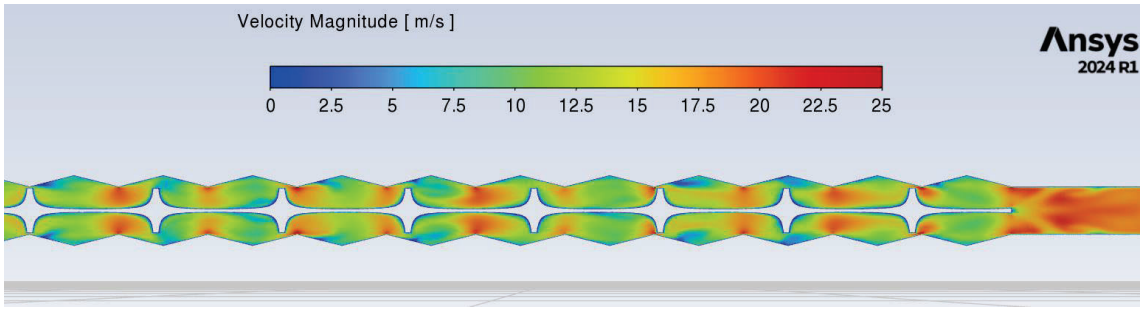

Figure 56: *Contour plot of velocity magnitude in streamwise direction.*

The temperature profiles show that the corrugated surface upon where the flow impacts are the ones with steeper temperature gradients, producing enhanced heat transfer. Behind the walls that are looking in the direction of the flow a slipstream of temperature gradient can be seen, which reduces the transferred heat. (figure 57)

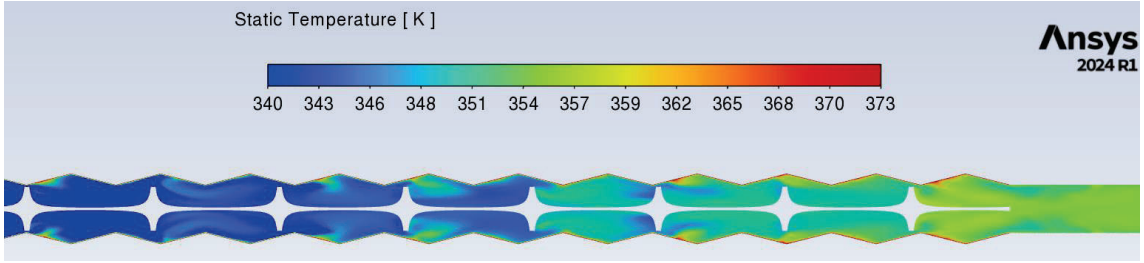

Figure 57: *Contour plot of temperature in streamwise direction.*

This effect can also be seen when looking at contours of heat transfer in the walls (figure 58 a). In this Figure it can be seen the aforementioned fact, walls facing opposite of the flux direction have less heat transfer than those facing it. It can be observed that a region

of very low heat transfer is created behind the points where the twisted tape is close to the external wall. Wall shear stress is related closely to heat transfer, as the points behind the twisted tape trail exhibit low inward velocity gradients, causing less heat transfer. The high heat transfer zones are also the ones that create more friction as seen by the wall shear stress contour.(Figure 58 (b)).

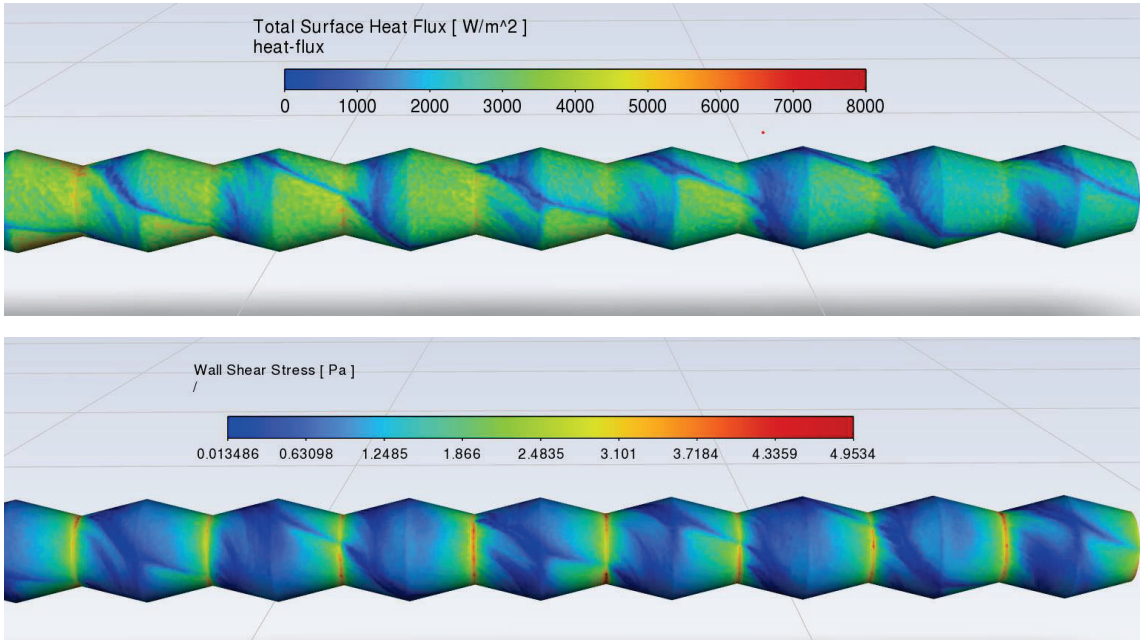

Figure 58: *Contour plots of wall fluxes in the external corrugated wall. a) Wall heat flux, b) Wall shear stress.*

Similar facts can be observed along longitudinal slices of the geometry (Figure 59). Temperature contours show more clearly how as the flow is induced in a clockwise rotation by the twisted tape, behind its trail there are high temperature zones of non-mixed fluid. This is also since these zones exhibit recirculation zones where the flow stagnates and/or changes direction (Figure 60).

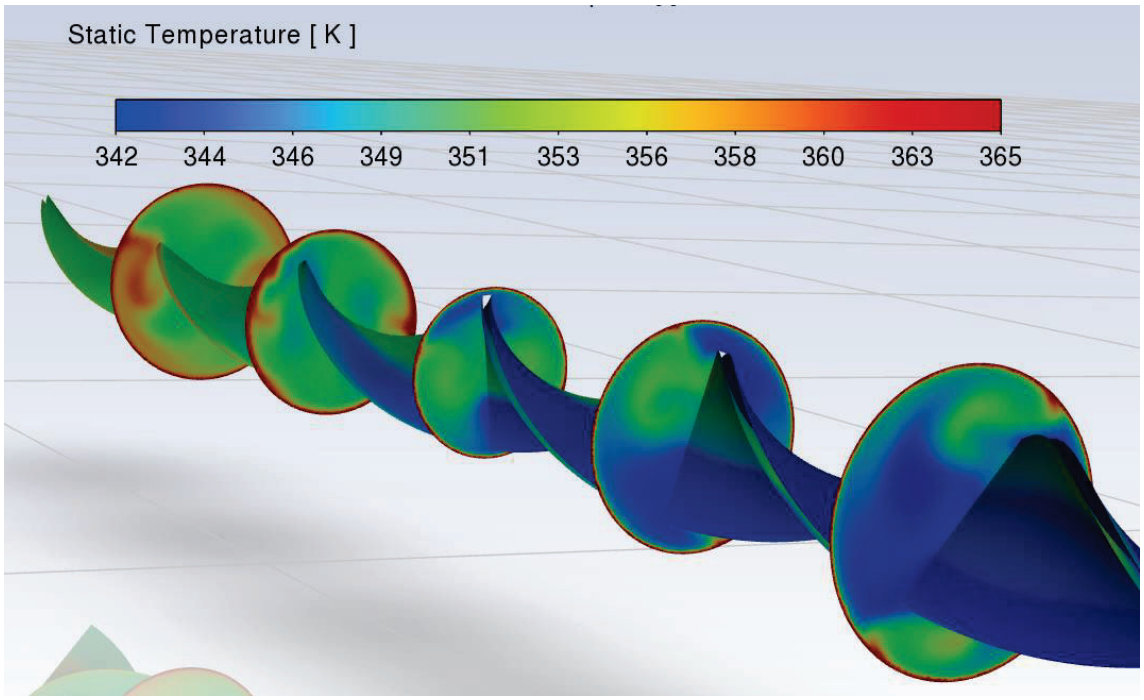

Figure 59: *Contours of temperature in the vicinity of the twisted tape and at various planes.*

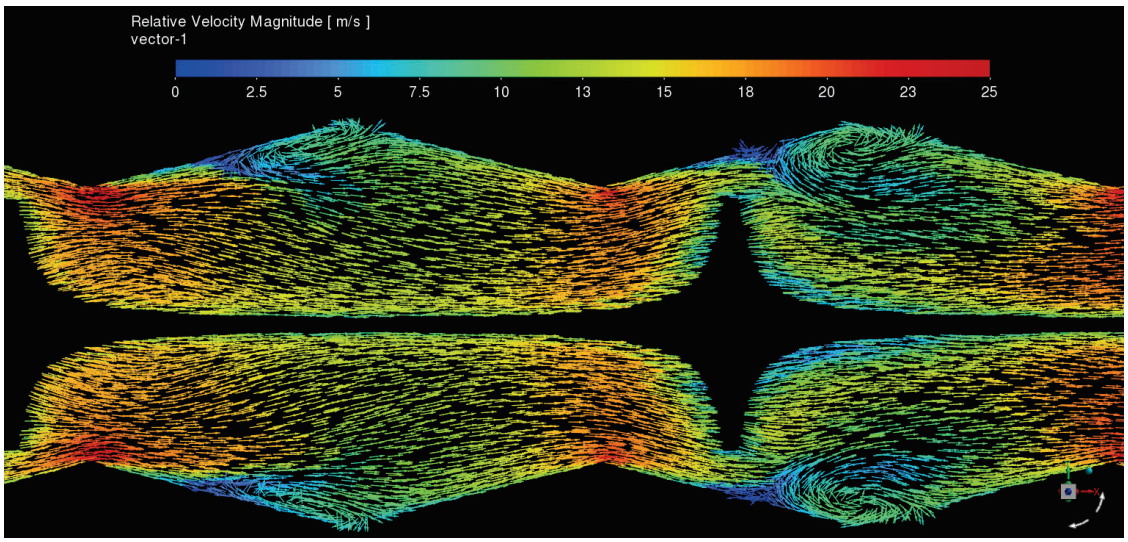

Figure 60: *Vector plot of the velocity across a plane coaxial with the streamflow.*

This also corresponds to the presence of low velocity zones behind the path of the twisted tape, which are most notable when the twisted tape passes through a crest (Figure 61 a & b). At flow passing through a crest two swirls can be observed at both sides of the twisted tape, which in these Figure rotates clockwise with flow direction. These two vortices form behind the tip of the twisted tape. When analysing the same contour for the valleys of the corrugation, the fact that the velocity turns more uniform can observed. It can also be noted that the two vortices are now formed at the sides of the twisted tape and rotate in the same direction of the fluid and the twisted tape, clockwise (Figure 61 b & d).

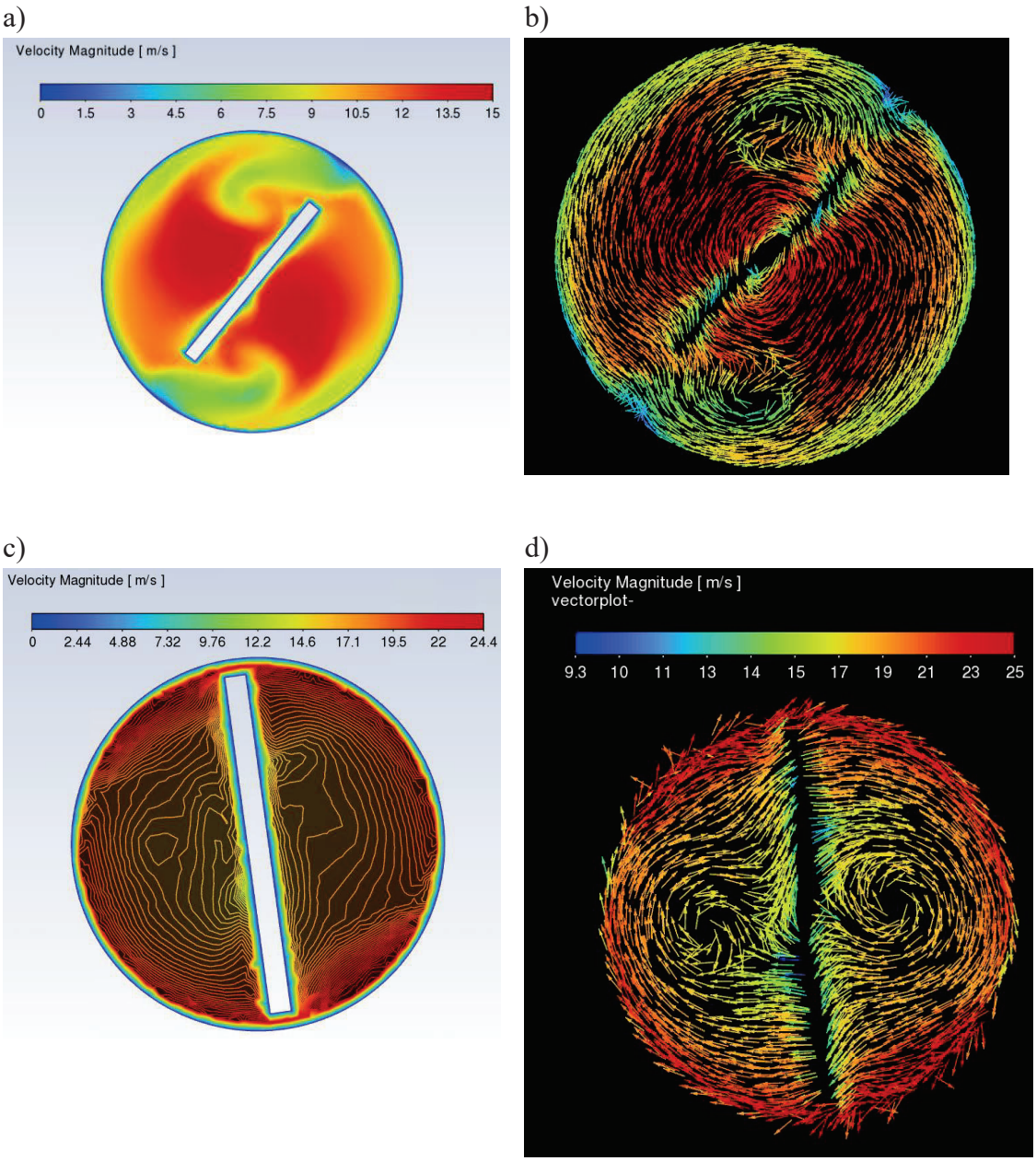

Figure 61: *Contours and vectorplots of different crossectional cuts of the corrugated tube. a) Contourplot of velocity magnitude at a crest. b) Vectorplot of velocity at crest. c) Contourplot of velocity magnitude at a valley. d) Vectorplot of velocity at valley.*

5.4. Concluding remarks

CFD turbulent models have been used and compared against empirical correlations for simple heat exchangers and twisted tape inserted heat exchangers. Results show great accuracy of the different models tested.

In the case of simple heat exchangers, the k-ε Standard gave best results both for pressure drop and heat transfer estimation, where the error with respect to mean correlation value

was of 9.8%. Moreover, when estimating pressure drop, the different turbulent models presented less discrepancy between themselves than the empirical correlations used.

When studying the tubes with twisted tape inserts, discrepancies between semi-empirical correlations and CFD become slightly larger. The k-ε wall treatments that have provided more accurate results when compared against experimental correlations are EWT and ML, both giving similar results. ML wall treatment is the method that comparatively produces less discrepancies with experimental, with an average deviation that ranges from 15% to 18% depending on the comparation method. The SST model is also a solid option with a deviation ranging from 17% to 20%. k-ω models prove to be accurate at predicting pressure loss and capturing important fluid features, especially k-ω SST. At different geometrical environments some models perform better than others. When *Re* are low and the swirl motion is more relevant ML and k-ω SST models provide more accurate results. k-ω's accuracy diminished at high TR, where shear flows are more dominant. Some model's accuracy increases with the Reynolds number, as it is the case with k-ω SST model, so for $Re>17{,}000$ and $TR\leq 4$, k-ω SST models are advised. Otherwise, in less extreme situations, any k-ε model with ML treatment will provide precise results.

Finally, now that the accuracy of the different models has been assessed, a novel geometry is optimized which combines corrugated tubes and twisted tapes, giving three dimensional parameters to optimize. Results are found at different Reynolds numbers with TPF being 1.50 at Re=16000, 1.43 at Re=24000 and 1.27 at Re=42000. These values would be greater if accounting for the increase in heat transfer area of the tube (Eq. 84): 2.23 at Re=16000, 2.2 at Re=24000 and 1.99 at Re=42000. Different points found allow for variability between greater heat exchange or lesser pressure drop depending on the case. The amount of transferred heat is found to be increased by 567.8% in the case of the optimal point at Re=24000. These results are very promising, and although they must be experimentally validated, they show the capabilities of CFD when optimizing geometrical problems. Complex flow interactions between the corrugation and the twisted tapes are observed and further deep study is required to understand the relationships between the different parameters at the optimal points.

6. CFD applied to pollutant dispersion study

The results obtained on the study of pollutant dispersion are presented in the following section. A deep effort is taken to validate the CFD codes and compare them to other commercial tools and methods for dispersion modelling. This comparison is performed both for plain and irregular terrains. Moreover, correlations are provided for the correct design of chimneys that ensures minimal impact on human populations.

6.1. Comparison against experimental data

The Prairie Grass Project sampling arrays are made up of five concentric arcs located 50, 100, 200, 400, and 800 m downwind of the release. The 180-degree arcs are centred on the release and positioned in the direction of the predominant air velocity. The measurements are taken at a height of 1.5 m. There is also a vertical sampling array providing measurements at nine heights at the 100-m arc: 0.5, 1.0, 1.5, 2.5, 4.5, 7.5, 10.5, 13.5, and 17.5 m. A total of seventy experiments are performed in Prairie Grass Project, with flow rates between 50 and 100 g/s (Morton L. Barad, 1958). Sulphur dioxide, SO2, is employed as a tracer. The release pipe has a diameter of two inches (5.08 cm) and a slight right-angle bend at the top to facilitate a horizontal release. The height of the release was 0.46 m for all experiments (Table 12). As in any empirical experiment, some incidents occur, and they are listed in the Prairie Grass Project volumes. For example, the gas rate release varied over 50 % of the average rate in run n˚ 47. Olesen et al. (2007) categorizes the data to be eliminated since they are highly likely to include anomalies. Similarly, this sort of experiment, as well as those with a 1.5 m release height, will not be studied. A total of 19 experiments have been selected to be simulated with ANSYS Fluent®, the Gaussian Plume Model (GPM), and ALOHA. Each of those experiments has different parameters that are considered in each simulation. Measurements are made at the same point as in the experiments.

Figures 62 and 63 show how concentration changes with distance and height, using data point 61 (annex 2) as an example. The different model profiles mimic the experimental concentration distribution pattern. ALOHA only provides results at the floor level and therefore is not included in Figure 63. The density of the pure SO_2 emission is 2.60 kg/m^3 that corresponds to its initial emitted concentration. In contrast to other programs, CFD maximizes its benefits close to the emission source and provides a good description of the dispersion in its initial meters.

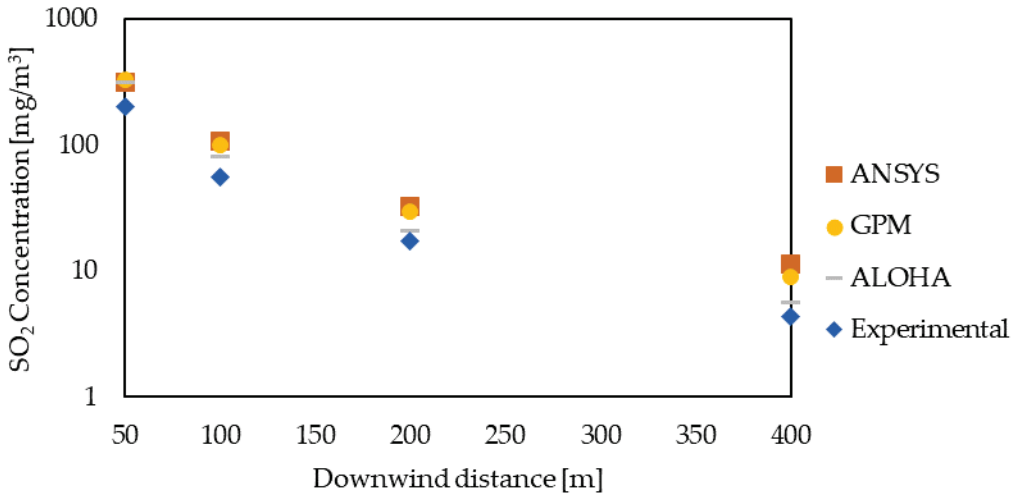

Figure 62: *Data 61 – Sulphur dioxide concentration distribution downwind at 1.5 m high*

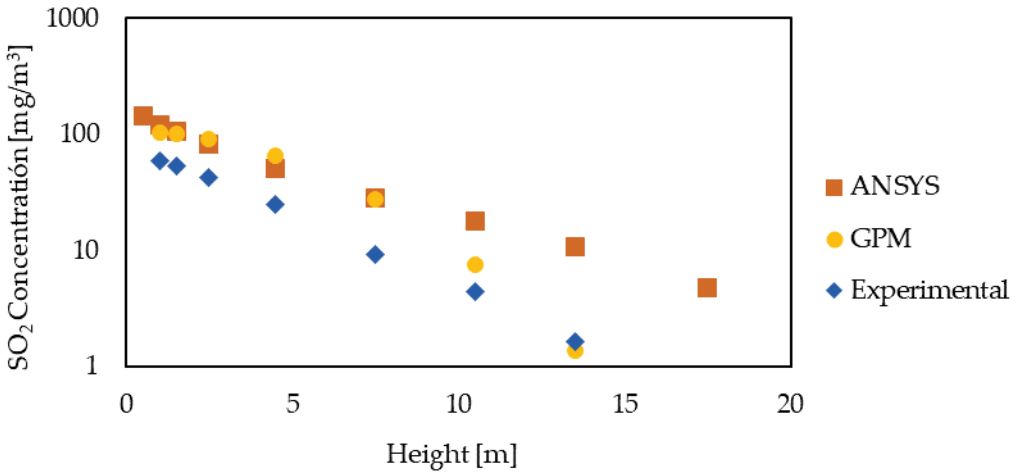

Figure 63. *Data 61 – Sulphur dioxide concentration height distribution at 100 m distance*

In both figures GPM and CFD values are higher than experimental. Simulation results being higher than experimental is a common thing. In the research performed by Habib et al. (2014) similar overestimations are found when comparing CFD (performed with CFX), AUSTAL2000 and the Prairie Grass Project. They found also that models based on Lagrangian methods can even be more precise than CFD for simple geometry cases. Their research studied concentrations at different distances downwind, and some of the overestimations or underestimations are often due to wind change in direction, which are not always possible to reproduce in the simulation domains. The present study focuses on steady state runs, as no transient data is available from the experiments reproduced. Therefore, those changes in wind direction are not considered. Such changes will have even more impact in the vertical dispersion comparisons present in this study.

ANSYS Fluent® has the benefit of easily visualizing the dispersion phenomena. Planes, lines, or points can be generated across the domain to represent the required variables using various sorts of graphics and charts.

Although each case can be examined individually, the model performance is more clearly demonstrated when all simulation results are seen together. The simulation concentration is represented in relation to the experimental concentration. Figures 64-65 plot the downwind results of ANSYS Fluent®, GPM, and ALOHA, respectively.

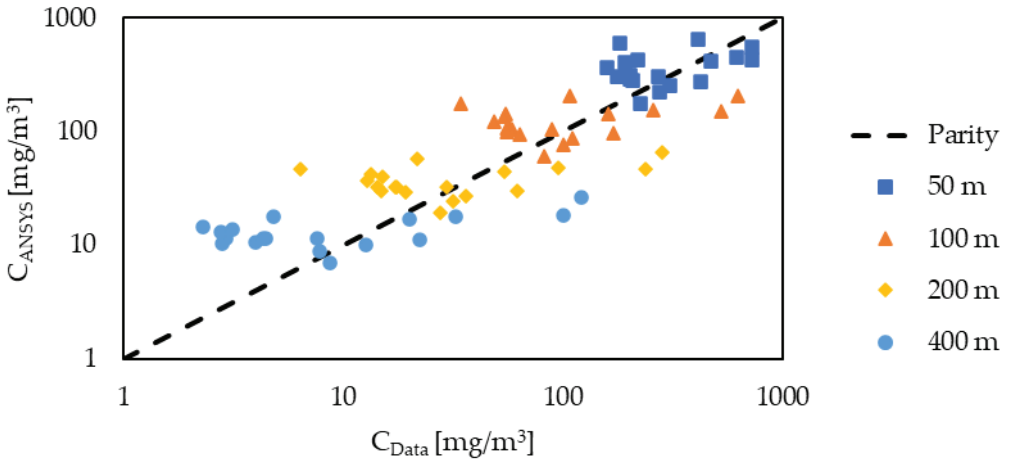

Figure 64: *ANSYS Fluent® findings at different downwind distances in relation to experimental data.*

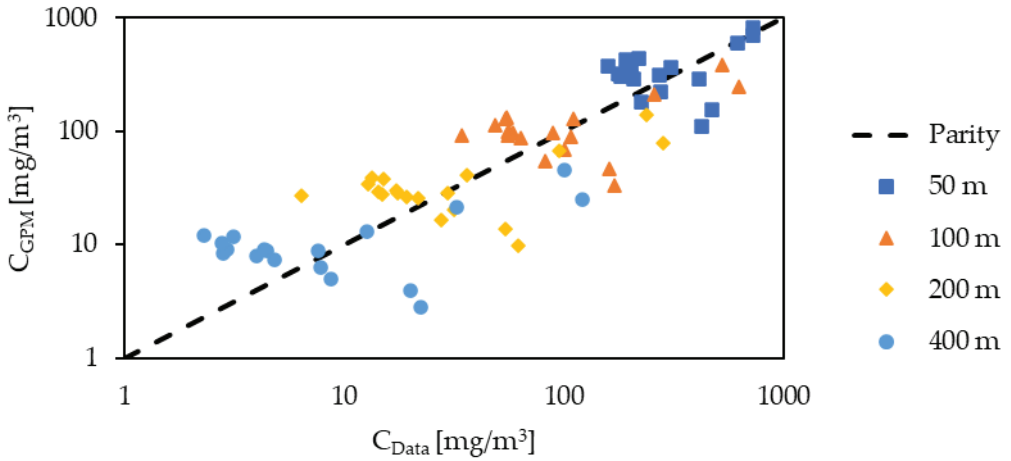

Figure 65. *Gaussian Plume Model downwind findings in relation to experimental data*

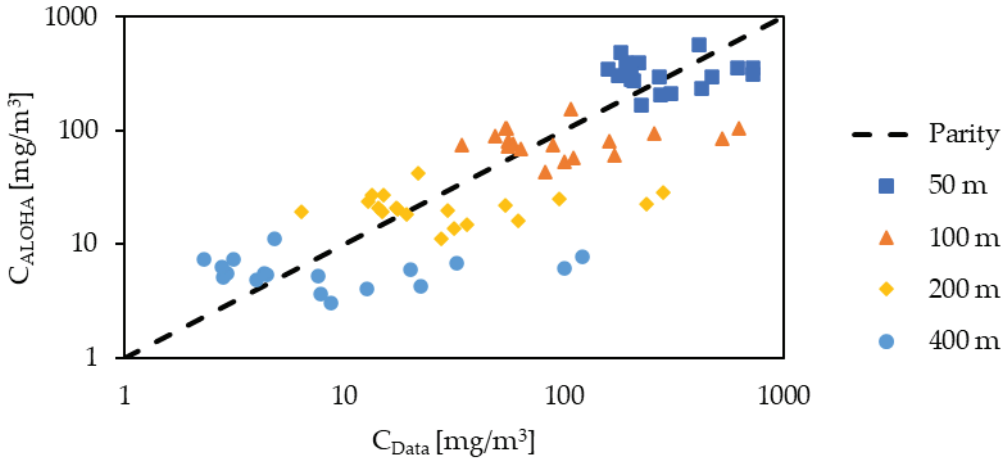

Figure 66: *ALOHA findings in relation to experimental data, downwind dispersion*

The downwind concentration points of ANSYS Fluent® and GPM are seen to be positioned around the parity line, and visually, the points might be regarded as being evenly dispersed above and below it. In the case of ALOHA, it seems to return slightly lower results than expected. Despite this, the discrepancy between the actual and predicted values in all models is rather large. It is usual to see readings that are twice or half, with maximum absolute error for all cases and models around 400 mg/m^3 at 50 m. When the measurements are taken diluted away from the release point, this value decreases steadily, reaching 55 mg/m^3 at 400 m.

A tendency to overestimate is evident in the ANSYS Fluent® vertical dispersion- Furthermore, because the values decrease with height, a "little" variation in a tiny concentration value reflects a very significant relative difference. The mean absolute error with respect to experimental values (MAE) considering all the measurements at different heights are 44.4 mg/m^3 for ANSYS Fluent® and 30.3 mg/m^3 for GPM. As the height increases, the system experiences more turbulence-inducing behaviours that have not been characterized, such as lateral air current entries. These promote contaminant dispersion, and the lack of dispersion found in the simulations is most likely owed to this. Nevertheless, these discrepancies are not very relevant because such low amounts generally do not represent a risk to human health. At lower heights, the Gaussian model's concentration predictions usually generate "slight" overestimations (Figure 68). With rising height, there is a trend towards less exact values. The results at the highest elevation (17.5 m) show a significant underestimation. Determining the concentration at high altitudes seems problematic for both ANSYS Fluent® and GPM, although the response is not the same. ALOHA only estimates concentration at ground level, hence vertical dispersion data is unavailable.

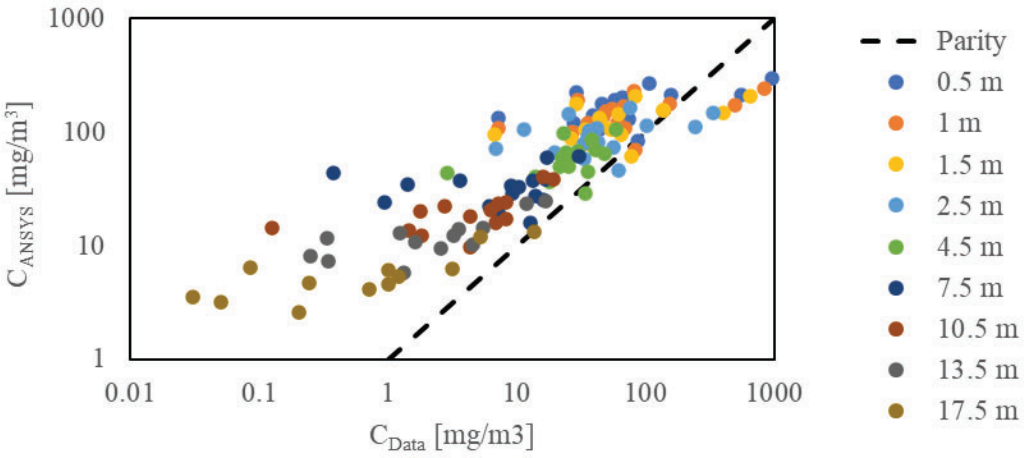

Figure 67: *Vertical dispersion results in ANSYS Fluent®*

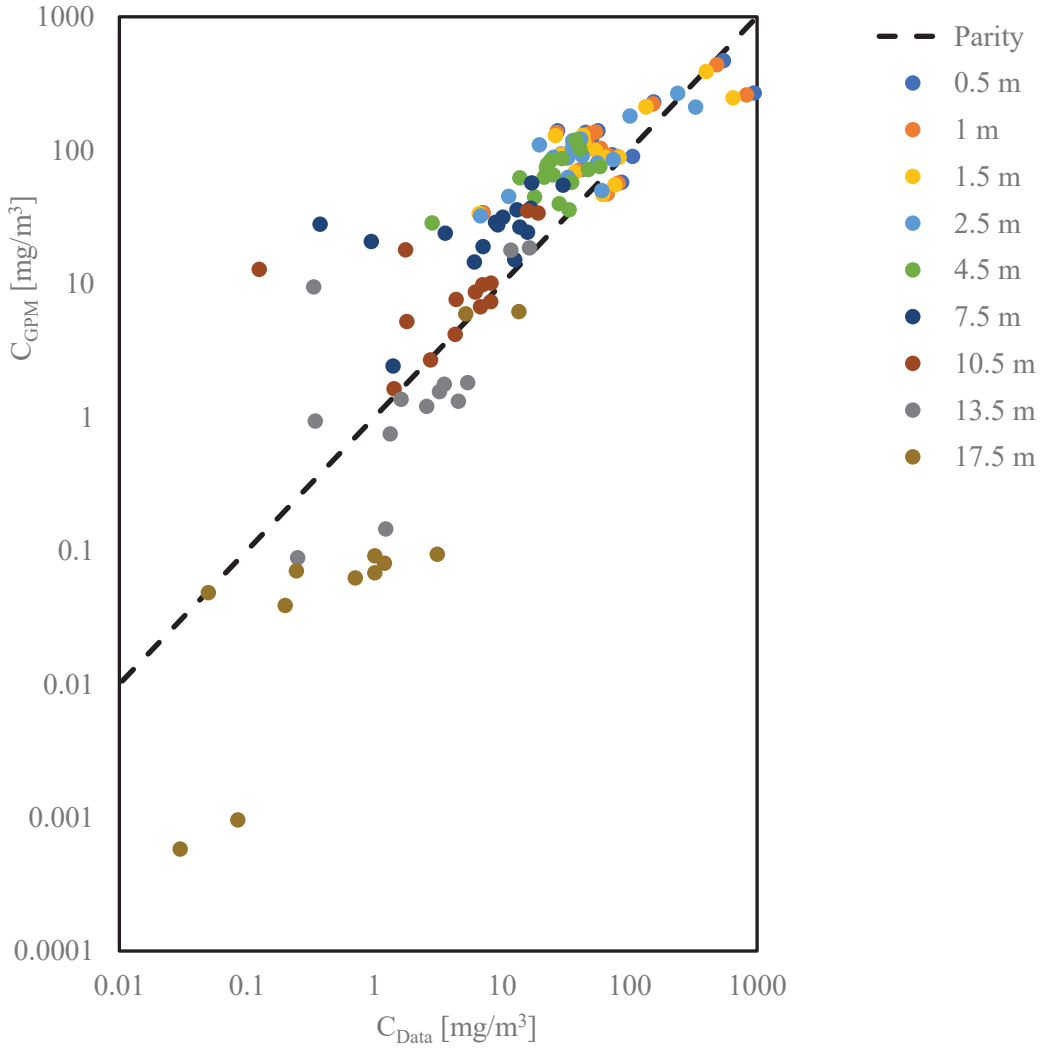

Figure 68: *GPM outcomes at different heights*

As these studies are often conducted to investigate potential health impacts, it is preferable to overstate reality, as in ANSYS Fluent®, than to underestimate it, as in the

GPM. Olesen et al. (2007) results also show an overestimation in OML and AERMOD models, especially when the wind velocities are very low. This trend is more accentuated in the AERMOD model. By cons, the values for the mean concentration profiles are underestimated in the CFD Trindade da Silva et al. (2021) study. Despite the possible deviations, CFD adjusts well to reality. This allows the study of more complex situations that cannot be studied with the other models due to their limitations. It must also be considered that these results are obtained at constant wind speed and direction, which for point taken downwind from the source, would justify the overestimation. Experimental conditions present in the Prairie Grass project (Barad M. L., 1958) have more or less experienced these kinds of changes in wind speed and direction which directly reduce the concentration lecture in the measurements downwind.

6.2. Model comparison

The ANSYS Fluent® results at 50 m are quite similar to ALOHA with GPM exhibiting less data dispersion (Figure 69). Despite this, the mean concentration variation across models is relatively close: MAE (Mean Absolute Error) values for ANSYS Fluent® and ALOHA exhibit a similar deviance from experimental (MAE_ANSYS = 150 mg/m^3, MAE_ALOHA = 167 mg/m^3). And GPM produce more accurate results in the emission vicinity (MAE_GPM = 108 mg/m^3). The concentration distribution representations are identical at 100 m. One difference is that the ALOHA model has a larger interquartile range, indicating that the data are less densely clustered.

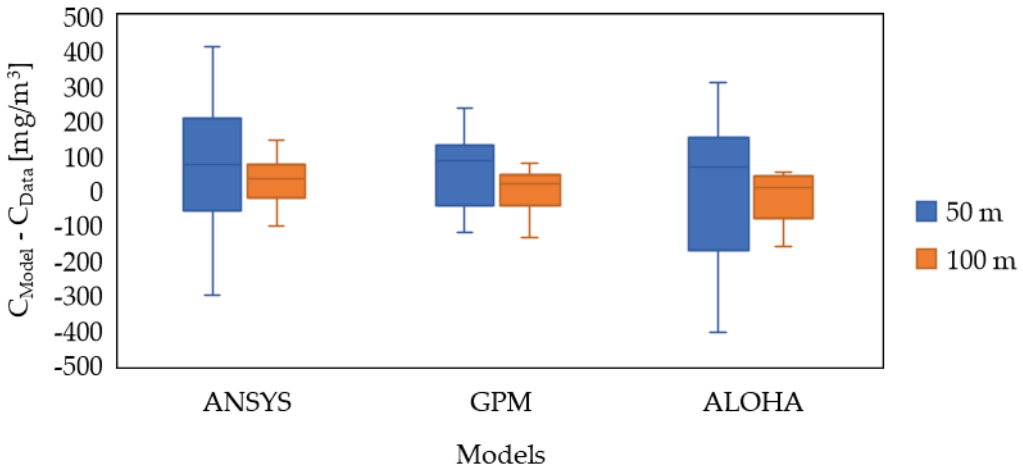

Figure 69: *A Box-and-whisker diagram for concentrations at 50 and 100 m downwind*

The extreme values achieved with the three models at 200 m are comparable, being most of them between ± 40 mg/m^3 (Figure 66). ALOHA yields the lowest values (60 mg/m^3). Similar results are observed at 400 m. The 400-m ANSYS Fluent® MAE value is between those from GPM (MAE_GPM= 9.4 mg/m^3) and ALOHA (MAE_ALOHA= 6.5 mg/m^3).

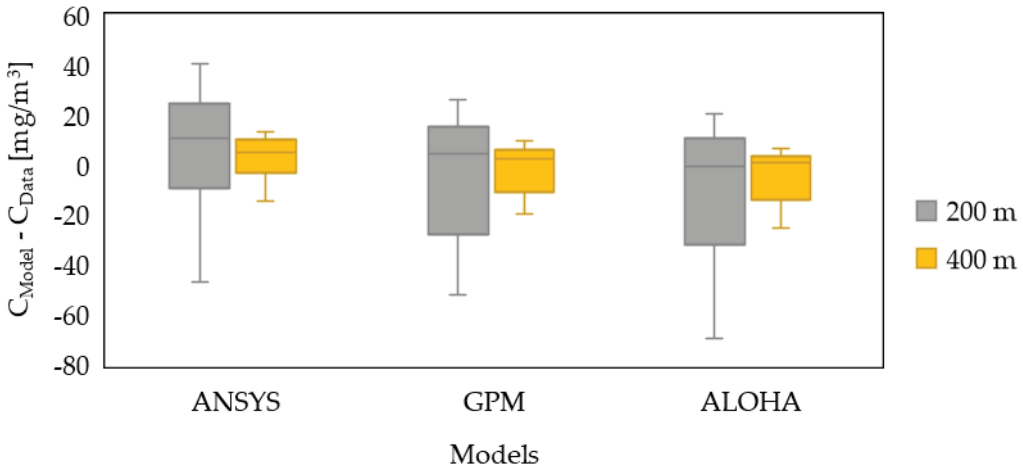

Figure 70: *Box-and-whisker diagram for 200 and 400 m downwind concentrations*

The overall MAE for downwind dispersion is 55.8 mg/m^3 for ANSYS Fluent® that is between ALOHA and GPM (47.7 mg/m^3 and 59.9 mg/m^3, respectively).

The horizontal dispersion (measured at 1.5 m height) does not correspond with the data at 1.5 m in the vertical dispersion evaluation. Samples are different. Those taken at different heights were much farther apart. To give an idea, there were 91 measurement points to evaluate the dispersion in the direction of the wind and only six towers to evaluate the vertical dispersion. As a result, the forecast of the outcome at 1.5 m height in vertical dispersion is less accurate than that from the downwind dispersion because the experimental value is also less accurate. Despite this, it is still useful to compare the models.

Even though the range of values across the models are similar (Figure 71), those provided by ANSYS Fluent® are frequently greater than zero. This suggests an overestimation. Similar phenomena happen with the GPM model at heights of 4.5 m or 7.5 m, it corrects this trend and gets closer to the empirical data at heights over 13 m (Figure 72).

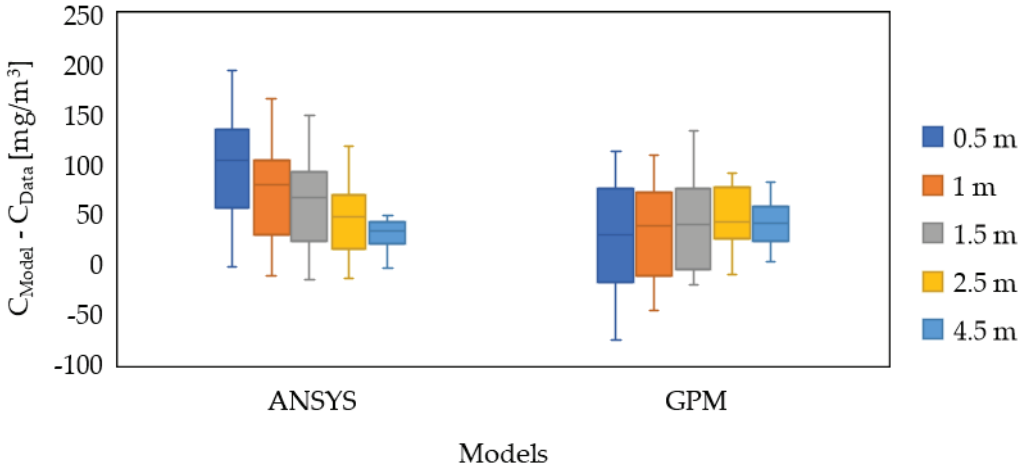

Figure 71: *Box-and-whisker diagram for heights less than 5 m*

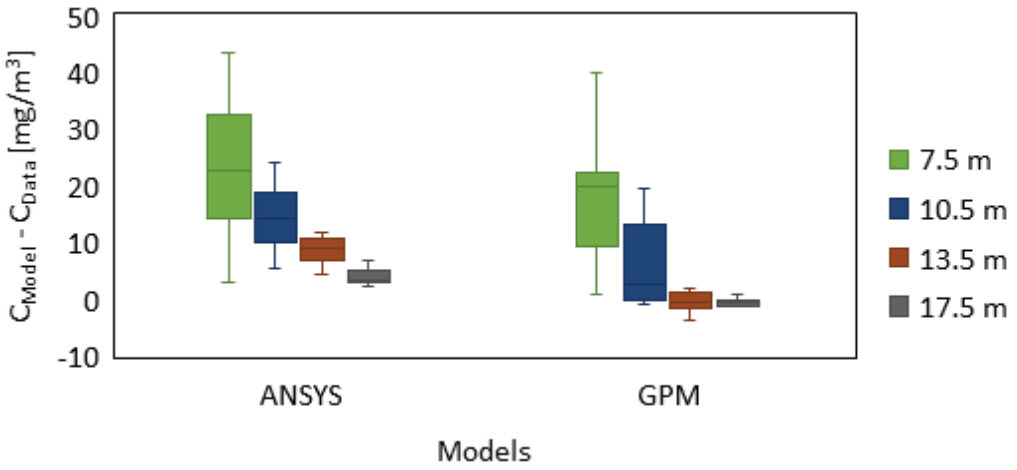

Figure 72: *Box-and-whisker diagram for heights from 7.5 m to 17.5 m*

The average absolute error of ANSYS Fluent® in the vertical dispersion is always higher than GPM. Nevertheless, the MAE values are quite similar, excluding the two last heights. The mean value for all height points is similar: 44.4 mg/m^3 for ANSYS Fluent® and 30.3 mg/m^3 for GPM. The relevant values that have been presented in the previous figures are provided in Annex 2.

6.3. Obstacle dispersion comparison

The simulations performed in this chapter are described in chapter 4.2.6. The geometry consists of a various rows of buildings of 10 m height. The simulation results display a deflection of the pollutant in the first layer of buildings which decreases considerably the concentration of SO_2 at ground level. Figure 73 depicts this phenomenon, showcasing in red 78 mg/m^3 which is equivalent to 30 ppm a value considered of high risk by the AEGL-3 (National Research Council (US) Committee on Acute Exposure Guideline Levels, 2010). The low (AEGL-1) 0.52 mg/m^3 concentrations correspond to 0.2 ppm, a concentration that does not seem to have immediate risks to human health (Instituto Nacional de Seguridad e Salud en el Trabajo (INSST), 2014).

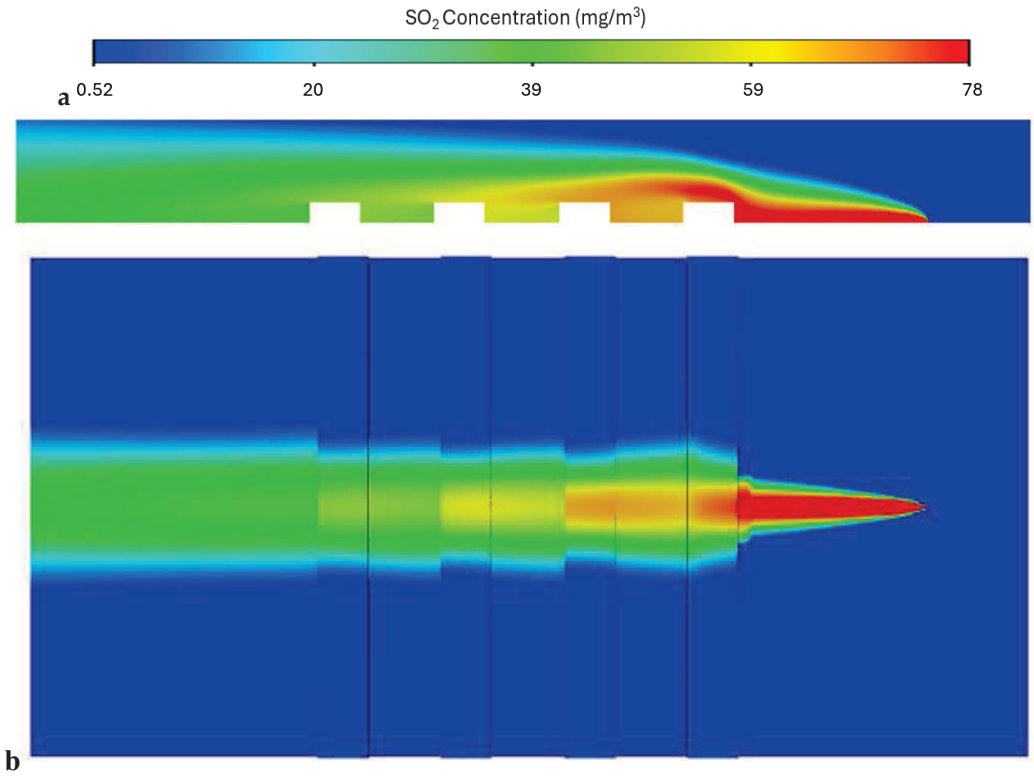

Figure 73: *Simulation results of an emission with obstacles, side view and top view*

Comparison between the various methods is shown in Figure 74, where the different models are compared between themselves. Until the first obstacle is encountered, the CFD concentration is between Heavy gas and Gaussian models, as it has a moderate molecular weight. Once the first obstacle is encountered, the CFD concentration resembles the one seen in Gaussian modelling. Zones where Gaussian and CFD differ are found just after each of the first obstacles, as CFD displays a clear decrease in concentration around 125 and 175 m. This is due to the fact that in CFD velocity and turbulence carry the pollutants around, while Aloha does not take into account those changes in speed and turbulence induced by the obstacles. It is also important to note the concentration at 10 m, that is, at the top of the buildings, which is higher than the one on the ground when the air passes over the obstacles. These obstacles act as a protection that decreases ground level pollution but when the presence of obstacles ceases the ground concentration returns to being higher than the one at 10 m. It can be concluded that Aloha and CFD can both give similar overall results but when the interest is in zones near abrupt geometries, CFD describes better the concentration distributions.

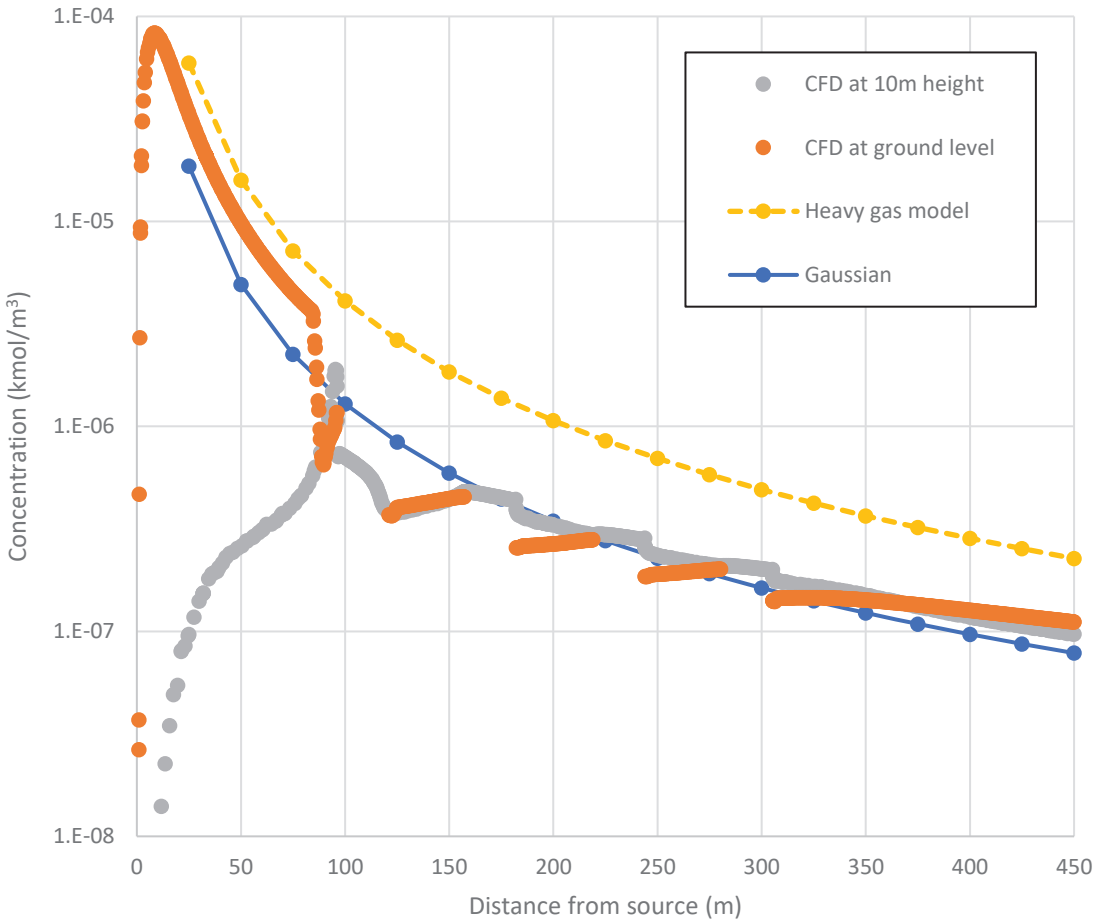

Figure 74: *Comparison between different Aloha models and CFD at different heights*

6.4. Worst case scenario assessment

In most practical design cases, the simplicity of tabulated values or semiempirical correlations is preferred by researchers. When designing a flue, various factors such as maximum concentration in the ground, wind speed, downwind distance from source of populated areas are to be taken into account. By using the GPM described earlier, a series of relationships have been developed to help and assist in such design problems. Emission is assumed at a certain flue height and the maximum pollutant concentration that reaches ground and its location are calculated for a large number of cases. The most hazardous case is considered at 1.7m above ground, the average height of a human. Equations are then fitted to make relationships between variables and the desired column height. Concentration is written in the form of $\frac{C\,v_w}{w}$ (m^{-2}), concentration times wind speed over emission rate.

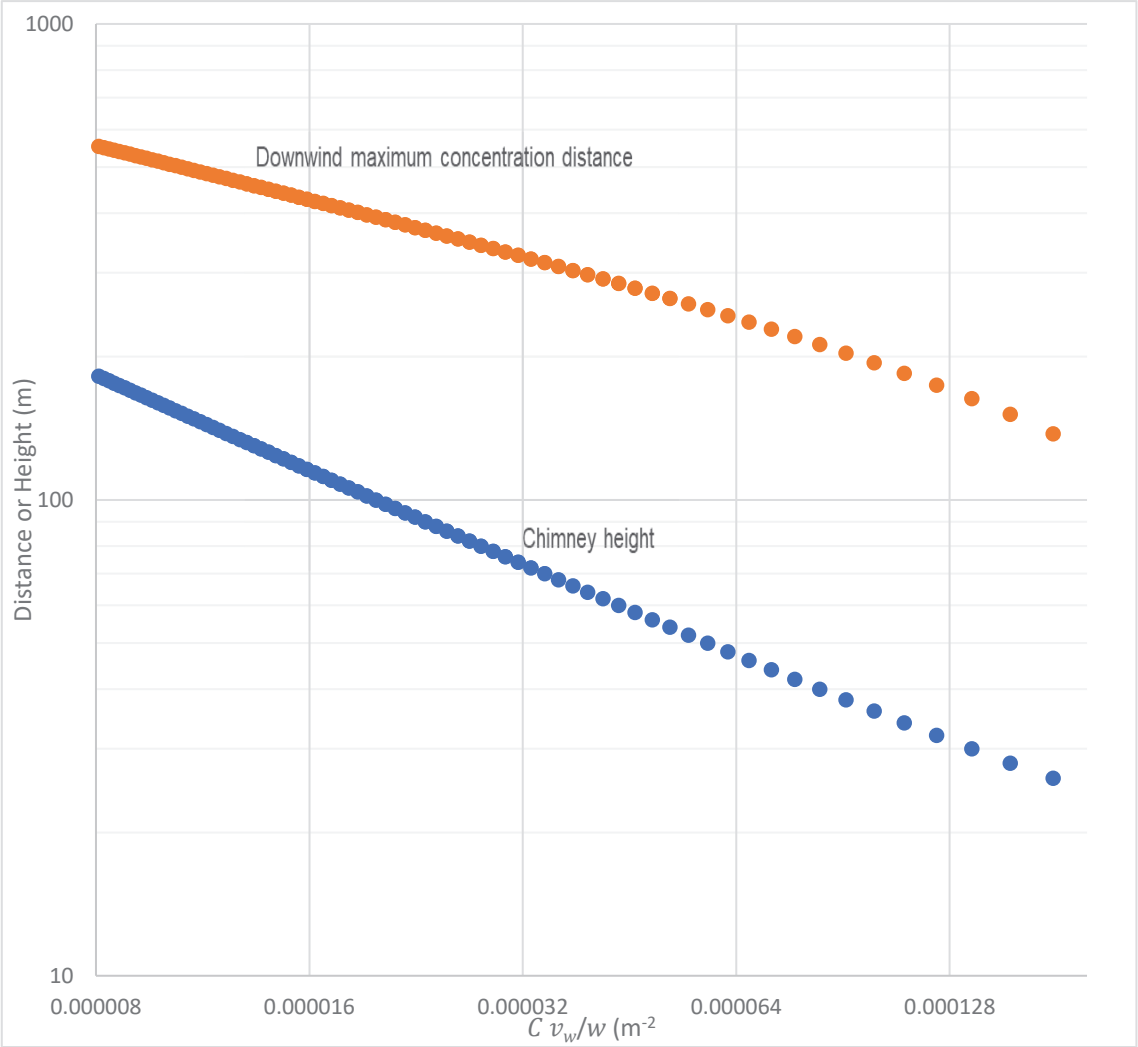

Figure 75: *Pollutant emission height and downwind maximum concentration distance as a function of maximum concentration allowed at 1.7 m height*

The equations fitted from the correlation seen in Figure 75 are, Eq. 85:

$$h = 0.1124x^{-0.628} \text{ with } R^2 = 0.99 \quad (85)$$

Where h is the emission height and x, Eq. 86.

$$x = \frac{C\ v_w}{w}\ (m^{-2}) \quad (86)$$

With C being the maximum allowable concentration, v_w the wind speed of the studied case and w the emission flow rate.

$d = 2.9646x^{-0.45}$ with $R^2 = 0.99$ (7)

Where d is the distance for which the concentration at 1.7m height is maximal.

The proper way to use these correlations is by first estimating the average wind speed of the environment and the mass flow that will be emitted. Then, from the nature of the pollutant the maximum allowable concentration can be found in literature or estimated with safety parameters. These input values can be for example a wind speed of 5 m/s, 100

g/s of mass flow of emission and assuming a maximum allowable SO_2 concentration of 0.2 ppm or 5.64 $\times 10^{-4}$ g/m^3 as found in the National Research Council (US) Committee on Acute Exposure Guideline Levels (2010).This totals to a x value of 2.82 $\times 10^{-5}$ m^{-2}. With that, the emissor height required to not surpass such concentration in 1.7m above ground can be found from equation 5 (blue line in Figure 75), resulting in 80.9 m high. Equation 6 (orange line in Figure 75) will then show where the zones are that will receive the maximum concentrations downwind from source, being at 330.6 m downwind from source. Figure 76 shows the comparison of the use of the suggested equations with Aloha. Note that the correlations are for a height of 1.7 m while Aloha estimates ground concentrations.

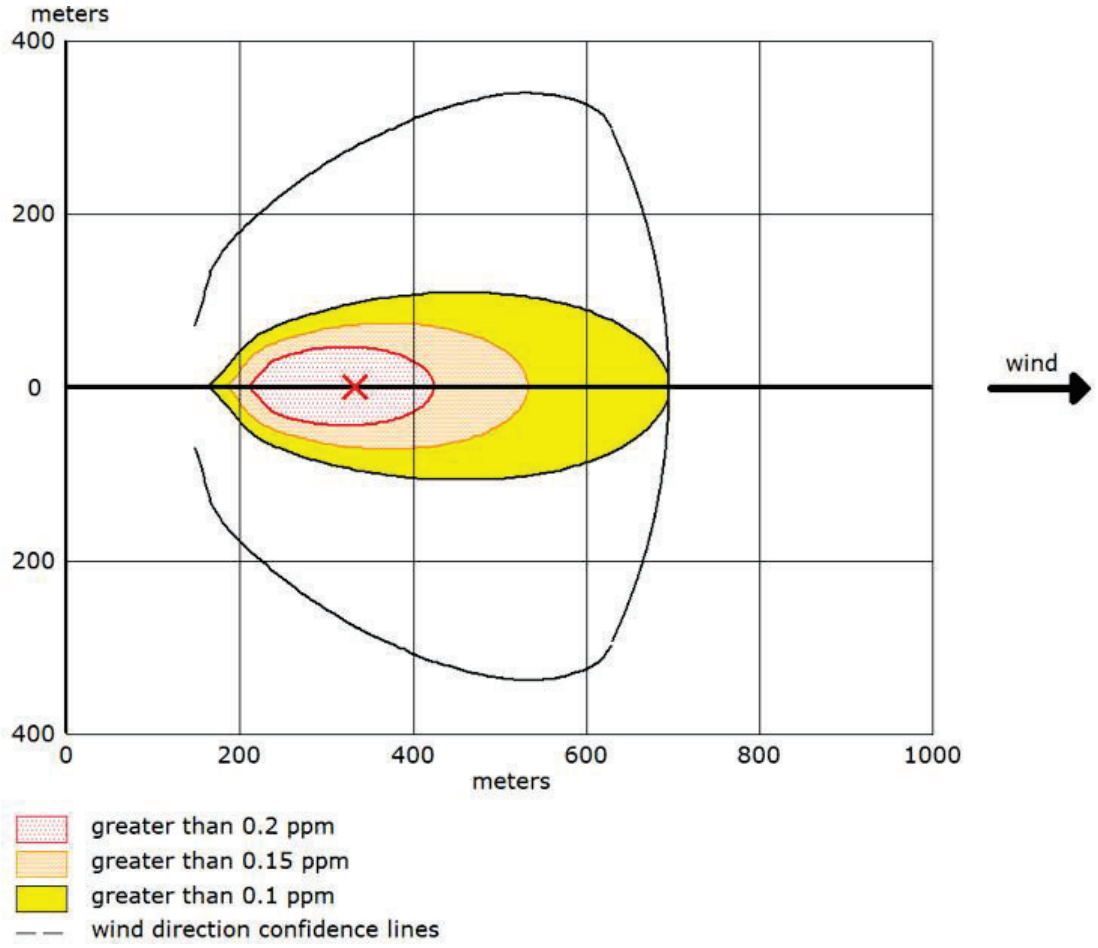

Figure 76: *Aloha simulation with the use of the worst-case scenario correlations. Red cross indicates where the found correlations predict the 0.2 ppm maximum concentration.*

Further research on this topic is being developed alongside CFD models to provide a wider range of "worst case scenario" calculations.

6.5. Concluding remarks

Accurate prediction of pollutants dispersion is essential to determining the impact on human health and ecosystems. SO_2, which is a pollutant generated by the combustion of sulfur-containing fuels, is used as a tracer in this research for comparing the dispersion results of different models: ALOHA, GPM, and CFD. Whereas the CFD advantages are

clearly seen near the emission source, in complex terrains, or in its capacity to consider pollutant reaction, the Prairie Grass scenario measures concentrations up to 800 m away from the emission source; the emission is done in a pretty flat open terrain; and uses a low reactive pollutant. So, it may be said that this studied scenario “benefits” GPM and ALOHA. Moreover, the GPM used Prairie Grass experiments to fit this model; ALOHA works well at distances up to 2 km, and both are unable to introduce pollutant reactions. Despite that, the results show that CFD is a valuable tool for emission analysis, performing comparably to established models like GPM and ALOHA, while offering greater versatility across a wider range of scenarios.

When comparing the models, the CFD (ANSYS Fluent®) shows a similar accuracy as GPM and ALOHA for downwind dispersion predictions, but CFD overestimates concentrations for vertical dispersion. Interestingly, GPM occasionally displayed similar overestimation tendencies, which may validate the correct configuration of our CFD model for predicting atmospheric gas dispersion in open terrain. Despite that, it must be considered that the domain's high may not be sufficient to ensure that no pollutants are accumulating. This might result in greater concentration values and make vertical dispersion challenging. Another possibility is that the lack of data results in an inaccurate representation of the atmospheric conditions, reducing vertical dispersion. CFD predictions are expected to be improved with a clear and wide atmospheric database throughout the emission, being able to reproduce the real-world atmospheric conditions that affect dispersion.

In terms of the time needed to obtain the results, this CFD setup took roughly six hours to compute, whereas GPM or ALOHA just took a few minutes. So, just looking at the required time, GPM or ALOHA are better for basic cases and in those situations where you are running out of time, e.g., emergencies. Otherwise, CFD has the potential to adapt itself to a particular scenario: terrain, obstacles, substance, or reaction, as clearly seen in the obstacle presence case. The study contributes to stablish the reliability on the prediction and risk evaluation of gas leakage accidents using the different methods available. Such design can be performed with the worst scenario equations provided that calculates at which distance is achieved the highest concentration and at which dilution, obtained from GPM models.

7. Stirred tank simulation results

In the first two sections the following stirred tank curves are displayed: NP vs. Re, Cf vs. Re and δ/D vs. Re. The aim is to evaluate the effect of fluid viscosity on power consumption and two parameters that are directly related to convective heat transfer at the tank wall, namely the thickness of the laminar layer and the shear stress. A model is then fitted to the simulation data to obtain an empirical correlation useful for the operation of the stirred tank. By knowing the physical properties of the fluid in a process, it is possible to determine the required agitation speed for a specific power consumption or laminar layer thickness using the empirical correlations.

In the next two sections the same curves displayed in the previous sections for the different tested blade angles (0º, 15º, 45º, 60º, 75º, 90º) are shown and compared with the real tank configuration (30º). The objective is to determine how the blade angle affects power consumption and heat transfer at the wall. For each of these parameters, it is investigated whether radial flow (90º) or axial flow (0º) blades are optimal, or if the optimal configuration lies in a setup that offers a mixed flow between the two.

It is validated that the relationships between dimensionless numbers derived from dimensional analysis are held within the typical operating conditions of the tank, ensuring no relevant variable has been excluded during the analysis. Finally, the simulation results are also validated to ensure they correspond with the behaviour of the physical stirred tank, confirming that the CFD model is a good representation of reality.

7.1. Fluid viscosity effect

Various simulations are performed varying the viscosity of the fluid in a typical range found in polymerization reactors, while maintaining constant agitation speed. When studying polymerization reactors, the viscosity increases as the reaction evolves, while the agitation speed is set to be constant throughout the operation. The simulation results demonstrate that by maintaining the agitation speed constant up to a certain viscosity, the flow inside the tank is entirely turbulent and the power consumption remains constant (turbulent range). Beyond this viscosity threshold, the effects of transitional flow become significant and the consumed power increases with the fluid viscosity. Characteristic curve (Figure 77) shows the power number (N_P) as a function of the Reynolds number (Re). In the laminar flow area (Re <100), N_P decreases as Re increases, fitting a model of the form, Eq. 87:

$$N_P = a \cdot Re^b \tag{87}$$

where b is a negative coefficient. In the turbulent flow area (Re >10 000), N_P remains constant as Re increases, fitting a model of the form, Eq. 88:

$$N_P = A \tag{88}$$

In the transition flow area (100<Re<10 000), where flow can be either turbulent or laminar, a gradual transition occurs between the behaviour in the laminar regime and the turbulent regime.

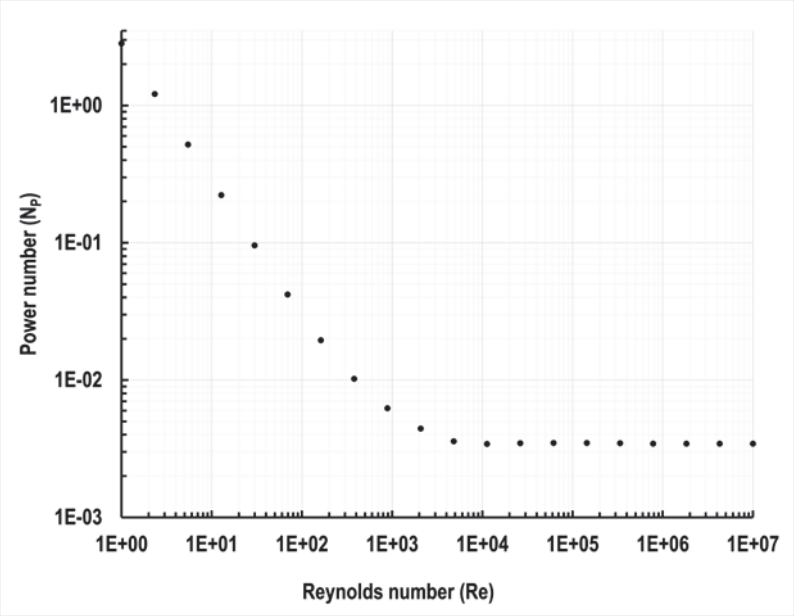

Figure 77: *Stirred tank reactor characteristic curve (N_P vs. Re)*

Accordingly, a candidate model that could fit the entire range of data is the following Eq. 89:

$$N_P = a + b \cdot Re^c \tag{89}$$

When fitting this model to the simulation data, the laminar and turbulent flow regions are well represented, but in the transitional is where the regression shows the poorest fit to the simulation data. The metrics used to evaluate the quality of the fits are the R-squared (R^2), the Mean Absolute Error (MAE) and the Mean Absolute Percentage Error (MAPE) Eqs. 90-92:

$$R^2 = 1 - \frac{\sum_{i=1}^{n}(y_i - \hat{y}_i)^2}{\sum_{i=1}^{n}(y_i - \bar{y})^2} \tag{90}$$

$$MAE = \frac{1}{n}\sum_{i=1}^{n}|y_i - \hat{y}_i| \tag{91}$$

$$MAPE = \frac{1}{n}\sum_{i=1}^{n}\left|\frac{y_i - \hat{y}_i}{y_i}\right| \cdot 100 \tag{92}$$

where y_i is the actual simulation value, $\hat{y}_i$ is the predicted value, $\bar{y}$ is the mean of the simulation values and n is the number of data points. Table 24 shows the coefficients, MAE, MAPE and R^2 of the fitted model.

Table 24: *Coefficients, MAE, MAPE and R^2 of the fitted models for N_P vs Re*

Model	Coefficients	MAE	MAPE (%)	R^2
(1) $N_P = a + b \cdot Re^c$	a = 0.00346 b = 2.82554 c =-1.00144	6.35E-04	3.02	0.99

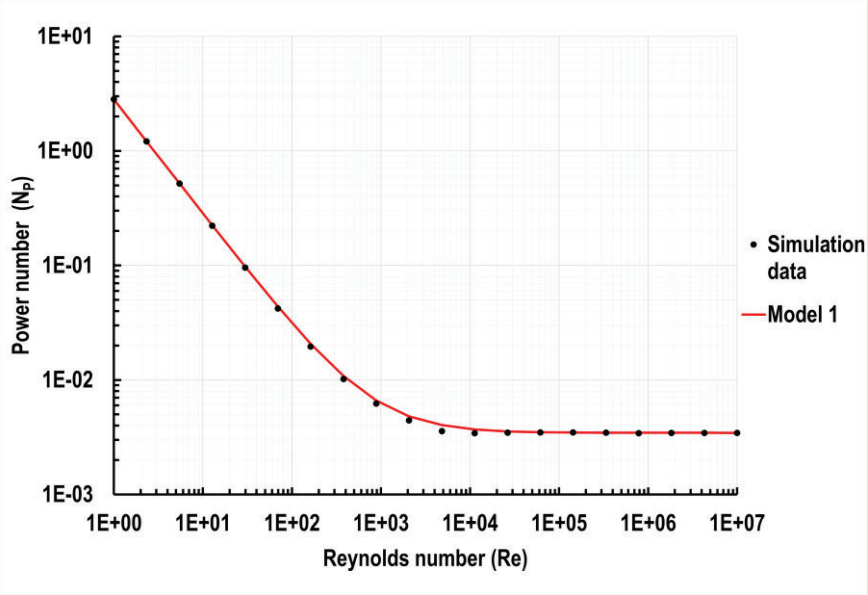

Figure 78: *Fit of Model 1 to N_P vs. Re simulation data*

Torque is primarily the result of the forces exerted by the fluid on the blades of the agitator, Eq. 93:

$$T = T_p + T_\tau \tag{93}$$

These forces can be decomposed into pressure forces (Eq. 94), which are normal to the blade surface, and viscous shear forces (Eq. 95), which are tangential to the blade surface.

$$T_p = \int p \cdot r \cdot dA \tag{94}$$

$$T_\tau = \int \tau \cdot r \cdot dA \tag{95}$$

Normal forces are visualized through pressure contours (Figure 79) and tangential forces are visualized through shear stress contours (Figure 80). The figures show how tangential forces and normal forces are distributed on the surface of the blades. The computed torque is the sum (integral) of all the individual force components acting on the impeller surface. Figures 79-80 allow for identification of the areas of the blade surface that encounter higher resistance and the areas that have a negligible contribution to the total torque. Reddish-orange colors represent zones of high pressure (3900-5000 Pa) and high shear stress (2400-3000 Pa), while bluish colors represent zones of low pressure (0-1500 Pa) and low shear stress (0-900 Pa). The rest of the colors represent average values between these two extremes.

Figure 79 shows that the areas of highest pressure are mainly concentrated at the tip of the blade. The upper surface of the inner part of the blades is inclined in the opposite direction to the tip, therefore it is not a direct contact surface, and it constitutes an area of

low pressure. Figure 80 shows that although areas of high shear stress are also predominantly located on the blade tip, the tangential forces are more evenly distributed over the entire surface of the blade compared to the normal forces. Comparing the two figures, it is also noted that the pressure exerted on the blades is of greater magnitude than the shear stresses.

Upon analysing all the contours with fluids of different viscosities simultaneously, when viscosity increases, the reddish surfaces of high pressure and high shear stress grow in size, leading to an overall increase in total torque. Although all contours belong to the transition flow regime (100 < Re < 10,000), it can be observed that as the flow regime becomes more turbulent (7000 cP and 3000 cP), the differences between the contours become less prominent.

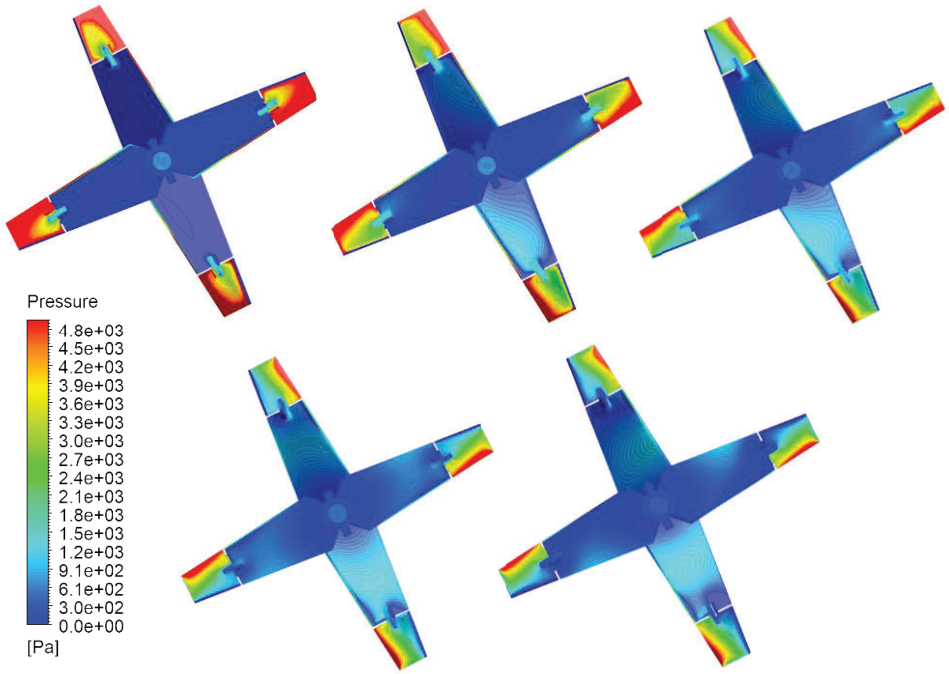

Figure 79: *Pressure [Pa] contours at 50 rpm and different fluid viscosities: 90000 cP, 39000 cP, 17000 cP, 7000 cP and 3000 cP*

Figure 81 shows that the relative thickness of the laminar layer at the tank wall (δ / D_{tank}) increases with the fluid viscosity (or decreases with Re). For viscous sublayer thicknesses greater than the tank radius ($\delta/D_{tank} > 0.71$) the entire fluid flow inside the tank is laminar. At this point ($\delta/D_{tank} = 0.71$), Reynolds number is approximately 100, which aligns with the theoretical boundary beyond which the flow regime shifts from transitional to fully laminar. Similarly, Figure 82 shows that the friction coefficient (Cf) increases with the fluid viscosity (or decreases with Re). This is because the friction coefficient on the wall is directly proportional to the shear stress, which in turn correlates with the viscosity of the fluid. Consequently, when comparing simulation results with different fluid viscosities, an increase in the wall shear stress does not lead to a higher velocity gradient along the tank wall and thus to an improved heat transfer; rather, it has the opposite effect.

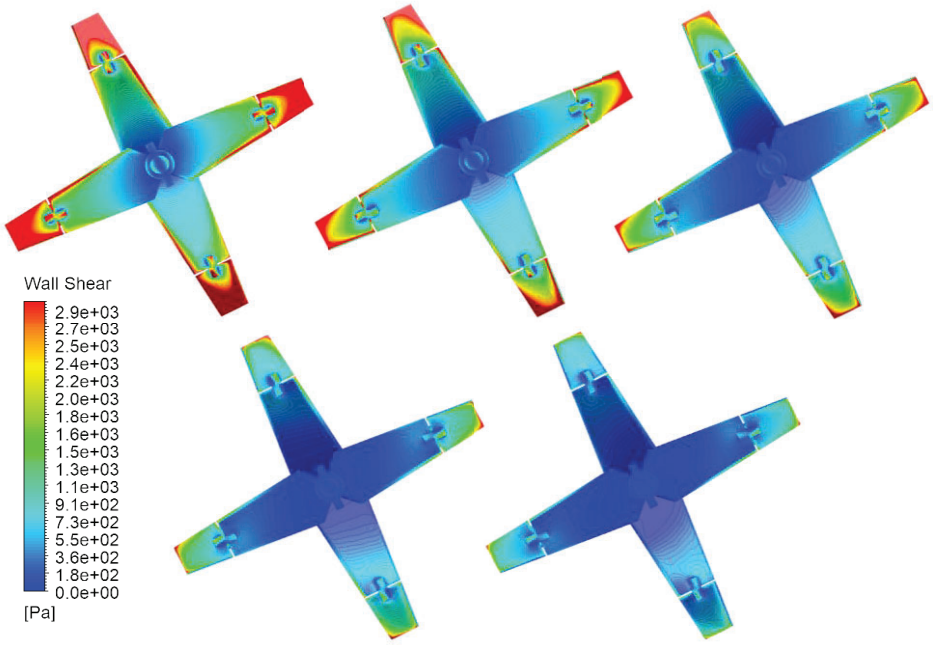

Figure 80: *Shear stress [Pa] contours at 50 rpm and different fluid viscosities: 90 000 cP, 39 000 cP, 17 000 cP, 7000 cP and 3000 cP*

As both dimensionless numbers (Re and δ/D) are directly related to convective heat transfer at the tank wall, the heat transfer coefficient decreases with the fluid viscosity. Since both dimensionless numbers are directly related to heat transfer at the wall, it can be affirmed that irrespective of the flow regime, the heat transfer coefficient decreases with fluid viscosity, this is usually the case since empirical correlations are of the form: $Nu \propto Re^a = (v\ D\ \rho/\mu)^a$, where a is some adjusted coefficient.

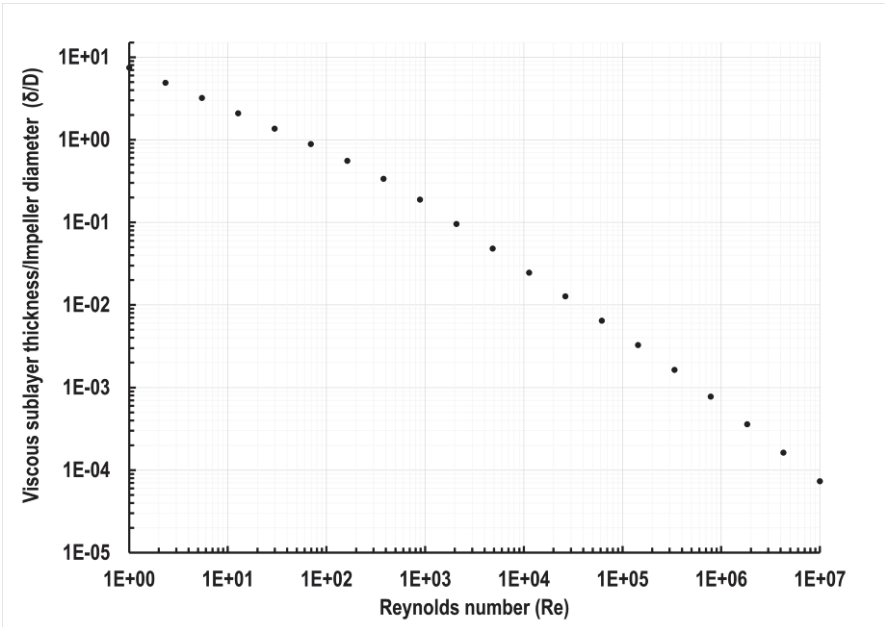

Figure 81: *Viscous sublayer thickness at the tank wall vs. Reynolds number (δ/D vs Re)*

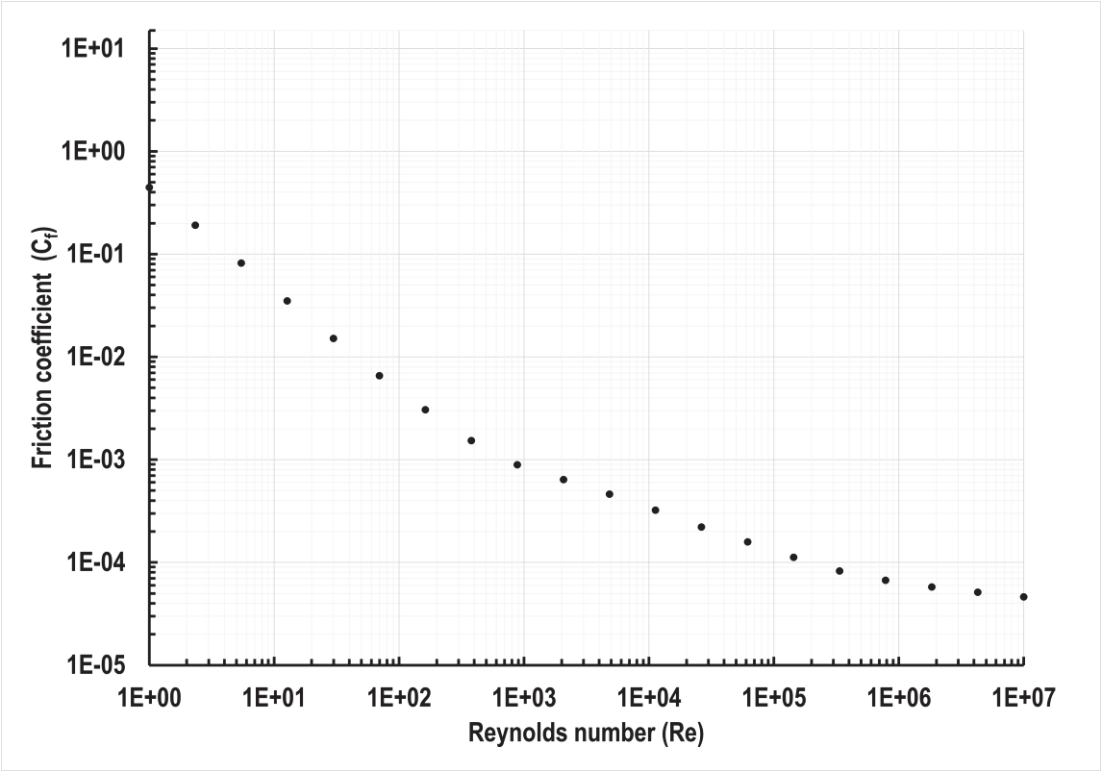

Figure 82: *Friction coefficient at the tank wall vs. Reynolds number (C_f vs Re)*

Both graphs are in logarithmic scale and based on the trend of the simulation data points, it is inferred that a polynomial model can be fitted to the logarithm of the data as follows in Eqs. 96-97:

$$\ln(\mathrm{y}) = q_0 + q_1 \cdot \ln Re + q_2 \cdot [\ln(Re)]^2 + \cdots + q_n \cdot [\ln(Re)]^n \tag{96}$$

Therefore, a plausible model that fits the simulation data have the following form:

$$\mathrm{y} = \exp\left[q_0 + q_1 \cdot \ln Re + q_2 \cdot [\ln(Re)]^2 + \cdots + q_n \cdot [\ln(Re)]^n\right] \tag{97}$$

where $q_0, q_1 \ldots q_n$ are the fitted model coefficients and the dependant variable, y , is either δ/D or C_f. As the degree of the polynomial and the number of coefficients increase, the fit improves, but the objective is to derive an empirical correlation that, while fitting the simulation data effectively, remains parsimonious in terms of its complexity. For this reason, the polynomial degree has been limited to three. For both simulation data curves, the polynomial fits demonstrate strong correlation, but the predicted values by the polynomial models provide a better fit to δ/D vs. Re data than $C_{f\,vs.}$ Re data. For δ/D vs. Re data, the second-degree polynomial fit already provides a satisfactory model. Model 2 (Figure 84) increases the MAE by $1.89 \cdot 10^{-2}$, while the only decreases MAPE by 1.11% compared to Model 1 (Figure 83). For C_f vs. Re data, with Model 2 (Figure 86), the MAE increases by $2.69 \cdot 10^{-3}$, while the MAPE decreases by 2.36 % compared to Model 1 (Figure 85).

This indicates that the average differences between the values of the simulations and the values predicted by the model are greater in the third-degree polynomial fit, but the differences between the actual values and the predicted values scaled to the magnitude of the simulation data are greater in the second-degree polynomial fit. This is because,

although considering the entire data range Model 2 is a better fit than Model 1, the latter fits better to the laminar flow zone where the data has higher magnitude. Tables 23-24 show the coefficients, MAE, MAPE, and R^2 of the fitted models for δ/D vs. Re and C_f vs. Re, respectively.

Table 25: *Coefficients, MAE, MAPE and R^2 of the fitted models for δ/D vs Re*

Model	Coefficients	MAE	MAPE (%)	R^2
(1) $\boldsymbol{\delta/D = exp[q0 + q1 \cdot ln(Re) + q2 \cdot [ln(Re)]^2]}$	q_0 = 2.02107 q_1 = -0.444561 q_2 = -0.0170778	3.57E-02	5.22	0.99
(2) $\boldsymbol{\delta/D = exp[q0 + q1 \cdot ln(Re) + q2 \cdot [ln(Re)]^2 + q3 \cdot [ln(Re)]^3]}$	q_0 = 1.94099 q_1 = -0.376007 q_2 =-0.0279879 q_3 = 0.0004513	5.46E-02	4.11	0.99

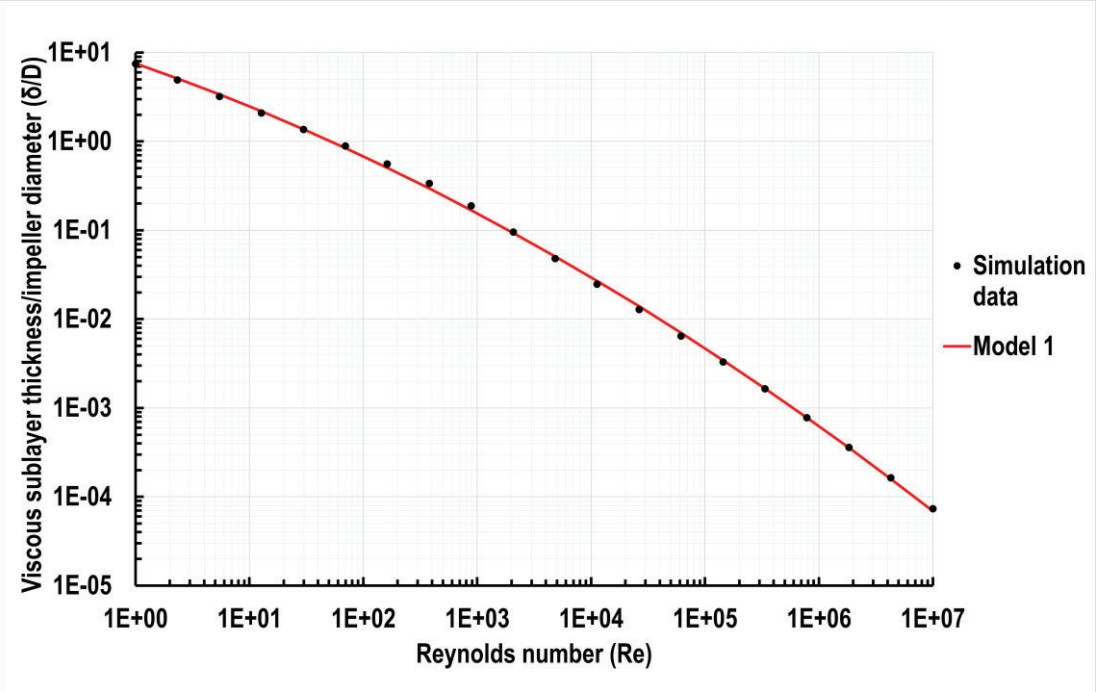

Figure 83: *Fit of Model 1 to δ/D vs. Re simulation data*

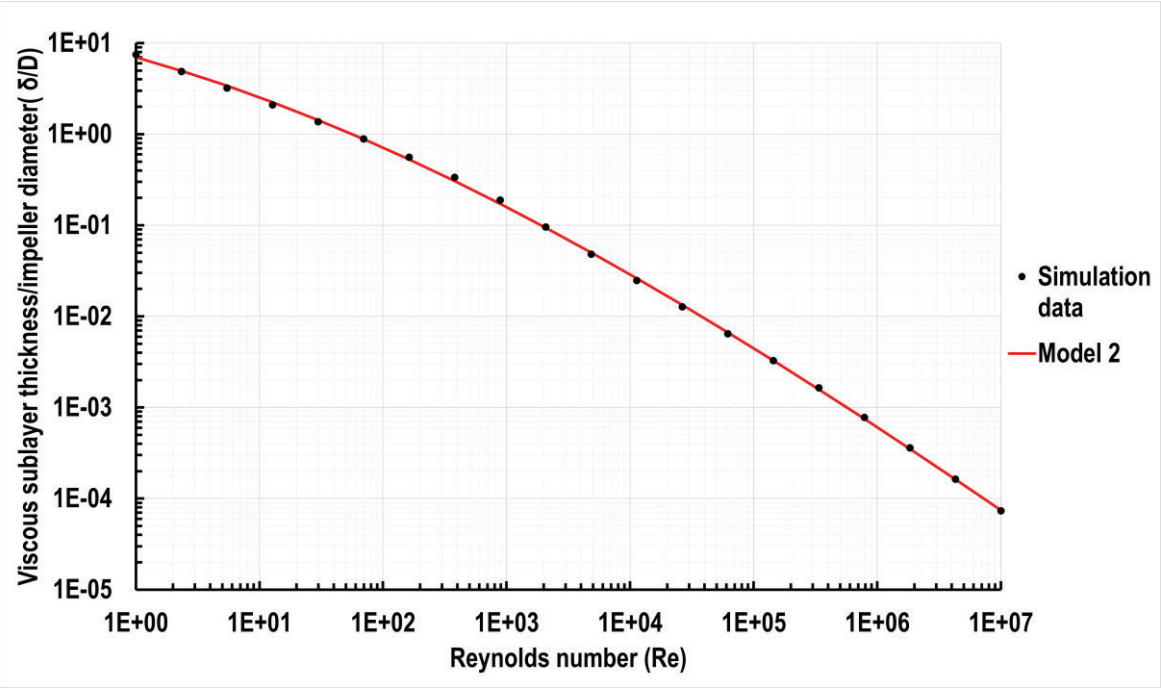

Figure 84: *Fit of Model 1 to δ/D vs. Re simulation data*

Table 26: *Coefficients, MAE, MAPE and R^2 of the fitted models for C_f vs Re*

Model	Coefficients	MAE	MAPE (%)	R^2
(1) $\boldsymbol{Cf = exp[q0 + q1 \cdot ln(Re) + q2 \cdot [ln(Re)]2]}$	q_0 = -0.823265 q_1 = -1.11088 q_2 = 0.0341556	1.83E-03	10.70	0.99
(2) $\boldsymbol{Cf = exp[q0 + q1 \cdot ln(Re) + q2 \cdot [ln(Re)]2 + q3 \cdot [ln(Re)]3]}$	q_0 = -0.663095 q_1 = -1.24799 q_2 = 0.0559758 q_3 = -0.000902515	4.52E-03	8.34	0.99

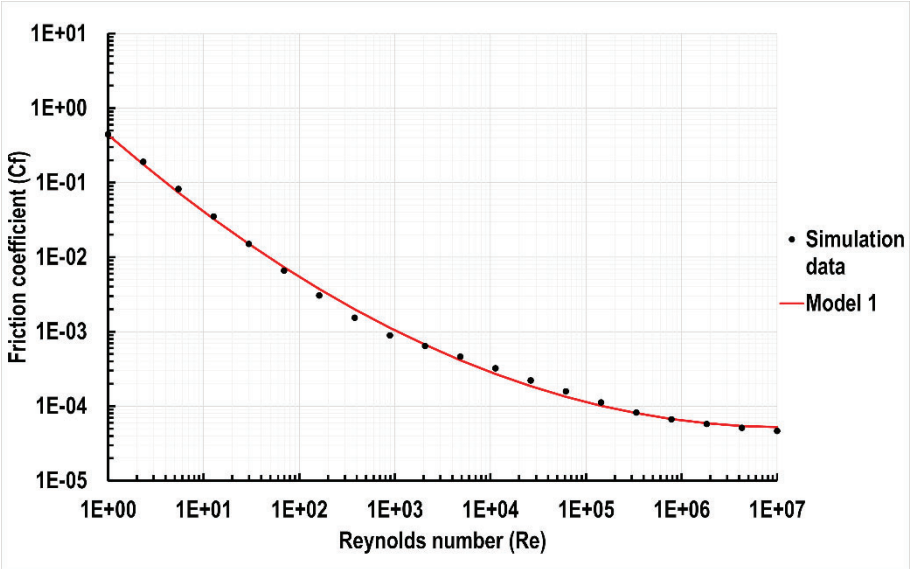

Figure 85: *Fit of Model 1 to Cf vs. Re simulation data*

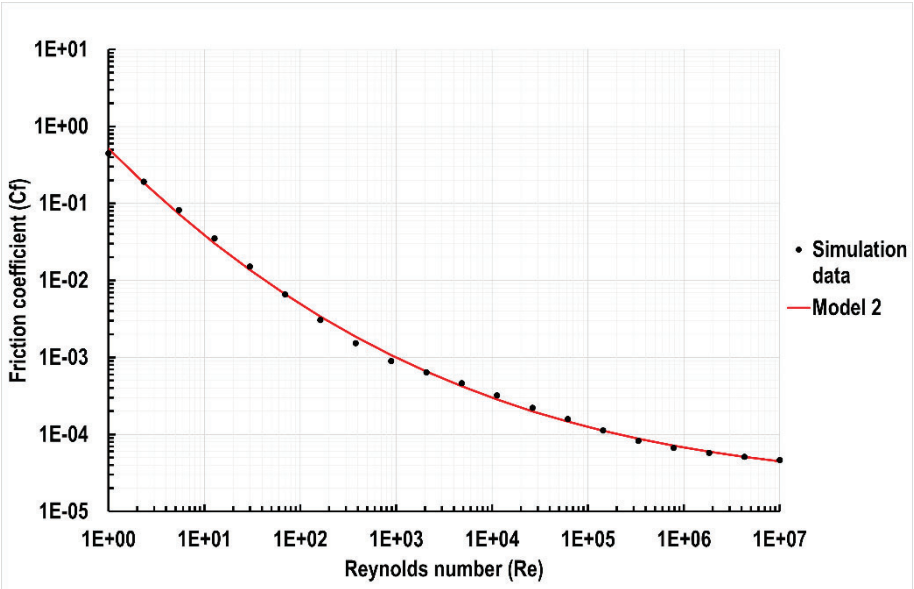

Figure 86: *Fit of Model 2 to C_f vs. Re simulation data*

Figure 87 depicts the distribution of shear stresses on the tank wall surface. The analysis of the contours enables the determination of areas on the tank wall where the velocity gradient is higher, thus leading to more efficient heat transfer, and dead zones where the velocity gradient on the wall is small, resulting in less efficient heat transfer.

Upon individual examination of the contours, surfaces coloured reddish-orange represent zones of high velocity gradient on the wall and better heat transfer (160-200 Pa), while bluish areas indicate zones of low shear stress and poorer heat transfer (0-61 Pa). The remaining colours correspond to intermediate values between the two extremes. At the bottom dish of the tank, there is efficient heat transfer because the semi-anchor of the agitator passes very close to the tank wall. On the left side of the areas between baffles where the flow impacts with the baffle, there is also efficient heat transfer. The baffles are attached to the tank wall by supports that leave a small gap between the tank wall and the baffle, resulting in a large velocity gradient right at this location. Conversely, the right side of the areas between the baffles experiences poorer heat transfer because the fluid has just impacted the previous baffle, and its tangential velocity to the wall is low, Figure 87.

Upon analysing all the contours with fluids of different viscosities simultaneously, it is observed that the wall shear stress increases with viscosity because it is proportional to it. However, the velocity gradient on the wall decreases, resulting in poorer heat transfer.

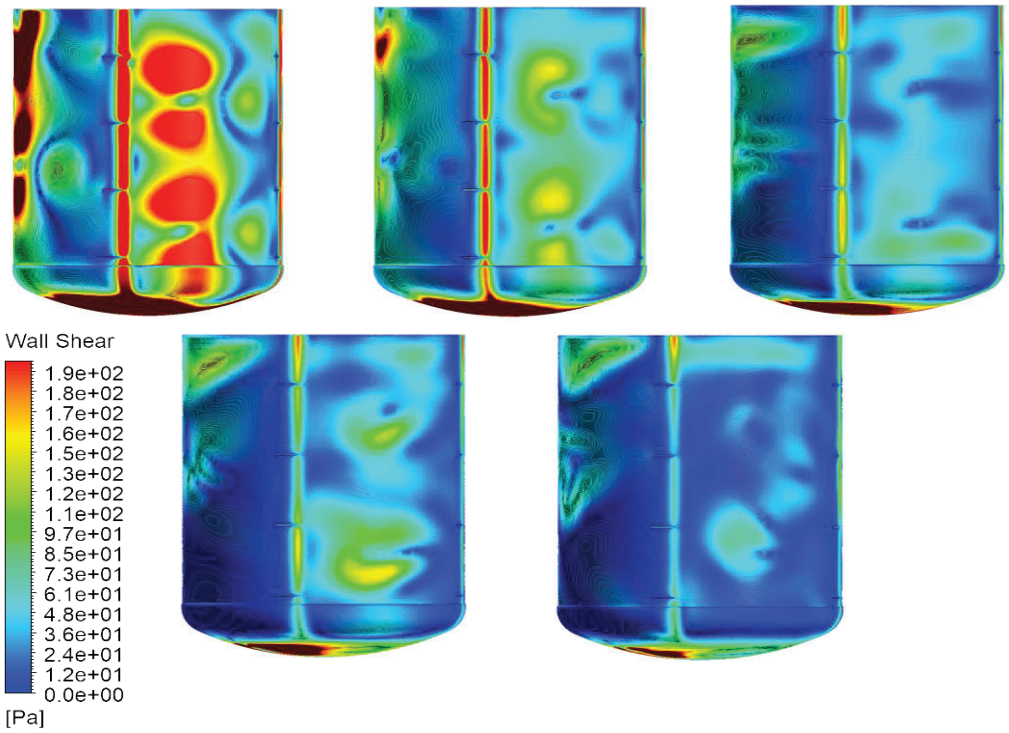

Figure 87: *Tank wall shear stress [Pa] contours at 50 for different fluid viscosities: 90 000 cP, 39 000 cP, 17 000 cP, 7000 cP and 3000 cP*

7.2. Blade angle effect results

The characteristic curves of the different geometries (Figure 88) show that power consumption increases with the blade angle. As the blade angle relative to the horizontal plane increases, more normal surface area interacts with the fluid, causing the displacement of a greater amount of fluid per unit of time (q) and potentially leading to more effective mixing. On the other hand, pressure forces acting on the blades escalate, and the blades encounter more resistance at a given Reynolds number. Accordingly, the axial flow blades (0º) minimize power consumption.

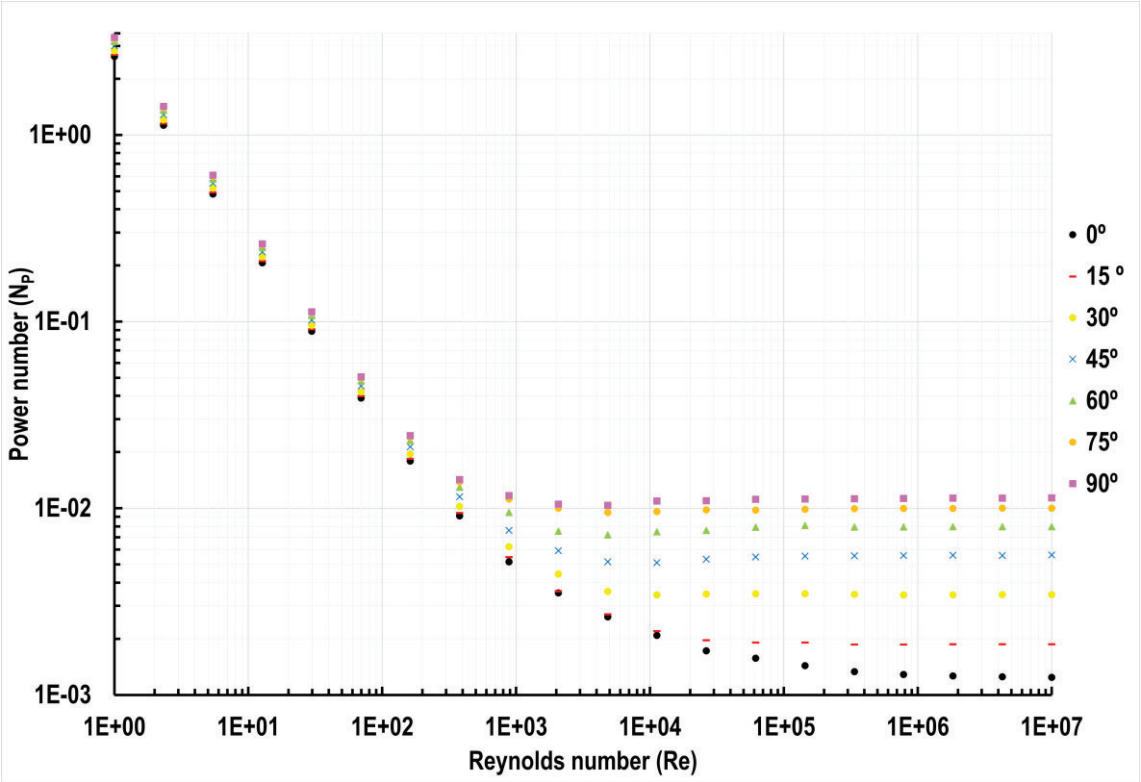

Figure 88: *Characteristic curves (N_P vs. Re) of the different blade angles tested*

In the turbulent flow zone, the percentual variation in power consumption between blade angles is more pronounced than in the laminar zone. Figure 89 shows the percentual variation in power consumption with respect to the reference angle (30º) for each Reynolds number, calculated as, Eq. 98:

$$\% \, \Delta N_P(Re, \theta) = \frac{N_P(Re, \theta) - N_P(Re, 30º)}{N_P(Re, 30º)} \cdot 100 \tag{98}$$

The results show that power consumption (N_P) can be reduced by up to 64% compared to the current configuration with axial flow blades (0º) in the turbulent regime zone. With mixed flow blades in the turbulent regime zone, at 15º, power consumption is reduced by 46%; at 45º, it increases by 63%; at 60º, it increases by 131%; and at 75º, it increases by 190%. Power consumption in the turbulent regime zone can increase by up to 230% compared to the current configuration with radial flow blades (90º).

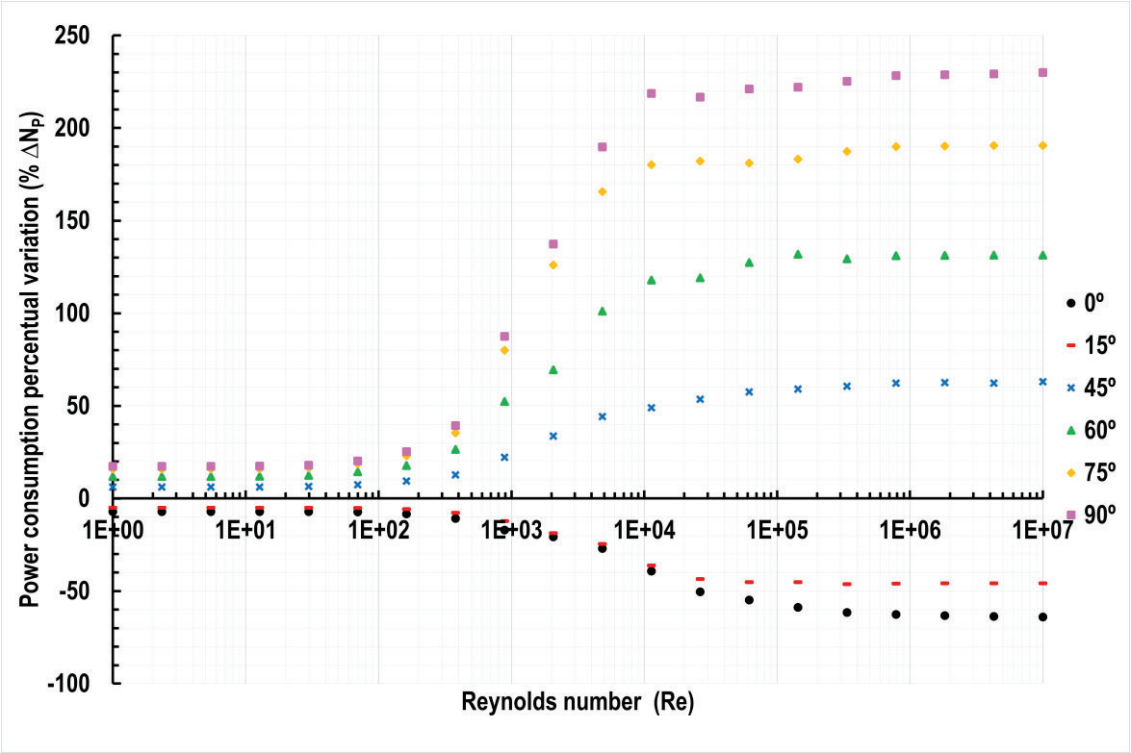

Figure 89: *Power consumption percentual variation (% ΔN_P) between the reference blade angle (30°) and the other tested blade angles (0°,15°,45°,60°,75° and 90°)*

Figure 90 shows impeller blades pressure contours differences between the different angles tested. It is demonstrated that as the effective surface area of the blades increases, the high-pressure zones (red-orange) occupy a larger part of the blade's total surface area, leading to an increase of pressure forces contribution to the total torque.

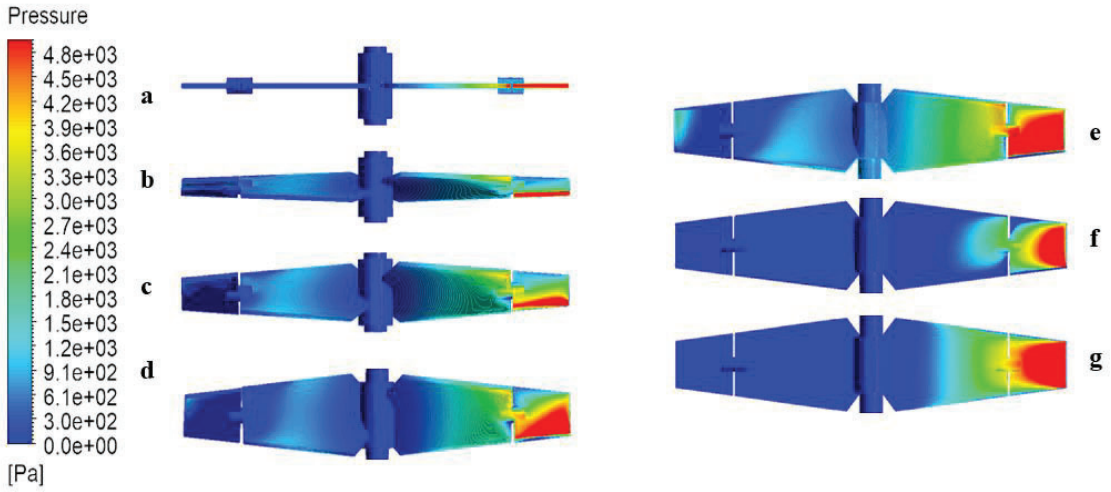

Figure 90: *Impeller blades pressure [Pa] contours at 50 rpm and 7000 cP for the different blade angles tested: a) 0°,b) 15°, c) 30°, d) 45°, e) 60°, f) 75° and g) 90°*

Figure 91 shows impeller blades shear stress contours differences between the different angles tested. It is noted that the tangential forces increase slightly with the augment of

blade angle, but to a much lesser extent than the normal forces. Accordingly, it can be inferred that the increase in the total torque with blade angle is mainly due to the rise in normal forces contribution.

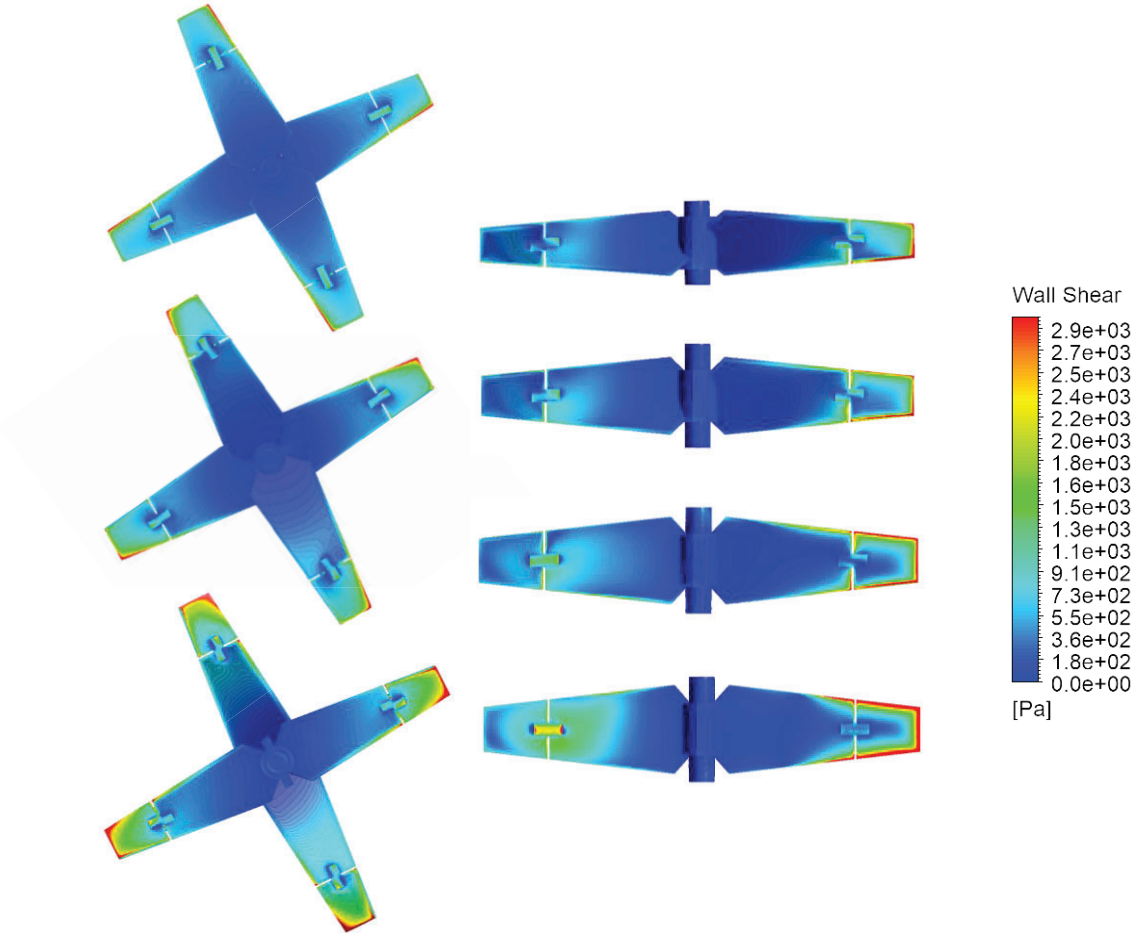

Figure 91: *Impeller blades shear stress [Pa] contours at 50 rpm and 7000 cP for the different blade angles tested: 0º,15º,30º,45º,60º,75º and 90º*

Figure 92 suggests that the thickness of the laminar layer at the tank wall (δ/D) decreases with the blade angle in all flow regimes. Analogously, Figure 88 shows that the velocity gradient near the tank wall (C_f) increases with the blade angle in all flow regimes. As blade angle augments, the radial component of the flow exiting the blade tip is enhanced, pushing more fluid towards the tank wall and then downwards or upwards along the wall, which enhances convective heat transfer. Accordingly, the radial flow blades (90º) convective heat transfer also diminishes.

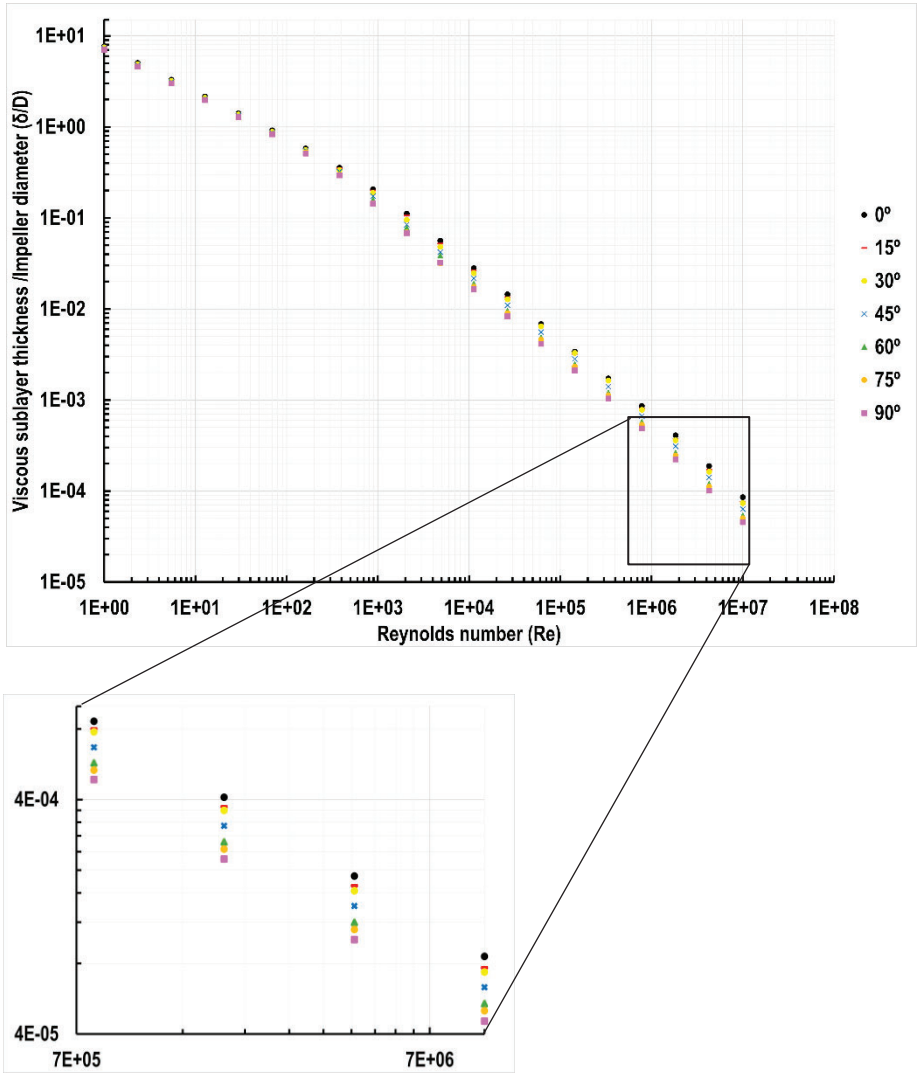

Figure 92: *δ/D vs. Re of the different blade angles tested.*

In a similar way to power consumption, the percentual variations of the layer thickness and wall shear stress at a given Reynolds number are more noticeable in the turbulent flow zone. Figure 94 shows the percentual variation in viscous sublayer thickness with respect to the reference angle (30º) for each Reynolds number. The results show that viscous sublayer thickness (δ/D) can be reduced by up to 38 % compared to the current configuration with radial flow blades (90º) in some areas of the turbulent and transitional regime zones. With mixed flow blades in some areas of the turbulent and transitional regime zones, at 75º, viscous sublayer thickness is reduced by 32 %; at 60º, it is reduced by 26%; at 45º, it is reduced by 14 %; and at 15º, it increases by 6%. Viscous sublayer thickness can increase by up to 17% compared to the current configuration with axial flow blades (0º). At certain points on the graph located within the turbulent flow regime ($10^5 < Re < 10^6$), the current impeller design (30º) does not exhibit enhanced heat transfer on the tank wall compared to blades with 15 º. Consequently, under typical operating conditions characterized by these turbulence intensities, it may prove more efficient to employ blades with a reduced inclination angle, as they require lower power consumption.

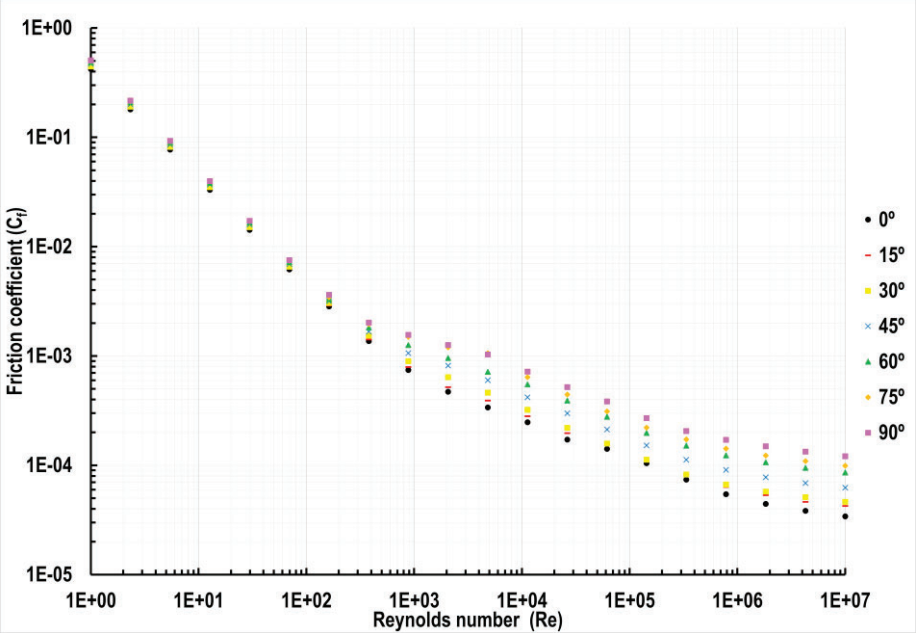

Figure 93: *C_f vs. Re of the different blade angles tested*

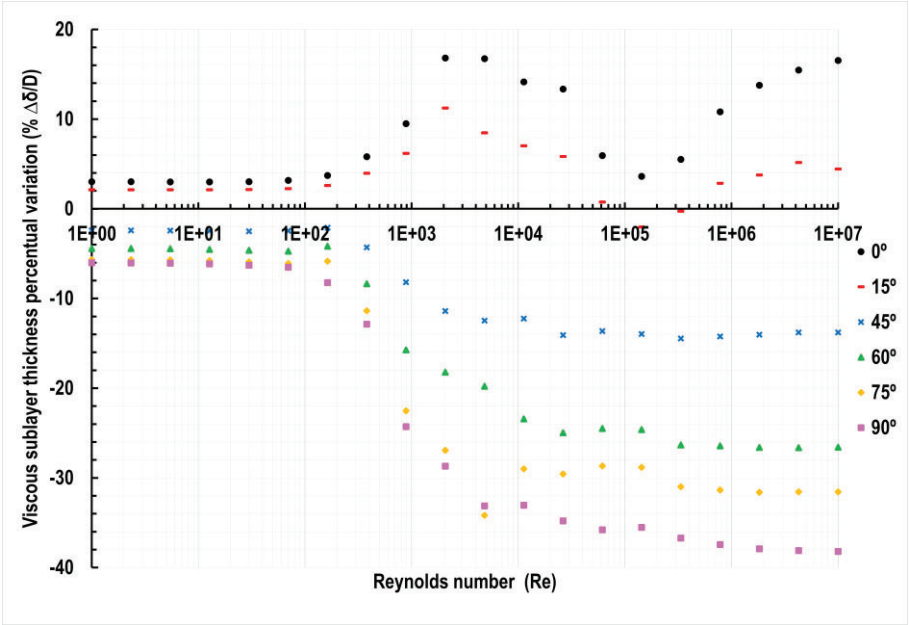

Figure 94: *Viscous sublayer thickness percentual variation (% Δδ/D) between the reference blade angle (30º) and the other tested blade angles (0º,15º,45º,60º,75º and 90º)*

Figure 95 illustrates that areas colored in red on the tank, where the velocity gradient is highest, expand as the inclination of the blades increases and radial flux component is enhanced. Heat transfer on the bottom dish remains constant since the lower blade geometrical parameters are not altered. Despite the greater magnitude of shear stress on

the more inclined blades configurations, those with smaller inclination angles distribute more uniformly the shear stress on the tank wall, resulting in less disparity in heat transfer between areas with high shear stress closer to the blade tips and dead zones.

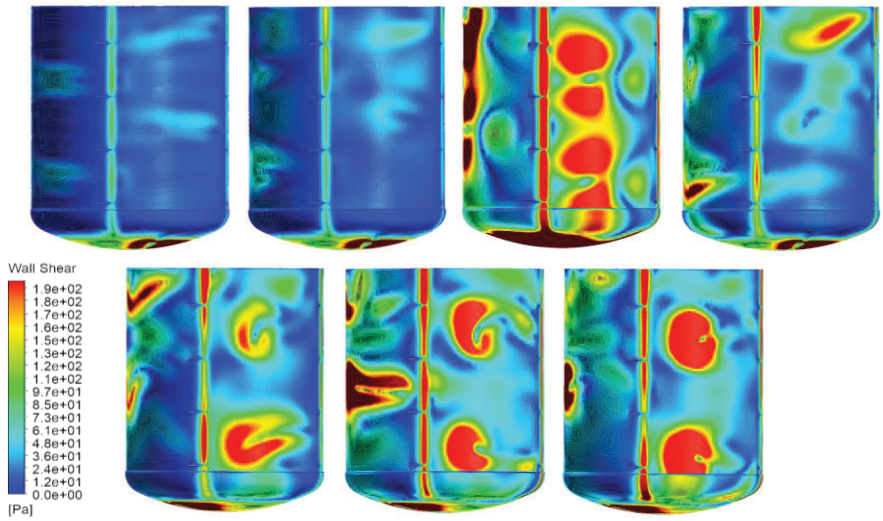

Figure 95: *Tank wall shear stress [Pa] contours at 50 rpm and 7000 cP for the different blade angles tested: 0º,15º,30º,45º,60º,75º and 90º*

7.3. Concluding remarks

In turbulent flow regime (Re > 10000), the power number remains constant regardless of the Reynolds number. In laminar flow regime (Re < 100), the power number increases with a power trend as the Reynolds number decreases. In the transitional flow regime, a gradual transition occurs between the behaviour in laminar and turbulent flows. The model that provides the best fits the entire range of simulation data is $NP = 0.00346 + 2.82554 \cdot Re^{-1.00144}$. The normal or pressure forces accumulate at the blade tip and increase significantly with the rising fluid viscosity. Similarly, the tangential or viscous forces, while also greater at the blade tip, exhibit a more uniform distribution across the entire blade surface. The forces likewise escalate notably with increasing fluid viscosity.

The thickness of the laminar layer at the tank wall decreases with Reynolds number, leading to more efficient heat transfer. The model that fits the correlation is $\delta/D = exp[2.02107 - 0.444561 \cdot ln(Re) - 0.0170778 \cdot [ln(Re)]^2]$. At the tank bottom dish where the semi-anchor is in close proximity to the wall, significant heat transfer occurs due to a substantial velocity gradient in that region. Favorable heat transfer is observed on the left side of the surface between baffles; however, a stagnant region emerges on the right side.

The power consumption increases with the blade angle due to a larger surface area interacting with the fluid, leading to an increase in pressure forces. Viscous forces also escalate with blade angle but to a lesser extent. Axial flow blades (0º) can reduce power

consumption by up to 64% in the turbulent regime compared to the current configuration.

On the other hand, the thickness of the laminar layer on the tank wall decreases with the blade angle, leading to more efficient heat transfer. Radial flow blades (90º) can reduce the thickness of the laminar layer by up to 38% compared to the current configuration.

If a balance between low energy consumption and good heat transfer is sought, the most suitable configurations are mixed flow blades (30º, 45º, 60º). The optimal design will depend on the importance given to power consumption and heat transfer. If power consumption takes priority over heat transfer, blades with a smaller angle and greater axial flux components (30º-45º) are recommended. If efficient heat transfer at the tank wall is of greater significance, blades with larger angle (45º-60º) are recommended.

8. Flow in partially full pipes' results

The first simulation is intended to check if given a Manning roughness (n), slope (S), volume flow (Q) and diameter (which defines the hydraulic radius, Rh), the mean cross-sectional velocity (v) matched the one given by Manning's equation when the inlet velocity is close to it. The second verification is about varying the initial conditions of the inlet, keeping the rest of parameters, to check if the simulation still converges into the solution that matches the same Manning equation result. The third verification is about varying the diameter of the tube, modifying the hydraulic radius of the flow, and keeping the rest of parameters to check if they are in accordance with Manning's equations.

8.1. Comparison with an inlet velocity close to Manning's results

The first simulation case is carried over a tube of 50 mm in diameter, 0.005 m/m of slope, 10^{-4} m^3/s and 2.247 mm of roughness height.

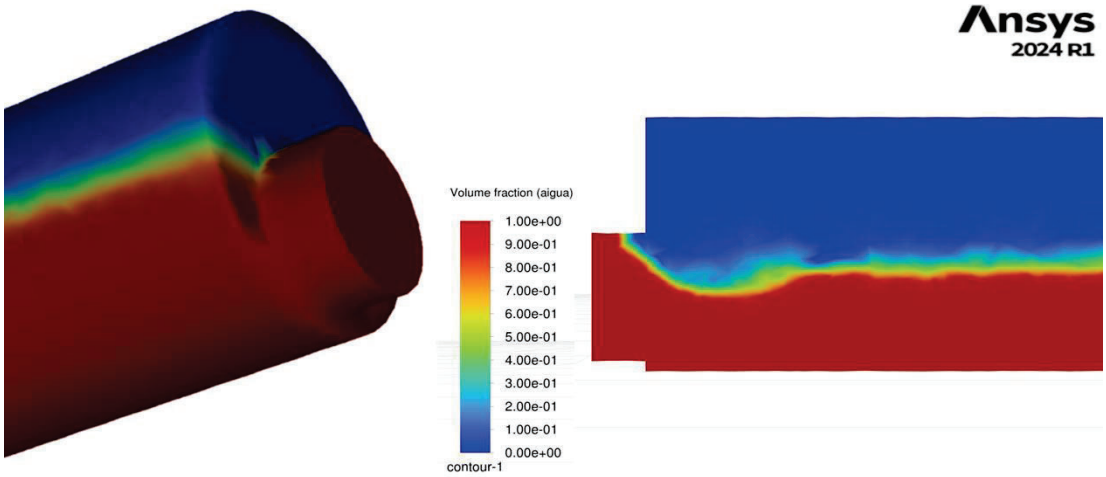

Figure 96: *Volume fraction of water contours through the wall and the velocity inlet (right) and through the symmetry plane (left)*

Throughout the first meter of the tube it is appreciable how the flow reaches uniformity, drawing a damping tendency. Right after the inlet, the velocity rises sharply due to the impact with the walls and its change of shape (from circular to an arc), reducing the depth of flow as well, but immediately after, due to the friction forces of the walls this magnitude decreases strongly. Then, the gravity and friction forces reach an equilibrium state.

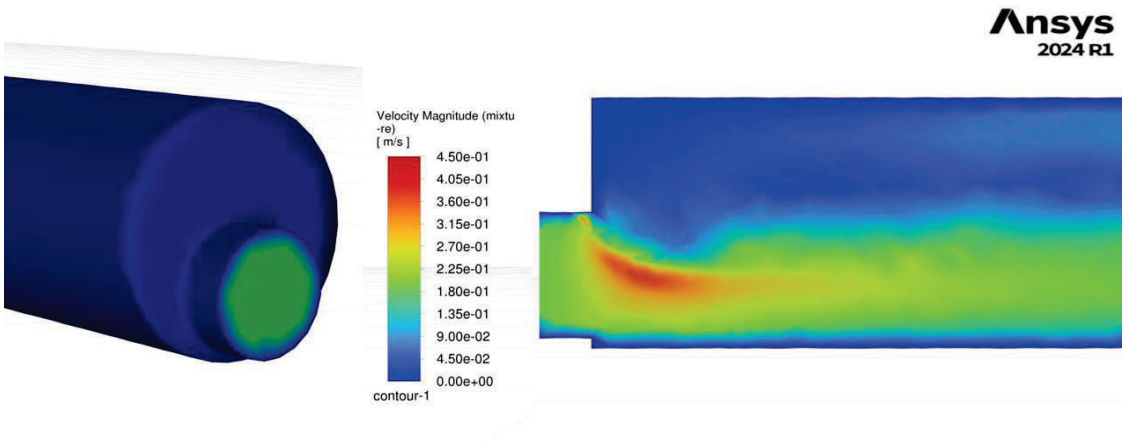

Figure 97: *Velocity magnitude contours through the wall and the velocity inlet (right) and through the symmetry plane (left)*

In Figure 97 it can be seen how velocity is zero near the walls. However, it also shows that mean velocity at x = 0 m, the origin of the tube and the point where the inlet is located, is lower than the inlet velocity but higher than zero. The water that is in contact with the walls of the origin of the tube has a velocity of zero, but the water that flows through the inlet travels at the inlet velocity, therefore the velocity at x = 0 m is the weighted average of those two velocities.

The air phase zone is not entirely motionless (Figure 97). Since there is no inlet of air phase, the air inside the tube moves cyclically. The zone nearer to the interface moves in the direction of the flow, dragged by it, while the zone nearer to the wall moves in the opposite direction. The layer in between the two zones mentioned in the air phase is still.

From the simulations we observe that near the outlet the velocity magnitude starts increasing. This problem is observed in most of the simulations in this work, independently of the length of the tube. However, the mass balance between the inlet and the outlet is fulfilled and this effect does not affect the velocities outside the last meter of the tube. The uniform flow zone, from which the mean velocity values are taken to calculate the average mean velocity, is defined between two surfaces with a difference of mean velocity lower than 0.5% for more than three intervals. Thus, by applying the uniform flow criteria, the outlet velocity problem becomes neglectable, as the increase exceeds that threshold. Nevertheless, this problem must be taken into consideration when the tube length reduction is carried out, as not only the first meter is not always valid as the flow may be not uniform yet, but the final meter is not valid as well. Then, the length of the tube should not become shorter than four meters.

The uniform flow zone starts at x = 0.2 m and ends at x = 9.25 m. The steady state velocity of this zone is 0.2010 m/s. As mentioned earlier, the Manning equation results in a mean velocity of 0.2047 m/s which makes an error percentage of 1.78 %.

8.2. Comparison with different inlet conditions

In Table 27 it can be observed the different inlet conditions between the first simulation (V0) and the three simulations of the first verification (V1_0.3, V1_0.1 and V1_10). The volume flow, slope, roughness and diameter are the same in all cases, so the solution obtained via the Manning equations is the same as the first simulation.

Table 27: *Inlet conditions for the second verification*

	Inlet conditions			
Code	Inlet area [m^2]	Inlet velocity [m/s]	Inlet Position	Inlet shape
V0	0.00050	0.2	Bottom	Circular
V1_0.3	0.00033	0.3	Bottom	Circular
V1_0.1	0.00100	0.1	Bottom	Circular
V1_10	0.00001	10	TOP	Squared

The following Figure 98 shows a comparison of the mean velocity profile for each of the four simulations represented in Table 27, as well as the value of the mean velocity calculated via Manning equation. The inlet conditions do affect the length required to uniformize the flow. The more extreme the inlet conditions to the steady state are the more length will require to reach the equilibrium. As the inlet area of V1_0.1 is larger, there is more amount of water that falls from a higher position to adapt its shape of the new bed, increasing slightly the maximum mean speed in front V0's and V1_0.3's.

V1_10 presents a much higher maximum mean velocity, as both the inlet position and velocity were set to maximize the energy of the impact. Figure 99 shows several contour graphics of the water phase in V1_10, throughout the symmetry plane (top) and throughout the wall (the two of the bottom). It can be seen how the impact creates a relatively large zone of small depth of flow before reaching the equilibrium state due to the action of friction forces. This splash required lots of mesh adaptations to be appreciated appropriately, hugely increasing the simulation costs.

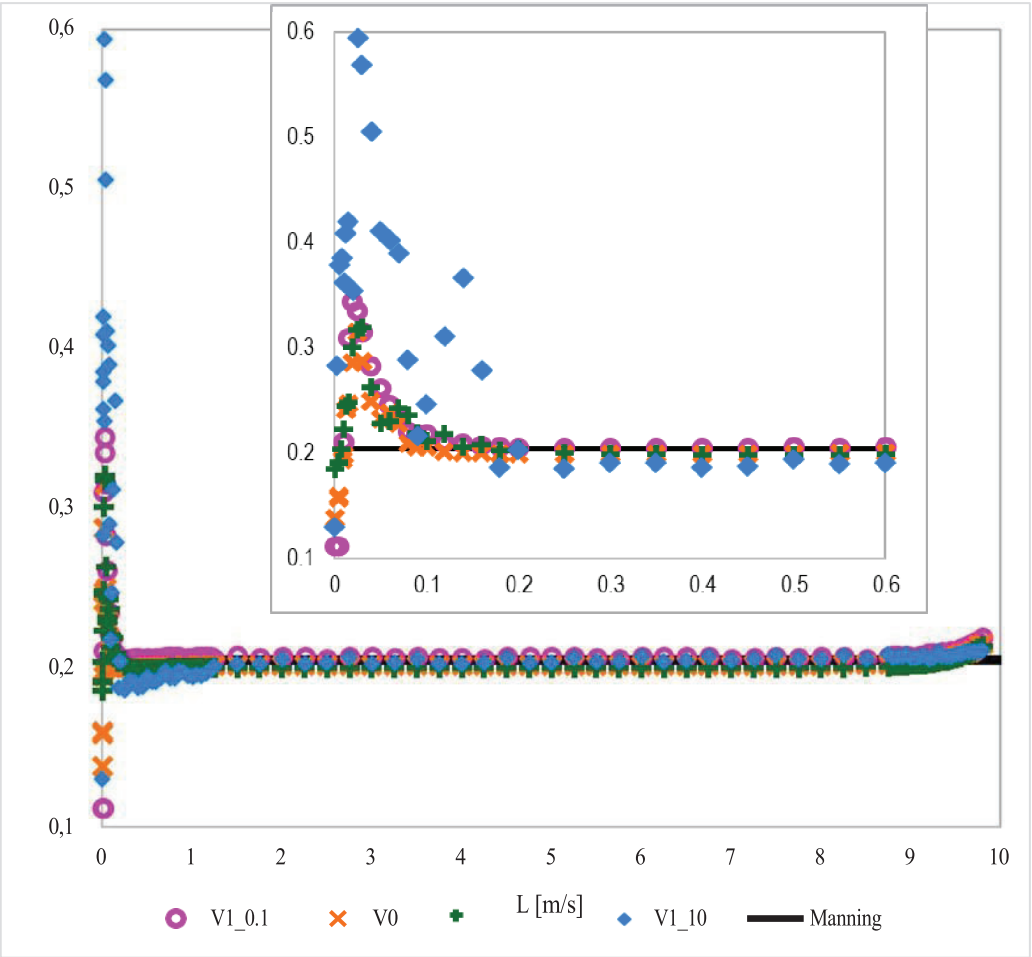

Figure 98: *Comparison of velocity profiles of the same tube with different inlet conditions*

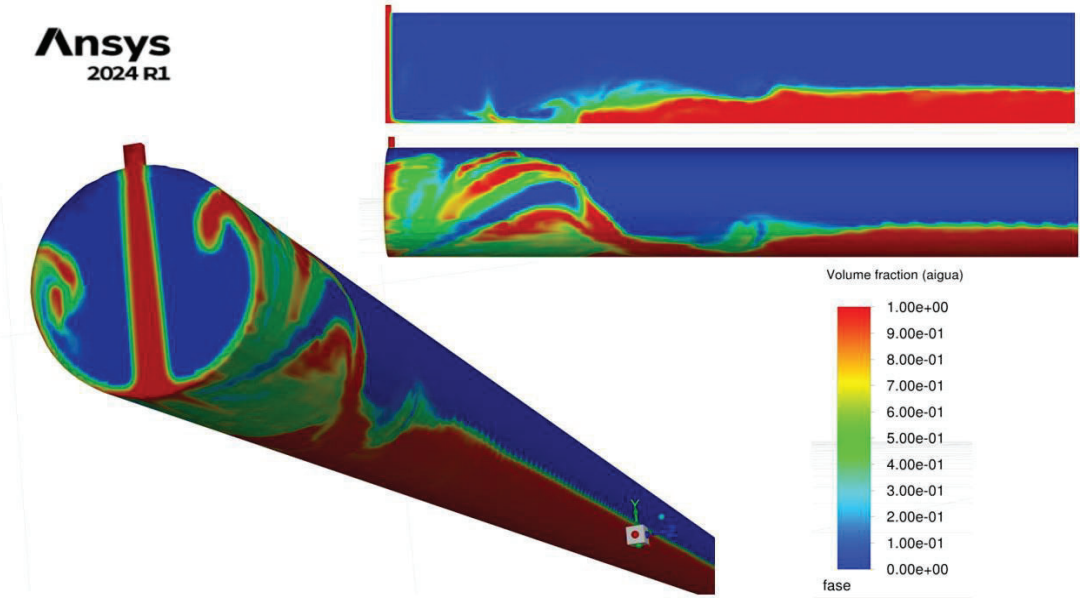

Figure 99: *Contour graphics of the water phase fraction in V1_10*

Table 28 shows the uniform flow zone start and end, the average mean velocity and the percentage of error of V0, V1_0.1, V1_0.3 and V1_10. As mentioned earlier, the Manning equation results in a mean velocity of 0.2047 m/s.

Table 28: *Average mean cross-sectional velocity and error percentage of first verification simulations*

Code	Start [m]	End [m]	Average mean velocity [m/s]	Percentage of error [%]
V0	0.2	9.25	0.2010	1.78
V1_0.1	0.3	9.05	0.2063	0.79
V1_0.3	0.4	9.45	0.2002	2.20
V1_10	1.25	8.75	0.2043	0.17

Table 28 shows how the inlet conditions do not affect the average mean velocity of the simulation after converging. Furthermore, it has been confirmed that there is only one equilibrium state between friction and gravity in the ANSYS Fluent solution algorithm, as the Manning equation points. The main effects of the initial conditions of the simulation are the simulation costs (number of iterations required to reach the solution) and the already mentioned length required to reach the equilibrium inside the tube. The existence of an unique equilibrium gives a first notion of the accuracy of the simulations for these cases, as the correlations match the simulations.

8.3. Manning's equation exponents

When linearizing the Manning equation (Eq. 39) with the natural logarithm the following expression is obtained, Eq. 99:

$$\ln v = \frac{2}{3}\ln R_h + \frac{1}{2}\ln S - \ln n \tag{99}$$

The slope of the relation between the natural logarithm of the velocity and the natural logarithm hydraulic radius is the exponent of the hydraulic radius in the Manning equation. Then, if simulation results show the same two-thirds slope after a linearization, it means that the exponent for the hydraulic radius in the Manning equation is indirectly respected by ANSYS Fluent in its calculations.

Table 29: *Average mean cross-sectional velocity, hydraulic radius and error percentage of second verification simulations*

Code	Diameter [m]	Hydraulic radius [m]	Average mean velocity [m/s]	Manning equation velocity [m/s]	Error percentage [%]
V0	0.10	0.007619	0.1845	0.1889	2.33
V2_100	0.075	0.008023	0.1924	0.1963	1.97
V2_75	0.06	0.008379	0.1959	0.2014	2.77
V2_60	0.05	0.008567	0.2010	0.2054	2.15
V2_30	0.03	0.008695	0.2023	0.2068	2.19

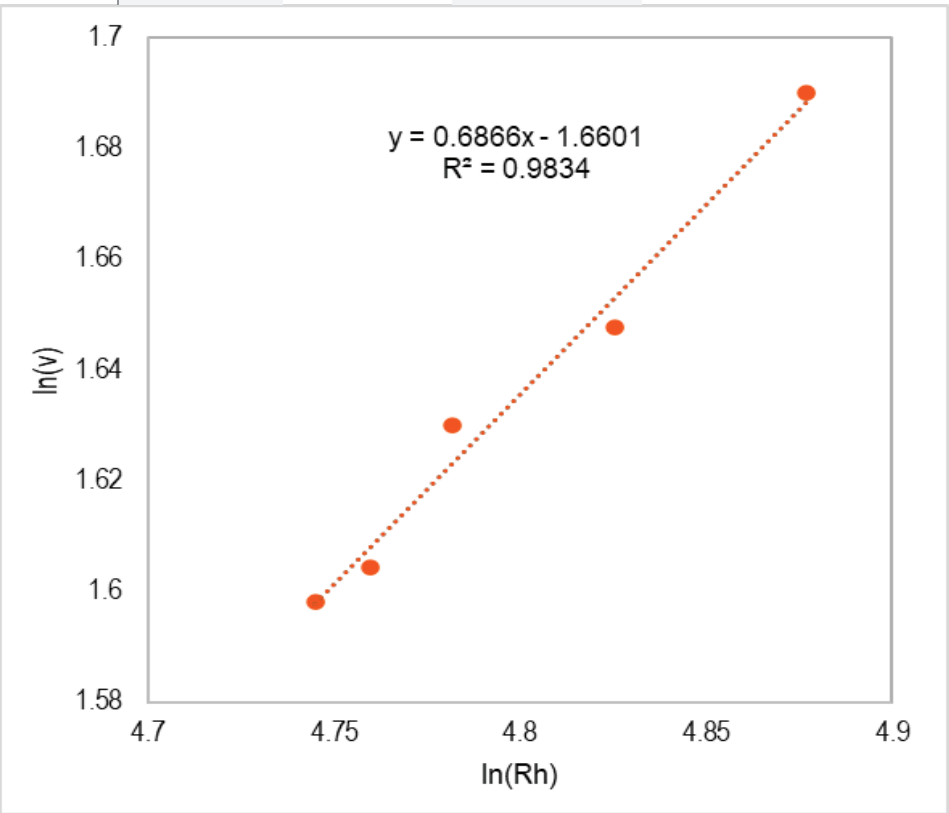

Figure 100: *Linearization of the values of the average mean velocity and the hydraulic radius*

The slope of the linearization of the simulation results is 0.69 (see Figure 100), while the slope of the linearization of the Manning equation is 2/3. That makes a percentage of error of around 3.5%. From Eq. 99 we substitute and obtain Eq. 100:

$$C_1 = \frac{1}{2}\ln S - \ln n \tag{100}$$

Where C_1 is the origin of the line from the graph in Figure 100. Rearranging the terms allows the ½ exponent to be found via simulations, Eq. 101:

$$\frac{C_1 - \ln n}{\ln S} = 0.477 \tag{101}$$

This makes a percentage of error for the slope exponent of 4.6%. The original Manning publication is not available on the Internet, making impossible to do a deeper evaluation of those exponent with Manning's experimental error margin. Thus, ANSYS Fluent proves to at least fairly respect the approximate two-thirds exponent of the Manning equation for the hydraulic radius, as well as the one-half exponent for the slope.

8.4. 90° elbow case

The 90° elbow case consists in a tube composed of two identical tubes in diameter, slope and roughness) of 2.5 and 3.5 meters connected by an elbow whose radius is equal to the radius of both tubes. The parameters like slope, diameter, volume flow and roughness height are the same as the ones of V0 simulation. Figure 101 shows the velocity profile throughout the tube composed of the two tubes connected with an elbow and the value of the velocity calculated via Manning equation. Figure 102 shows the velocity profile throughout the elbow in terms of angle of turn, from zero to ninety degrees.

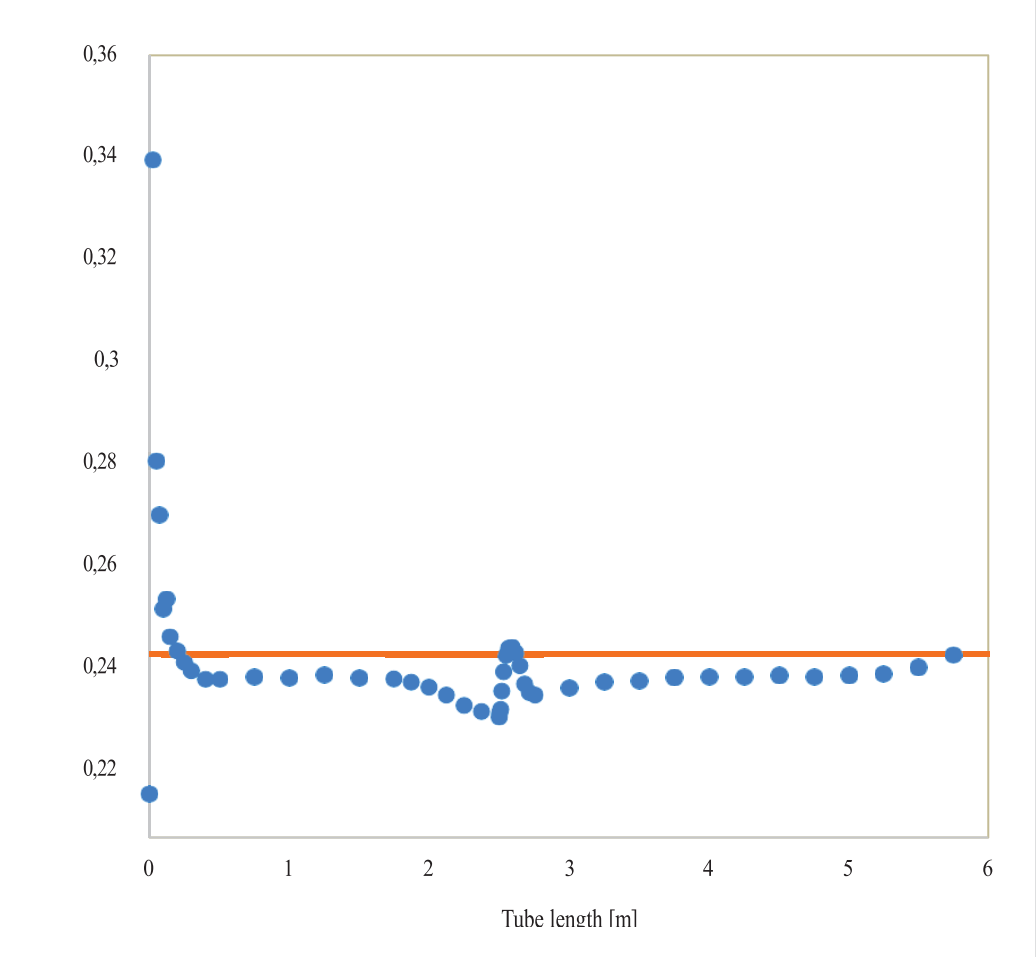

Figure 101: *Velocity profile throughout both tubes and the elbow*

After getting uniform there are no significant variations in the velocity until half a meter before the elbow, where the velocity starts dropping due to the friction of the element that lies ahead, similarly to a racing car breaking right before the turn and not during it. At the start of the elbow the velocity is at its minimum. This velocity is not contemplated by Manning equation, although the Manning number, volume flow, diameter and slope are still the same as before; there is an altered state caused by a strong increase of friction forces occasioned by a new point sourced element, the elbow. The friction forces decrease as the flow moves slower than it should, and in response the velocity bounces back sharply due to the gravity forces. As the velocity increases, friction does too, and around halfway of the elbow the velocity starts dropping again but reaching a minimum velocity higher than before. This cycle is repeated with every maximum being closer to the next minimum, and vice versa, until there is no difference between both. Essentially, this is a damping tendency as the one present at the beginning of each tube simulated. When the extra friction forces are no longer present, the flow moves from the altered state towards the equilibrium state between friction and gravity forces. And, as the parameters of the Manning equation in the tube after the elbow are the same as in the tube before it, the equilibrium velocity is the same as well.

The behaviour of an open channel flow can be compared to an object falling in terminal velocity, where the object does not accelerate due to the gravity and friction equilibrium. If the initial velocity is zero, gravity will accelerate it with no opposition due to the minimal friction forces, which will increase until reaching the equilibrium. If the initial velocity is too high, friction forces will decelerate it until the equilibrium is reached. This is exactly what happens in each simulation of the inlet. When in a channel there is a turn, the increasing friction forces disrupt the balance, slowing down the flow. However, this increase of friction forces is temporary, and if the rest of parameters are the same the previous state of equilibrium will be back.

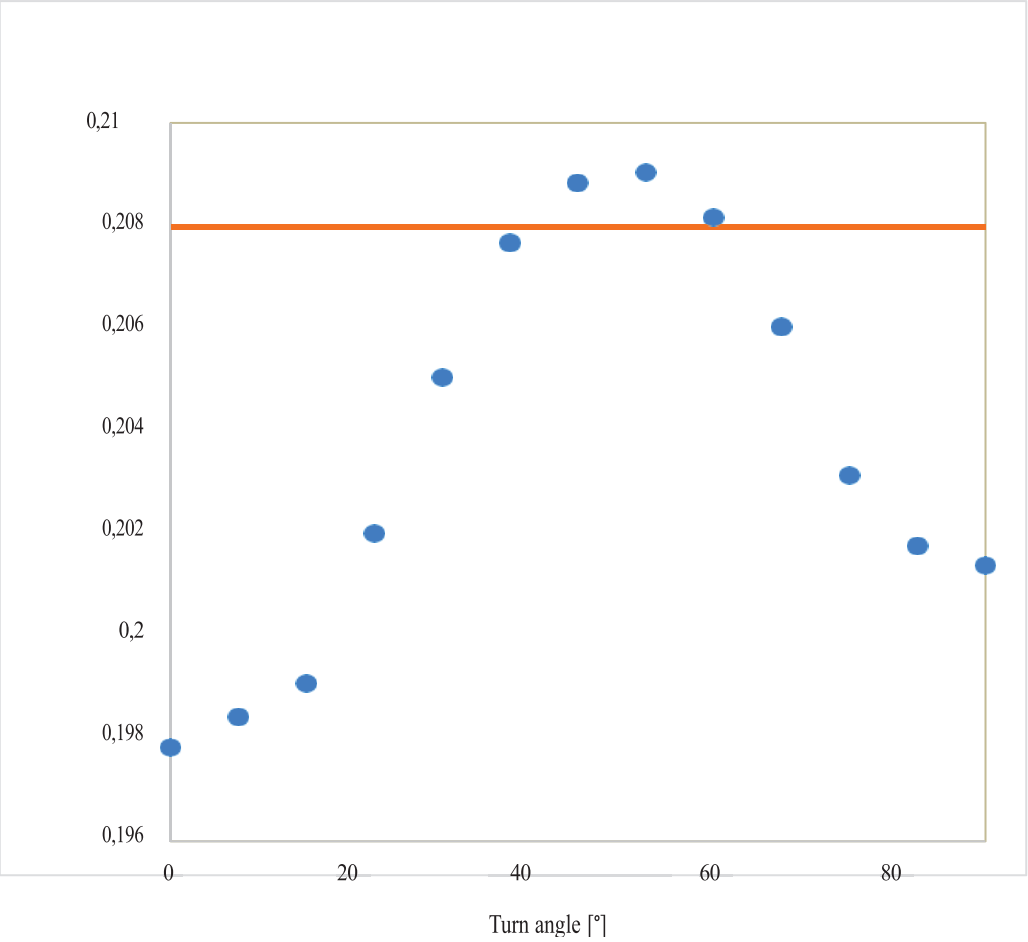

Figure 102: *Velocity profile throughout the elbow*

8.5. Concluding remarks

It has been confirmed that there is only one equilibrium state between friction and gravity in the ANSYS Fluent solution algorithm, as the Manning equation points. The initial conditions do not affect the solution. The main effects of the inlet and initial conditions of the simulation are the simulation costs (the number of iterations required to converge) and the already mentioned length required to reach the equilibrium inside the tube. From second verification results, despite not using the Manning equation in its solution algorithm, ANSYS Fluent proves to at least fairly respect the approximate two-thirds exponent for the hydraulic radius and the one-half exponent for the slope. From the case of the 90° elbow, it is concluded that the average mean velocity is equal in both uniform zones, due to the elbow only affecting temporarily the velocity of the flow, as parameters are kept. The average mean velocity is the product of the equilibrium of forces of friction and gravity. If the parameters behind those forces (the Manning number and the slope, respectively) as well as the volume flow and the hydraulic radius remain unchanged, the flow will return to the previous state of equilibrium once the extra friction forces from the elbow are no longer affecting the flow. All average mean cross-sectional velocities

obtained from the simulations carried out kept the error percentage in relation to their respective Manning equation iterative resolution mean cross sectional velocity below 5%.

9. Results of simulations in Materials Engineering

9.1. Discrete Element method results

This section presents the most relevant DEM results. Four setups are present that are involved in the production of the copper-graphene particles: planetary ball mill simulations with only the steel balls and the ones that include both the grinding and grinded materials (graphite). Additionally, a model is created to relate the DEM results to the PSD (Particle Size Distribution) results obtained experimentally. Finally, the mixing process of graphene with copper particles to see their interactions inside the mill.

9.1.1. Simulations involving only grinding balls

These simulations are created to find energy collision spectra and mill dynamics with low computational effort, as only the grinding balls are accounted for. For more accurate and precise analysis, the addition of the material and its interaction with the grinded material has to be simulated. These simulations, though, give a good estimation of some variables inside the mill, like power consumption or maximum impact collision energies.

A relevant aspect in design is the power consumption of the mill. When creating the design of experiments, the total mass is set to be similar for all the simulations, varying the size and revolution speed of the mill. Consequently, as when mass is constant through the studied cases, power draw seems to depend almost solely on the angular momentum of the mill, as seen in table 30:

Table 30: *Power draw at different angular speed and ball size*

Power draw (W)	**Ball size (mm)**		
Angular speed (rpm)	3	5	10
100	$3.56 \cdot 10^{-3}$	$2.85 \cdot 10^{-3}$	$3.03 \cdot 10^{-3}$
300	0.105	$9.98 \cdot 10^{-2}$	0.110
500	0.428	0.392	0.442

Collision energy is categorized in two types: impact and shearing collisions. Impact collisions when contain enough energy can break down and material, reducing its size arbitrarily and independently of its geometry. These collisions are important to reduce the size of big chunks of material down to the desired material size. Shear impacts, on the

other hand, are more likely to peel off layers (in the case of layered anisotropic materials such as graphite) and are of great use when trying to transform those into various graphene layers.

As shown in Figures 103 and 104, both shearing and impact collisions are more frequent at high energies as the angular speed increases. Such energies are of greater interest, as are the ones that can break or peel material off, and not only deform it or be dissipated into heat. The most desirable speed to work, despite the higher consumption would then be 500 rpm. In this operational point, the high power consumption is compensated by a high frequency of high energy impacts that lead to less operational time.

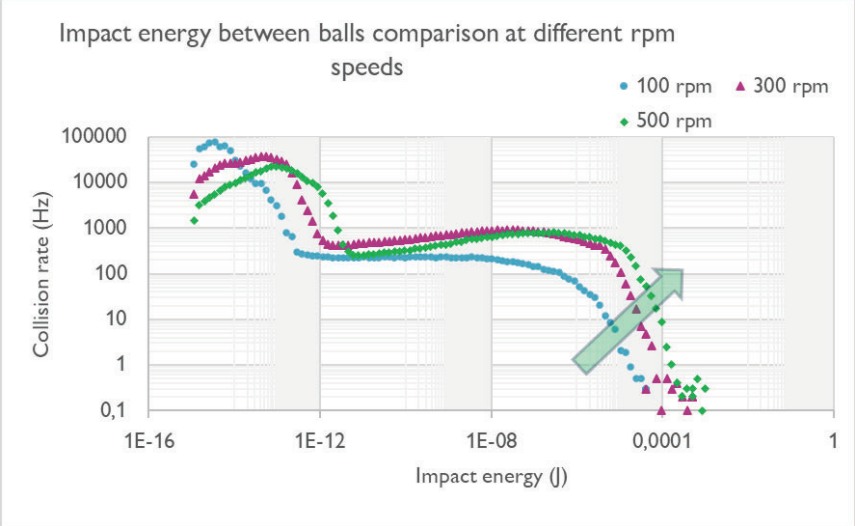

Figure 103: *Impact energy spectra for 0.5 cm steel balls at different angular speeds*

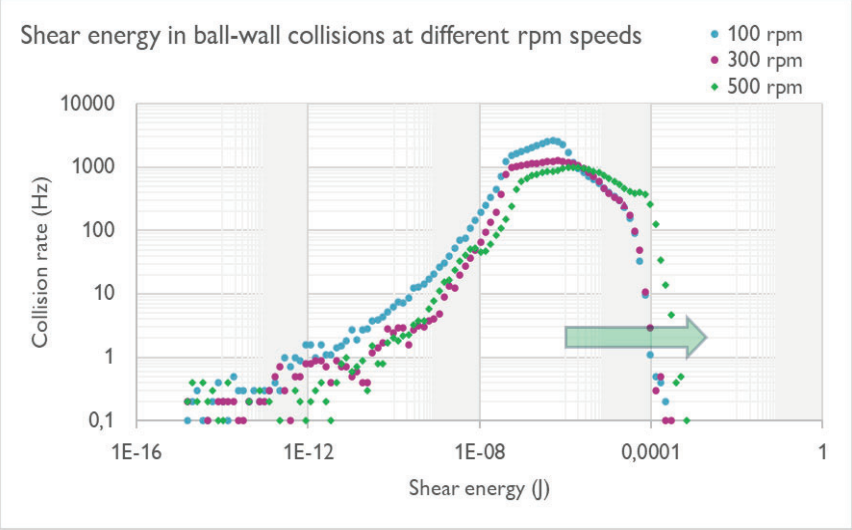

Figure 104: *Shear energy spectra for 0.5 cm steel balls at different angular speeds*

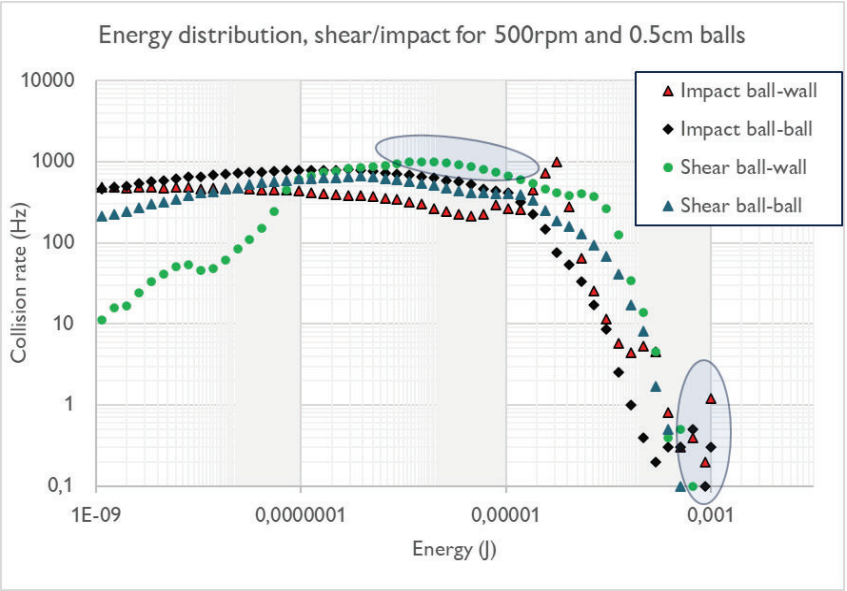

Figure 105: *Energy frequency between different types of collisions*

All materials have an energetic threshold depending on the particle size that separates "useful" collisions from "not useful" ones that do not produce size reduction. Low energy collisions may be dissipated into heat or just able to break down the smallest dust particles. In this sense, it is more desirable to have high energy impact collisions as these are destined to reduce the material to a size where shear impacts (which require less energy as the particles are smaller) can separate layers off them. High angular speed seems to give the most promising results, as 500 rpm gives makes both high energy impact and shearing collisions more frequent.

Figure 105 depicts how frequent and energetic different types of collisions are. The most energetic collisions are from impacts between balls and against the walls of the vessel. Shearing collisions against the wall seem to be frequent in medium range energetic levels, which can be useful to provide shear exfoliation between graphene layers and therefore produce graphene sheets from graphite particles.

The dynamics inside the mill play a critical role in the grinding process. Such dynamics depend greatly on the angular momentum.

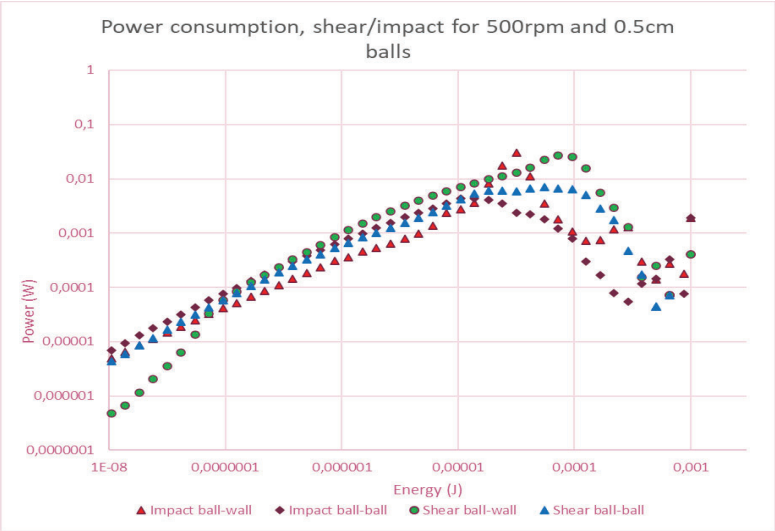

Figure 106: *Power consumption between different types of collisions at each energy level*

Figure 106 shows the power consumed by each type of collision at each energy level. Although previous figures showed that low energy collisions are more frequent, the total sum of them is not enough to overcome the energy that goes into highly energetic collisions. Most effective power is dissipated in ball impacts against the wall ranging from 2.9 $x10^{-5}$ to 3.5 $x10^{-5}$ J and in shearing between the balls and the walls at collisions ranging from 7.0 $x10^{-5}$ J to 8.5 $\cdot 10^{-5}$ J.

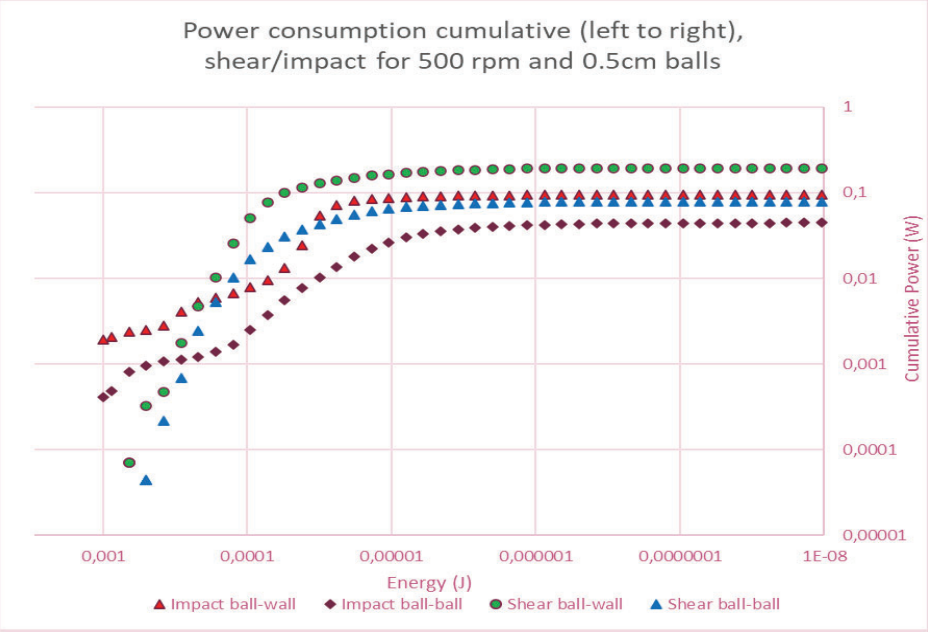

Figure 107: *Cumulative power consumption between different types of collisions at each energy level*

Figure 107 shows the same graph but in a cumulative way, from higher energy levels to the lower ones. Here it can clearly be seen that almost all the power that goes into the interesting collisions (impact and shear) goes into collisions with more than $1x10^{-5}$ J of energy.

While angular speed clearly has a direct effect on the amount of energy that goes into the system, it is not so clear for different ball sizes, as simulations are set up to have similar total masses. The grinding ball size therefore must have an effect not on the amount of energy but on the energy distribution itself and the way the energy is distributed between impact and shearing collisions.

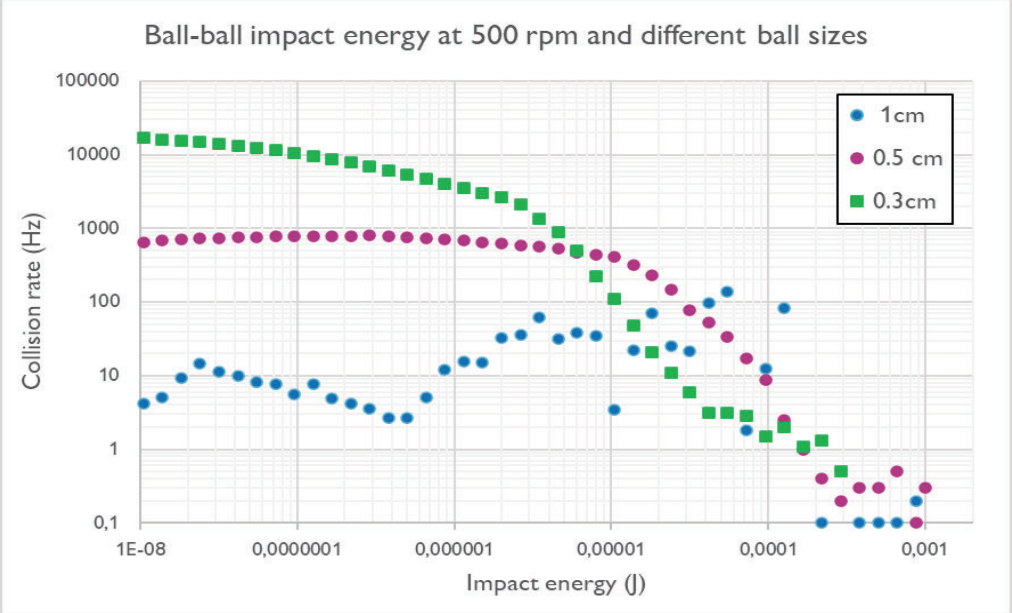

Figure 108: *Impact energy frequency of collision between balls at different ball sizes (500rpm)*

Results show that the size of the ball greatly influences the energy distribution inside the mill. The higher energy impact collisions occur more often only for 0.5 and 1 cm steel balls, while for 0.3 cm balls more power is dissipated in low energy impacts (Figure 108). In order to optimize the mill for impact collisions, 0.5 cm balls give the best results among the tests performed. Steel balls with 1 cm in diameter seem to also provide good performance.

When looking at shear energy, it seems that the greater the ball size, the more energy shearing collisions have and the more frequent those are. Steel balls of 1 cm and at 500 rpm produce ~170 shearing collisions of more than $1x10^{-3}$ J per second (Figure 108).

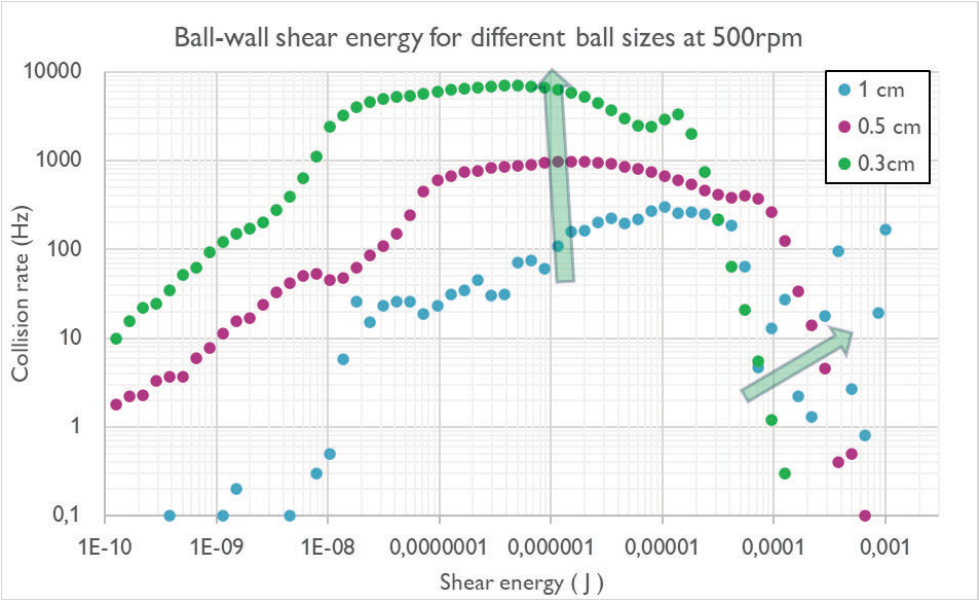

Figure 109: *Shear energy frequency of collision between balls at different ball sizes (500rpm)*

The way in which energy is distributed inside the mill for different ball sizes is a complicated subject. As the angular speed is fixed in all simulations, depending on the mass of the particles, different behaviors may be present, from sticking to the walls to bouncing randomly inside the vessel. Figure 109 represents power draw collision statistics on ball-ball and ball-wall impacts. For all cases shear collisions take more total power than impact collisions, as is expected for a planetary ball mill. For 1 cm balls, most energy is dissipated in shearing collisions against the walls, as lower number of balls make ball-ball collisions less probable. It is also notable that most of the power is consumed in high energy ball-wall collisions ($1x10^{-3}$ J) while in other sizes most power goes to ($1x10^{-5}$ J) ball-wall collisions or ($1x10^{-4}$ J) ball-ball collisions. The 0.5 cm size seems to draw the most power in highly energetic ball-ball collisions while smaller ball sample (0.3 cm) uses similar total power but at lower energy shearing collisions. Some clear trends arise from Figure 110:

The larger balls are the less numerous they become and therefore they are more probable to collide with the walls than between themselves.

The smaller the balls are, the less energetic the collisions are, and more power is dissipated in lower energy collisions.

From all the useful power (which does not directly dissipate into heat) 65.4% and 54.0% go into ball-wall shearing collisions for both 1 cm and 0.3 cm balls respectively. Around 0.5 cm balls there seems to be a minimum as only 46.7% goes into ball-wall shear collisions. Despite this, those types of collisions take more power than any other for all the cases studied.

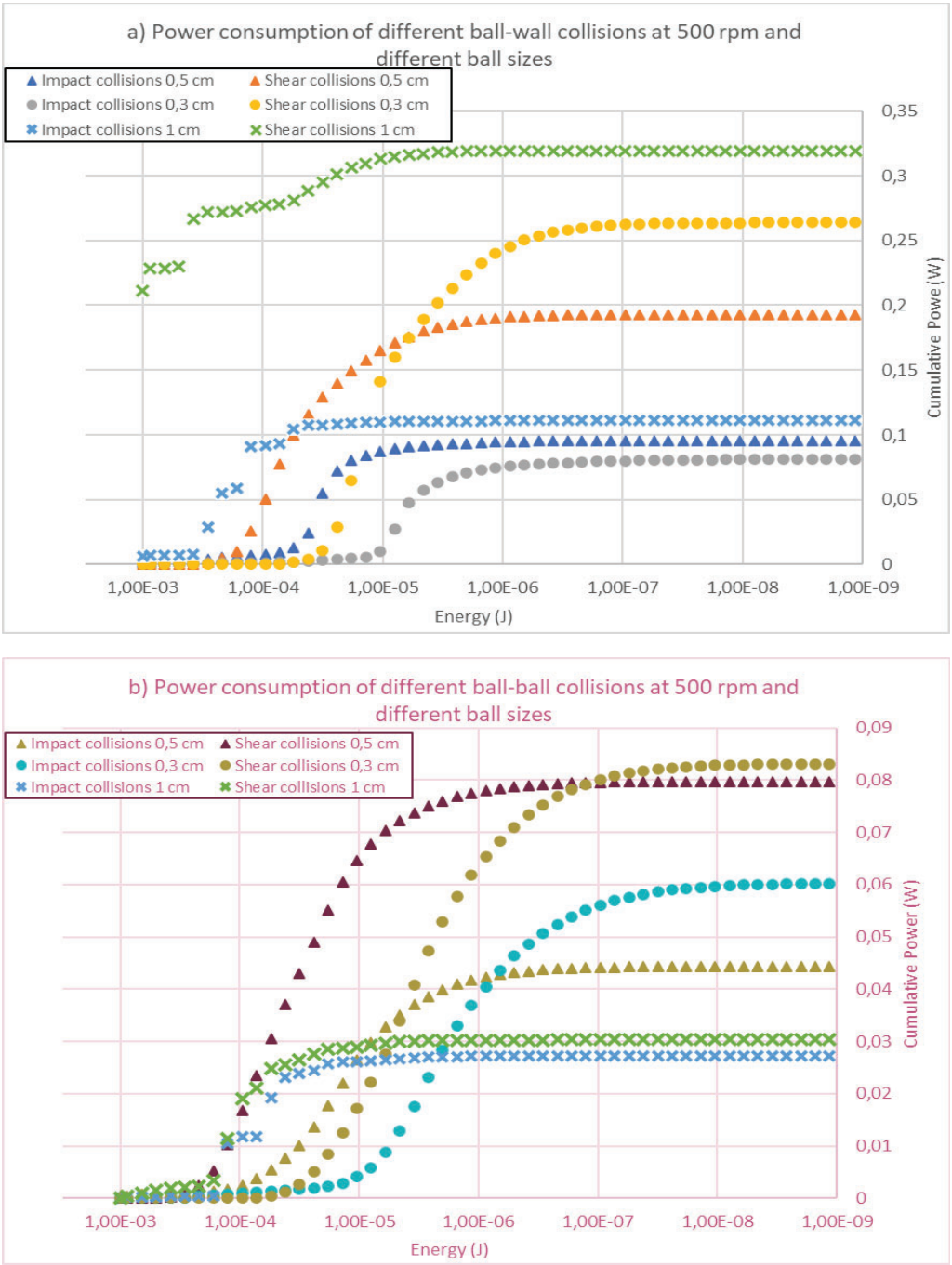

Figure 110: *Power consumption of different collisions at 500 rpm and different sizes. a) Ball-wall collisions. b) Ball-ball collisions*

9.1.2. Simulations involving grinded particles

To better understand the behaviour of materials inside the mill, a simulation has been performed with 10.2 g of 0.5 cm steel balls at 300 rpm and with 0.5 g of graphite material of 150 µm. The total number of graphite particles is 125196 and remains constant. This allows to compute statistics on the truly important collisions which happen against the graphite material particles. Simulations are run for 0.5 seconds and took over a week to complete with current hardware. The total power draw increases from 0.103 W to 0.139 W. Simulations have been performed at 150, 300, 400 and 500 rpm to match

experimental findings. The goal is to find the rotational speed of the mill and time that it takes to produce the graphene flakes and justify the results.

So far, this exploration has been developed experimentally and graphene flakes are only found in high revolution speeds, 400 and 500.

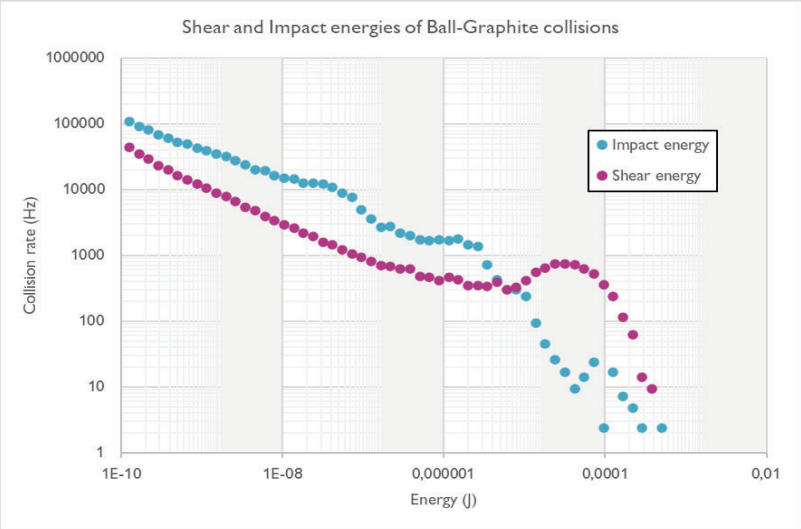

Figure 111: *Collision energy statistics of ball-particle collisions*

Figure 111 shows the energy collision statistics for ball-graphite collisions. At higher energies, shear collisions are more frequent and thus produce more "shearing effects" on the graphite particles such as peeling off layers.

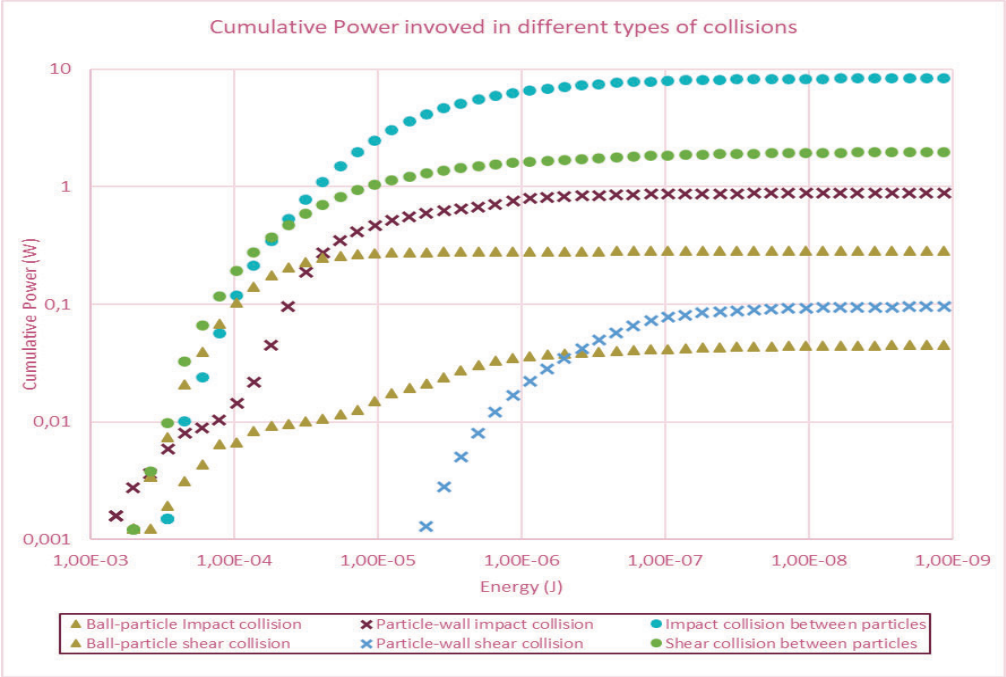

Figure 112: *Cumulative power distribution of all collisions involving graphite particles*

Inside the mill, most of the energy is transferred via impact and shear collisions between graphite particles (Figure 112). Such collisions can be key to understand the grinding properties of the mill, as while not being effective at breaking material down, they are responsible for the transport of most of the kinetic and rotational energy inside the mill. Note that the total cumulative power of impact collisions between particles (8.36 W) is greater than the power draw of the mill. This is since the collisions depicted do not dissipate all the energy, instead transferring it through the system. As opposed to mill power, which measures power flowing into or out of the system, this figure represents power exchanged between particles. Ball-graphite shear collisions also play an important role at high energy bumps, as well as wall-graphite impact collisions. Similarly to the case without grinded particles, different dynamics arise at different revolution speeds. Figure 113 shows the subtle difference between 400 rpm and 500 rpm with the same amount of material.

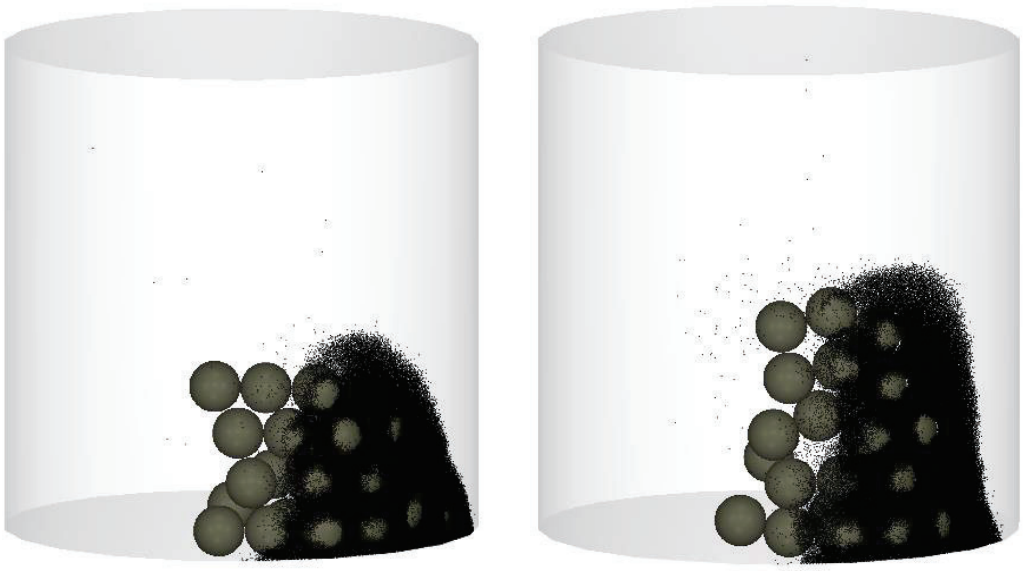

a) b)

Figure 113: *Internal dynamics at different speeds, a) 500 rpm b) 400 rpm*

With increasing speed, again, more energy goes into high energetic collisions, and these become more frequent. Experimental findings suggest that at 500 rpm it takes 8h to start to obtain graphene while at 400 rpm it takes almost 12h. These differences can be explained by the energy spectra of both cases (Figure 109). The useful interactions are the ones that involve graphite particles. All other energies are wasted into deforming the walls or the grinding steel balls or dissipated into heat.

DEM findings indicate that this energy threshold required to break the interlayer bonding of graphene (0.4 J/m2) is surpassed even under low-revolution conditions (100-150 rpm). However, at higher revolutions, collisions surpassing this threshold occur more frequently (approximately twice as frequently between speeds of 150 rpm and 500 rpm). This results in accelerated particle size reduction and increased production of 2D materials at higher milling speeds.

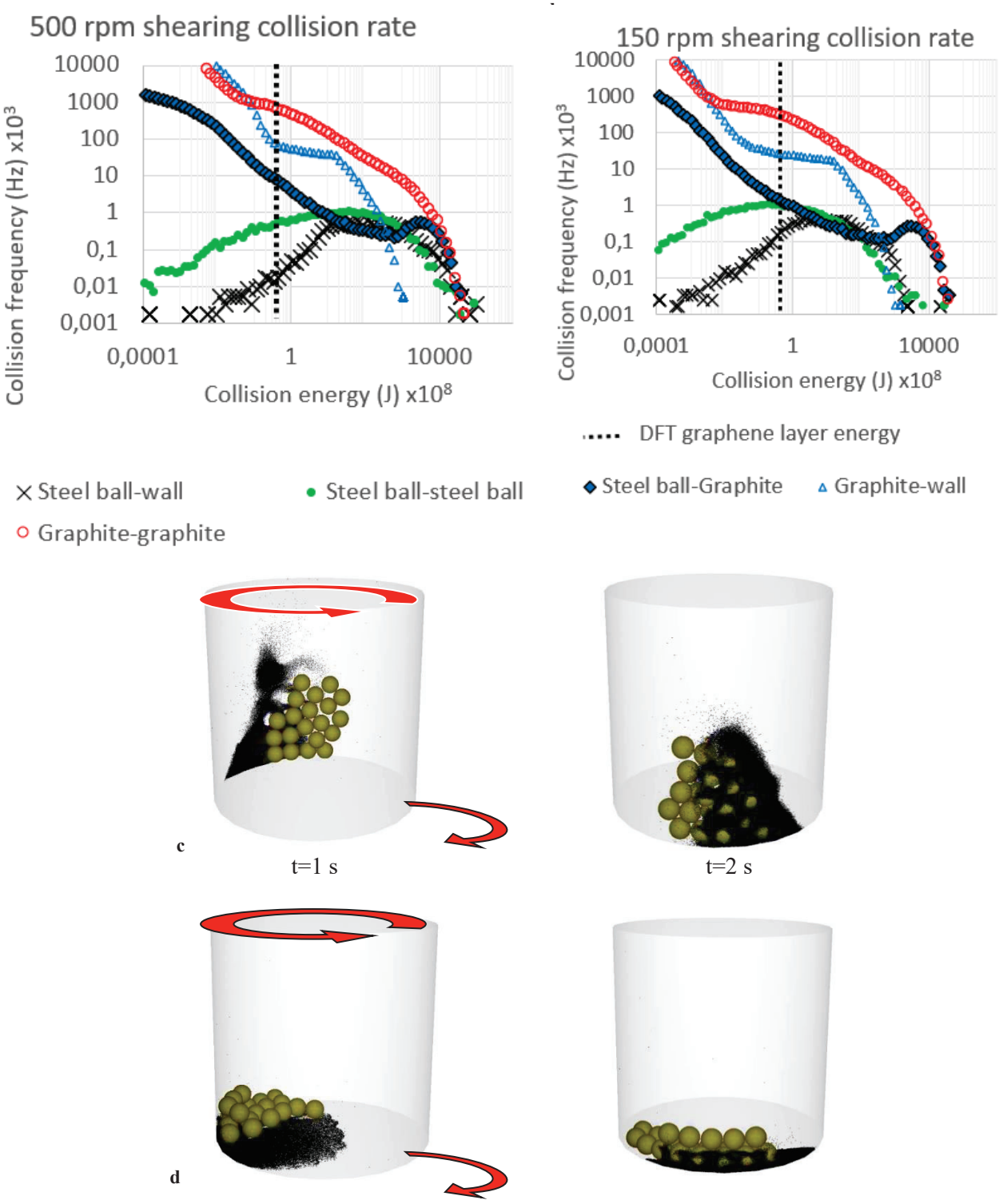

Figure 114: *Collision rate for each shearing energy range and their corresponding 3D simulation image. Vertical line represents the energy threshold required to break graphene layers. Collision rate graph and particle motion inside the mill at, a) 500rpm energy spectra. Black vertical line depicts the threshold found with DFT, b) 150 rpm energy spectra, c) Particle state inside the mill at various times at 500 rpm. In yellow are the grinding steel balls and in black the graphite/graphene material, d) Particle state inside the mill at different times at 150 rpm*

As seen in Figure 109, at 500 rpm balls and particles adhere to the vessel walls, whereas at 150 rpm they remain on the vessel floor. This difference corresponds to the normal forces exerted on the particles by the balls; at 150 rpm, these forces are of the order are comparable to gravity, whereas at 500 rpm, they exceed gravity due to the centripetal forces produced by the mill. DEM simulations combined with Density-Functional Theory predict that exfoliation is feasible even at lower speeds; the key factor then becomes the duration of the operational time to achieve the desired concentration of 2D materials. However, it's noteworthy that 2D materials were not detected experimentally at lower speeds (150-300 rpm), suggesting that they break randomly while retaining their average shape before exfoliation. Exfoliation begins to occur frequently enough to produce significant amounts of 2D materials only after the material has sufficiently reduced in size (from a D50 of 313 μm up to 15 μm at 500 rpm). Because collisions at 150 rpm are less energetic, it takes considerably longer to achieve smaller particle sizes and subsequently initiate significant exfoliation of the material.

9.1.3. Size reduction modelling

In order to relate the size reduction of the graphite particles to the energy spectra obtained from the DEM simulations a model is required. Simple models like Bond's law are considered as they directly relate energy with size reduction. These models are suitable for rough estimations as they use the D50 or D80 particle sizes. The data extracted from experimental conditions is in the form of PSD (Particle Size Distribution) and to take full advantage of this rich data a Population Balance Model (PBM) is used. Contrarily to simpler models, this model has to be tuned with experimental results as most parameters are not available form literature. The model formulation is as follows in Eq. 102 and Eq. 103:

$$\frac{dm_i}{dt} = -K_i(t) * m_i + \sum_{j=i+1}^{N} K_j(t) * m_j * \gamma_{ij} \tag{102}$$

$$K_i(t) = f_{mat} * (\sum_{i=i}^{n} x_i f_{coll} * E_{ml} - \sum_{i=i}^{n} x_i f_{coll} * E_{mmin}) \tag{103}$$

Where i is sieve size, m_i is the mass of particles of size i, $K_i(t)$ is a linear constant dependent on time and size and γ_{ij} refers to the proportion of material of sieve size j (greater that i) that is broken into size i. This parameter has been fitted to a gaussian distribution, requiring two additional fitting parameters. F_{mat} and E_{mmin} are two constants that depend on the grinded material and the particle shape. Finally, f_{coll} and E_{ml} are the frequency of each collision, and the energy involved, which are extracted from the DEM simulations.

As of now, the model assumes that f_{coll} and E_{ml} are constant trough all material sizes, which may not be necessarily true, but it is a useful simplification that allows for the reduction of computational costs in DEM simulations. This simplification can be overturned in the future to fit an even more accurate model.

The model has been adjusted for 500 and 400 rpm cases at different milling times obtaining a suitable accuracy for predicting future results and aiding in the scale up production of graphene. More results are required in order to increase the accuracy of the model and be able to widen the prediction range with different ball sizes or at more revolution speeds, although once fitted with enough data all the geometrical considerations will be considered in the DEM simulations making the model suitable for all cases with various energy spectra results.

To validate the model a prediction is made for a case inside the model range. The model predicts that at 450 rpm the time needed to start exfoliation is around 9h, whereas at 500 rpm was 8h and at 400 rpm it took 12h. These results alongside with the PSD have been confirmed experimentally.

9.1.4. Copper-graphene milling simulations

DEM simulations involving graphene-graphite and copper are performed in order to study the interactions and dynamics present in this process. The goal is to find a process where copper particles remain spherical while adequately covered (minimize the impacts in copper particles but maximizing copper-graphene interactions).

It has been experimentally found that copper balls deform excessively at high rotation speeds like 500 rpm. The only conditions at which balls did not deform significantly were at 150 rpm. Graphene coverage was found to be satisfactory in both cases although several hours are needed at 150 rpm to achieve the desired coverage.

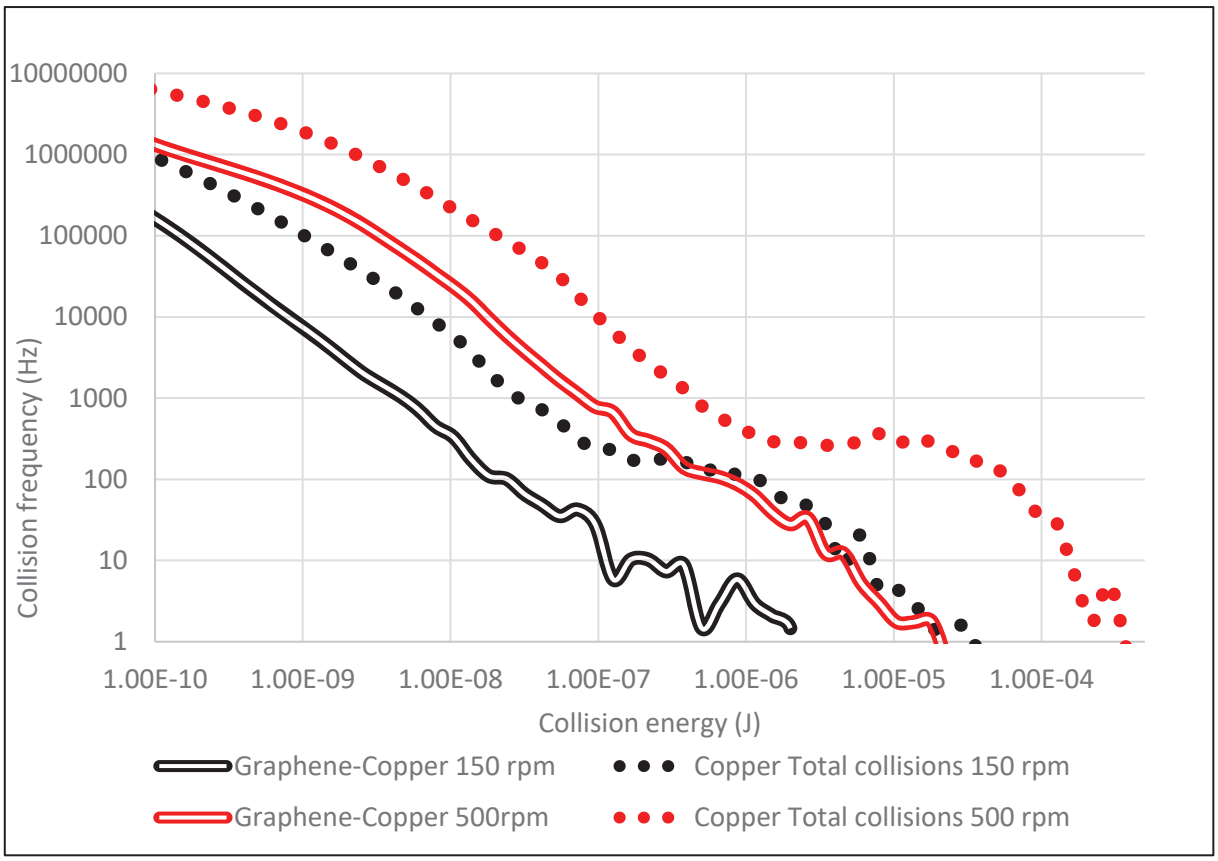

Figure 115: *Energy spectra of graphene-copper interactions and copper total interactions. The comparison is made between the 500-rpm case and the best experimental case at 150 rpm*

In Figure 115, a comparison between 150 rpm and 500 rpm of graphene copper coverage simulations can be seen. Similar results as experimental can be observed: At 500 rpm the interactions between graphene and copper are more energetic and frequent than at 150 rpm which translates to less operational time to achieve the desired coverage. This results in 15 times more energy per second that is involved in these types of interactions. The contrary effect is also notable: as the angular momentum of the mill is increased by 330%, the copper particles are involved in more energetic collisions. This results in 26 times more energy per second that is directly used for the copper deformation.

Increasing the revolution speed means increasing the deformation of copper balls without increasing as much the copper-graphene interactions and therefore the coverage of the copper particles. If the desired product has minimal deformation on copper and maximal coverage, the less angular momentum the better, although this comes with the cost of more operational time to obtain the desired powder.

Experimental results found that somehow the deformation of copper particles was dependant on the presence of graphene inside the mil. It was found that when graphene was not present, copper underwent a much more notable deformation. This analysis is not made numerically but the tendency is clear. DEM simulations are performed to numerically explain this phenomenon.

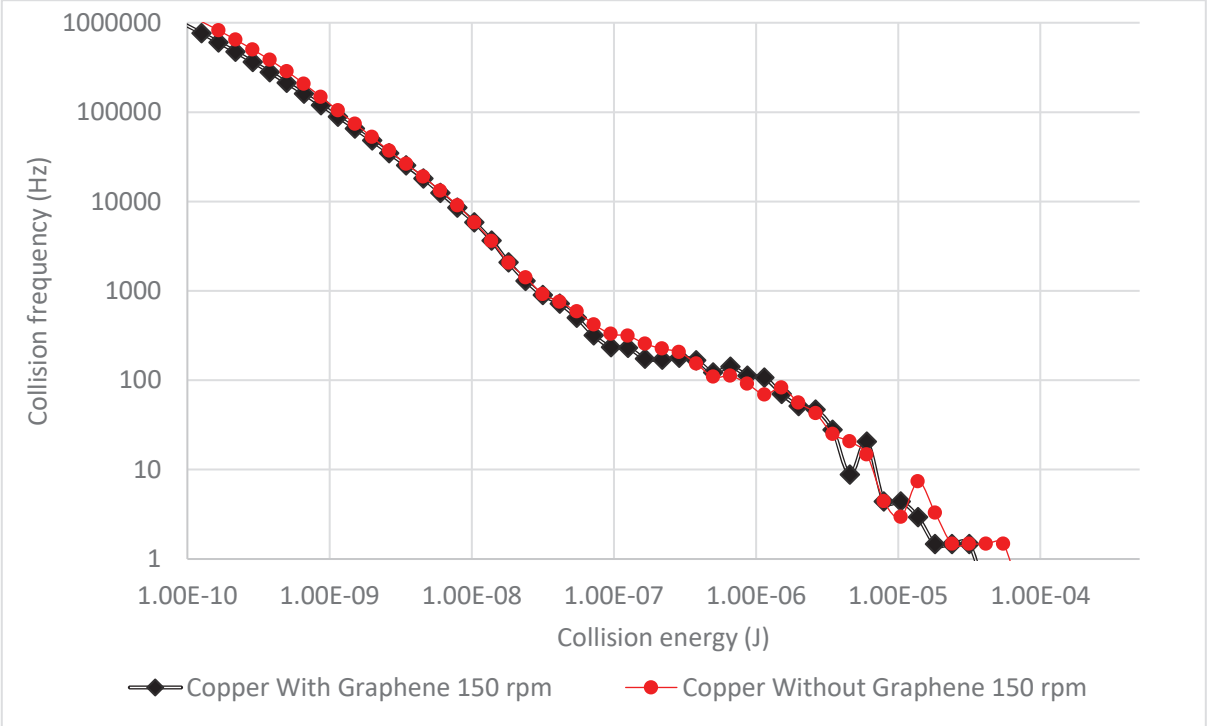

Figure 116: *Energy spectra of copper total interactions with and without graphene present. The comparison is made at 150 rpm*

Figure 116 exhibits these sets of simulations and although the comparison is not as clear as the increase in angular momentum, between a 8-10% more energy is found to be

required to maintain the speed of the mill when graphene is present. Despite this, when graphene is present copper receives from 5-10% less energy (depending on the revolution speed: 8% at 150 rpm) than when the copper is alone. This is a low energy difference, but it accumulates with time making it visible experimentally. This discrepancy is believed to be due to the graphene particles covering the copper ones and absorbing most of its collision energy as seen in Figure 112. The more graphite/graphene particles are present, more damping is thought to be produced for the copper collisions.

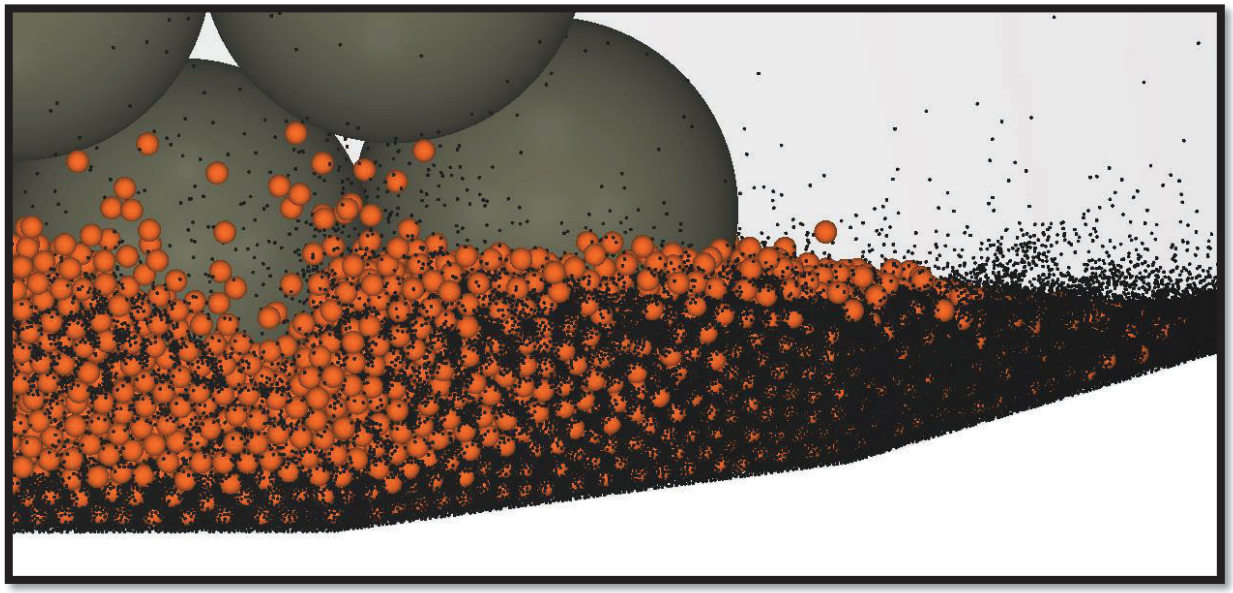

Figure 117: *Snapshot of a DEM simulation involving copper and graphene particles. Graphene covers most of the copper particles dissipating energy to avoid copper deformation*

Despite the presence of graphene, at high revolutions the copper particles still undergo deformation. Therefore, it can be stated that when it comes to deforming the copper, the revolution speed is a much more relevant parameter than the amount of graphene in the mill.

A model for copper-graphene coverage is yet to be proposed, namely because the interactions are not easy to define and because experimentally the coverage analysis is not straightforward. Additionally, the DEM simulations take days or even weeks depending on the number of particles. Multiple variables are to be considered like particle coverage % or graphene thickness. For creating a viable model, more experimental and DEM data are needed.

9.2. Collision simulations of simple cuboids: Finite Element Method

To understand the graphite breakage phenomena, single particle collisions are studied. With these simulations we will be able to discern which collisions and under what conditions cause breakage, delamination or other type of damage. Collisions are

configured at various speeds and impact angles and the stresses inside the particle are obtained. With this data the damage inflicted upon the particle can be derived. Finite Element simulations are performed with LS-DYNA software, an Ansys specialized for impacts and used for crash tests. The simulations involve steel and graphite to see the breakage of graphite. Figure 118 shows the internal energy vs time plot of a graphite particle colliding against a steel ball.

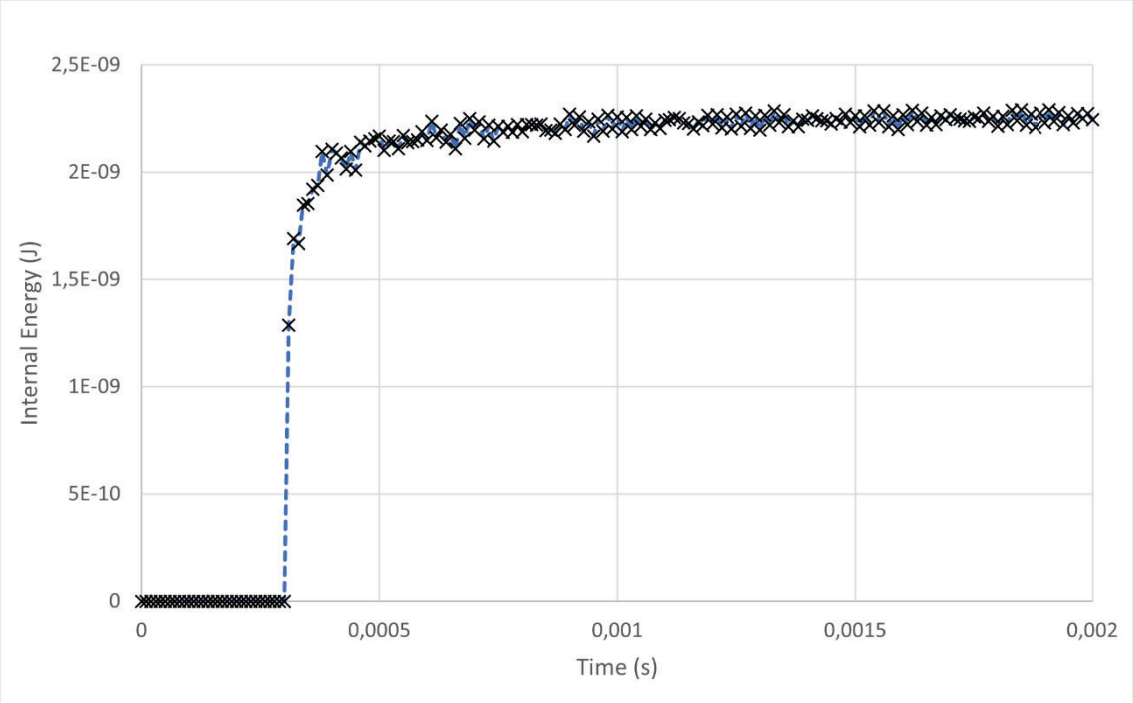

Figure 118: *Internal energy of graphene-steel particle impact at 0.5 m/s*

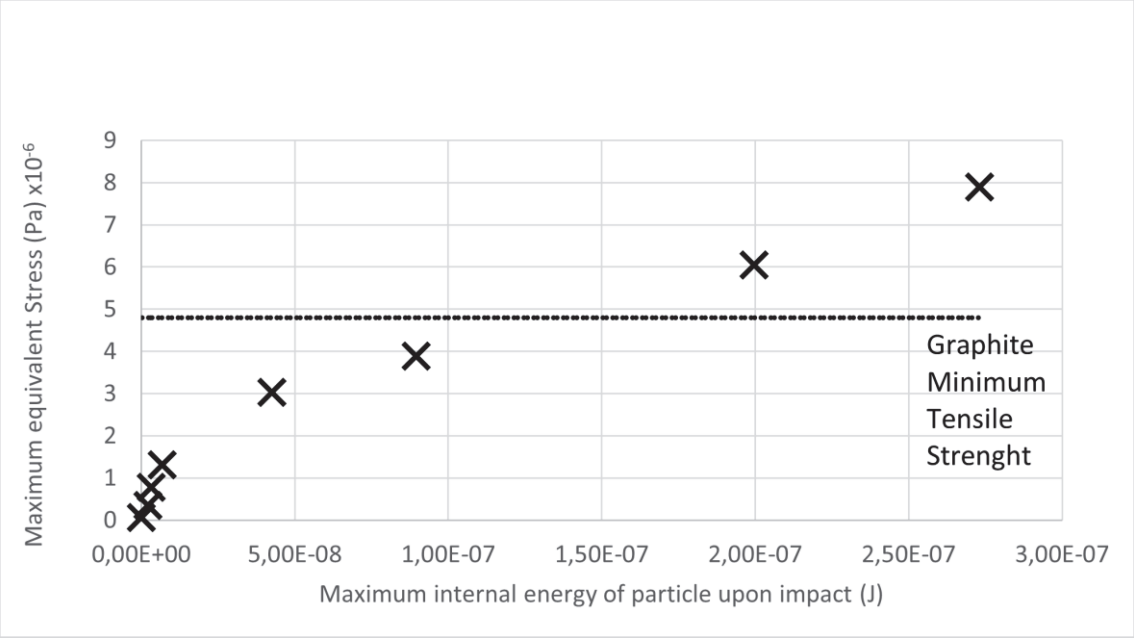

Figure 119: *Internal Energy vs Maximum equivalent stress in graphene particle*

The tested cases ranged along various collision speeds that were seen from DEM simulations (from 0.1 to 5 m/s) and various angles of collision. Figure 119 displays the relationship between the internal energy absorbed in each collision (at different speeds) and the maximum equivalent stress found on the particle. This stress is compared with the tensile strength of graphene and collisions over $1.5x10^{-7}$ J can start exfoliation or graphite breakage for this particle size and shape. This phenomenon will only occur when the particles have enough momentum upon collision and therefore when looking at DEM simulations this fact must be taken into account.

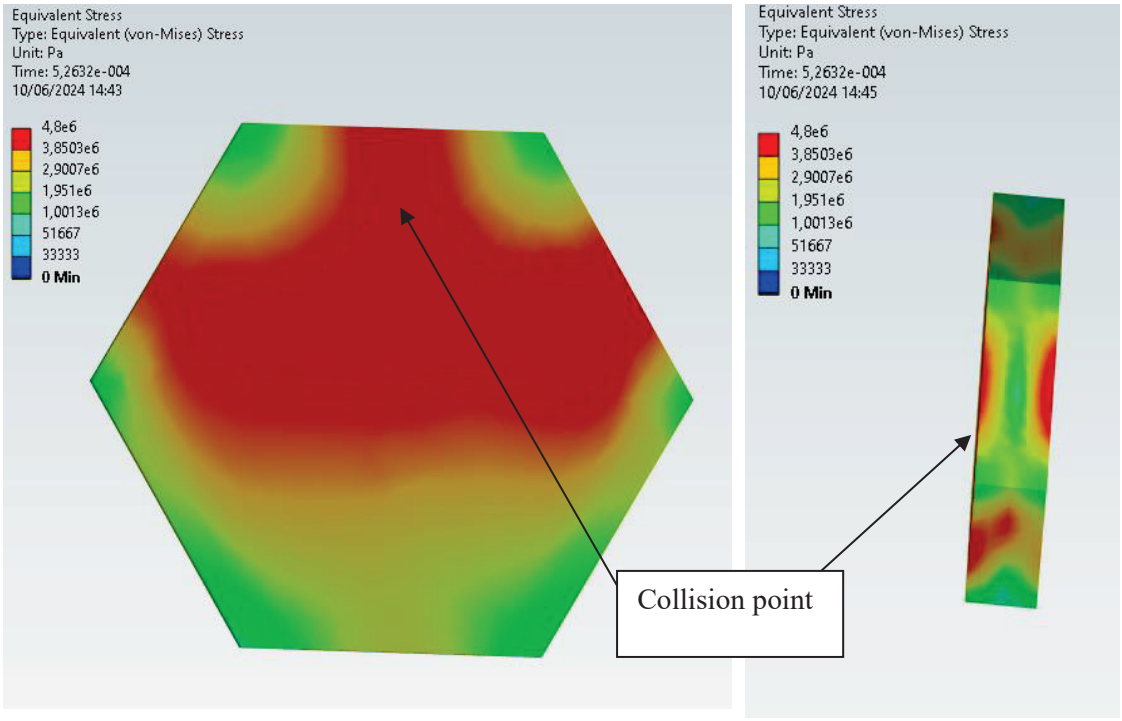

Figure 120: *Equivalent stress distribution on the surface of the particle. Stress upon collision at 5 m/s*

As seen on Figure 120, for a hexagonal shaped particle of 1mm the stresses distribute longitudinally on the particle. This phenomenon means that exfoliation could be produced even in direct normal collisions. And shear collisions are not necessarily more important than the impact ones considered.

Additionally, graphene-copper collisions were also studied interactions in search for some kind of attachment between the two materials. In the simulations performed no sign of attachment has been found, even when the interactions involved multiple collisions between particles. The attachment is in part produced by Van der Waals forces which will be studied at atomic level simulations.

9.3. Density Functional Theory

The attachment between graphene and copper is in due to interatomic forces that allow the binding of those two materials. In order to study these forces, the simulations have to be at an atomic level. DFT (Density Functional Theory) is a technique that allows for the estimation of electronic orbitals and their interactions, making it a reliable tool for this scenario. Density-Functional Theory is used to obtain information about the energy required to delaminate layers of graphene and other 2D material. A lattice of carbon atoms is positioned at distances equivalent to those present in graphite layers and the energy interaction between the carbon orbitals is resolved by solving the Kohn-Sham equations numerically using the VASP software. Density-Functional Theory results predict that the energy required for the exfoliation of graphene is 0.4 J/m2. For spherical particles of an initial size of 150 µm an energy of $7 \cdot 10^{-9}$ J is required in a collision for exfoliation to take place. When studying graphene-copper interactions DFT is limited to a maximum of few hundreds of atoms, as DFT scales as an O(N2~3) algorithm. For this reason, reliably calculating the interaction of large multilayer graphene structures with a lattice of copper atoms is unviable with this technique. DFT will still prove useful for providing accuracy to the Molecular Dynamics technique, as shall be discussed in the next section.

9.4. Molecular Dynamics

The search for a suitable force field that encapsulates all the complicated atomic interactions seems extremely difficult. Some success is found with a force field found in NIST database (National Institute of Standards and Technology, 2025). These simulations consider the carbon bonding of the graphene structure. As seen in Figure 121, the graphene layer bends in a wave shaped style. This has been documented in literature (see Figure 121 footnote).

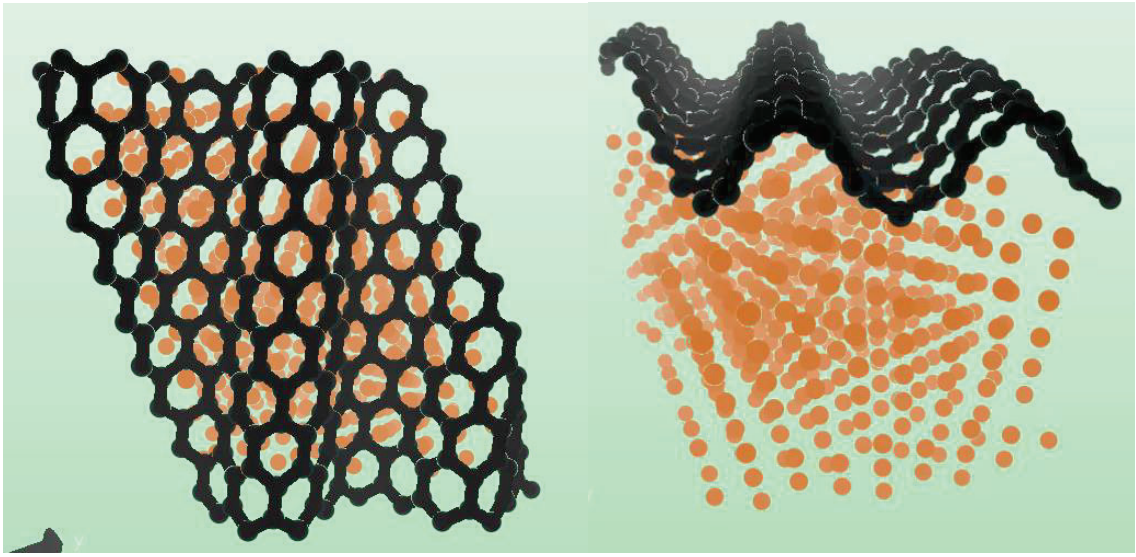

***Figure 121**: Molecular Dynamics simulations of graphene layer on top of copper lattice. Top and side view. The wave shape produced is well documented in literature like the research article form Kowalik et al. (https://www.mdpi.com/2073-4344/11/2/208)*

Although the results seem promising with this force field, they are hard to validate quantitatively. Furthermore, some carbon-copper interactions are missing which means that it is not an entirely accurate model. Therefore, a new technique is developed to increase accuracy and validate the results at the same time in conjunction with DFT.

A high dimensional neural network potential (HDNNP) is used as the complex force field, and it is trained with DFT simulated data for graphene/copper interactions. DFT provides high accuracy in reliably estimating the electronic orbitals. Such precision is encapsuled in the HDNNP which uses the atomic positions and type (Copper or Graphene) and produces a force field very close to what a DFT method would produce. This method is novel and, to our knowledge, has never been applied to copper-graphene interactions. This will allow us to simulate large atomic systems like nanoparticles with high accuracy.

The training models contain graphene/copper with different graphene sizes and defects to account for most of the possible atomic configurations. The copper structure used for these simulations is a Cu(111) surface. A few extra cases are created with DFT outside the training set as a validation set in order to assess the precision of the neural network. In all cases from the validation set the error in formation energy of carbon did not exceed 0.5%.

With this method, the formation energies of graphene/Cu(111) are obtained from MD simulations with the formula, Eq. 104:

$$E_f = \frac{E(\mathrm{Cn/Cu(111)}) - E(Cu_{111}) - n * E(C)}{n} \tag{104}$$

E(Cn/Cu(111)), E(Cu(111)), and E(C) is the energy of graphene/Cu(111), Cu(111) surface, and single C atom, respectively. n is the number of carbon atoms. A study has been conducted on the relationship between this formation energy and the number of carbon atoms present in the graphene particle as seen in Figure 122.

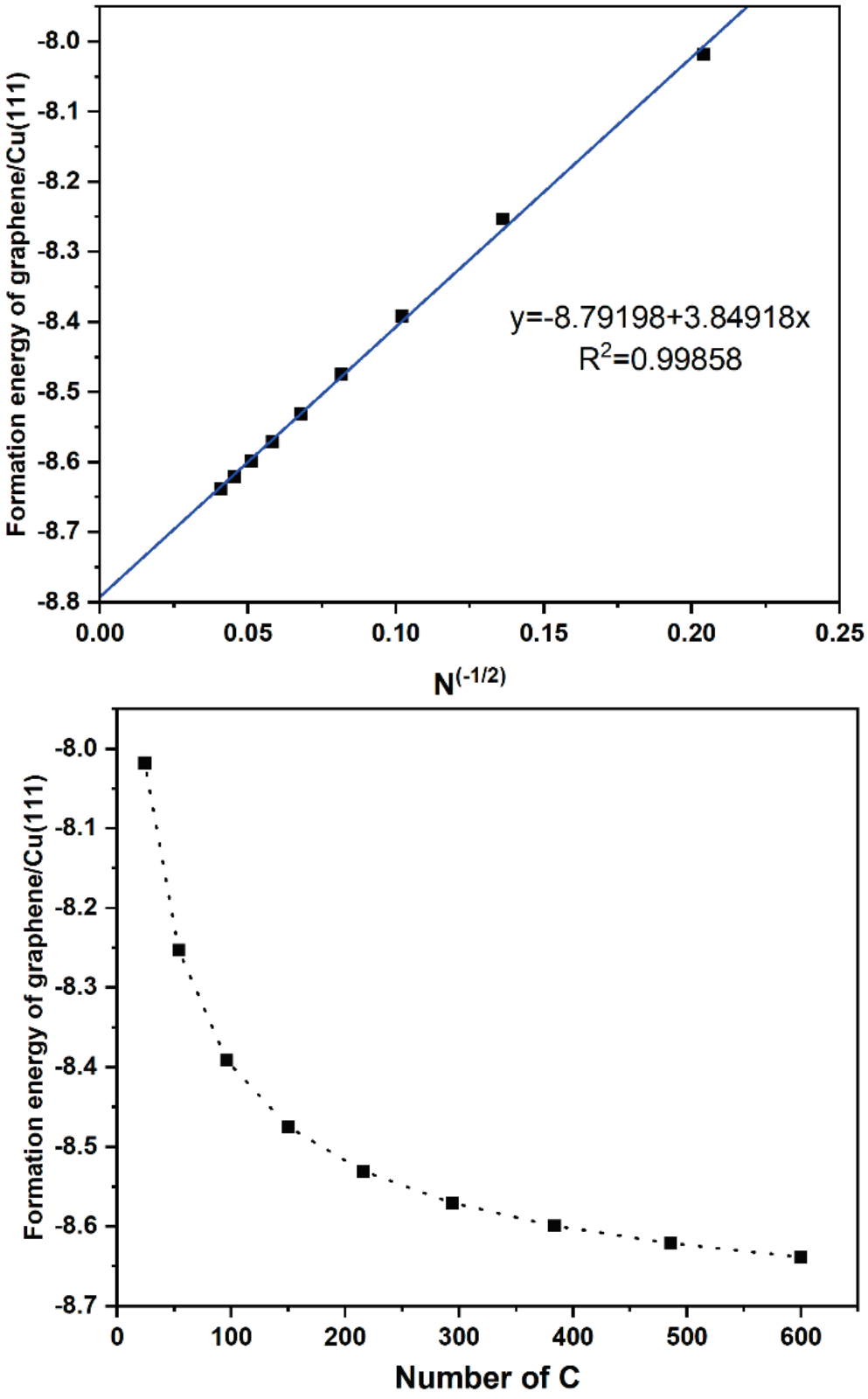

Figure 122: *The per atom formation energy of graphene/Cu(111) versus the number of carbon atoms and the linear relationship between formation energy of graphene/Cu(111) versus* $N^{(-1/2)}$

This relationship establishes that the more carbon atoms are present in a graphene sheet, the more stable the structure becomes. Python code is being created in order to estimate the adsorption energy between copper and graphene which will give useful information

about how strong the graphene-copper attachment is and under which conditions can be produced.

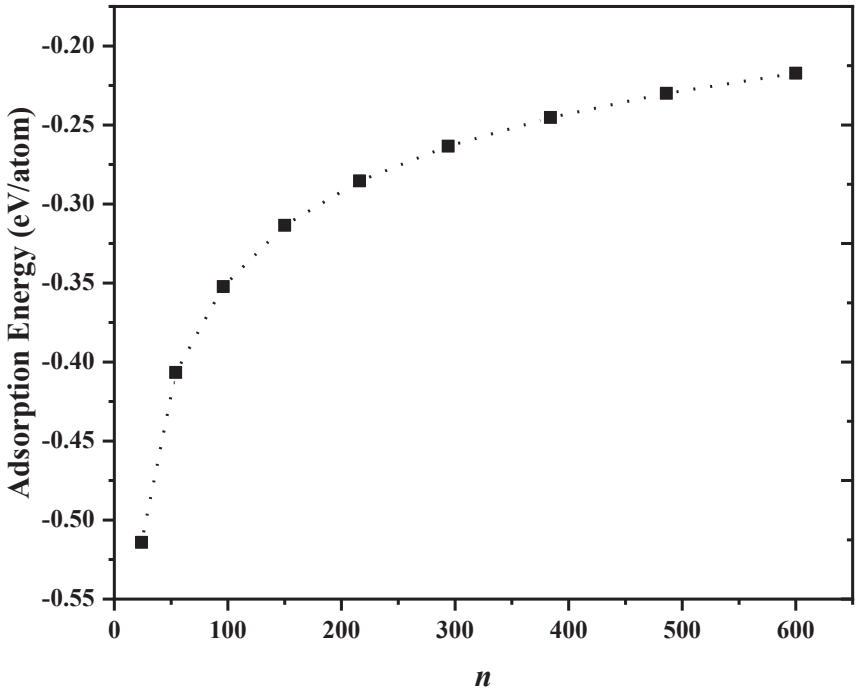

Figure 123: *Variation of the adsorption energy with the number n of carbon atoms. Variation of the adsorption energy with* $N^{-0.5}$

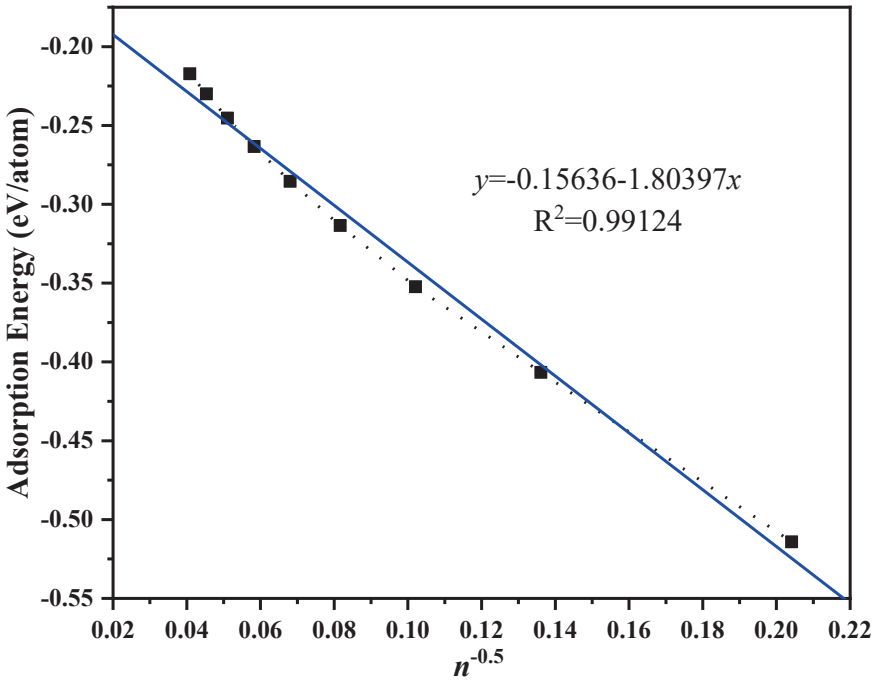

Figure 124: *Relationship between the adsorption energy and the number n of carbon atoms*

It can be seen from Figure 124 that as the number of carbon atoms in graphene increases, the adsorption energy between graphene and the copper surface increases. The adsorption

energy and $n^{0.5}$ exhibit a strong linear correlation, and the coefficient of determination R^2 is 0.99.

9.5. Concluding remarks

A wide range of simulation tools used for this project. Discrete Element Method tools proved to be extremely useful for mill process study. The collected collision energy spectra can be directly correlated with breakage and other processes present inside the unit. Once this model was fitted, the predictions found accordance with experimental reality. For the copper-graphene adhesion, DEM simulations described why the optimal is found at low revolution speeds, and how the presence of different amounts of particles can affect the result. The Finite Element Method simulations performed on the breakage of graphene provided useful information in explaining the delamination process. They also helped describe the energy threshold required to break and delaminate graphite particles down to graphene layers. This method with the setup used, failed to predict attachment between copper and graphene particles, leading the investigation to atomic scale simulations. DFT and MD simulations provided the tools required to estimate reliably the copper-graphene interactions and their energies. A HDNNP trained with DFT model was proposed as force field for MD simulations. MD allowed us to find the adsorption energy of graphene sheets on top of copper, which is key to understand the properties of this nanomaterial.

More work is to be developed in the scope of the Thermodust project, the current focus is in the scale up of the production and finding the operational parameters that correlate with the various powder thermal properties of interest.

10. Conclusions

Computational methods, specially CFD, have been utilized in a wide range of typical Chemical Engineering cases. CFD has been tested in scenarios where momentum, heat and matter transfer are present, and compared against empirical, semiempirical, and other widely used models and Software of each unit. The results showed promising perspectives in all the studied cases: CFD tools provided an accurate description of global engineering variables such as heat transfer coefficients or friction factors, while also being able to describe local variables at specific points of the system such as pollutant concentration.

CFD applied to heat transfer units

In the case of heat transfer, CFD turbulent models have been compared against empirical correlations for simple heat exchangers and twisted tape inserted heat exchangers. Results show great accuracy of the different models tested. The k-ε Standard model provided the best results for pressure drop and heat transfer estimation in simple heat exchangers, with a 9.8% error with respect to mean correlation value. For twisted tape inserted heat exchangers, the k-ε wall treatments, EWT and ML, provided more accurate results compared to experimental correlations. The SST model was also a solid option, with a deviation ranging from 17% to 20%. K-ω models are accurate at predicting pressure loss and capturing fluid features, especially k-ω SST. A novel geometry is optimized by combining corrugated tubes and twisted tapes, resulting in three-dimensional parameters. Results show TPF values at different Reynolds numbers, with heat exchange increasing by 567.8% at the optimal point at Re=24000. These results demonstrate the capabilities of computational fluid dynamics (CFD) in optimizing geometrical problems, but further study is needed to understand the relationships between parameters.

CFD applied to pollutant dispersion

In the case of pollutant dispersion, ANSYS Fluent® is accurate for downwind dispersion and vertical dispersion but tends to overestimate vertical dispersion due to lack of disturbances. This is better than underestimating health impact studies. The mesh refinement function reduces node numbering, preserving accuracy. GPM or ALOHA are preferred for basic cases, but ANSYS Fluent® is reliable for evaluating complex gas emission sources due to its simplicity. This study contributes to gas leakage accident prediction and risk evaluation using various methods.

CFD applied to stirred tank hydrodynamics

For the agitation of stirred tanks, a model is created to correlate Reynolds and power number: $NP = 0.00346 + 2.83 \cdot Re^{-1.00144}$. Velocity gradients induce enhanced heat transfer at the tank bottom dish, thanks to the anchor presence that agitated vividly the fluid. Because of the increased surface area interaction with fluid, power consumption

rises with blade angle. In turbulent regimes, axial flow blades can cut power consumption by up to 64%, while radial flow blades can reduce the thickness of the laminar layer by up to 38%. For a balance between good heat transfer and low energy consumption, mixed flow blades (30º, 45º, and 60º) are advised.

CFD applied to flow in partially full pipes

The ANSYS Fluent solution algorithm has confirmed one equilibrium state between friction and gravity, as found in the Manning equation. Initial conditions do not affect the solution, but the main effects are simulation costs and tube length. Despite not using the Manning equation, ANSYS Fluent respects hydraulic radius and slope exponents. The average mean velocity is equal in both uniform zones, with the elbow only temporarily affecting flow velocity. All simulations kept error percentages below 5%.

Simulation tools for materials engineering

A variety of simulation tools were employed in the Thermodust project's simulations. Tools from the Discrete Element Method were very helpful for studying mill processes. Breakage and other internal unit processes can be directly linked to the gathered collision energy spectra. The predictions were found to be in line with experimental reality after this model was fitted. DEM simulations explained why the optimal copper-graphene adhesion is found at low revolution speeds and how the presence of varying particle concentrations can impact the outcome. Simulations of graphene breakage using the Finite Element Method yielded valuable insights into the delamination process. Additionally, its study contributed to the description of the energy threshold needed to delaminate and break graphite particles down to graphene layers. The investigation proceeded with atomic scale simulations because the setup of this method failed to predict attachment between copper and graphene particles. The methods needed to accurately estimate the copper-graphene interactions, and their energies were made available by DFT and MD simulations. For MD simulations, an HDNNP trained using a DFT model was suggested as the force field. To comprehend the characteristics of this nanomaterial, MD enabled us to determine the adsorption energy of graphene sheets on top of copper.

All the reviewed cases show how multidisciplinary these models and methodologies can be. CFD proved useful in all the cases studied, allowing for optimization or consulting the critical aspects of a unit.

11. Future work

The multiple topics presented on this thesis are still being studied, with different approaches and methods depending on the case.

CFD applied to heat transfer units

In the case of the study of heat exchangers, new geometries can be tested, with a novel approach or combining various already efficient mechanisms like the twisted tape and the corrugated tube presented in this thesis. This inserts not only enhance heat transfer but also increase turbulence, which may be interesting to test for other more complex units like reactors, mixers, or extractors. Plate heat exchangers, other common industrial heat exchanger, are also being researched and analysed from a CFD standpoint.

CFD applied to pollutant dispersion

For pollutant dispersion, CFD offers a great range of possibilities. In this thesis some considerations about the gases in the atmosphere are omitted, like the reactivity of various gases in the atmosphere. These considerations can be accounted for in further cases with more complex emission scenarios. Furthermore, real life cases can be studied by reproducing the exact geometry present in a system.

CFD applied to stirred tank hydrodynamics

Once the hydrodynamics of the stirred tank are dealt with, the next logical step is to add heat transfer and the involved reactions that take place inside the unit.

CFD applied to flow in partially full pipes

Now that CFD has been validated for channel flow and partially full pipes, new cases can be considered, with more complex geometries, or by introducing some interaction between the phases such as reaction or phase change.

Simulation tools for materials engineering

Research in the scope of the Thermodust project is still ongoing and the results presented here are being completed and expanded. The current tasks are aiding in the scale up process by using DEM simulations alongside the PBM modelling. The PBM can be refined to account for additional parameters and different materials. Additionally, the DFT-MD is also being researched, trying to create a HDNNP that can reliably reproduce the force field for multilayer graphene structures.

12. References

Abbasian Arani, A. A., & Uosofvand, H. (2021). Double-pass shell-and-tube heat exchanger performance enhancement with new combined baffle and elliptical tube bundle arrangement. *International Journal of Thermal Sciences*, *167*, 106999. https://doi.org/10.1016/j.ijthermalsci.2021.106999

Abdullah, M. S., & Hussein, A. M. (2023). Thermal Performance of a Helical Coil Heat Exchanger Utilizing Nanofluids: A Review. In *Journal of Heat and Mass Transfer Research* (Vol. 10, Issue 1, pp. 121–134). Semnan University, Center of Excellence in Nonlinear Analysis and Applications. https://doi.org/10.22075/jhmtr.2023.30124.1428

Ahmad, M. A., A. Rashid, Z., El-Harbawi, M., & Al-Awadi, A. S. (2022). High-pressure methanol synthesis case study: safety and environmental impact assessment using consequence analysis. *International Journal of Environmental Science and Technology*, *19*(9), 8555–8572. https://doi.org/10.1007/s13762-021-03724-1

Ahmed, S. K., Kabir, G., & Khan, M. S. A. (2022). Development of a Consequence-Based Decision-Making Framework for Natural Gas Transmission Pipeline. *Innovative Infrastructure Solutions*, *7*(5). https://doi.org/10.1007/s41062-022-00910-z

Air Resources Laboratory. (n.d.). *READY Tools - Pasquill Stability Classes*. Modified: January 3, 2022. Retrieved January 15, 2023, from https://www.ready.noaa.gov/READYpgclass.php

Ajmi, M., Hnaien, N., Marzouk, S., Kolsi, L., Ghachem, K., Ben Aissia, H., & Almeshaal, M. A. (2020). Numerical investigation of heat transfer enhancement of an inclined heated offset jet. *International Communications in Heat and Mass Transfer*, *116*, 104682. https://doi.org/10.1016/j.icheatmasstransfer.2020.104682

Akgiray, Ö. (2004). Simple Formulae for Velocity, Depth of Flow, and Slope Calculations in Partially Filled Circular Pipes. *Environmental Engineering Science*, *21*(3), 371–385. https://doi.org/10.1089/109287504323067012

Akhter, M. N., Ali, M. E., Rahman, M. M., Hossain, M. N., & Molla, M. M. (2021). Simulation of air pollution dispersion in Dhaka city street canyon. *AIP Advances*, *11*(6). https://doi.org/10.1063/5.0033948

ALOHA Software | US EPA. (n.d.-a). Retrieved February 9, 2023, from https://www.epa.gov/cameo/aloha-software

ALOHA Software | US EPA. (n.d.-b). Retrieved February 9, 2023, from https://www.epa.gov/cameo/aloha-software

Alqallaf, J., & Teixeira, J. A. (2022). Numerical study of effects of solid particle erosion on compressor and engine performance. *Results in Engineering*, *15*. https://doi.org/10.1016/j.rineng.2022.100462

Ansys. Engineering Simulation Software. (n.d.). Retrieved February 9, 2023, from https://www.ansys.com/

ANSYS Fluent Theory Guide. (2024). http://www.ansys.com

Aparicio Medrano, E., van de Wiel, B. J. H., Uittenbogaard, R. E., Dionisio Pires, L. M., & Clercx, H. J. H. (2016). Simulations of the diurnal migration of Microcystis aeruginosa based on a scaling model for physical-biological interactions. *Ecological Modelling*, *337*, 200–210. https://doi.org/10.1016/j.ecolmodel.2016.06.019

Barad M. L. (1958). Project Prairie Grass. In *Geophysical Research Papers no 59: Vols. I and II* (Issue 59).

Bernatik, A., Zimmerman, W., Pitt, M., Strizik, M., Nevrly, V., & Zelinger, Z. (2008). Modelling accidental releases of dangerous gases into the lower troposphere from mobile sources. *Process Safety and Environmental Protection*, *86*(3), 198–207. https://doi.org/10.1016/j.psep.2007.12.002

Bhuiya, M. M. K., Chowdhury, M. S. U., Saha, M., & Islam, M. T. (2013). Heat transfer and friction factor characteristics in turbulent flow through a tube fitted with perforated twisted tape inserts. *International Communications in Heat and Mass Transfer*, *46*, 49–57. https://doi.org/10.1016/j.icheatmasstransfer.2013.05.012

Boussinesq, J. (1903). Theórie analytiche de la chaleur mise en harmonie avec la thermodynamique et avec la théorie mécanique de la lumière. *Monatshefte Für Mathematik Und Physik*, *14*(1), A11–A12. https://doi.org/10.1007/BF01706901

Bousso, S., & Fuamba, M. (2014). Numerical and Experimental Analysis of the Pressurized Wave Front in a Circular Pipe. *Journal of Hydraulic Engineering*, *140*(3), 300–312. https://doi.org/10.1061/(ASCE)HY.1943-7900.0000827

Buckingham, E. (1914). On Physically Similar Systems; Illustrations of the Use of Dimensional Equations. *Physical Review*, *4*(4), 345–376. https://doi.org/10.1103/PhysRev.4.345

Camp, T. R. (1946). Design of Sewers to Facilitate Flow. *Sewage Works Journal*, *18*(1), 3–16. http://www.jstor.org/stable/25030187

Chang, J. C., & Hanna, S. R. (n.d.). *Modelers' Data Archive. A Collection of Atmospgeric Transport and Dispersion Data Sets*.

Chang, S. W., Jan, Y. J., & Liou, J. S. (2007). Turbulent heat transfer and pressure drop in tube fitted with serrated twisted tape. *International Journal of Thermal Sciences*, *46*(5), 506–518. https://doi.org/10.1016/j.ijthermalsci.2006.07.009

Chu, W. X., Tsai, C. A., Lee, B. H., Cheng, K. Y., & Wang, C. C. (2020). Experimental investigation on heat transfer enhancement with twisted tape having various V-cut configurations. *Applied Thermal Engineering*, *172*. https://doi.org/10.1016/j.applthermaleng.2020.115148

da Silva, F. T., Reis, N. C., Santos, J. M., Goulart, E. V., & de Alvarez, C. E. (2022). Influence of urban form on air quality: The combined effect of block typology and urban planning indices on city breathability. *Science of the Total Environment*, *814*. https://doi.org/10.1016/j.scitotenv.2021.152670

Date, A. W. (1974). Prediction of fully-developed flow in a tube containing a twisted-tape. *International Journal of Heat and Mass Transfer*, *17*(8), 845–859. https://doi.org/https://doi.org/10.1016/0017-9310(74)90152-5

Dzyaloshinskii, I. E., Lifshitz, E. M., & Pitaevskii, L. P. (1961). General Theory Of Van Der Waals' Forces. *Soviet Physics Uspekhi*, *4*(2), 153–176. https://doi.org/10.1070/PU1961v004n02ABEH003330

Eiamsa-ard, S., Thianpong, C., Eiamsa-ard, P., & Promvonge, P. (2009a). Convective heat transfer in a circular tube with short-length twisted tape insert. *International Communications in Heat and Mass Transfer*, *36*(4), 365–371. https://doi.org/10.1016/j.icheatmasstransfer.2009.01.006

Eiamsa-ard, S., Thianpong, C., Eiamsa-ard, P., & Promvonge, P. (2009b). Convective heat transfer in a circular tube with short-length twisted tape insert. *International Communications in Heat and Mass Transfer*, *36*(4), 365–371. https://doi.org/10.1016/j.icheatmasstransfer.2009.01.006

Eiamsa-ard, S., Thianpong, C., Eiamsa-ard, P., & Promvonge, P. (2010). Thermal characteristics in a heat exchanger tube fitted with dual twisted tape elements in tandem. *International Communications in Heat and Mass Transfer*, *37*(1), 39–46. https://doi.org/10.1016/j.icheatmasstransfer.2009.08.010

Escarti-Guillem, M. S., Hoyas, S., & García-Raffi, L. M. (2019). Rocket plume URANS simulation using OpenFOAM. *Results in Engineering*, *4*. https://doi.org/10.1016/j.rineng.2019.100056

Fischen, C. (2000). *Robert Manning (A Historical Perspective)*. https://erdc-library.erdc.dren.mil/server/api/core/bitstreams/de30b63c-2d7a-4816-8902-337e818e9548/content

Gadave, N. M., & Kothmire, P. P. (2019). Thermo-Hydraulic Performance Evaluation of Shell & Tube Heat Exchanger with Different Tube Geometries. *International Journal of Engineering and Advanced Technology*, *9*(1), 2125–2132. https://doi.org/10.35940/ijeat.A9672.109119

Gant, S. E., & Tucker, H. (2018). Computational Fluid Dynamics (CFD) modelling of atmospheric dispersion for land-use planning around major hazards sites in Great Britain. *Journal of Loss Prevention in the Process Industries*, *54*, 340–345. https://doi.org/10.1016/j.jlp.2018.03.015

George Mason University. (n.d.). *Field Data Sets*. Retrieved February 4, 2023, from http://camp.cos.gmu.edu/FieldDatasetInventory.htm

Gianfelice, M., Aboshosha, H., & Ghazal, T. (2022). Real-time Wind Predictions for Safe Drone Flights in Toronto. *Results in Engineering*, *15*. https://doi.org/10.1016/j.rineng.2022.100534

Habib, A., Schalau, B., & Schmidt, D. (2014). Comparing tools of varying complexity for calculating the gas dispersion. *Process Safety and Environmental Protection*, *92*(4), 305–310. https://doi.org/10.1016/j.psep.2014.02.014

Hanjalić, K., & Kenjereš, S. (2005). Dynamic simulation of pollutant dispersion over complex urban terrains: A tool for sustainable development, control and management. *Energy*, *30*(8 SPEC. ISS.), 1481–1497. https://doi.org/10.1016/j.energy.2004.05.001

Hasanpour, A., Farhadi, M., & Sedighi, K. (2016a). Experimental heat transfer and pressure drop study on typical, perforated, V-cut and U-cut twisted tapes in a helically corrugated heat exchanger. *International Communications in Heat and*

Mass Transfer, *71*, 126–136. https://doi.org/10.1016/j.icheatmasstransfer.2015.12.032

Hasanpour, A., Farhadi, M., & Sedighi, K. (2016b). Experimental heat transfer and pressure drop study on typical, perforated, V-cut and U-cut twisted tapes in a helically corrugated heat exchanger. *International Communications in Heat and Mass Transfer*, *71*, 126–136. https://doi.org/10.1016/j.icheatmasstransfer.2015.12.032

He, W., Toghraie, D., Lotfipour, A., Pourfattah, F., Karimipour, A., & Afrand, M. (2020). Effect of twisted-tape inserts and nanofluid on flow field and heat transfer characteristics in a tube. *International Communications in Heat and Mass Transfer*, *110*. https://doi.org/10.1016/j.icheatmasstransfer.2019.104440

Instituto Nacional de Seguridad e Salud en el Trabajo (INSST). (2014). *Documentación toxicológica para el establecimiento del límite de exposición profesional del dióxido de azufre*. https://www.insst.es/documents/94886/431980/DLEP+86+DIOXIDO+DE+AZUFRE.pdf/d339b938-aa66-4f09-a056-39c2866676af?version=1.0&t=1531400826114

Iskender, H. (2021). Risk assessment for an acetone storage tank in a chemical plant in Istanbul, Turkey: Simulation of dangerous scenarios. *Process Safety Progress*, *40*(4), 234–239. https://doi.org/10.1002/prs.12252

Kohn, W., & Sham, L. J. (1965). Self-Consistent Equations Including Exchange and Correlation Effects. *Physical Review*, *140*(4A), A1133–A1138. https://doi.org/10.1103/PhysRev.140.A1133

Kolmogorov, A. N. (1962). A refinement of previous hypotheses concerning the local structure of turbulence in a viscous incompressible fluid at high Reynolds number. *Journal of Fluid Mechanics*, *13*(1), 82–85. https://doi.org/DOI: 10.1017/S0022112062000518

Kumar, A. (2000). Investigation of twisted tape inserted solar water heatersÐheat transfer, friction factor and thermal performance results. In *Prasad / Renewable Energy* (Vol. 19). www.elsevier.com/locate/renene

Kumar, A., Kumar, M., & Chamoli, S. (2016). Comparative study for thermal-hydraulic performance of circular tube with inserts. *Alexandria Engineering Journal*, *55*(1), 343–349. https://doi.org/10.1016/j.aej.2015.12.013

Kumaresan, T., & Joshi, J. B. (2006). Effect of impeller design on the flow pattern and mixing in stirred tanks. *Chemical Engineering Journal*, *115*(3), 173–193. https://doi.org/10.1016/j.cej.2005.10.002

Lateb, M., Meroney, R. N., Yataghene, M., Fellouah, H., Saleh, F., & Boufadel, M. C. (2016). On the use of numerical modelling for near-field pollutant dispersion in urban environments - A review. In *Environmental Pollution* (Vol. 208, pp. 271–283). Elsevier Ltd. https://doi.org/10.1016/j.envpol.2015.07.039

Launder, B. E., & Spalding, D. B. (1974). The numerical computation of turbulent flows. *Computer Methods in Applied Mechanics and Engineering*, *3*(2), 269–289. https://doi.org/10.1016/0045-7825(74)90029-2

Leelőssy, Á., Molnár, F., Izsák, F., Havasi, Á., Lagzi, I., & Mészáros, R. (2014). Dispersion Modeling of Air Pollutants in the Atmosphere: A Review. *Central*

European Journal of Geosciences, *6*(3), 257–278. https://doi.org/10.2478/s13533-012-0188-6

Liao, Q. (2000). Augmentation of convective heat transfer inside tubes with three-dimensional internal extended surfaces and twisted-tape inserts. In *Chemical Engineering Journal* (Vol. 78).

Lilly, D. K. (1966). *Pre-publication review copy THE REPRESENTATION OF SMALL-SCALE TURBULENCE IN NUMERICAL SIMULATION EXPERIMENTS*.

Lippert, G., Hutter, J., & Parrinello, M. (1997). A hybrid Gaussian and plane wave density functional scheme. *Molecular Physics*, *92*, 477–487. https://api.semanticscholar.org/CorpusID:98127432

Manglik, R. M., & Bergles, A. E. (1992). Heat transfer and pressure drop correlations for twisted-tape inserts in isothermal tubes. Part II. Transition and turbulent flows. *American Society of Mechanical Engineers, Heat Transfer Division, (Publication) HTD*, *202*, 99–106.

Manning, R. (1891). On the flow of water in open channels and pipes. *Transactions of the Institution of Civil Engineers of Ireland, Vol. XX, Pp. 161-207, 1891, Vol. XXIV, Pp. 179-207, 1895*.

Martin, D. O. (1976). Comment On "The Change of Concentration Standard Deviations with Distance." *Journal of the Air Pollution Control Association*, *26*(2), 145–147. https://doi.org/10.1080/00022470.1976.10470238

Mehdi, M., & Panin, M. P. (2021). Use of computational fluid dynamics tools to calculate the dispersion of gas and aerosol emissions in conditions of a complex terrain. *Nuclear Energy and Technology*, *7*(1), 21–26. https://doi.org/10.3897/nucet.7.64366

Menter, F. R. (1994). Two-equation eddy-viscosity turbulence models for engineering applications. *AIAA Journal*, *32*(8), 1598–1605. https://doi.org/10.2514/3.12149

Mittal, S., & Raghuvanshi, A. (2001). Control of vortex shedding behind circular cylinder for flows at low Reynolds numbers. *International Journal for Numerical Methods in Fluids*, *35*(4), 421–447. https://doi.org/10.1002/1097-0363(20010228)35:4<421::AID-FLD100>3.0.CO;2-M

Morton L. Barad. (1958). Project Prairie Grass. In *Geophysical Research Papers No. 59: Vols. I and II (Issue 59)*.

Mouilleau, Y., & Champassith, A. (2009). CFD simulations of atmospheric gas dispersion using the Fire Dynamics Simulator (FDS). *Journal of Loss Prevention in the Process Industries*, *22*(3), 316–323. https://doi.org/10.1016/j.jlp.2008.11.009

Naga Sarada, S., Sita Rama Raju, A. v., Kalyani Radha, K., & Syam Sunder, L. (2012). Augmentation of turbulent flow heat transfer in a horizontal tube with varying width twisted tape inserts. *International Journal of Automotive and Mechanical Engineering*, *6*(1), 797–810. https://doi.org/10.15282/ijame.6.2012.11.0065

Nakhchi, M. E., & Esfahani, J. A. (2020). CFD approach for two-phase CuO nanofluid flow through heat exchangers enhanced by double perforated louvered strip insert. *Powder Technology*, *367*, 877–888. https://doi.org/10.1016/j.powtec.2020.04.043

Natarajan, A., Venkatesh, R., Gobinath, S., Devakumar, L., & Gopalakrishnan, K. (2020). CFD simulation of heat transfer enhancement in circular tube with twisted tape insert

by using nanofluids. *Materials Today: Proceedings*, *21*, 572–577. https://doi.org/10.1016/j.matpr.2019.06.717

National Institute of Standards and Technology. (2025). *IPR (Interatomic Potentials Repository), NIST*. https://www.ctcms.nist.gov/potentials/system/Cu/#C-Cu

National Oceanic and Atmospheric Administration (NOAA). (2013). *ALOHA® (Areal Locations Of Hazardous Atmospheres) 5.4.4: Technical Documentation*.

National Research Council (US) Committee on Acute Exposure Guideline Levels. (2010). *Acute Exposure Guideline Levels for Selected Airborne Chemicals*. National Academies Press. https://doi.org/10.17226/12770

New Zealand. Ministry for the Environment., National Institute of Water and Atmospheric Research (N.Z.), Aurora Pacific (Firm), & Earth Tech (Firm). (2004). *Good Practice Guide for Atmospheric Dispersion Modelling*. Ministry for the Environment.

Nie, W., Cha, X., Bao, Q., Peng, H., Xu, C., Zhang, S., Zhang, X., Ma, Q., Guo, C., Yi, S., & Jiang, C. (2023). Study on dust pollution suppression of mine wind-assisted spray device based on orthogonal test and CFD simulation. *Energy*, *263*, 125590. https://doi.org/10.1016/J.ENERGY.2022.125590

Noorbakhsh, M., Zaboli, M., & Mousavi Ajarostaghi, S. S. (2020). Numerical evaluation of the effect of using twisted tapes as turbulator with various geometries in both sides of a double-pipe heat exchanger. *Journal of Thermal Analysis and Calorimetry*, *140*(3), 1341–1353. https://doi.org/10.1007/s10973-019-08509-w

Nouri, J. M., & Hockey, R. M. (1998). Power Number Correlation between Newtonian and Non-Newtonian Fluids in a Mixing Vessel. *JOURNAL OF CHEMICAL ENGINEERING OF JAPAN*, *31*(5), 848–852. https://doi.org/10.1252/jcej.31.848

Olesen, H. R., Berkowicz, R., & Løfstrøm, P. (2007). Evaluation of OML and AERMOD. *International Conference on Harmonisation within Atmospheric Dispersion Modelling for Regulatory Purposes* .

Oliver, A., Montero, G., Montenegro, R., Rodríguez, E., Escobar, J. M., & Pérez-Foguet, A. (2013). Adaptive finite element simulation of stack pollutant emissions over complex terrains. *Energy*, *49*(1), 47–60. https://doi.org/10.1016/j.energy.2012.10.051

Olsen, N. R. B. (2003). Three-Dimensional CFD Modeling of Self-Forming Meandering Channel. *Journal of Hydraulic Engineering*, *129*(5), 366–372. https://doi.org/10.1061/(ASCE)0733-9429(2003)129:5(366)

Oni, T. O. (2021). Analysis of laminar flow and heat transfer characteristics of fluid in plain and induced tubes. *Engineering Research Express*, *3*(2). https://doi.org/10.1088/2631-8695/abf842

OpenFOAM: User Guide: atmBoundaryLayer. (n.d.). Retrieved September 21, 2022, from https://www.openfoam.com/documentation/guides/latest/doc/guide-bcs-inlet-atm-atmBoundaryLayer.html

Oswald, M. (2015). *ANSYS Best Practicse Guidelines*.

Our World in Data. (2020). *Moore's Law: The number of transistors on microchips doubles every two years*. https://assets.ourworldindata.org/uploads/2020/11/Transistor-Count-over-time.png

Pakchotanon, P., Veawab, A., Aroonwilas, A., & Sema, T. (2022). Atmospheric Dispersion of Gaseous Amine Emitted from Absorption-Based Carbon Capture Plants in Saskatchewan, Canada. *Energies*, *15*(3). https://doi.org/10.3390/en15031221

Pal, E., Kumar, I., Joshi, J. B., & Maheshwari, N. K. (2016). CFD simulations of shell-side flow in a shell-and-tube type heat exchanger with and without baffles. *Chemical Engineering Science*, *143*, 314–340. https://doi.org/10.1016/j.ces.2016.01.011

Perdew, J. P., Burke, K., & Ernzerhof, M. (1996). Generalized Gradient Approximation Made Simple. *Physical Review Letters*, *77*(18), 3865–3868. https://doi.org/10.1103/PhysRevLett.77.3865

Petrik, M., & Szepesi, G. L. (2018). Shell side CFD analysis of a model shell-and-tube heat exchanger. *Chemical Engineering Transactions*, *70*, 313–318. https://doi.org/10.3303/CET1870053

Pourfattah, F., Sabzpooshani, M., Toghraie, D., & Asadi, A. (2021). On the optimization of a vertical twisted tape arrangement in a channel subjected to MWCNT–water nanofluid by coupling numerical simulation and genetic algorithm. *Journal of Thermal Analysis and Calorimetry*, *144*(1), 189–201. https://doi.org/10.1007/s10973-020-09490-5

Promvonge, P., Suwannapan, S., Pimsarn, M., & Thianpong, C. (2014). Experimental study on heat transfer in square duct with combined twisted-tape and winglet vortex generators. *International Communications in Heat and Mass Transfer*, *59*, 158–165. https://doi.org/10.1016/j.icheatmasstransfer.2014.10.005

Rocky DEM. (2020). *DEM Technical Manual*. https://ansyshelp.ansys.com/public/account/secured?returnurl=/Views/Secured/corp/v242/en/dem_tec/dem_tec.html

Saatci, A. (1990). Velocity and Depth of Flow Calculations in Partially Filled Pipes. *Journal of Environmental Engineering*, *116*(6), 1202–1208. https://doi.org/10.1061/(ASCE)0733-9372(1990)116:6(1202)

San José, R., Pérez, J. L., Pérez, L., & Gonzalez Barras, R. M. (2018). Effects of climate change on the health of citizens modelling urban weather and air pollution. *Energy*, *165*, 53–62. https://doi.org/10.1016/J.ENERGY.2018.09.088

Sánchez, P., & Scheeres, D. J. (2011). Simulating Asteroid Rubble Piles With A Self-Gravitating Soft-Sphere Distinct Element Method Model. *The Astrophysical Journal*, *727*(2), 120. https://doi.org/10.1088/0004-637X/727/2/120

Sánchez-Pérez, J. F., García-Ros, G., & Castro, E. (2022). Simultaneous determination of the position, release time and mass release rate of an unknown gas emission source in short-term emissions by inverse problem. *Chemical Engineering Journal*, *445*. https://doi.org/10.1016/j.cej.2022.136782

Schleder, A. M., & Martins, M. R. (2016). Experimental Data and CFD Performance for CO2 Cloud Dispersion Analysis. *Journal of Loss Prevention in the Process Industries*, *43*, 688–699. https://doi.org/10.1016/j.jlp.2016.03.027

Shabanian, S. R., Rahimi, M., Shahhosseini, M., & Alsairafi, A. A. (2011). CFD and experimental studies on heat transfer enhancement in an air cooler equipped with different tube inserts. *International Communications in Heat and Mass Transfer*, *38*(3), 383–390. https://doi.org/10.1016/j.icheatmasstransfer.2010.12.015

Sharma, P., & Kumar Patel, V. (2020). Computational investigation of the thermo-fluidic effects of inserting twisted tape with alternating twists with notches. *Materials Today: Proceedings*, *28*, 1968–1972. https://doi.org/10.1016/j.matpr.2020.05.565

Shen, Z., Lang, J., Li, M., Mao, S., Hu, F., & Xuan, B. (2022). Impact of inlet boundary number and locations on gas diffusion and flow in a typical chemical industrial park near uneven terrain. *Process Safety and Environmental Protection*, *159*, 281–293. https://doi.org/10.1016/j.psep.2022.01.004

Shih, T.-H., Liou, W. W., Shabbir, A., Yang, Z., & Zhu, J. (1995). A new k-ϵ eddy viscosity model for high reynolds number turbulent flows. *Computers & Fluids*, *24*(3), 227–238. https://doi.org/https://doi.org/10.1016/0045-7930(94)00032-T

Shojaee Barjoee, S., Mohammad, &, Elmi, R., Talebi Varaoon, V., Seyed, &, Keykhosravi, S., & Karimi, F. (2022). Hazards of toluene storage tanks in a petrochemical plant: modeling effects, consequence analysis, and comparison of two modeling programs. *Environmental Science and Pollution Research*. https://doi.org/10.1007/s11356-021-15864-5/Published

Smargonsky, J. (1963). General circulation experiments with the primitive equations. *Monthly Weather Review*, *91*(3), 99–164. https://doi.org/10.1175/1520-0493(1963)091<0099:GCEWTP>2.3.CO;2

Spalart, P., & Allmaras, S. (1992, January 6). A one-equation turbulence model for aerodynamic flows. *30th Aerospace Sciences Meeting and Exhibit*. https://doi.org/10.2514/6.1992-439

Sruthi, B., Sasidhar, A., Surendra Kumar, A., & Sahu, M. K. (2021). Comparative analysis of corrugation effect on thermohydraulic performance of double-pipe heat exchangers. *Heat Transfer*, *50*(5), 4622–4642. https://doi.org/10.1002/htj.22092

Synylo, K., Krupko, A., Zaporozhets, O., & Makarenko, R. (2020). CFD simulation of exhaust gases jet from aircraft engine. *Energy*, *213*, 118610. https://doi.org/10.1016/J.ENERGY.2020.118610

Terzioglu, L., & Iskender, H. (2021). Modeling the Consequences of Gas Leakage and Explosion Fire in Liquefied Petroleum Gas Storage Tank in Istanbul Technical University, Maslak Campus. *Process Safety Progress*, *40*(4). https://doi.org/10.1002/prs.12263

Th., M., Schaer, E., Abildskov, J., Feise, H., Glassey, J., Liauw, M., Ó'Súilleabháin, C., & Wilk, M. (2022). The importance/role of education in chemical engineering. *Chemical Engineering Research and Design*, *187*, 164–173. https://doi.org/10.1016/j.cherd.2022.08.061

Tiwari, A. K., Javed, S., Oztop, H. F., Said, Z., & Pandya, N. S. (2021). Experimental and numerical investigation on the thermal performance of triple tube heat exchanger equipped with different inserts with WO3/water nanofluid under turbulent condition. *International Journal of Thermal Sciences*, *164*. https://doi.org/10.1016/j.ijthermalsci.2021.106861

Trindade da Silva, F., Reis, N. C., Santos, J. M., Goulart, E. V., & Engel de Alvarez, C. (2021). The impact of urban block typology on pollutant dispersion. *Journal of Wind Engineering and Industrial Aerodynamics*, *210*, 104524. https://doi.org/10.1016/j.jweia.2021.104524

United Nations Development Programme. (n.d.). *Sustainable Development Goals*. Retrieved November 28, 2024, from https://www.undp.org/sustainable-development-goals

VandeVondele, J., & Hutter, J. (2007). Gaussian basis sets for accurate calculations on molecular systems in gas and condensed phases. *The Journal of Chemical Physics*, *127*(11), 114105. https://doi.org/10.1063/1.2770708

VandeVondele, J., Krack, M., Mohamed, F., Parrinello, M., Chassaing, T., & Hutter, J. (2005). Quickstep: Fast and accurate density functional calculations using a mixed Gaussian and plane waves approach. *Computer Physics Communications*, *167*(2), 103–128. https://doi.org/https://doi.org/10.1016/j.cpc.2004.12.014

Venkatram, A., & Thé, J. (2003). *Introduction to Gaussian Plume Models: Vol. Vol. I* (P. Zannetti, Ed.). The EnviroComp Institute. http://www.awma.org/

Vitali, M., Zuliani, C., Corvaro, F., Marchetti, B., Terenzi, A., & Tallone, F. (2021). Risks and Safety of CO2 Transport Via Pipeline: A Review of Risk Analysis and Modeling Approaches for Accidental Releases. *Energies*, *14*(15). https://doi.org/10.3390/en14154601

Walton, O. R., & Braun, R. L. (1986). Viscosity, granular-temperature, and stress calculations for shearing assemblies of inelastic, frictional disks. *Journal of Rheology*, *30*(5), 949–980. https://doi.org/10.1122/1.549893

Wang, S., Wang, K., Lu, K., & Zhang, Q. (2020). Experimental and numerical analysis for thermal-hydraulic characteristics in circular tubes with twisted tape and wire coil inserts. *E3S Web of Conferences*, *165*. https://doi.org/10.1051/e3sconf/202016506051

Wang, X., Bao, W., Huang, X., Wang, X., Du, F., Wang, D., & Wang, B. (2019). A CFD model based on wet deposition of large-scale natural draft cooling tower. *Revista Internacional de Contaminacion Ambiental*, *35*(Special Issue 1), 23–32. https://doi.org/10.20937/RICA.2019.35.esp01.03

Warsi, Z. U. A. (2005). *Fluid Dynamics*. CRC Press. https://doi.org/10.1201/9781420057881

Węsierski, T., Piec, R., Majder-łopatka, M., Król, B., Gawroński, W., & Kwiatkowski, M. (2021). Hazards Generated by an LNG Road Tanker Leak: Field Investigation of Vapour Propagation Under Class B Conditions of Atmospheric Stability. *Energies*, *14*(24). https://doi.org/10.3390/en14248483

Wilcox, D. C. (1988). Reassessment of the scale-determining equation for advanced turbulence models. *AIAA Journal*, *26*, 1299–1310. https://api.semanticscholar.org/CorpusID:119826448

Wilcox, D. C. (1993). Turbulence modeling. *DCW Industries*.

Wójtowicz-Wróbel, A., Kania, O., Kocewiak, K., Wójtowicz, R., Dzierwa, P., & Trojan, M. (2023). Thermal-flow calculations for a thermal waste treatment plant and CFD modelling of the spread of gases in the context of urban structures. *Energy*, *263*, 125952. https://doi.org/10.1016/J.ENERGY.2022.125952

Wu, W., Rodi, W., & Wenka, T. (2000). 3D Numerical Modeling of Flow and Sediment Transport in Open Channels. *Journal of Hydraulic Engineering*, *126*(1), 4–15. https://doi.org/10.1061/(ASCE)0733-9429(2000)126:1(4)

Xin, B., Dang, W., Yan, X., Yu, J., & Bai, Y. (2021). Dispersion characteristics and hazard area prediction of mixed natural gas based on wind tunnel experiments and risk theory. *Process Safety and Environmental Protection*, *152*, 278–290. https://doi.org/10.1016/j.psep.2021.06.012

Yang, T., & Takahashi, K. (2010). Effect of Impeller Blade Angle on Power Consumption and Flow Pattern in Horizontal Stirred Vessel. *JOURNAL OF CHEMICAL ENGINEERING OF JAPAN*, *43*(8), 635–640. https://doi.org/10.1252/jcej.10we046

Zaboli, M., Nourbakhsh, M., & Ajarostaghi, S. S. M. (2022). Numerical evaluation of the heat transfer and fluid flow in a corrugated coil tube with lobe-shaped cross-section and two types of spiral twisted tape as swirl generator. *Journal of Thermal Analysis and Calorimetry*, *147*(1), 999–1015. https://doi.org/10.1007/s10973-020-10219-7

Zhang, B., & Chen, G. M. (2010). Quantitative risk analysis of toxic gas release caused poisoning - A CFD and dose-response model combined approach. *Process Safety and Environmental Protection*, *88*(4), 253–262. https://doi.org/10.1016/j.psep.2010.03.003

Zhang, C., Wang, D., Ren, K., Han, Y., Zhu, Y., Peng, X., Deng, J., & Zhang, X. (2016). A comparative review of self-rotating and stationary twisted tape inserts in heat exchanger. In *Renewable and Sustainable Energy Reviews* (Vol. 53, pp. 433–449). Elsevier Ltd. https://doi.org/10.1016/j.rser.2015.08.048

Zhang, Z., Lv, J., Li, W., Long, J., Wang, S., Tan, D., & Yin, Z. (2022). Performance and Emission Evaluation of a Marine Diesel Engine Fueled with Natural Gas Ignited by Biodiesel-Diesel Blended Fuel. *Energy*, *256*. https://doi.org/10.1016/j.energy.2022.124662

Appendix

I. Optimization results for the corrugated tube with twisted tape inserts

Table 1: *Optimization results at 15 m/s*

Case	N1	N2	N3	f	f_o	Nu	Nu_o	TPF	Nu/Nu_o	Heat transfer area increase
1	1.041	0.594	0.238	0.136	0.0243	83.9	60.8	0.770	1.38	5.21
2	1.103	2.844	0.837	0.063	0.0246	71.3	58.9	0.887	1.21	2.16
3	1.165	1.719	1.438	0.077	0.0250	79.8	55.8	0.990	1.43	1.64
4	1.227	3.969	0.438	0.143	0.0255	76.0	52.5	0.800	1.45	3.36
5	1.289	1.156	1.037	0.128	0.0258	95.4	50.7	1.09	1.88	1.92
6	1.351	3.406	1.638	0.110	0.0260	84.7	49.4	1.06	1.71	1.53
7	1.414	2.281	0.638	0.226	0.0266	90.5	46.2	1.10	1.96	2.68
8	1.476	4.531	1.238	0.346	0.0267	116.4	45.3	1.13	2.57	1.77
9	1.538	0.875	1.838	0.276	0.0269	95.5	44.3	1.01	2.16	1.46
10	1.600	3.125	0.304	0.289	0.0277	41.5	40.9	0.497	1.01	5.45
11	1.662	2.000	0.904	0.260	0.0278	106.4	40.3	1.22	2.64	2.24
12	1.724	4.250	1.504	0.506	0.0279	100.6	40.0	0.981	2.52	1.64
13	1.786	1.438	0.504	0.608	0.0285	89.3	37.4	0.890	2.39	3.77
14	1.848	3.688	1.104	0.797	0.0285	89.4	37.2	0.842	2.40	2.05
15	1.910	2.563	1.704	0.515	0.0287	131.2	36.6	1.30	3.59	1.58
16	1.972	4.813	0.704	0.541	0.0292	56.5	34.9	0.604	1.62	3.05
17	2.034	0.734	1.304	0.585	0.0292	112.8	34.7	1.14	3.25	1.92
18	2.096	2.984	1.904	0.848	0.0295	122.6	33.9	1.21	3.62	1.53
19	2.159	1.859	0.371	0.717	0.0303	44.8	31.1	0.478	1.44	5.94
20	2.221	4.109	0.971	0.908	0.0302	69.1	31.5	0.737	2.19	2.54
21	2.283	1.297	1.571	0.823	0.0303	108.7	31.3	1.26	3.47	1.79
22	2.345	3.547	0.571	0.618	0.0309	35.4	29.4	0.465	1.20	4.25
23	2.407	2.422	1.171	1.473	0.0309	122.6	29.4	1.08	4.17	2.31
24	2.469	4.672	1.771	1.351	0.0309	67.2	29.4	0.836	2.29	1.72
25	1.414	2.281	0.581	0.330	0.0266	118.1	46.2	1.04	2.56	2.87
26	1.910	2.563	1.760	0.483	0.0287	127.8	36.6	1.30	3.49	1.55
27	1.103	2.232	0.645	0.071	0.0247	77.4	58.4	0.935	1.33	2.52
28	1.414	2.893	0.830	0.282	0.0265	114.7	46.6	0.919	2.46	2.23
29	1.476	3.052	1.238	0.224	0.0267	97.7	45.3	1.17	2.16	1.77
30	2.096	4.464	1.904	0.943	0.0294	123.6	34.0	1.02	3.63	1.53
31	2.407	2.422	0.906	0.782	0.0310	86.6	29.1	1.01	2.98	2.87

32	1.662	2.000	1.169	0.302	0.0277	119.1	40.8	1.23	2.92	1.89
33	1.166	2.984	0.899	0.079	0.0250	73.3	56.0	0.917	1.31	2.07
34	2.034	2.844	1.843	0.725	0.0292	93.4	34.7	1.22	2.69	1.54
35	2.034	0.904	1.306	0.505	0.0293	105.5	34.5	1.18	3.05	1.92
36	1.351	3.237	1.635	0.111	0.0260	86.3	49.5	1.02	1.74	1.53
37	1.655	0.710	0.904	0.336	0.0276	97.9	40.9	0.995	2.39	2.24
38	2.041	2.025	1.304	0.817	0.0294	129.2	34.1	1.24	3.79	1.92
39	2.099	2.984	1.904	0.855	0.0295	117.2	33.8	1.18	3.46	1.53
40	1.469	0.734	1.243	0.204	0.0267	92.8	45.6	1.04	2.04	1.76
41	2.041	4.531	1.299	0.791	0.0293	84.0	34.5	0.948	2.44	1.93
42	2.041	2.013	1.304	0.842	0.0294	131.4	34.1	1.22	3.85	1.92
43	2.096	2.996	1.904	0.796	0.0294	121.8	33.9	1.17	3.59	1.53
44	2.030	2.843	1.900	0.786	0.0292	137.3	34.8	1.28	3.94	1.51
45	1.682	1.927	0.894	0.305	0.0279	108.6	39.8	1.21	2.73	2.28
46	1.890	2.635	1.771	0.571	0.0286	133.8	36.9	1.36	3.62	1.54
47	1.476	4.531	0.911	0.448	0.0268	103.3	45.2	0.907	2.28	2.13
48	1.662	2.000	1.231	0.335	0.0277	123.3	40.6	1.30	3.03	1.83
49	1.446	1.324	0.638	0.161	0.0268	75.2	45.2	1.04	1.66	2.71
50	2.250	2.254	1.571	1.034	0.0302	115.2	31.5	1.18	3.66	1.78
51	2.030	2.843	0.819	0.855	0.0295	108.3	33.8	1.04	3.21	2.74
52	1.662	2.000	1.984	0.267	0.0276	110.1	41.2	1.23	2.67	1.41
53	1.573	2.000	0.904	0.241	0.0273	95.5	42.3	1.19	2.26	2.19
54	2.372	1.297	1.571	0.931	0.0306	125.2	30.3	1.18	4.14	1.83
55	1.662	2.000	0.911	0.260	0.0278	106.4	40.3	1.22	2.64	2.23
56	1.662	2.000	1.224	0.335	0.0277	123.3	40.6	1.30	3.03	1.83
57	1.658	1.309	0.954	0.386	0.0277	113.2	40.5	1.16	2.79	2.16
58	2.287	1.988	1.521	1.080	0.0303	117.5	31.1	1.19	3.78	1.84
59	1.910	2.563	1.704	0.515	0.0287	131.2	36.6	1.30	3.59	1.58
60	1.910	2.563	1.760	0.483	0.0287	127.8	36.6	1.30	3.49	1.55
61	1.889	2.563	1.704	0.550	0.0286	134.4	36.9	1.33	3.64	1.57
62	1.911	2.635	1.771	0.612	0.0287	111.6	36.6	1.15	3.05	1.54
63	1.647	2.000	1.157	0.261	0.0276	125.5	41.0	1.26	3.06	1.89
64	1.905	2.635	1.782	0.617	0.0287	139.8	36.7	1.35	3.81	1.54
65	2.031	2.848	1.900	0.769	0.0292	99.2	34.7	1.24	2.86	1.51
66	2.083	2.979	1.904	0.738	0.0294	126.2	34.0	1.24	3.71	1.52
67	1.692	2.013	1.304	0.349	0.0278	117.3	40.2	1.26	2.92	1.78
68	2.011	2.000	0.904	0.751	0.0294	105.0	34.2	1.07	3.07	2.51
69	1.680	2.000	1.232	0.338	0.0278	122.2	40.4	1.27	3.02	1.83
70	2.265	1.297	1.570	0.832	0.0302	128.4	31.5	1.31	4.08	1.79
71	2.265	1.329	1.570	0.897	0.0302	122.2	31.5	1.25	3.88	1.79
72	1.910	2.530	1.704	0.565	0.0287	131.1	36.5	1.30	3.59	1.58
73	1.910	2.563	1.704	0.515	0.0287	131.2	36.6	1.30	3.59	1.58
74	1.694	1.275	1.220	0.406	0.0278	117.4	40.1	1.19	2.93	1.85
75	2.269	2.022	1.583	1.015	0.0302	113.7	31.4	1.17	3.62	1.78
76	1.890	2.571	1.704	0.529	0.0286	122.8	36.9	1.23	3.33	1.57
77	1.904	2.627	1.782	0.539	0.0287	127.1	36.7	1.33	3.47	1.54

78	1.905	1.953	1.782	0.578	0.0287	120.4	36.6	1.20	3.29	1.54
79	2.041	2.542	1.304	0.826	0.0294	134.3	34.1	1.25	3.94	1.92
80	1.910	2.563	1.704	0.515	0.0287	131.2	36.6	1.30	3.59	1.58
81	1.910	2.563	1.760	0.483	0.0287	127.8	36.6	1.30	3.49	1.55
82	1.910	2.563	1.760	0.483	0.0287	127.8	36.6	1.30	3.49	1.55
83	1.910	2.563	1.760	0.483	0.0287	127.8	36.6	1.30	3.49	1.55
84	1.910	2.563	1.760	0.483	0.0287	127.8	36.6	1.30	3.49	1.55
85	1.888	2.562	1.709	0.535	0.0286	120.5	36.9	1.25	3.27	1.57
86	1.912	2.636	1.766	0.562	0.0287	120.6	36.6	1.40	3.30	1.55
87	1.662	1.942	1.231	0.309	0.0277	113.5	40.7	1.22	2.79	1.83
88	2.030	2.901	1.900	0.828	0.0292	107.9	34.8	1.13	3.10	1.51
89	1.905	1.317	1.704	0.538	0.0287	135.5	36.5	1.32	3.71	1.58
90	2.288	2.542	1.571	1.023	0.0303	103.2	31.1	1.13	3.32	1.80
91	1.905	2.563	1.704	0.591	0.0287	113.4	36.7	1.24	3.09	1.58
92	1.911	1.317	1.704	0.518	0.0287	126.4	36.5	1.33	3.47	1.58
93	1.910	2.563	1.704	0.515	0.0287	131.2	36.6	1.30	3.59	1.58
94	1.910	2.563	1.760	0.483	0.0287	127.8	36.6	1.30	3.49	1.55
95	1.912	1.351	1.564	0.542	0.0288	120.9	36.4	1.27	3.33	1.66
96	2.265	2.582	1.772	1.173	0.0302	139.4	31.5	1.19	4.43	1.65
97	1.911	2.563	1.704	0.561	0.0287	122.1	36.5	1.27	3.35	1.58
98	1.905	2.635	1.771	0.617	0.0287	139.8	36.7	1.35	3.81	1.54
99	1.890	2.635	1.782	0.571	0.0286	133.8	36.9	1.36	3.62	1.53
100	1.890	1.297	1.570	0.508	0.0287	116.6	36.7	1.25	3.18	1.65
101	2.264	2.635	1.771	1.180	0.0302	131.9	31.5	1.25	4.19	1.65
102	1.905	2.562	1.704	0.538	0.0287	133.5	36.7	1.34	3.64	1.58
103	1.910	2.563	1.704	0.515	0.0287	131.2	36.6	1.30	3.59	1.58
104	1.912	2.636	1.706	0.603	0.0287	123.8	36.5	1.28	3.39	1.58
105	1.889	2.563	1.764	0.526	0.0286	132.9	36.9	1.31	3.60	1.54
106	1.890	2.635	1.770	0.489	0.0287	116.5	36.8	1.24	3.17	1.54
107	1.903	2.627	1.782	0.526	0.0287	112.6	36.7	1.20	3.07	1.54
108	1.905	2.562	1.703	0.538	0.0287	133.5	36.7	1.34	3.64	1.58
109	1.905	2.635	1.784	0.617	0.0287	139.8	36.7	1.35	3.81	1.54
110	1.888	2.563	1.704	0.586	0.0286	128.1	36.8	1.33	3.48	1.57
111	1.905	2.635	1.783	0.573	0.0287	137.1	36.6	1.31	3.74	1.54
112	1.905	2.635	1.771	0.617	0.0287	139.8	36.7	1.35	3.81	1.54
113	1.905	2.635	1.782	0.617	0.0287	139.8	36.7	1.35	3.81	1.54
114	1.890	2.635	1.782	0.516	0.0286	131.4	37.0	1.29	3.56	1.53
115	1.905	2.635	1.782	0.573	0.0287	122.7	36.6	1.28	3.35	1.54
116	1.905	2.566	1.698	0.617	0.0287	132.3	36.7	1.27	3.61	1.58
117	1.904	2.623	1.782	0.559	0.0287	126.9	36.7	1.33	3.45	1.54
118	1.904	2.635	1.782	0.575	0.0287	119.0	36.7	1.25	3.24	1.54
119	1.905	2.627	1.782	0.563	0.0287	123.2	36.7	1.26	3.36	1.54
120	1.903	1.320	1.704	0.531	0.0287	125.9	36.5	1.36	3.45	1.58
121	1.911	2.624	1.782	0.653	0.0287	135.0	36.6	1.37	3.69	1.54
122	1.890	2.635	1.766	0.581	0.0286	131.8	37.0	1.32	3.56	1.54
123	1.912	2.636	1.782	0.611	0.0287	133.7	36.5	1.22	3.66	1.54

124	1.903	2.561	1.704	0.578	0.0287	129.5	36.7	1.21	3.53	1.58
125	1.905	2.628	1.782	0.600	0.0287	129.6	36.7	1.31	3.53	1.54
126	1.905	2.635	1.782	0.617	0.0287	139.8	36.7	1.35	3.81	1.54
127	1.904	2.627	1.782	0.539	0.0287	127.1	36.7	1.33	3.47	1.54
128	1.903	2.635	1.782	0.573	0.0287	135.7	36.7	1.43	3.70	1.54
129	1.905	2.627	1.782	0.600	0.0287	123.4	36.7	1.32	3.36	1.54
130	1.903	2.635	1.782	0.573	0.0287	135.7	36.7	1.43	3.70	1.54
131	1.912	2.636	1.766	0.562	0.0287	120.6	36.6	1.40	3.30	1.55
132	1.903	2.627	1.782	0.586	0.0287	129.7	36.7	1.31	3.53	1.54
133	1.911	2.624	1.782	0.653	0.0287	135.0	36.6	1.37	3.69	1.54
134	1.903	1.320	1.704	0.531	0.0287	125.9	36.5	1.36	3.45	1.58
135	1.890	2.635	1.771	0.571	0.0286	133.8	36.9	1.36	3.62	1.54
136	1.890	2.635	1.782	0.571	0.0286	133.8	36.9	1.36	3.62	1.53
137	1.905	2.635	1.782	0.617	0.0287	139.8	36.7	1.35	3.81	1.54
138	1.905	2.635	1.771	0.617	0.0287	139.8	36.7	1.35	3.81	1.54
139	1.905	2.635	1.784	0.617	0.0287	139.8	36.7	1.35	3.81	1.54
140	1.905	2.635	1.771	0.617	0.0287	139.8	36.7	1.35	3.81	1.54
141	1.905	2.635	1.782	0.617	0.0287	139.8	36.7	1.35	3.81	1.54
142	1.905	2.562	1.704	0.538	0.0287	133.5	36.7	1.34	3.64	1.58
143	1.905	2.562	1.703	0.538	0.0287	133.5	36.7	1.34	3.64	1.58
144	1.904	2.623	1.782	0.559	0.0287	126.9	36.7	1.33	3.45	1.54
145	1.904	2.627	1.782	0.539	0.0287	127.1	36.7	1.33	3.47	1.54
146	1.911	1.317	1.704	0.518	0.0287	126.4	36.5	1.33	3.47	1.58
147	1.889	2.563	1.704	0.550	0.0286	134.4	36.9	1.33	3.64	1.57

Table 2: *Optimization results at 10 m/s*

Case	N1	N2	N3	f	f_o	Nu	Nu_o	TPF	Nu/Nu_o	Heat transfer area increase
1	2.05	2.87	1.80	0.893	0.0329	92.5	24.4	1.15	3.79	1.57
2	2.28	2.82	1.89	1.154	0.0341	80.2	22.1	1.17	3.63	1.59
3	1.86	2.99	1.62	0.637	0.0320	95.7	26.5	1.29	3.61	1.61
4	2.17	3.05	2.03	1.022	0.0335	84.4	23.3	1.15	3.63	1.49
5	1.90	3.11	1.98	0.646	0.0321	81.8	26.2	1.24	3.12	1.45
6	1.82	2.70	1.85	0.540	0.0318	93.9	27.0	1.35	3.48	1.49
7	1.93	2.64	1.57	0.757	0.0325	96.5	25.5	1.31	3.79	1.66
8	2.20	2.59	1.66	1.109	0.0338	90.4	22.6	1.15	4.00	1.70
9	2.24	3.16	1.75	1.084	0.0339	82.9	22.4	1.26	3.69	1.65
10	2.13	2.93	1.52	1.014	0.0334	88.5	23.4	1.19	3.79	1.77
11	2.09	2.53	1.94	0.891	0.0332	89.4	23.9	1.41	3.74	1.51
12	1.97	2.76	2.08	0.737	0.0325	96.9	25.3	1.35	3.84	1.43
13	2.01	3.22	1.71	0.828	0.0328	99.9	24.8	1.30	4.03	1.60
14	1.80	2.50	2.10	0.453	0.0316	81.9	27.4	1.27	2.99	1.39
15	1.80	3.25	1.50	0.676	0.0317	93.3	27.3	1.20	3.42	1.67
16	1.90	2.50	1.74	0.700	0.0323	90.8	25.9	1.28	3.50	1.56
17	1.86	2.50	1.97	0.580	0.0320	88.9	26.5	1.30	3.35	1.45
18	2.04	2.69	2.10	0.816	0.0329	89.6	24.5	1.31	3.66	1.43

19	1.94	2.55	2.03	0.707	0.0324	99.5	25.6	1.40	3.89	1.44
20	1.97	2.53	1.84	0.769	0.0326	106.5	25.1	1.48	4.24	1.53
21	2.07	2.78	1.55	0.919	0.0331	93.5	24.0	1.27	3.90	1.72
22	1.89	2.54	1.63	0.708	0.0322	100.0	26.1	1.40	3.83	1.61
23	1.80	3.25	2.02	0.493	0.0316	84.4	27.6	1.19	3.06	1.42
24	1.97	2.50	1.84	0.774	0.0326	93.3	25.1	1.22	3.71	1.53
25	1.92	2.79	1.80	0.670	0.0323	89.5	25.8	1.34	3.47	1.53
26	1.84	2.60	1.91	0.575	0.0319	94.8	26.8	1.36	3.54	1.47
27	1.98	2.58	1.59	0.840	0.0327	96.2	24.9	1.31	3.87	1.67
28	1.84	2.62	1.66	0.624	0.0320	100.4	26.7	1.41	3.77	1.58
29	2.07	2.74	1.76	0.941	0.0331	82.1	24.1	1.22	3.40	1.59
30	1.94	2.71	1.66	0.778	0.0324	95.0	25.5	1.23	3.72	1.61
31	1.91	2.68	1.98	0.663	0.0322	92.7	26.0	1.24	3.57	1.45
32	2.11	2.55	1.70	0.979	0.0333	89.8	23.5	1.28	3.82	1.64
33	2.02	2.65	1.88	0.818	0.0328	85.4	24.7	1.22	3.46	1.52
34	1.99	2.53	2.00	0.727	0.0326	91.8	25.1	1.33	3.67	1.46
35	2.03	2.55	2.05	0.819	0.0328	88.0	24.6	1.30	3.57	1.45
36	1.94	2.61	1.95	0.685	0.0324	78.7	25.6	1.18	3.07	1.47
37	2.04	2.52	1.91	0.777	0.0329	83.5	24.4	1.28	3.42	1.51
38	2.01	2.60	2.01	0.767	0.0327	90.2	24.8	1.25	3.63	1.46
39	1.95	2.59	2.09	0.720	0.0325	93.3	25.4	1.33	3.67	1.42
40	1.91	2.56	1.89	0.710	0.0323	108.1	25.9	1.39	4.17	1.49
41	1.93	2.51	1.97	0.730	0.0324	100.7	25.7	1.39	3.92	1.46
42	1.94	2.58	1.78	0.725	0.0325	88.1	25.5	1.20	3.46	1.55
43	2.02	2.57	1.81	0.809	0.0328	97.0	24.6	1.24	3.94	1.55
44	2.00	2.62	1.87	0.805	0.0327	92.6	24.9	1.35	3.72	1.52
45	1.91	2.51	2.06	0.640	0.0323	93.2	25.9	1.31	3.60	1.42
46	1.97	2.55	1.97	0.783	0.0326	111.7	25.2	1.32	4.44	1.47
47	1.91	2.51	1.93	0.625	0.0323	77.7	25.8	1.28	3.01	1.47
48	1.97	2.53	1.84	0.785	0.0326	104.1	25.2	1.43	4.14	1.53
49	1.93	2.52	1.91	0.722	0.0324	102.0	25.7	1.39	3.97	1.48
50	1.98	2.56	1.86	0.778	0.0326	96.1	25.0	1.38	3.84	1.52
51	1.92	2.54	1.85	0.717	0.0324	96.3	25.7	1.33	3.75	1.51
52	1.97	2.53	2.05	0.708	0.0325	91.7	25.3	1.29	3.62	1.44
53	1.94	2.57	1.99	0.688	0.0324	95.6	25.6	1.33	3.73	1.45
54	1.96	2.57	1.91	0.716	0.0325	87.3	25.3	1.25	3.45	1.49
55	1.95	2.54	1.93	0.777	0.0325	114.2	25.4	1.50	4.49	1.48
56	1.95	2.55	1.81	0.793	0.0325	96.0	25.3	1.31	3.80	1.54
57	1.92	2.53	2.00	0.645	0.0323	97.0	25.8	1.41	3.76	1.45
58	1.98	2.53	1.95	0.781	0.0326	105.9	25.1	1.49	4.21	1.48
59	1.99	2.52	1.80	0.803	0.0327	97.3	25.0	1.32	3.90	1.55
60	1.97	2.53	1.92	0.755	0.0325	108.8	25.3	1.46	4.30	1.49
61	1.94	2.53	1.95	0.761	0.0324	108.3	25.5	1.43	4.24	1.47
62	1.98	2.52	1.90	0.773	0.0327	85.3	25.0	1.26	3.41	1.50
63	1.91	2.54	2.01	0.643	0.0323	106.0	25.9	1.37	4.09	1.44
64	1.95	2.54	1.93	0.730	0.0325	98.9	25.4	1.34	3.89	1.48

65	1.95	2.55	1.98	0.718	0.0325	87.0	25.5	1.18	3.42	1.46
66	1.94	2.53	1.99	0.711	0.0324	96.5	25.6	1.38	3.77	1.46
67	1.95	2.54	1.99	0.714	0.0325	95.5	25.4	1.37	3.76	1.46
68	1.96	2.53	1.92	0.752	0.0325	106.9	25.3	1.43	4.22	1.49
69	1.96	2.54	1.96	0.707	0.0325	77.2	25.3	1.15	3.05	1.47
70	1.93	2.54	1.97	0.691	0.0324	91.9	25.6	1.34	3.59	1.46
71	1.94	2.54	1.90	0.742	0.0324	97.5	25.5	1.40	3.82	1.49
72	1.93	2.53	1.94	0.713	0.0324	106.4	25.7	1.49	4.14	1.47
73	1.94	2.53	1.91	0.706	0.0324	99.7	25.5	1.37	3.91	1.49
74	1.95	2.53	1.97	0.752	0.0325	102.8	25.4	1.38	4.04	1.47
75	1.94	2.55	1.93	0.690	0.0324	92.5	25.6	1.29	3.61	1.48
76	1.96	2.55	1.90	0.752	0.0325	90.7	25.3	1.18	3.59	1.50
77	1.96	2.53	1.90	0.717	0.0325	91.1	25.3	1.38	3.60	1.50
78	1.96	2.53	2.00	0.725	0.0325	98.7	25.4	1.38	3.89	1.46

Table 3: *Optimization results at 25 m/s*

Case	N1	N2	N3	f	f_o	Nu	Nu_o	TPF	Nu/Nu_o	Heat transfer area increase
1	1.041	0.594	0.238	0.120	0.021	122	95.8	0.702	1.27	5.21
2	1.103	2.844	0.837	0.050	0.022	92.8	89.5	0.783	1.04	2.16
3	1.165	1.719	1.438	0.063	0.022	107	84.9	0.889	1.26	1.64
4	1.227	3.969	0.438	0.173	0.022	91.3	80.4	0.646	1.13	3.36
5	1.289	1.156	1.037	0.106	0.023	125	77.6	0.945	1.61	1.92
6	1.351	3.406	1.638	0.090	0.023	115	75.3	0.955	1.52	1.53
7	1.414	2.281	0.638	0.275	0.023	161	71.1	0.924	2.26	2.68
8	1.476	4.531	1.238	0.269	0.023	178	69.4	0.973	2.56	1.77
9	1.538	0.875	1.838	0.253	0.023	131	68.3	0.885	1.92	1.46
10	1.600	3.125	0.304	0.306	0.024	78.2	62.7	0.477	1.25	5.45
11	1.662	2.000	0.904	0.292	0.024	144	62.5	1.03	2.30	2.24
12	1.724	4.250	1.504	0.497	0.024	154	61.4	0.959	2.50	1.64
13	1.786	1.438	0.504	0.511	0.024	122	59.7	0.784	2.05	3.77
14	1.848	3.688	1.104	0.825	0.025	182	57.9	0.868	3.14	2.05
15	1.910	2.563	1.704	0.473	0.025	172	56.4	1.14	3.05	1.58
16	1.972	4.813	0.704	0.483	0.025	80.5	53.4	0.559	1.51	3.05
17	2.034	0.734	1.304	0.489	0.025	117	54.5	0.912	2.14	1.92
18	2.096	2.984	1.904	0.759	0.026	179	52.3	1.07	3.43	1.53
19	2.159	1.859	0.371	0.447	0.026	62.9	49.1	0.483	1.28	5.94
20	2.221	4.109	0.971	0.872	0.026	109	48.7	0.734	2.25	2.54
21	2.283	1.297	1.571	0.735	0.026	176	48.9	1.19	3.60	1.79
22	2.345	3.547	0.571	0.659	0.027	54.0	45.3	0.448	1.19	4.25
23	2.407	2.422	1.171	1.223	0.026	165	46.7	1.03	3.53	2.31
24	2.469	4.672	1.771	1.391	0.027	179	45.4	1.06	3.95	1.72
25	1.414	2.281	0.581	0.255	0.023	141	71.0	0.893	1.98	2.87
26	1.910	2.563	1.760	0.506	0.025	167	56.5	1.07	2.95	1.55
27	1.103	1.009	0.845	0.080	0.022	110	88.6	0.805	1.24	2.15
28	1.289	2.991	1.030	0.117	0.023	125	77.7	0.923	1.61	1.92

29	1.848	3.695	1.104	0.840	0.025	188	57.8	0.834	3.25	2.05
30	1.476	3.052	1.238	0.188	0.023	125	69.3	0.894	1.81	1.77
31	2.096	4.464	1.904	0.974	0.026	185	52.4	1.00	3.53	1.53
32	2.407	2.422	0.906	1.07	0.027	152	46.0	0.872	3.30	2.87
33	1.662	2.000	1.169	0.303	0.024	129	63.0	1.02	2.05	1.89
34	1.166	2.984	0.899	0.065	0.022	101	85.1	0.822	1.18	2.07
35	2.034	2.844	1.843	0.672	0.025	228	53.6	1.20	4.25	1.54
36	1.289	1.291	1.041	0.106	0.023	131	77.5	1.01	1.69	1.91
37	1.351	3.271	1.634	0.090	0.023	113	75.4	0.947	1.50	1.53
38	1.655	0.710	0.904	0.302	0.024	138	64.3	0.893	2.14	2.24
39	2.041	2.025	1.304	0.505	0.025	169	53.2	1.20	3.17	1.92
40	2.469	4.672	1.230	1.22	0.027	114	44.7	0.692	2.54	2.26
41	1.476	4.531	1.779	0.157	0.023	129	70.0	1.02	1.84	1.47
42	2.096	2.984	1.904	0.759	0.026	179	52.3	1.07	3.43	1.53
43	1.293	2.000	0.904	0.110	0.023	123	77.1	0.954	1.59	2.07
44	1.659	1.156	1.037	0.299	0.024	155	63.1	1.05	2.46	2.04
45	1.287	1.291	1.058	0.103	0.023	126	77.7	0.971	1.62	1.90
46	1.478	4.531	1.221	0.226	0.023	137	69.4	1.01	1.97	1.78
47	1.663	1.993	1.704	0.271	0.024	150	63.1	1.09	2.38	1.52
48	1.909	2.569	0.904	0.902	0.025	225	57.4	1.08	3.91	2.43
49	1.730	2.425	1.152	0.390	0.024	179	60.6	1.15	2.95	1.94
50	2.401	4.247	1.523	1.090	0.027	129	46.3	0.898	2.80	1.89
51	2.091	3.003	1.905	0.731	0.026	203	52.4	1.19	3.88	1.53
52	1.476	4.531	1.251	0.236	0.023	142	69.4	0.982	2.05	1.76
53	2.096	2.984	1.890	0.699	0.026	161	52.3	1.11	3.08	1.53
54	1.745	1.378	1.504	0.322	0.024	154	60.7	1.08	2.54	1.65
55	2.092	2.977	1.762	0.670	0.026	150	52.4	1.10	2.87	1.60
56	2.105	2.976	1.762	0.799	0.026	194	52.1	1.04	3.72	1.60
57	2.105	2.976	1.826	0.767	0.026	190	52.1	1.12	3.64	1.57
58	2.105	2.976	1.826	0.797	0.026	206	52.2	1.23	3.94	1.57
59	2.105	2.976	1.826	0.803	0.026	205	52.2	1.27	3.93	1.57
60	2.099	2.975	1.830	0.769	0.026	202	52.3	1.07	3.86	1.56
61	2.101	2.975	1.831	0.713	0.026	162	52.2	1.08	3.10	1.56
62	2.091	3.072	1.905	0.683	0.025	193	52.5	1.03	3.67	1.53
63	2.092	3.070	1.900	0.745	0.026	171	52.4	1.22	3.25	1.53
64	2.091	3.070	1.905	0.731	0.025	160	52.5	1.07	3.06	1.53
65	2.099	2.975	1.846	0.769	0.026	202	52.3	1.07	3.86	1.56
66	2.099	2.975	1.847	0.769	0.026	202	52.3	1.07	3.86	1.56
67	2.099	2.973	1.847	0.840	0.026	219	52.3	1.14	4.18	1.56
68	2.099	2.973	1.847	0.750	0.026	185	52.1	1.00	3.55	1.56
69	2.099	3.068	1.894	0.699	0.026	180	52.2	1.16	3.45	1.53
70	2.091	2.975	1.858	0.606	0.026	151	52.4	1.02	2.88	1.55
71	2.105	3.069	1.905	0.752	0.026	186	52.2	1.14	3.57	1.53
72	2.421	2.531	1.825	1.21	0.027	173	46.4	1.07	3.73	1.67
73	2.421	2.531	1.824	1.21	0.027	173	46.4	1.07	3.73	1.67
74	2.418	2.973	1.847	1.23	0.027	210	46.4	1.15	4.53	1.66

I. Gas dispersion of pollutants supplementary material

Quartile, maximum, and minimum values of the box and whisker plots for each model and point (Figures 72-73) are presented in Tables 4 and 5.

Table 4. *Downwind dispersion parameters of the box-and-whisker diagrams.*

Downwind dispersion	**Model**	**Minimum value**	**First quartile**	**Second quartile**	**Third quartile**	**Maximum value**
50 m	ANSYS	-299	-56	72	167	412
	GPM	-121	-18	96	129	235
	ALOHA	-407	-135	65	138	310
100 m	ANSYS	-102	-21	43	74	142
	GPM	-138	-30	22	44	79
	ALOHA	-162	-47	18	40	50
200 m	ANSYS	-47	-8	12	24	40
	GPM	-52	-11	7	15	26
	ALOHA	-70	-18	3	11	20
400 m	ANSYS	-14	-2	7	10	13
	GPM	-96	-7	3	6	10
	ALOHA	-113	-11	1	3	7

Table 5. *Vertical dispersion parameters of the box-and-whisker diagram*

Vertical dispersion	Model	Minimum	First quartile	Second quartile	Third quartile	Maximum
0.5 m	ANSYS	-4	62	114	134	193
	GPM	-77	-7	46	74	113
1 m	ANSYS	-12	52	88	104	165
	GPM	-47	15	44	71	109
1.5 m	ANSYS	-16	43	75	91	148
	GPM	-22	15	46	74	133
2.5 m	ANSYS	-14	29	53	68	118
	GPM	-11	27	48	74	90
4.5 m	ANSYS	-5	22	29	40	48
	GPM	2	24	41	56	82
7.5 m	ANSYS	3	15	23	32	44
	GPM	1	11	20	22	40
10.5 m	ANSYS	5.5	10.9	14.4	17.9	24.1
	GPM	-0.8	0.0	2.6	10.4	19.4
13.5 m	ANSYS	4.5	6.9	8.9	10.4	11.7
	GPM	-3.6	-1.7	-0.6	0.6	9.1
17.5 m	ANSYS	3.1	3.5	3.9	5.0	6.8
	GPM	-1.1	-0.9	-0.2	-0.1	0.7